A New Crystal Plasticity Framework to Simulate Plastic Deformation Phenomena in Precipitation Hardened Aluminum Alloys

by

Larry Li

A thesis
presented to the University of Waterloo
in fulfillment of the
thesis requirement for the degree of
Doctor of Philosophy
in
Mechanical and Mechatronics Engineering

Waterloo, Ontario, Canada, 2022

© Larry Li 2022

Examining Committee Membership

The following served on the Examining Committee for this thesis. The decision of the Examining Committee is by majority vote.

Supervisor(s)	Kaan Inal, PhD NSERC/General Motors Industrial Research Chair; Professor, University of Waterloo
External Examiner	Frédéric Barlat, PhD Professor, Pohang University of Science and Technology
Internal Examiner	Cliff Butcher, PhD Assistant Professor, University of Waterloo
Internal Examiner	Patricia Nieva, PhD Deputy Chair; Professor, University of Waterloo
Internal-External Examiner	Hassan Baaj, PhD, PEng Associate Chair for Research; Professor, University of Waterloo

Author's Declaration

This thesis consists of material of which I authored or co-authored: see Statement of Contributions included in this thesis. This is a true copy of the thesis, including any required final revisions, as accepted by my examiners.

I understand that my thesis may be made electronically available to the public.

Statement of Contributions

The following co-authors have contributed to the current work as outlined below:

Professor Kaan Inal supervised this PhD thesis.

Dr. Christopher Kohar provided guidance, discussions, conceptualization, and editing of the work. He also provided experimental support including EBSD images for AA6060 and mechanical test data for both AA6060 and AA6061.

Dr. Waqas Muhammad provided experimental support in the form of sample preparation and EBSD measurements for AA6061.

Dr. Raja Mishra provided valuable discussions and conceptualization of the work.

The balance of this work is my own.

Abstract

This thesis outlines the development of a numerical framework for simulating aluminum alloys that exhibit the precipitation hardening phenomenon. A novel crystal plasticity-based precipitation strengthening model is introduced to predict the effects of artificial ageing on the alloy's mechanical properties. In this model, the effect of the precipitate distribution is incorporated via two mechanisms. First, the reduction in the dislocation mean-free path is captured using a yield strength model based on the Peach-Koehler effect. Second, the strain (and stress) accumulated in the precipitates are simulated through an Eshelby inclusion homogenization scheme. The homogenization directly incorporates the orientation-dependence and morphology of the precipitates into the constitutive single crystal response. The model is then implemented into the crystal plasticity finite element method to study the bulk material properties for an AA6060-T6 alloy. The properties of this alloy are characterized using electron backscatter diffraction (EBSD) as well as mechanical testing in both tension and shear. Results of the model are presented and compared to the experiments, and an investigation is performed with the model over a range of different parameters.

To build onto the initial crystal plasticity framework, the model is subsequently modified to incorporate the effect of solute on the yield and work hardening behaviors. This is accomplished by incorporating solid solution strengthening into the model as well as a new dislocation generation factor into the hardening law. In addition, the thermodynamics of the artificial ageing process is simulated using a classical nucleation and growth (CNGT) model for AA6000-series alloys. The CNGT model is used to generate realistic distributions of precipitate over a wide range of heat treatment conditions that are subsequently used as inputs into the proposed crystal plasticity model. The results from the combined kinetics and plasticity framework are presented in a series of simulations for sheet AA6061 alloy. The material is characterized using both EBSD and mechanical testing across various heat treatment conditions to calibrate and evaluate the framework. Simulation results show the ability to predict the yield strength, work hardening, plastic anisotropy and Bauschinger effect across different tempers and demonstrates the applicability of crystal plasticity modeling in age-hardening applications.

Acknowledgements

I would like to express my sincere gratitude to my supervisor, Professor Kaan Inal, for the leadership, assistance, and supervision he has provided me. I am grateful not only for his academic and technical expertise, but also for the moral support and guidance he has provided me to grow as a researcher.

I would like to offer my deepest appreciation and gratitude to Dr. Christopher Kohar for his expertise, motivation, helpful discussions, and for being a great friend and mentor throughout my studies. I cannot express my thankfulness enough for the countless hours of debugging, experimentation, and editing you have spent to make my PhD complete.

I would like to thank all those who were a part of the Computational Mechanics Research Group during my tenure: Dr. Abhijit Brahme for all of his assistance and guidance in microstructure and materials science; Dr. Waqas Muhammad for his experimental assistance and friendly discussions; Dr. Daniel Connolly for being the go-to Python expert and for the occasional anime suggestion; David Booth for his friendship since even before my PhD; Olga Ibragimova for her help in understanding AI and numerous other discussions; Dr. Alena Gracheva for her always entertaining company in the office; Jonathan Tham for all the interesting discussions in the EC4 cafeteria.

I would like to acknowledge all of my friends who were there to support me during this long journey. Special thanks to: Issa Rishmawi, my EC4 neighbor, for all of the life talks and non-technical discussions to keep me sane; Yeaser Abdullah for our countless journeys to Timmy's; Bilun Sun for all of the interesting thoughts on philosophy and finance.

Last and certainly not least, I would like to thank my beloved family. To my parents for all of their support throughout my graduate studies and for sparking my initial interest in engineering. To my partner in crime, Melissa Lee, thank you for keeping me well-balanced, focused and invested – I could not have done this without you.

This work was supported by the Engineering Research Council of Canada – Industrial Research Chair (NSERC-IRC) under grant no. IRCPJ-503185-2016, General Motors of Canada, Ontario Graduate Scholarship (OGS), Queen Elizabeth II Graduate Scholarship in Science and Technology (QEII-GSST), Arthur F. Church Scholarship, and President's Graduate Scholarship of Waterloo.

Table of Contents

List of Figures

List of Tables

1 Introduction

The widespread adoption of electric vehicles, automation, and autonomous driving has attracted a surge of interest to the automotive industry. Automakers today are tasked with developing faster, smarter, and more aesthetic vehicles while simultaneously required to abide to ever more stringent safety and emissions standards [1]. As a result, the industry is pressured to invest in new research to produce superior vehicles with better utility and at higher production rates. Research in the development of lightweight materials is a proven method for advancing innovation in the automotive industry. Heavier components can be replaced with equivalent lighter materials through detailed material characterization and intelligent design optimization. This allows automakers to reduce vehicle emissions, maintain safety standards and offer possibilities for new features and technologies.

Aluminum alloys are a class of lightweight metals that are suitable for many different automotive applications [2]. Research in alloy design has resulted in the development of several classes of aluminum alloys that are categorized based on their physical properties. Among these categories are precipitation hardening aluminum alloys that can be strengthened from an artificial heat treatment process. These materials have vastly superior strengths compared to pure aluminum and offer considerable potential for weight reduction applications. Their high strength is achieved by the controlled nucleation of small particles, called precipitates, that offer rigidity at the nanoscale. A large advantage in using precipitation hardenable alloys is the ability to tune the material's physical properties during production. For example, aluminum alloys can be formed into components in their most ductile state and then artificially aged at a later time to raise their overall strength.

Owing to the intricate behaviors in many of the new lightweight materials, the research and development process is rapidly transitioning into a virtual environment by use of computer simulations. Numerical models help expedite new products to market by reducing the amount of experimental work that is both costly and time-consuming to perform. Examples include simulations of forming processes to investigate the possibility of failure or the use of machine learning for the optimization of component geometries [3–7]. For precipitation hardening alloys, numerical modeling is particularly important as the material's properties are highly sensitive to the heat treatment and the underlying precipitate distribution. Even small changes in the characteristics of the precipitates can result in major effects on the alloy's strength and ductility.

It is therefore of interest to be able to simulate the heat treatment process and its effect on the physical properties of the alloy.

This thesis aims to develop a simulation framework that can be used to model precipitation hardened aluminum alloys over a wide range of heat treatment conditions. While there are various theories and models in the literature, there has been substantial development in the experimental characterization of precipitates that can be leveraged to enhance existing models. The proposed methodology in this research includes both the simulation of precipitation kinetics as well as the effect of the precipitates on the resulting mechanical properties. The kinetics portion will be based upon classical nucleation and growth methodology while the mechanical portion will be developed within a crystal plasticity framework. The model will be used to investigate the impact of various heat treatment conditions on both the single crystal and polycrystal response in aluminum alloys. As part of this work, mechanical characterization will be conducted on AA6000-series alloys to calibrate and evaluate the performance of the simulations. This includes new experimental data for precipitation-induced anisotropy and kinematic hardening. Ultimately, the goal of this research is to provide a set of tools and methodologies to support the design and implementation of advanced aluminum alloys into commercial applications.

This thesis is constructed as follows: Chapter 2 presents the general background knowledge that is helpful for understanding this document. This includes an introduction to microstructure, strengthening mechanisms in crystals, precipitation hardening, some experimental methods, and an overview of numerical modeling techniques. Chapter 3 presents a literature review on state-of-the-art models for simulating artificial ageing and precipitation hardening. Chapter 4 describes the research objectives and strategy used throughout this work. Chapter 5 and Chapter 6 present the research results of this thesis. These chapters are based on works that have been published into literature. Finally, Chapter 7 presents the conclusions of this work as well as a summary of the model's limitations and potential solutions. In addition, possible future research that can be done to improve on this work is also suggested.

2 Background

2.1 Microstructure

Microstructure forms the backbone of metallics and is responsible for many of their physical properties and behaviors. This section provides a brief introduction on several microstructural concepts that are used in this dissertation.

2.1.1 Crystal Structure

The atoms in metallic elements are joined by metallic bonding where the cations are embedded in a sea of valence electrons. An example of metallic bonding is shown in the schematic of Fig. 2-1. The electrons are delocalized and scattered randomly across the sample while the cations have fixed positions that repeat in a regular arrangement. The ordered behavior of the cations forms what is known as a crystal and metallics in particular have high degrees of structural crystallinity.

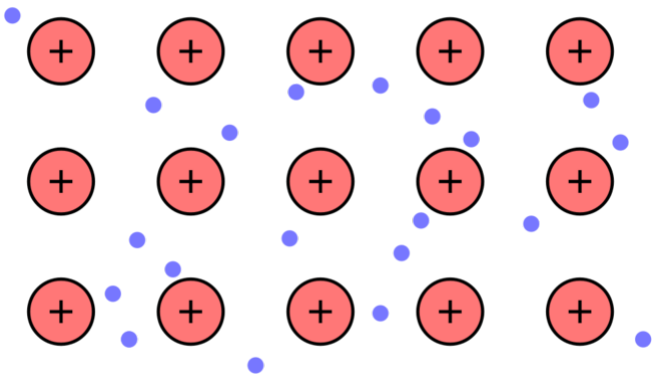

Fig. 2-1. Schematic of metallic bonding showing possible electron positions (blue) around the nuclei of atoms (red) [8].

Crystalline materials are defined by the smallest repeating arrangement of atoms in the structure, also known as a unit cell. Common unit cells are shown in Fig. 2-2, which include the body-centered cubic (BCC), face-centered cubic (FCC), and hexagonal closed pack (HCP) arrangements. The lattice structure plays a critical role in determining the crystal's physical properties. In particular, they define the planes and directions of maximum atomic packing, which is a fundamental factor in plastic deformation. At standard temperature and pressure, examples of metallic materials with each type of lattice are presented in Table 2-1.

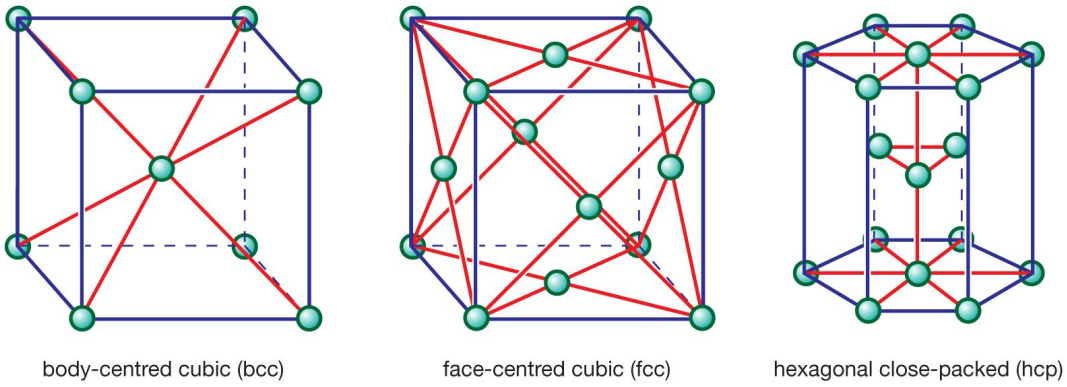

Fig. 2-2. Arrangement of atoms in BCC, FCC, and HCP unit cells [9].

Table 2-1. Crystal structures of common metals.

Crystal Structure	Examples
FCC	Aluminum, Copper, Nickel
BCC	Iron, Chromium, Tungsten
HCP	Magnesium, Titanium, Zinc

2.1.2 Dislocations

Dislocations are a specific type of defect that are present in crystals. The concept of a dislocation was first hypothesized in the early 1930's [10] to explain the cause of plastic deformation. However, it was not until much later before researchers were finally able to validate this theory using electron microscopy [11]. The initial motivation for the theory of dislocations was because there was a large discrepancy between the theoretical and actual strength of single crystals. The actual strength was observed to be several orders of magnitude lower than the calculated theoretical strength, so the idea of crystal defects was introduced to help explain this difference. To be specific, dislocations are atomic line defects in an otherwise perfectly arranged crystal lattice. The defect disrupts the natural arrangement of atoms in the crystal structure. There are primarily two types of dislocations: edge and screw. However, most dislocations exist as mixed dislocations that have both edge and screw characteristics. Fig. 2-3 shows examples of an edge dislocation, screw dislocation, as well as a mixed dislocation. The primary difference between the types of dislocations is the orientation of the dislocation line relative to the vector

associated with the lattice distortion. This vector is commonly known as the Burgers vector, denoted as b in Fig. 2-3. For edge dislocations, the line defect is orthogonal to the Burgers vector while for screw dislocations, the line defect is parallel to the Burgers vector. Mixed dislocations have a curvature that is both parallel and orthogonal to the Burgers vector at different points along the line.

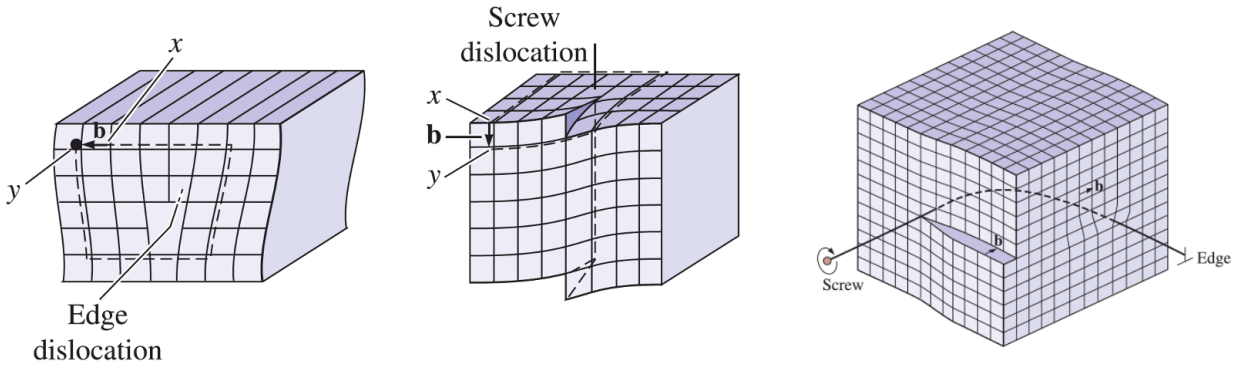

Fig. 2-3. Schematic illustrations of an edge dislocation, screw dislocation and mixed dislocation [12].

Dislocations play an important role in plastic deformation by reducing the stress required to separate atomic bonds. When an external load is applied to the crystal, only the bonds near the dislocation line are broken at any time. This contrasts with the much higher theoretical strength of the crystal that is calculated assuming that an entire plane of atoms must be sheared at once. The slipping mechanism is shown in Fig. 2-4 for an edge dislocation. Under an external shear stress, the dislocation line propagates in the direction of the Burgers vector in a stepwise fashion until the material above the slip plane is displaced by vector b. A similar mechanism occurs for screw and mixed dislocations. The aggregate movement of many dislocations across different planes and directions is responsible for plastic deformation at the macroscopic scale.

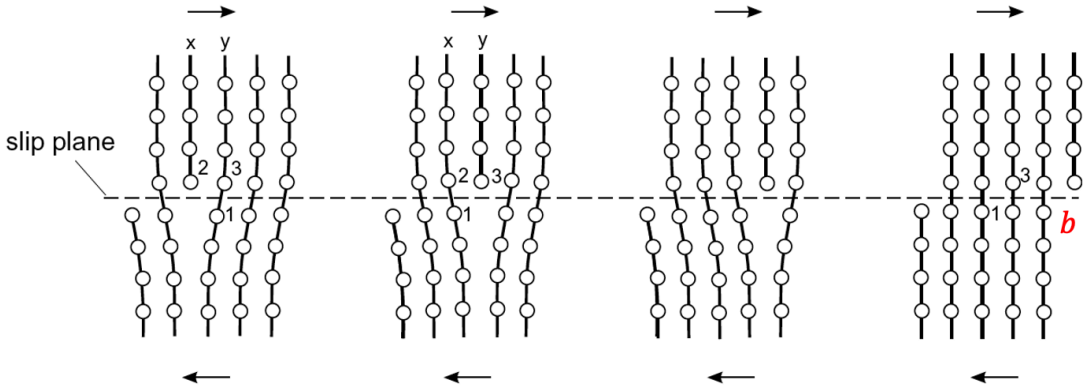

Fig. 2-4. Slipping of a single edge dislocation under an applied shear stress [13].

A crystal's lattice structure has a large effect on the slip behavior of dislocations. This is because crystallographic slip occurs only on specific planes and directions, called slip systems, that have the maximum atomic packing for each type of crystal. For instance, in FCC unit cells, there are 12 slip systems: each of the four {111} lattice planes consist of three <110> slip directions, shown in Fig. 2-5.

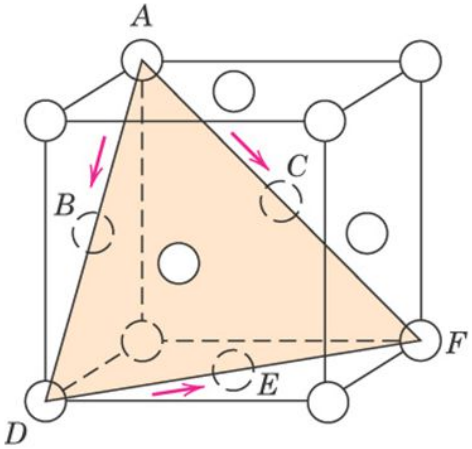

Fig. 2-5. FCC unit cell showing three slip systems (ABD, DEF, ACF) on the (111) slip plane [14].

The onset of slip occurs when the resolved shear stress acting on a slip system reaches the critical shear stress (CSS) value. The resolved shear stress is calculated with Schmid's Law, which relates the macroscopic stress state to the shear stress on any defined crystal plane and direction

$$\tau^{\alpha} = \boldsymbol{s}^{\alpha} \cdot \boldsymbol{\sigma} \cdot \boldsymbol{n}^{\alpha} \qquad (1)$$

where τ^{α} is the resolved shear stress on slip system α, $\boldsymbol{\sigma}$ is the macroscopic stress state in the crystal and $\boldsymbol{s}^{\alpha}$ and $\boldsymbol{n}^{\alpha}$ are slip system vectors defining the slip direction and slip plane normal. Once τ^{α} reaches the CSS value, dislocations begin to slip along slip system α.

2.1.3 Grains

Metals can be categorized as single crystals or polycrystals depending on the continuity of the crystal lattice. When a material has a continuous lattice structure throughout the entire sample, it is known as a single crystal. Alternatively, if the material is composed of many regions of different lattice orientations, it is known as a polycrystal. The arrangement of a typical polycrystal is shown in Fig. 2-6. Each bounded region in the polycrystal is called a grain and grains are separated by grain boundaries. The lattice within each grain is relatively uniform and is essentially a single crystal enclosed by other single crystals. The grain boundaries accommodate the transition of lattice orientations between neighboring grains and are composed of high densities of dislocations.

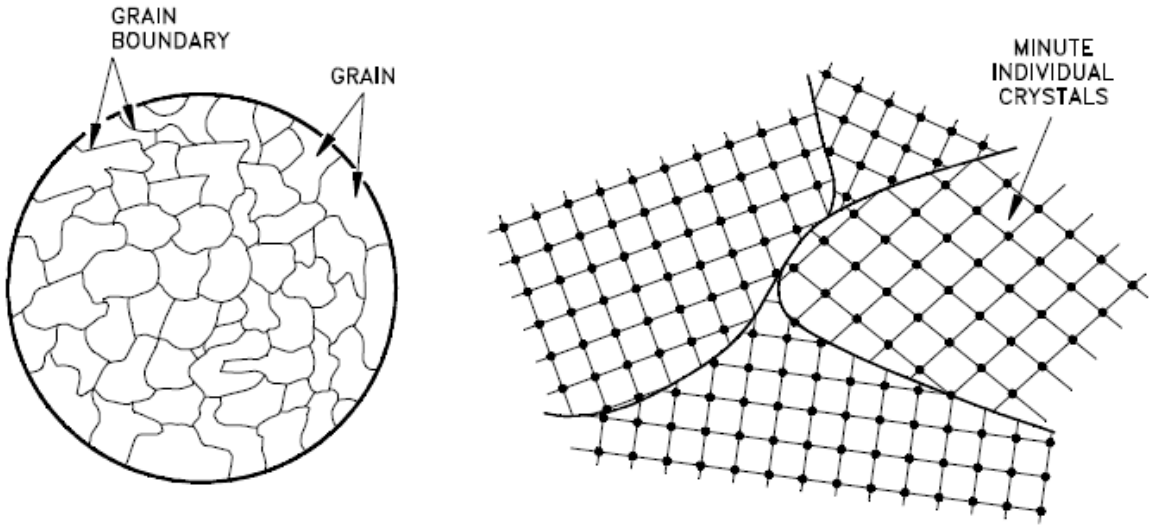

Fig. 2-6. Schematic of a typical polycrystal with grains and grain boundaries [15].

2.1.4 Texture

The distribution of orientations in a polycrystal is normally not random and depends largely on the material's fabrication history as well as any subsequent plastic deformation. The collective representation of all crystal orientations in a material is called its texture. Texture is important because it influences the directional properties of the material. The size and shape of

grains also affects several other properties such as the material's strength and ductility. Examples of common textures appearing in FCC materials are shown in Table 2-2. The orientation of crystals is often represented using Bunge Euler angles (ϕ_1, Φ, ϕ_2) that describe the rotation of the sample coordinate frame into the crystal coordinate frame. The parameter ϕ refers to rotation about the Z axis while Φ refers to rotation about X.

Table 2-2. Common texture components in FCC polycrystals.

Texture component	Euler angles (°) – (ϕ_1, Φ, ϕ_2)
Cube	(0, 0, 0)
Goss	(0, 45, 0)
Copper	(90, 35, 45)
Brass	(35, 45, 0)

2.2 Strengthening Mechanisms

Common strengthening mechanisms in metallics include work hardening, solid solution strengthening, grain boundary strengthening, and precipitation hardening. A review of each process is provided in this chapter. These mechanisms are especially important for aluminum materials that are the focus of the current research. However, it should be mentioned that some alloys can also be strengthened via additional means (e.g. transformation kinetics in steels), which will not be discussed in detail in this document.

2.2.1 Work Hardening

Work hardening (or strain hardening) refers to the strengthening of an alloy during plastic deformation and is observed as the increase in stress on a standard uniaxial stress-strain curve. This hardening effect is shown in Fig. 2-7. The slope of the stress-strain curve is known as the work hardening rate and is important for applications involving large plastic deformations, such as forming or bending. Work hardening occurs due to the generation and accumulation of dislocations. During plastic deformation, dislocations are generated via Frank-Read sources and other mechanisms in the microstructure [16]. The load applied to the crystal causes these dislocations to propagate via crystallographic slip. When the dislocations on different slip

systems intersect, they form substructures such as junctions, intersections or entanglements [17]. These substructures then become barriers to the motion of other dislocations. The growing quantity of barriers in the crystal raises the alloy's overall resistance to subsequent dislocation motion, which ultimately results in an increase in strength.

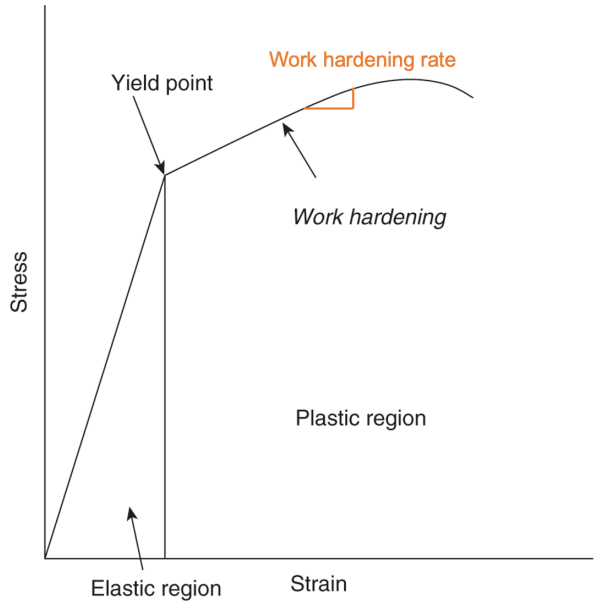

Fig. 2-7. Sample engineering stress-strain curve showing elastic and plastic regions [18].

The work hardening rate is normally highest during the early stages of plastic deformation and gradually decreases with further plastic strain. This decrease is caused by the dynamic recovery mechanism of dislocations, which reduces the dislocation density in the microstructure. Dynamic recovery can occur from either the annihilation of dislocations of opposing signs or from the rearrangement of dislocations into energetically favorable substructures [19]. Both mechanisms become more prominent as the dislocation density accumulates. The instantaneous rate of work hardening at any point on the stress-strain curve is determined by the competing mechanisms of dislocation generation and recovery.

2.2.2 Solid Solution Strengthening

Solid solution strengthening is the process of introducing interstitial or substitutional solutes into a crystal lattice. Both types of solute additions are shown in the schematic of Fig. 2-8. The solutes distort the crystal lattice in a way that causes local straining of the atoms near the solute.

This strain field then acts as resistance to the motion of dislocations, which results in an increase in the material's strength.

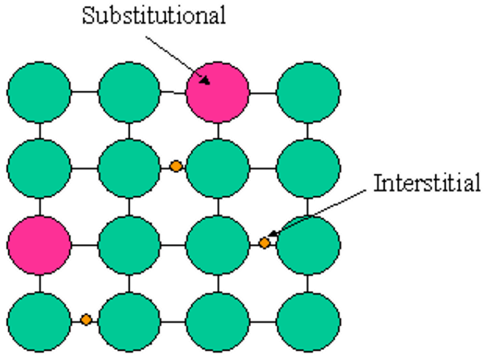

Fig. 2-8. Substitutional and interstitial solutes in a regular crystal lattice [20].

2.2.3 Grain Boundary Strengthening

Grain boundary strengthening is the process of reducing the grain size in a polycrystal to improve its strength [21, 22]. This can be accomplished via wrought processing or from fine tuning the fabrication process. By reducing the grain size, the total area of grain boundaries increases, which are strong obstacles to dislocation slip. Dislocations that encounter a grain boundary are forced to change directions and cross a highly dislocated interface in order to travel between grains. It is important to mention that grain sizes cannot be decreased indefinitely as grain boundary sliding begins to occur when the grain size is reduced to nanometers [23].

2.2.4 Precipitation Hardening

Precipitation hardening is the process of strengthening by introducing a fine dispersion of small particles into a material. Only certain alloys are able to be precipitation hardened as the precipitates are formed from a thermodynamic process that is intrinsic to the material. The precipitates act as obstacles to dislocation motion by directly hindering their movement on slip planes. Precipitates also trap dislocations as loops and act as a source for dislocation generation. As discussed in a later chapter, the interaction between precipitates and dislocations can be quite complex and the degree of strengthening depends on several factors, including the quantity, size, shape, and coherency of the particles.

2.3 Precipitation Hardening in Aluminum Alloys

2.3.1 Aluminum Alloys

Aluminum alloys are materials where aluminum (Al) is the predominant element in a mixture of solutes. They have high specific strengths in combination with remarkable corrosion resistance, manufacturability, and several other advantageous properties. Table 2-3 shows the different classes of aluminum alloys defined by the Aluminum Association (AA) of North America. The alloy series are differentiated by the primary alloying elements introduced during production and fabrication. Alloying alters the physical properties of the metal and allows researchers to carefully tailor the material properties to specific engineering applications. The classes of aluminum alloys can be further subdivided into heat-treatable and non-heat-treatable alloys. AA2000, AA6000, AA7000 and some AA8000 series aluminum alloys are heat-treatable, which means that their mechanical properties can be additionally improved from an artificial ageing process. AA1000, AA3000, AA4000, and AA5000 series alloys are non-heat-treatable and are normally strengthened from cold working. The popularity and success of aluminum alloys has been largely driven by the heat-treatable alloy series. The heat treatment process, known as artificial ageing, produces a dense distribution of small particles called precipitates in the crystal lattice. The precipitates provide an additional source of strengthening, which allows for these aluminum alloys to compete with heavier materials such as steel and iron in structural and lightweighting applications.

Table 2-3. Designation of aluminum alloys and their major alloying elements by the Aluminum Association.

Alloy Series	Primary Alloying Elements	Heat Treatable
1XXX	None	No
2XXX	Copper (Cu)	Yes
3XXX	Manganese (Mn)	No
4XXX	Silicon (Si)	No
5XXX	Magnesium (Mg)	No
6XXX	Magnesium and Silicon (Mg-Si)	Yes
7XXX	Zinc (Zn)	Yes
8XXX	Other	Yes

2.3.2 Brief History

The first observance of precipitation hardening dates back to 1906 when Wilm [24] discovered that a rapidly quenched Al-Cu alloy would increase in strength when left at room temperature for a period of time. Later in 1919, Merica [25] hypothesized that this "age hardening" was due to solutes precipitating out from solid solution. Unfortunately, the theory was disputed because nothing could be observed from microscopes at the time. It was not until 1938 before Guinier and Preston [26] were finally able to find evidence for solute clustering using state-of-the-art X-ray diffraction techniques. Even then, direct observation of these particles was not possible until 1959 with the invention and adoption of the transmission electron microscope. Today, the concept of precipitation hardening or age hardening is possibly one of the most utilized areas of materials science research and spans across numerous types of alloys, including aluminum, steel, magnesium, and others [27–29].

2.3.3 Heat Treatment Process

The artificial ageing process is generally composed of four steps. First, the material is solution heat treated at a temperature close to its melting point in order to dissolve existing precipitates in the microstructure. This solutionizing process results in a roughly homogeneous solid solution. Next, the material is quenched rapidly to room temperature, which prevents the diffusion of solute elements out of the solid solution. At this point, the material is in a supersaturated state with a positive chemical driving force for nucleation. The material is then heated to a specific artificial ageing temperature for a period of time to allow for the diffusion of solutes out of the solid solution. This stage is when the precipitates form; the precipitates evolve and grow with the duration of ageing until a desired particle distribution is achieved in the microstructure. Finally, the material is brought back to room temperature to stabilize the precipitates, which completes the heat treatment process. Fig. 2-9 shows a diagram of a standard artificial ageing process for aluminum alloys, where T_0 is the solutionizing temperature, T_1 is room temperature and T_2 is the artificial ageing temperature. Some alloys will precipitate even at room temperature while others may require additional processing steps, such as an additional heat treatment, in order to achieve the desired precipitate characteristics.

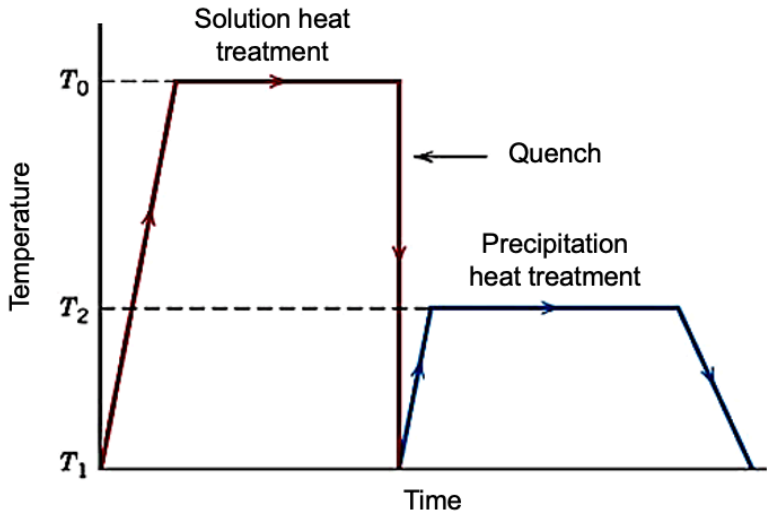

Fig. 2-9. Standard precipitation heat treatment process for aluminum alloys [30].

2.3.4 Kinetics of Precipitation Hardening

The formation of precipitates in the crystal is predominantly driven by two mechanisms: nucleation and growth. Nucleation refers to the initial formation of solute clusters from a solid solution state while growth is the subsequent evolution of the nuclei into larger precipitate structures. The nucleation process is largely statistical in nature and clusters are formed from the random gathering of solute atoms in solid solution. If a cluster of solutes gathers to reach some critical size, it becomes stable; otherwise, the cluster will dissolve. The driving force for this behavior is the degree of undercooling below the equilibrium temperature, which is achieved through rapid quenching of the alloy. Undercooling causes the energy associated with the solutionized state to be higher than the energy of forming a secondary phase, thereby favoring precipitate formation [12].

Nucleation can be classified as homogeneous or heterogeneous depending on the degree of impurities in the material. Homogeneous nucleation occurs when the material is relatively free of impurities and the formation of precipitates is mainly driven by the degree of undercooling. Heterogeneous nucleation occurs when a large number of impurities exist (e.g. grain boundaries, dislocations, intermetallics) that supports the nucleation of solute clusters. In this case, precipitates can form directly on these impurities, which reduces the amount of undercooling required to start precipitation. Precipitation in metallic materials is typically a heterogeneous process owing to the large number of dislocations in most commercial alloys [31].

Precipitate growth occurs by the diffusion of solute from the solid solution matrix into precipitate nuclei. This diffusion occurs due to a natural concentration gradient that exists between the matrix and the interface of the precipitate. The concentration gradient is illustrated in Fig. 2-10, where C_β is the solute concentration inside the precipitate, C_e is the solute concentration at the precipitate-matrix interface, and C_0 is the solute concentration inside the matrix. The gradient causes solutes from C_0 to diffuse into C_e until the concentration inside the matrix approaches the equilibrium value, C_e. At this point, the volume fraction of precipitates reaches a peak and nucleation no longer occurs due to the flattening of the concentration gradient.

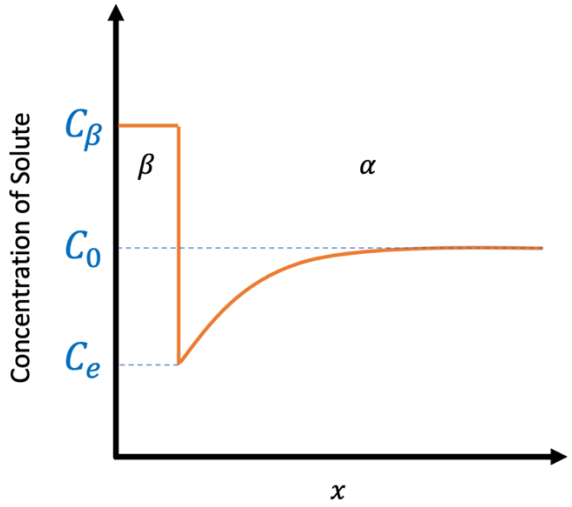

Fig. 2-10. Concentration gradient of solute inside the matrix (C_0), precipitate (C_β) and at the precipitate-matrix interface (C_e).

It should be mentioned that once the solutes have been depleted from the matrix, the precipitates are still able to grow even if nucleation is inhibited. This process is known as Ostwald ripening or coarsening [32, 33]. During the coarsening regime, the solutes from smaller precipitates are dissolved and redistributed to grow existing larger precipitates. This causes an increase in the average particle size but a decrease in the quantity of individual precipitates. The transfer of solute occurs because smaller precipitate structures are less energetically stable than larger precipitates [34]. In theory, coarsening can occur indefinitely until a single particle remains that contains the entire concentration of excess solute; however, this is neither desirable nor practical given the long ageing durations required.

Temperature plays a fundamental role in the precipitation process as it affects both nucleation and growth. However, the two mechanisms are competing processes since growth prefers higher temperatures while nucleation prefers slightly lower temperatures (to obtain a higher degree of undercooling). Careful selection of an ageing temperature is required to ensure an optimal balance between the two processes. Temperatures that are excessively high will result in faster artificial ageing but may result in lower strengthening, while temperatures that are too low will result in higher strengths but undesirable ageing times.

2.4 Experimental Methods

In this section, a description of certain experimental methods is presented. These methods are particularly relevant for this work as they are either used directly in the research or are a key component for the development of numerical models.

2.4.1 Electron Backscatter Diffraction

Electron backscatter diffraction (EBSD) is an imaging technique used with a scanning electron microscope (SEM). For metallic samples, EBSD can be applied to characterize the specimen's microstructure as well as its crystallographic orientations. In EBSD imaging, an electron beam is aimed at a tilted sample and the resulting diffraction of the electrons produces a Kikuchi pattern on the detector screen. These patterns are subsequently used to evaluate the crystal structure and orientation of the region underneath the beam. The electron beam is probed in a scanning motion across a large section of the specimen to obtain a representative detection of the crystallographic texture throughout the material. A schematic of the EBSD apparatus is presented in Fig. 2-11.

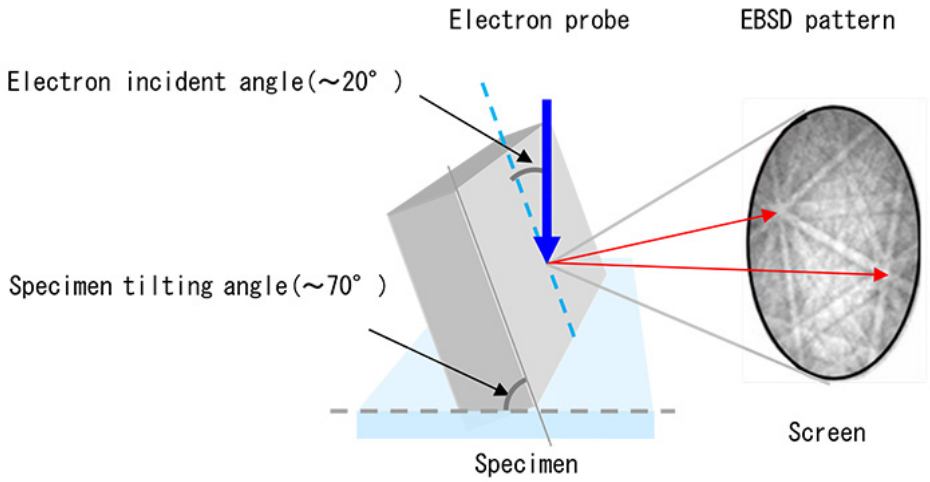

Fig. 2-11. Diagram of EBSD apparatus and the resultant Kikuchi patterns detected from electron beam diffraction [35].

In Fig. 2-12, the left-hand side shows the EBSD image for an extruded AA6060 aluminum alloy. Each color in the image refers to a grain with a particular orientation that follows the color mapping defined by the inverse pole figure (IPF) shown on the right. The EBSD not only provides a spatial representation of the crystallographic orientations of the sample, but also the grain size, grain morphology and details about the grain boundaries. In some cases, EBSD can further be used to investigate the distribution of secondary phases as well as other mechanisms such as twinning [36]. Alternatively, the crystallographic orientations of a sample can also be represented with an orientation distribution function (ODF) plot, commonly known as a pole figure, which provides an aggregate measure of texture. Pole figures are useful for determining the dominant texture components in the sample, but do not provide any spatial information. A sample (111) pole figure for an AA5754 direct chill-cast (DC) alloy is shown in Fig. 2-13.

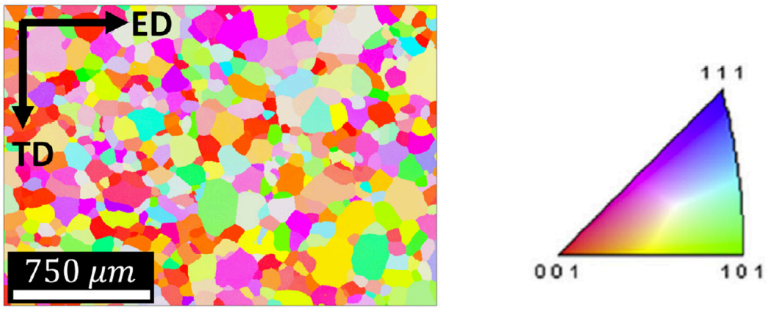

Fig. 2-12. EBSD image of extruded AA6060-T6 in the ED-TD plane with IPF map [37].

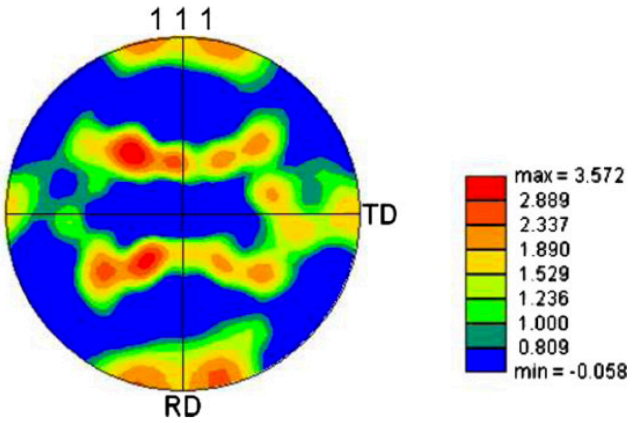

Fig. 2-13. Pole figure of AA5754DC in the RD-TD plane [38].

2.4.2 Transmission Electron Microscopy

Transmission electron microscopy (TEM) is an advanced imaging technique that is used to characterize samples at extremely high resolutions. The scale of TEM images can be on the order of a few Angstroms (10^{-10} m), making it one of few techniques suitable for characterizing precipitates. The apparatus transmits a strong electron beam through an ultra-thin specimen and the resulting diffraction is directly projected onto a screen. It is different from SEM as the electron beam is significantly stronger and the images are produced from the electrons passing through the specimen rather than those scattered from the surface. However, TEM requires laborious preparation and considerable expertise as the samples must be less than 150 nm thick. It is also not uncommon to introduce artifacts during the delicate sample preparation stage that may reduce the fidelity of the resulting image [36, 39]. In Fig. 2-14, TEM images of precipitates in different alloys are presented, illustrating the scale and level of detail obtainable with TEM.

(a) (b)

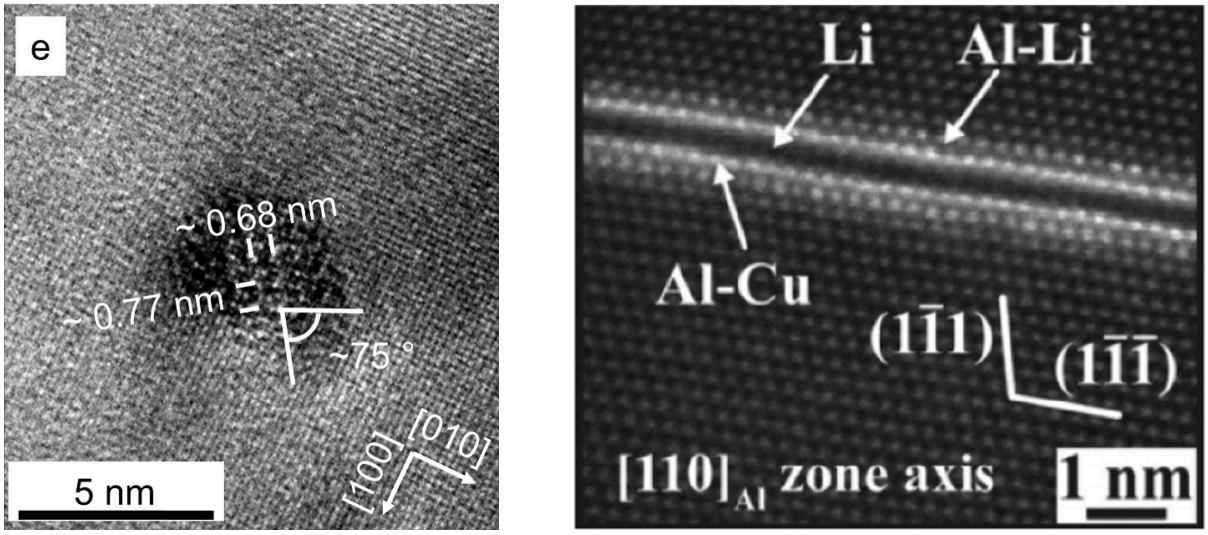

Fig. 2-14. TEM images of (a) the cross-section of a precipitate in an AA6000-series alloy [40]; (b) the side-view of a plate shaped precipitate in AA2050 [41].

2.4.3 Digital Image Correlation

A method for measuring strain during mechanical testing is with a technique called digital image correlation (DIC). DIC is a non-contact optical method that can be applied to both small and large regions. In this technique, a speckle pattern is spray painted onto the specimen prior to testing. The deformation is then recorded with optical cameras that track the displacement and position of the speckle pattern over time. The recorded images are later used to generate a full strain map for the specimen at specified time steps. This allows the tester to obtain the complete strain history across the speckled region. What is particularly useful with DIC imaging is the ability to measure local strains near the location of failure that cannot be easily obtained with conventional strain gauges or extensometers [42]. The resolution of DIC depends on the specifications of the camera lenses as well as the quality of the sprayed speckle pattern; though, it is possible to obtain failure strains for mini-sized specimens with high magnification lenses [37, 42, 43]. Fig. 2-15 illustrates a schematic of the DIC technique and the resulting strain map.

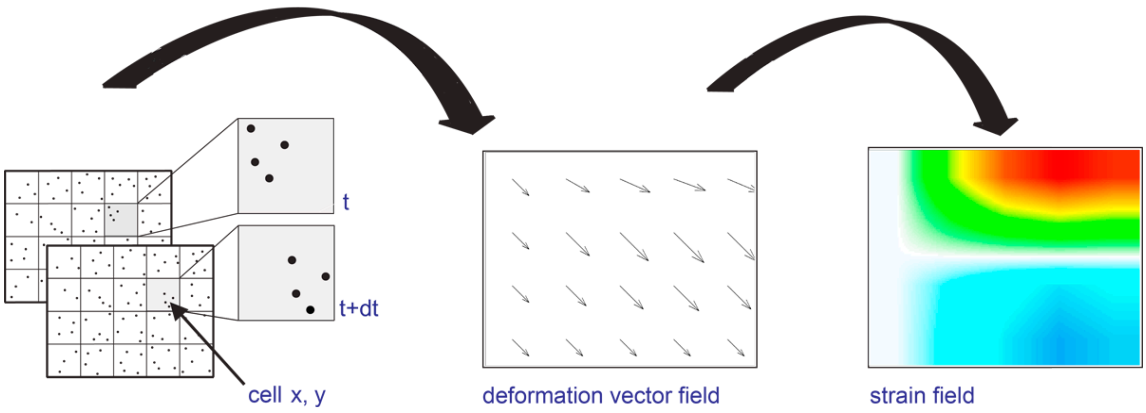

Fig. 2-15. Diagram showing the process of DIC [44].

2.5 Numerical Models

2.5.1 Constitutive Modeling

Constitutive equations in the field of plasticity are mathematical functions that relate stresses to strains during deformation. Constitutive models are often categorized as phenomenological or mechanistic depending on the theory governing the model. Phenomenological models attempt to capture the stress-strain behavior of a material with only minor consideration of the underlying physics. This is accomplished using empirical functions that can be easily fit to experiments. These models are normally much more computationally efficient compared to mechanistic models and can be used to simulate full-scale component geometries and products with ease.

Mechanistic constitutive models are influenced by the underlying mechanisms that govern a material's deformation behavior. They are also called physics-based models as they attempt to incorporate material physics into their framework. The advantage of mechanistic models is the ability to relate a macroscopic phenomenon to microscopic features in the material. This allows the model to provide insight to the function of specific physical mechanisms. For example, it is common for the stress and strain behavior to be related to the dislocation density within the crystal [45–47]. Doing so allows for a researcher to investigate the effects of different deformation modes on dislocation behavior, or vice versa. Many times, the variables can even be compared with experiments to validate their relationship. Physics-based models also typically contain fewer calibration parameters; however, they contain more material constants that must be obtained from experiments or other simulation modes. The biggest disadvantage with

mechanistic models is reduced computational speed, which makes them inefficient in larger simulations.

2.5.2 Crystal Plasticity

A particular type of physics-based constitutive model that is used for simulating metallics is crystal plasticity. Crystal plasticity is a continuum model that is derived from the movement of dislocations on individual slip systems. In this type of constitutive model, the orientation of each crystal lattice is considered for the simulation of the stress-strain results. The lattice is captured using slip system vectors that define the orientation of the slip plane and slip direction for each slip system. The first introduction of crystal plasticity was by Asaro and Rice [48] who proposed a rate-independent theory to model localization during single slip. The model was later improved by Peirce, Asaro and Needleman [49–51] with the introduction of a rate-dependent theory that was applicable on all possible slip systems. The framework by Peirce et al. [49] is used in the current work and their single crystal constitutive model is summarized below.

The kinematics of single crystal plasticity is based on a hyperelastic decomposition of the deformation gradient into elastic and plastic components

$$\boldsymbol{F} = \boldsymbol{F}^{*}\boldsymbol{F}^{p} \tag{2}$$

where $\boldsymbol{F}^{p}$ is the plastic deformation gradient and $\boldsymbol{F}^{*}$ is the elastic deformation gradient. As illustrated in Fig. 2-16, this decomposition can be thought of as crystallographic slip followed by an elastic stretch and rotation of the crystal lattice.

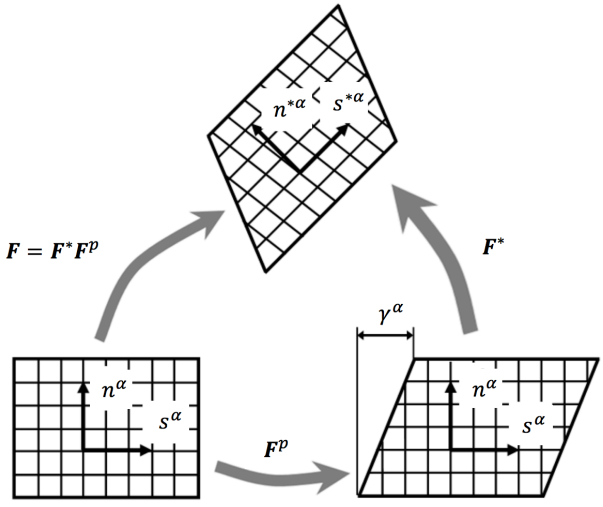

Fig. 2-16. Kinematic framework of crystal plasticity.

Lattice vectors, $\boldsymbol{s}^{(\alpha)}$ and $\boldsymbol{n}^{(\alpha)}$, are used to define the orientation of slip system α. These vectors are subsequently used to calculate the plastic strain on each slip system via the rate-dependent flow rule [49, 52]

$$\dot{\gamma}^{(\alpha)} = \dot{\gamma}_0 \left| \frac{\tau^{(\alpha)}}{g^{(\alpha)}} \right|^{\frac{1}{m}} \quad (3)$$

where $\dot{\gamma}^{(\alpha)}$ is the calculated plastic shear strain, $\dot{\gamma}_0$ is a reference shear strain, $\tau^{(\alpha)}$ is the resolved shear stress, m is the rate sensitivity parameter, and $g^{(\alpha)}$ is the critical shear stress or hardness. The final constitutive update for the single crystal is defined by the relationship

$$\widehat{\boldsymbol{\sigma}} = \mathbb{L}^e : \boldsymbol{D} - \sum_{\alpha} \boldsymbol{R}^{(\alpha)} \dot{\gamma}^{(\alpha)} - \boldsymbol{\sigma} \mathrm{tr}(\boldsymbol{D}) \quad (4)$$

where $\widehat{\boldsymbol{\sigma}}$ is the Jaumann rate of Cauchy stress, $\mathbb{L}^e$ is the elastic modulus, $\boldsymbol{D}$ is the rate of strain tensor, and $\boldsymbol{R}^{(\alpha)}$ is a tensor that defines the slip system. In a similar fashion to other constitutive models, the first term on the right-hand side is used as an elastic update, the second term is a viscoplastic correction, and the last term is related to dilatation. A detailed explanation of the model and all parameters is presented in a later chapter.

The foundations and kinematics of single crystal plasticity is well-developed and unless an effort is made to include additional kinetics such as temperature [53–56], much of the recent research is on the definition of the slip hardness, $g^{(\alpha)}$. This is because the CSS must account for the mechanisms involved in work hardening, which can be rather complex, especially in alloys with advanced hardening methods such as precipitates. A common approach for modeling the hardness is with the use of dislocation density

$$g^{(\alpha)} = \tau_0 + \kappa \mu b \sqrt{\rho} \quad (5)$$

where τ_0 is the initial CSS, κ is the dislocation obstacle strength, μ is the shear modulus of the crystal, b is Burgers vector and ρ is the total dislocation density. The dislocation density can be related to the state of plastic deformation through a Kocks and Mecking type approach [45, 46, 57, 58].

2.5.2.1 Polycrystal Plasticity

In polycrystal plasticity, each grain is governed by the single crystal constitutive model described in the previous section. However, the distribution of stresses and strains into different grains is not trivial and requires some assumptions on the aggregate behavior of polycrystals.

The earliest solution to this was introduced by Sachs [59] who proposed that each grain in a polycrystal is subject to the same stress state as every other grain. The Sachs model is rarely used in the literature today as it violates the compatibility condition between grains. Taylor [60] then introduced the assumption that all grains are subject to the same plastic strain state. This was further developed by Lin [61], who extended the assumption so that each grain is subject to the same total strain state. Taylor-type approaches have been widely employed in the literature due to their ease of implementation; however, the assumption violates stress equilibrium across grains, which results in an overly stiff stress-strain response.

The weakness in the Sachs and Taylor models is that they neglect the interactions between grains that result in variations to both stress and strain across the material. Physically, the polycrystal must satisfy both compatibility and equilibrium conditions, only one of which is captured by the Sachs and Taylor schemes. Kroner [62] and Budiansky and Wu [63] were of the first to develop polycrystal aggregation schemes that incorporated the interactions between grains. Their models were based on simplified assumptions of grain size and interaction strength. Hill [64] then furthered the development of these models by being the first to employ Eshelby mechanics for the homogenization of elastic-plastic crystals. Hutchinson [52] later modified Hill's model for purely viscoplastic materials. The theories by Hill and Hutchinson were the foundations for the elastic-plastic self-consistent (EPSC) and viscoplastic self-consistent (VPSC) schemes, which are still used in the literature today [65–68]. Kouddane et al. [69] and Molinari et al. [70] were the first to develop an aggregate model for elastic-viscoplastic materials. Later, Wang et al. [71] formalized the elastic-viscoplastic self-consistent (EVPSC) scheme and demonstrated its application for numerous types of crystals.

2.5.3 Eshelby Homogenization

The Eshelby homogenization framework is a solution method for calculating the stresses and strains of an inclusion or inhomogeneity embedded within an assumed infinitely-large matrix [72]. As shown in Fig. 2-17, the Eshelby problem is to find the strain inside the inclusion $\boldsymbol{\epsilon}_i$, relative to the strain applied at the boundary of the matrix $\boldsymbol{\epsilon}_0$. Any variable with the subscript i is used to denote a property of the inclusion, while the subscript 0 is used to refer to the matrix.

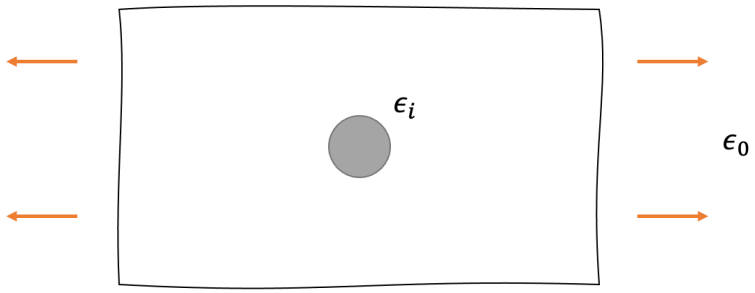

Fig. 2-17. Schematic of an Eshelby inclusion problem.

Eshelby was able to propose a solution for this problem with the use of Green's functions. The heterogeneity introduced by the inclusion was replaced with a fictitious "eigenstrain" and the entire problem was made linear with the use of a "reference" matrix. Eshelby found that if the inclusion could be assumed to be ellipsoidal in geometry, the strain inside the inclusion could be calculated with the expression

$$\boldsymbol{\epsilon}_i = [\mathbb{S}: \mathbb{L}_0^{-1}: (\mathbb{L}_i - \mathbb{L}_0) + \mathbb{I}]^{-1}: \boldsymbol{\epsilon}_0 \qquad (6)$$

where $\mathbb{L}$ is the stiffness matrix, $\mathbb{I}$ is the identity tensor, and $\mathbb{S}$ is the so-called Eshelby tensor that accounts for both the geometry of the inclusion and the strength of the inclusion-matrix interaction. The Eshelby tensor is found with the aid of Green's functions, which is described in the next section. The terms inside the square brackets is often called the strain concentration tensor as it defines a relationship between the strain outside and inside the inclusion. In an alternative form, the properties of the inclusion can be directly related to the properties of the matrix using the interaction law

$$\boldsymbol{\epsilon}_i - \boldsymbol{\epsilon}_0 = -\mathbb{M}^*: (\boldsymbol{\sigma}_i - \boldsymbol{\sigma}_0) \qquad (7)$$

where $\mathbb{M}^*$ is called the interaction tensor that is a function of $\mathbb{S}$ and $\mathbb{L}_0$.

The Eshelby solution is useful in many applications as countless commercial materials contain secondary particles. The framework is also used in self-consistent crystal plasticity schemes to determine the stress and strain across different grains. When the volume fraction of inclusions is relatively low (i.e. less than 1%), the solution is straightforward as ϵ_0 can be assumed the same as the macroscopic strain applied to the entire alloy. However, the solution becomes more demanding when inclusions have high volume fractions as ϵ_0 must be implicitly calculated along with ϵ_i. Different assumptions on how this can be accomplished has led to the

development of many homogenization frameworks, such as the Mori-Tanaka [73] method, double inclusion method [74] or the self-consistent method [52, 64].

2.5.3.1 Green's Function

Consider the standard equilibrium equation for an elastostatic body with an applied body force

$$\mathbb{L}_{kpim} u_{i,mp}(\boldsymbol{x}) + f_k(\boldsymbol{x}) = 0 \qquad (8)$$

where $\mathbb{L}$ is the elastic modulus, $\boldsymbol{u}$ is the displacement and $\boldsymbol{f}$ is the body force (per unit volume). It is possible to define a mathematical relationship for the solution of $\boldsymbol{u}$ such that

$$u_i(\boldsymbol{x}) = \int G_{ij}(\boldsymbol{x} - \boldsymbol{x}') f_j(\boldsymbol{x}')\, dV(\boldsymbol{x}') \qquad (9)$$

where G_{ij} is called Green's function that relates the displacement at position $\boldsymbol{x}$ to a force at position $\boldsymbol{x}'$. Now, the difficulty in this solution method is the determination of G_{ij}. To accomplish this, Eq. (9) can be substituted into Eq. (8) and after some manipulation, the following equation can be obtained

$$\delta_{kj}\delta(\boldsymbol{x} - \boldsymbol{x}') + \mathbb{L}_{kpim} G_{ij,mp}(\boldsymbol{x} - \boldsymbol{x}') = 0 \qquad (10)$$

where δ_{kj} is the Kronecker delta and $\delta(\boldsymbol{x} - \boldsymbol{x}')$ is the Dirac delta function. Eq. (10) is the equilibrium equation represented using Green's function, which is conveniently expressed in a form that can be further interpreted using an inverse Fourier transform

$$\begin{aligned} \delta_{kj}\left(\frac{1}{2\pi}\right)^3 \int_{-\infty}^{\infty} \exp(-i\boldsymbol{k}\cdot(\boldsymbol{x} - \boldsymbol{x}'))\, d\boldsymbol{k} \\ + \mathbb{L}_{kpim}\left(\frac{1}{2\pi}\right)^3 \int_{-\infty}^{\infty} -k_m k_p G_{ij}(\boldsymbol{k}) \exp(-i\boldsymbol{k}\cdot(\boldsymbol{x} - \boldsymbol{x}'))\, d\boldsymbol{k} = 0 \end{aligned} \qquad (11)$$

where $\boldsymbol{k}$ denotes Fourier space. Introducing the parameters $\boldsymbol{z} = \frac{\boldsymbol{k}}{|\boldsymbol{k}|}$ and $(zz)_{ki} = \mathbb{L}_{kpim} z_m z_p$, Eq. (11) can be reduced to

$$\left(\frac{1}{2\pi}\right)^3 \int_{-\infty}^{\infty} \left[\delta_{kj} - (zz)_{ki} G_{ij}(\boldsymbol{k})|\boldsymbol{k}|^2\right] \exp(-i\boldsymbol{k}\cdot(\boldsymbol{x} - \boldsymbol{x}'))\, d\boldsymbol{k} = 0 \qquad (12)$$

Since the terms in the square brackets must equal to zero, Green's tensor in Fourier space can be calculated as

$$G_{ij}(\boldsymbol{k}) = \frac{(zz)^{-1}_{ij}}{|\boldsymbol{k}|^2} \qquad (13)$$

In real space, Green's function can be expressed as

$$G_{ij}(\boldsymbol{x}-\boldsymbol{x}') = \left(\frac{1}{2\pi}\right)^3 \int_{-\infty}^{\infty} \frac{(zz)_{ij}^{-1}}{|\boldsymbol{k}|^2} \exp(-i\boldsymbol{k}\cdot(\boldsymbol{x}-\boldsymbol{x}'))\, d\boldsymbol{k} \qquad \textbf{(14)}$$

and its double derivative as

$$G_{ij,kl}(\boldsymbol{x}-\boldsymbol{x}') = \left(\frac{1}{2\pi}\right)^3 \int_{-\infty}^{\infty} -z_k z_l (zz)_{ij}^{-1} \exp(-i\boldsymbol{k}\cdot(\boldsymbol{x}-\boldsymbol{x}'))\, d\boldsymbol{k} \qquad \textbf{(15)}$$

Now consider if the body force in Eq. (8) is represented with

$$f_i(\boldsymbol{x}) = \Delta_{ij,j}(\boldsymbol{x}) \qquad \textbf{(16)}$$

where Δ_{ij} is an arbitrary variable. The displacement $\boldsymbol{u}$ can then be expressed as

$$u_i(\boldsymbol{x}) = \int G_{ij}(\boldsymbol{x}-\boldsymbol{x}')\Delta_{jl,l}(\boldsymbol{x}')\, dV(\boldsymbol{x}') \qquad \textbf{(17)}$$

Using integration by parts, it is possible to obtain the following relationship for the displacement gradient

$$u_{i,j}(\boldsymbol{x}) = \int G_{ik,lj}(\boldsymbol{x}-\boldsymbol{x}')\Delta_{kl}(\boldsymbol{x}')\, dV(\boldsymbol{x}') \qquad \textbf{(18)}$$

If $\Delta_{kl}(\boldsymbol{x})$ can be assumed a constant value within the region defined by $\boldsymbol{x}'$, then Eq. (18) can be reduced to

$$u_{i,j}(\boldsymbol{x}) = \mathbb{T}_{ijkl}\Delta_{kl} \qquad \textbf{(19)}$$

where $\mathbb{T}$ is a fourth order auxiliary tensor $\mathbb{T}_{ijkl} = \int G_{ik,lj}(\boldsymbol{x}-\boldsymbol{x}')\, dV(\boldsymbol{x}')$. Substitution of Eq. (15) results in the expression

$$\mathbb{T}_{ijkl} = \int \left(\frac{1}{2\pi}\right)^3 \int_{-\infty}^{\infty} -z_l z_j (zz)_{ik}^{-1} \exp\left(-i\boldsymbol{k}\cdot(\boldsymbol{x}-\boldsymbol{x}')\right) d\boldsymbol{k} dV(\boldsymbol{x}') \qquad \textbf{(20)}$$

This integral can be more easily calculated if the region encompassed by $\boldsymbol{x}'$ is ellipsoidal. In this case, $\mathbb{T}_{ijkl}$ reduces to a surface integral

$$\mathbb{T}_{ijkl} = -\frac{abc}{4\pi}\int_0^{2\pi}\int_0^{\pi} z_l z_j (zz)_{ik}^{-1} \frac{sin\phi}{\beta^3} d\phi d\theta \qquad \textbf{(21)}$$

where z is now defined as

$$z = \begin{bmatrix} \sin\phi\cos\theta \\ \sin\phi\sin\theta \\ \cos\phi \end{bmatrix} \qquad \textbf{(22)}$$

and

$$\beta = \sqrt{a^2(\sin\phi\cos\theta)^2 + b^2(\sin\phi\sin\theta) + c^2(\cos\phi)^2} \quad (23)$$

for ellipsoids of the form $\frac{x^2}{a^2} + \frac{y^2}{b^2} + \frac{z^2}{c^2} = 1$.

What is shown in this derivation is that the displacement gradient for an elastostatic body under the body force $f_i(\boldsymbol{x}) = \Delta_{ij,j}(\boldsymbol{x})$ can be calculated using Eq. (19). This is an important solution for Eshelby-type problems as Δ_{ij} is often related to the eigenstrain $\boldsymbol{\epsilon}^*$ via $\Delta_{ij} = \mathbb{L}_{ijkl}\epsilon^*_{kl}$.

2.5.4 Finite Element Analysis

Finite element analysis (FEA) is a numerical method for solving partial differential equations (PDEs). FEA can be used for heat transfer, fluid flow, electromagnetism, vibrations, and many other applications. In the field of solid mechanics, FEA is most often used to simulate the deformation behavior of geometries subject to various types of loading. For this application, the governing PDE is stress equilibrium, defined by

$$\boldsymbol{\nabla} \cdot \boldsymbol{\sigma}(\boldsymbol{x}, t) + \rho(\boldsymbol{x})\boldsymbol{b}(\boldsymbol{x}) = \rho(\boldsymbol{x})\ddot{\boldsymbol{u}}(\boldsymbol{x}, t) \quad (24)$$

where ρ is the material density, $\boldsymbol{b}$ is the body force, and $\boldsymbol{u}$ is the displacement at point $\boldsymbol{x}$ and time t. With the use of Green's theorem, an integral form of Eq. (24) can be obtained

$$\int_V \delta\boldsymbol{v} \cdot \rho\ddot{\boldsymbol{u}}\,\mathrm{d}V - \int_S \delta\boldsymbol{v} \cdot \boldsymbol{t}\,\mathrm{dS} + \int_V \delta\boldsymbol{D} : \boldsymbol{\sigma}\,\mathrm{d}V - \int_V \delta\boldsymbol{v} \cdot \rho\boldsymbol{b}\,\mathrm{d}V = 0 \quad (25)$$

where $\boldsymbol{t}$ is the traction applied on surface boundary S and $\delta\boldsymbol{v}$ is the variation of velocity introduced via the principle of virtual power. This integral is solved for displacement $\boldsymbol{u}$ by discretizing the geometry contained in volume V into individual elements, each defined by a specific number of nodes. The displacement at each node is approximated with polynomial interpolation functions (also known as shape functions) such that

$$\boldsymbol{u}(\boldsymbol{x}, t) \approx \boldsymbol{N}_I(\boldsymbol{x})\boldsymbol{u}_I(t) \quad (26)$$

where $\boldsymbol{u}(\boldsymbol{x}, t)$ is the displacement at any position $\boldsymbol{x}$, $\boldsymbol{N}_I$ contains the shape functions for a single element that embodies $\boldsymbol{x}$, and $\boldsymbol{u}_I$ contains the displacements at the nodes of this element. The introduction of shape functions reduces the continuity requirements for the full field displacement solution and only the values at the nodes are calculated at any given time. The discretized form of Eq. (25) for each element can be written as

$$\int_{V^e} (\delta \boldsymbol{v}_I^e)^T (\boldsymbol{N}_I^e)^T (\boldsymbol{N}_I^e)(\ddot{\boldsymbol{u}}_I^e)\rho \, \mathrm{d}V - \int_{S^e} (\delta \boldsymbol{v}_I^e)^T (\boldsymbol{N}_I^e)^T \{\boldsymbol{t}^e\} \, \mathrm{d}S + \int_{V^e} (\delta \boldsymbol{v}_I^e)^T (\boldsymbol{B}_I^e)^T \{\boldsymbol{\sigma}^e\} \, \mathrm{d}V - \int_{V^e} (\delta \boldsymbol{v}_I^e)^T (\boldsymbol{N}_I^e)^T \{\boldsymbol{b}^e\} \rho \, \mathrm{d}V = 0 \quad \textbf{(27)}$$

where $\boldsymbol{B}_I$ is the derivative of the shape functions $\boldsymbol{N}_I$ with respect to $\boldsymbol{x}$. The superscript e is used to refer to elemental values while curly brackets are used to denote values at any arbitrary position $\boldsymbol{x}$. Finally, the global form of the equilibrium equation can be expressed as

$$\delta v^T [M\ddot{u} + F_{int} - F_{ext}] = 0 \quad \textbf{(28)}$$

where the values inside the square brackets can be solved for using a numerical scheme (explicit or implicit).

Practically speaking, FEA can be combined with different constitutive models to simulate the behaviors of various materials. The crystal plasticity finite element method (CPFEM) is particularly important for this research as it enables the simulation of spatial features such as localization or shear banding. An example of this is presented in Fig. 2-18 where each grain in a polycrystal is meshed and simulated with FEA.

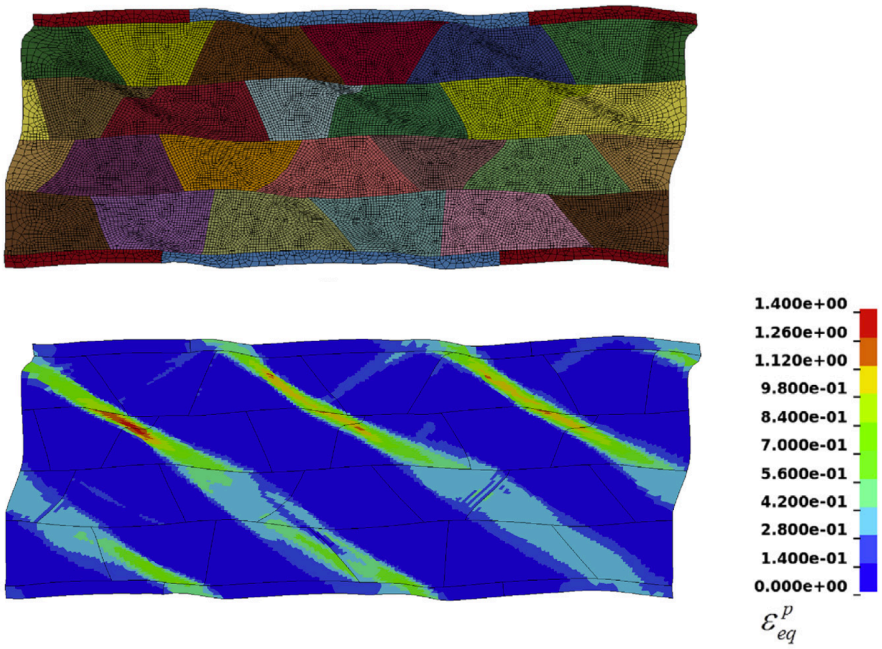

Fig. 2-18. 2D CPFEM simulation of a polycrystal showing shear banding during plane strain tension [75].

2.5.5 Classical Nucleation and Growth Theory

Classical nucleation and growth theory (CNGT) is a commonly used set of equations for simulating the kinetics of precipitation as well as many other thermodynamic processes. The kinetics process is separated into three primary equations: the rate of nucleation, the rate of growth, and a mass balance equation. Each of these equations are solved in a continuous fashion as a function of time. Myhr et al. [76] popularized the use of CNGT for artificial ageing in aluminum alloys. Their precipitation framework is summarized as follows.

The nucleation rate $\dot{N}$ of stable clusters is represented using an Arrhenius equation of the form

$$\dot{N} = j_0 \exp\left(\frac{-\Delta G_c}{KT}\right) \exp\left(\frac{-Q_d}{KT}\right) \quad \textbf{(29)}$$

where j_0 is a calibrated parameter, Q_d is the activation energy for diffusion, K is the Boltzmann constant, T is the ageing temperature, and ΔG_c is the energy barrier for nucleation. The energy barrier is defined using the Gibbs free energy change for the transformation of the solid solution into precipitate. The growth of the stable nuclei is expressed as

$$\frac{dR}{dt} = \frac{\bar{C} - C^i}{C^p - C^i}\frac{D}{R} \quad \textbf{(30)}$$

where R is the radius of the precipitate, D is the diffusion coefficient for solute, $\bar{C}$ is the concentration of solute in the matrix, C^i is the concentration of solute at the precipitate-matrix interface, and C^p is the concentration of solute in the precipitate. C^i is influenced by the shape of the precipitate through the Gibbs-Thomson effect [77], while C^p and D are material constants that can be obtained from experimentation or via a thermodynamic database. Finally, the mass balance equation is expressed as

$$\bar{C} = C^0 - (C^p - \bar{C})\frac{4}{3}\pi R^3 N \quad \textbf{(31)}$$

where C^0 is the initial solute concentration in the matrix and N is the number density of precipitates.

2.5.5.1 Gibbs-Thomson Effect

The Gibbs-Thomson effect is a phenomenon where the equilibrium solute concentration at the interface is affected by the curvature of the nucleus [77]. This is particularly important during precipitation processes as the initial nucleus is very small and thus has a large curvature. In the

simple case of a binary precipitation process driven by a single solute, the Gibbs-Thomson equation is expressed as

$$C^i = C^e \exp\left(\frac{2\sigma V_m}{R_g RT}\right) \quad \textbf{(32)}$$

where σ is the interface energy, V_m is the molar volume of the precipitate phase, and R_g is the universal gas constant. The concentration at the interface C^i is adjusted based on the radius R of the precipitate. This effect is most prevalent when the radius is small and as R becomes larger, C^i approaches the equilibrium concentration C^e. From a practical perspective, the Gibbs-Thomson equation is responsible for driving the coarsening process during the late stages of ageing. This is because smaller particles have higher interface solubilities than larger particles, which generates a concentration gradient between particles of different size.

2.5.5.2 Kampmann and Wagner Numerical Method

The Kampmann and Wagner Numerical (KWN) method is a mathematical approach used to solve the equations in CNGT. In this method, a discretization of the particle radius is made so that the resulting particle-size distribution can be simulated over time. The particle radius R is discretized into equal spaced intervals (i.e. elements) for which the number density N is calculated at the center of each element. An illustration of this discretization is shown in Fig. 2-19.

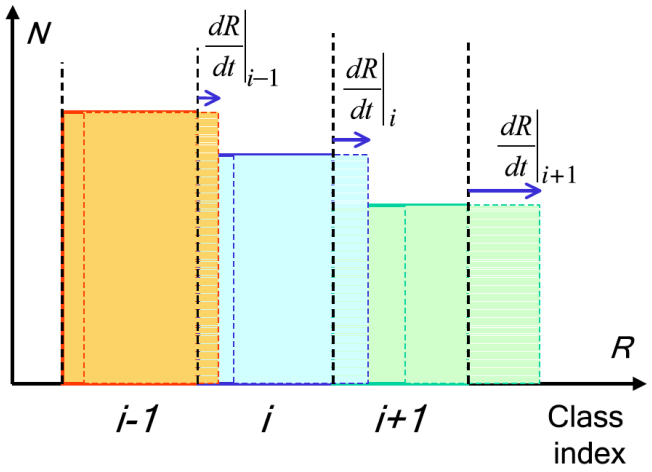

Fig. 2-19. Finite control volume discretization for simulating precipitation kinetics using the KWN method [78].

The flux of matter between elements is obtained from the solution of the following governing equation

$$\frac{\partial N}{\partial t} = -\frac{\partial (Nv)}{\partial R} + S \qquad \textbf{(33)}$$

where $N(t, R)$ is a function of both time and radius, v is the growth rate defined by Eq. (30) and S is the nucleation rate defined by Eq. (29). In the solution by Myhr et al. [76], the governing equation is discretized using an upwind finite-volume scheme such that the number density for class i is calculated as

$$\begin{aligned} N_{i,t+\Delta t} = N_{i,t} &+ \frac{\Delta t}{\Delta R} v_{i-1,t}\left[\mathrm{SIGN}\left(v_{i-1,t}\right)N_{i-1,t} + \mathrm{SIGN}\left(-v_{i-1,t}\right)N_{i,t}\right] \\ &- \frac{\Delta t}{\Delta R} v_{i,t}\left[\mathrm{SIGN}\left(v_{i,t}\right)N_{i,t} + \mathrm{SIGN}\left(-v_{i,t}\right)N_{i+1,t}\right] \end{aligned} \qquad \textbf{(34)}$$

where the $\mathrm{SIGN}(x)$ function is 1 if $x > 0$ and 0 otherwise. N is defined at the center of each element while the flux between classes is calculated at the interface between elements.

One of the advantages in using the KWN method is the ability for the model to directly initiate coarsening without adjustments to the kinetics equations. Coarsening occurs when the solute in the matrix reaches its equilibrium concentration, at which point the nucleation rate of new precipitates reduces to zero. Since the KWN method contains the entire distribution of particle sizes, further growth can still occur from the Gibbs-Thomson effect that creates a positive solute flux from smaller precipitates to larger precipitates. This results in a reduction in number density of smaller particles and an increase in number density of larger ones. An example is shown in Fig. 2-20 where the evolution of the particle-size distribution in AA6082 is illustrated as a function of time.

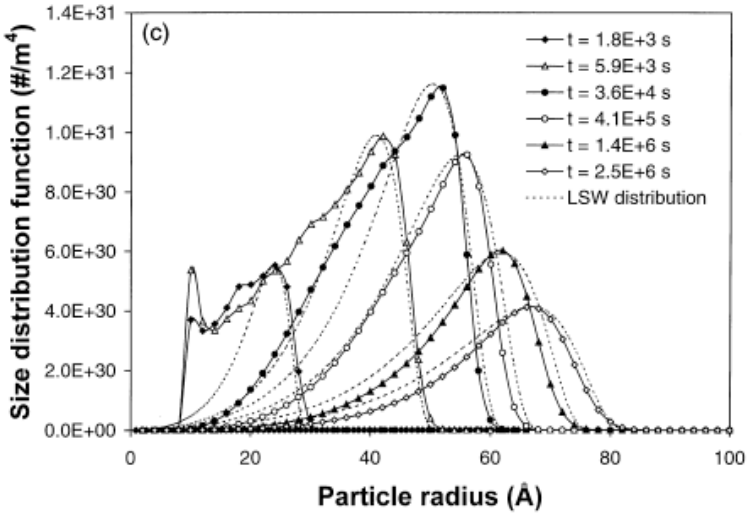

Fig. 2-20. Simulated particle-size distribution over time for AA6082 aged at 180°C [76].

2.5.6 Cluster Dynamics

Cluster dynamics is a relatively new concept that can be used to simulate thermodynamic processes. It was originally developed to simulate irradiation in the nuclear industry; however, it has characteristics that allow it to be more accurate than CNGT [79]. The theory is similar to the KWN method of classical nucleation and growth but applied at a lower length scale with the simulation of individual clusters. The time evolution of a cluster containing n solute atoms is simulated by the equation

$$\frac{\partial C_n}{\partial t} = J_{n-1\rightarrow n} - J_{n\rightarrow n+1} \quad (35)$$

where C_n is the concentration of clusters containing n solute atoms and J is the flux between clusters of different size. The simulation is initiated with several clusters of various sizes, n. The flux between them is calculated with

$$J_{n\rightarrow n+1} = C_n\beta_n - C_{n+1}\alpha_{n+1} \quad (36)$$

where β is the condensation rate and α is the emission rate that are both calculated based on the thermodynamic properties of the solutes being studied. These parameters may be obtained from certain thermo-databases or directly calibrated to atomistic models. The accuracy of cluster dynamics is determined by the number of cluster sizes used during the simulation, with more clusters having better resolution but higher computational demand. However, these models can

quickly become complex when the solute concentration is larger than 1 at-%, at which point many of the simplifying assumptions begin to break down [80].

2.5.7 Atomistic Models

Atomistic models refer to numerical frameworks used to simulate the behavior of individual atoms. Examples include molecular dynamics (MD), density functional theory (DFT), or kinetic Monte Carlo (KMC). In MD, an equilibrium equation is solved for each atom in a cluster of atoms so that the deformation between them is captured at the nanoscale. MD can be utilized to investigate plasticity at much higher resolutions than any constitutive model can provide [81, 82]. DFT occurs on an even lower length scale and is used to model the electron structure of atoms via quantum mechanics. DFT can help understand the structure and properties of individual molecules and nanoparticles that are challenging to characterize otherwise [83, 84]. KMC is a stochastic precipitation kinetics model where the atoms of the solute and matrix elements are modeled directly. The precipitation process is initiated by introducing vacancies that causes the jumping of solute atoms to reduced energy states. KMC is used to capture the diffusion process at high resolutions and is not plagued with numerous calibration parameters as in other kinetics models [80, 85].

Atomistic techniques are important for developing a better understanding of materials that are difficult to experiment with. However, these methods are typically not suitable for simulating the length scale of bulk material properties. Furthermore, time increments for atomistic models are usually on the order of pico (10^{-12}) to nano (10^{-9}) seconds to best capture the resolution and time interval of atomic processes. This time stepping is also not feasible for simulating the deformations observed in quasi-static tensile testing or the artificial ageing process that can be several hours in duration.

3 Literature Review

In this chapter, a review of the literature is presented on several aspects of precipitation hardening, with a particular focus on the modeling of these alloys. Special attention is given to the AA6000-series of aluminum materials as they are the material of focus for this research. However, many of the concepts and modeling techniques discussed are transferrable across different classes of precipitation hardening alloys.

3.1 Phase Transformations

The AA6000-series or Al-Mg-Si aluminum alloys have high concentrations of magnesium (Mg) and silicon (Si) solute elements. They are used in many engineering applications and are particularly important in the automotive industry for their excellent strength to weight ratios. The precipitates of AA6000-series materials are composed of Mg and Si, which nucleate out during the artificial ageing process. The particles are typically on the order of nm-μm size and form within the crystal lattice. A standard precipitation sequence for Al-Mg-Si alloys is:

$$\text{SSSS} \rightarrow \text{Clusters} \rightarrow \text{GP Zones} \rightarrow \beta' \rightarrow \beta'' \rightarrow \beta \text{ (stable)}$$

however, the sequence of phase transformations also depends on the concentration of secondary solute elements. Each phase involves a transformation of the precipitate as they evolve in size, quantity, composition, and coherency during artificial ageing.

A brief description of each phase in the precipitation sequence is discussed as follows: SSSS is the supersaturated solid solution obtained after the initial solution heat treatment. The degree of supersaturation is important for artificial ageing as it determines the driving force for nucleation and is dependent on several factors, including the solutionizing temperature, quench rate and initial solute concentration. Clusters and Guinier-Preston (GP) zones are the first observable phases from artificial ageing and are generally believed to have an Mg-Si ratio of close to unity [86]. GP zones in particular are either spherical or plate shaped with a size that is typically less than 3 nm [87, 88]. They are not very effective strengthening agents due to their small size and coherent bond with the matrix. With additional ageing, GP zones transform into β'' precipitate, which is perhaps the most important phase in the precipitation sequence as it is attributed to the condition with the highest strength. β'' is semi-coherent with the aluminum matrix and its composition is commonly found to be Mg_5Si_6 [89, 90]. The precipitate has a needle-shaped morphology and while its radius is not much larger than the size of GP zones, its

length is far greater, typically between 10 nm – 30 nm and occasionally much higher depending on the initial concentration of solute [91]. The subsequent β' precipitate is also semi-coherent with a composition that is said to be $Mg_{18}Si_{10}$ [92]. The β' phase is associated with a reduction in the quantity of particles relative to β'' but with an increase in individual particle length, caused by the initiation of Ostwald ripening [93, 94]. Typically, the average length is well-over 30 nm and can reach up to 500 nm depending on the parameters of the heat treatment process [95]. Finally, the stable β phase is perhaps the most well-understood phase with a stoichiometry of Mg_2Si. The β phase is incoherent with the aluminum matrix, has a sparse number density of particles and has very large individual particle sizes due to extensive coarsening [27, 94, 96]. Mg_2Si is normally plate-shaped with lengths and widths that can grow up to several microns in scale [97, 98].

One of the distinguishable characteristics of precipitates in Al-Mg-Si alloys is that they are normally needle or rod-shaped and aligned in specific directions of the FCC crystal. This is especially true for β-type particles that have large length-to-radius aspect ratios. The needles are aligned such that their lengths are parallel to the <100> directions of each lattice. A schematic of this alignment is shown in Fig. 3-1 for the FCC unit cell, where the left-hand side illustrates the three orthogonal precipitate variants and the right-hand side is a section view of a larger population of precipitates on the (111) glide plane. Their orientation is an important characteristic as it introduces a separate source of anisotropy to each crystal compared to fully spherical particles. The strengthening caused by these precipitates are also accounted for differently as they affect the dislocation mean-free path in a nonlinear way [99, 100].

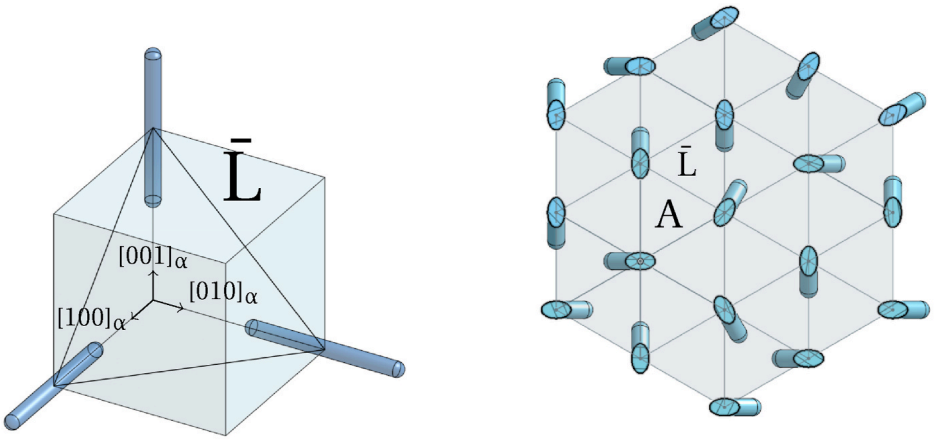

Fig. 3-1. Representation of β-type precipitates in precipitation hardened FCC crystals [101].

The coherency of a phase refers to the type of bonding at the interface between the precipitate and the matrix. Fig. 3-2 illustrates the difference between coherent and incoherent precipitates in a perfect crystal lattice. Coherent precipitates have a lattice structure that is similar to the matrix, which allows for a continuous bond at their interface. Incoherent precipitates have a lattice that has no relationship with the matrix and is bounded by a well-defined interface. Some phases may also be semi-coherent, which have both coherent and incoherent interfaces on different sides of the precipitate. In the precipitation of AA6000-series alloys, the precipitates are coherent during the early stages of ageing and transition to being incoherent at the late stages of ageing.

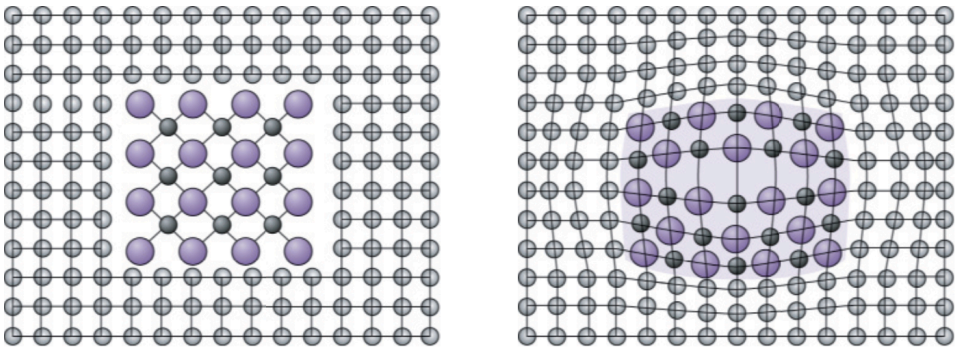

Fig. 3-2. Crystal lattices illustrating the bonding for (left) incoherent precipitates and (right) coherent precipitates [12].

3.2 Mechanical Properties of Precipitation Hardened Alloys

This section provides a brief introduction to the physical effects of precipitation hardening in aluminum alloys. These effects are not specific to AA6000-series materials in particular, but prevail across all series of precipitation hardenable aluminums. The major topics that are discussed here are variations in the yield strength, work hardening behavior, plastic anisotropy and Bauschinger effect.

3.2.1 Yield Strength

The evolution of yield stress with artificial ageing is perhaps the physical property that is affected with the greatest magnitude. The increase in yield strength was first observed by Wilm [24] who noticed a non-negligible hardening after leaving an Al-Cu alloy in room temperature over several days. Today, this strengthening has been characterized in detail in all series of

precipitation hardening aluminums with numerous types of heat treatment settings. All types of alloys demonstrate a similar hardening pattern: from the quenched state, the yield strength increases with the duration of artificial ageing until peak strength is achieved. At this point, any subsequent ageing begins to reduce the strength of the alloy. The yield strength also defines the state of ageing: under-aged refers to the regime before peak strength, peak-aged refers to the peak-strength state and over-aged refers to the regime after peak strength.

As shown in Fig. 3-3 for different Al-Mg-Si alloys, the increase in the yield strength can be several multiples between the under-aged and peak-aged states. This behavior is largely responsible for the success of aluminum alloys as this increase in strength does not correspond to any increase in material weight. However, achieving peak strength requires precise control over the heat treatment, as additional ageing can result in detrimental effects that are not limited to reductions in strength. On a similar note, the maximum stress at peak strength also depends on the parameters of the heat treatment process. While higher temperatures can expedite the artificial ageing process, the resulting peak stress may be lower.

(a)

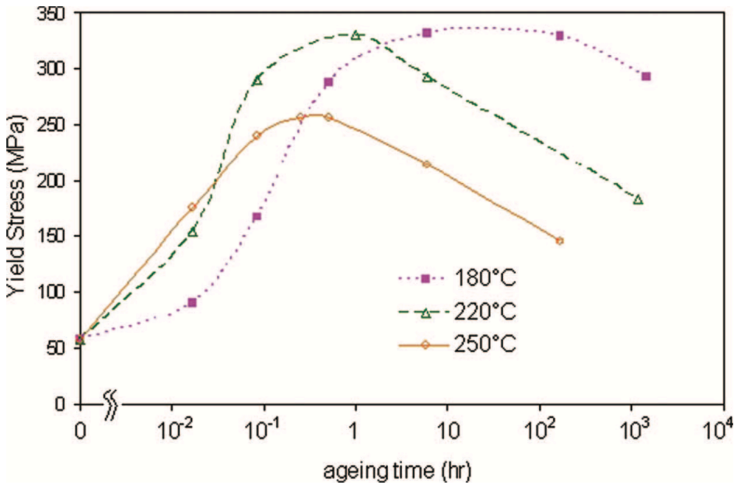

(b)

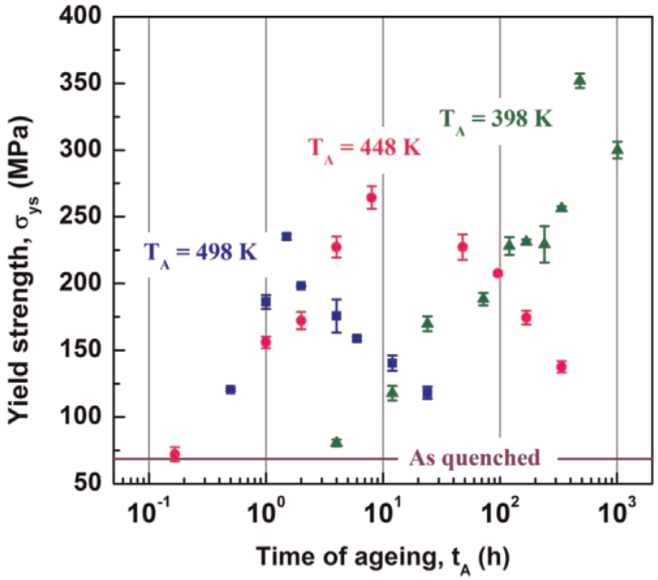

Fig. 3-3. Yield strengths of (a) AA6111 [102] and (b) AA6063 [103] as a function of artificial ageing time.

3.2.2 Work Hardening

The impact of artificial ageing on the work hardening rate is rather complex due to the numerous artifacts introduced by precipitation. Typically, the work hardening rate is highest in the as-quenched condition, which then decreases with the duration of ageing. This is shown in the work hardening rate curves of Fig. 3-4 for an AA6111 alloy aged at 180°C. The reduction in the height of the curves with the duration of ageing shows that the overall work hardening rate

decreases with time. In some alloys, additional ageing after peak strength begins to increase the work hardening rate. This is shown in Fig. 3-5 for an AA7000-series alloy, where the overall work hardening rate improves from the peak-aged to over-aged states.

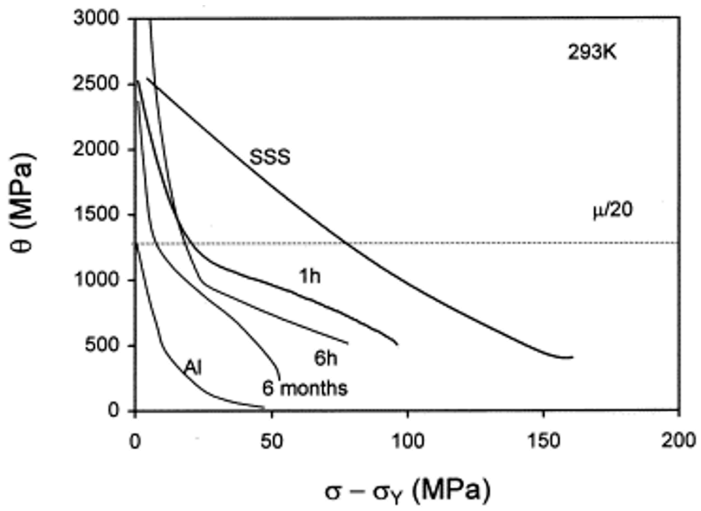

Fig. 3-4. Work hardening rates for AA6111 at multiple heat treatment conditions aged at 180°C [104].

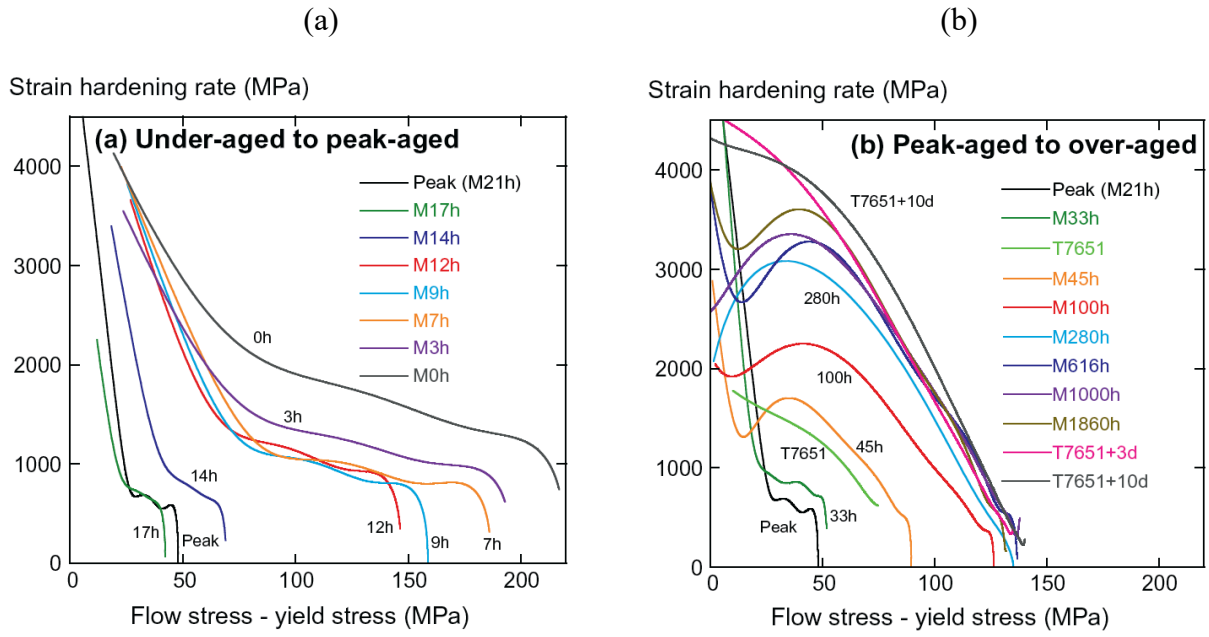

Fig. 3-5. Work hardening rates for AA7449 in the (a) under-aged regime and (b) over-aged regime [105].

3.2.3 Plastic Anisotropy

Plastic anisotropy refers to the directionality of a material's mechanical properties when deformed in the plastic regime. Artificial ageing in aluminum alloys has been observed to reduce plastic anisotropy, as observed in both AA2000-series [106–108] and AA7000-series [65] alloys. However, the effect in AA6000-series alloys is somewhat controversial as some authors have found the effect nearly negligible [109]. This is likely due to the relatively low precipitate volume fractions compared to the other series of precipitation hardening alloys. This difference is presented clearly in Fig. 3-6 and Fig. 3-7 with observations of the strain ratios (i.e. Lankford coefficients) in two different alloys at multiple ageing conditions. In the Al-Cu alloy, there is a strong change in the anisotropic behavior as the material is aged. However, testing of an AA6063 alloy shows a much weaker effect. In these figures, perfect isotropy is defined by a horizontal line measured with respect to orientation.

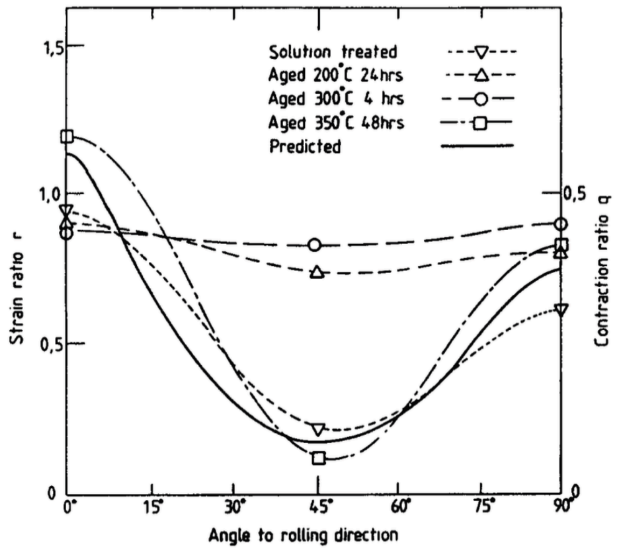

Fig. 3-6. Plastic anisotropy represented using strain ratios for an Al-4%Cu alloy [106]

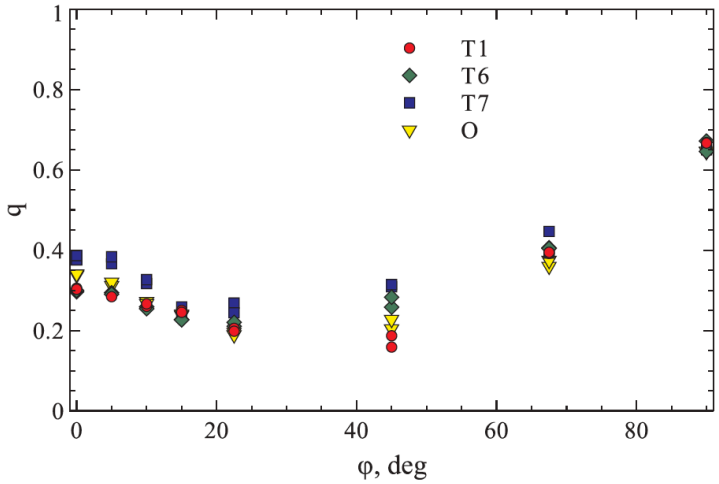

Fig. 3-7. Plastic anisotropy represented using strain ratios for an AA6063 alloy [109].

3.2.4 Bauschinger Effect

The Bauschinger effect is a change in the mechanical properties of an alloy when subject to a strain path change. This is most often observed as a reduction in yield strength during cyclic loading, though the work hardening can also change. Artificial ageing has been shown to introduce a larger Bauschinger effect with longer durations of ageing. This is shown in Fig. 3-8 for an AA6111 alloy at different heat treatment conditions. In the under-aged experiment, the material returns to its original yield and work hardening behavior almost immediately after reloading. However, in the over-aged experiments, there is a notable drop in the yield strength as well as a transient region where the stress-strain response is inverted. Similar patterns have been shown in other AA6000-series alloys [110–112] and is also prevalent among other series of aluminum materials [65, 113, 114].

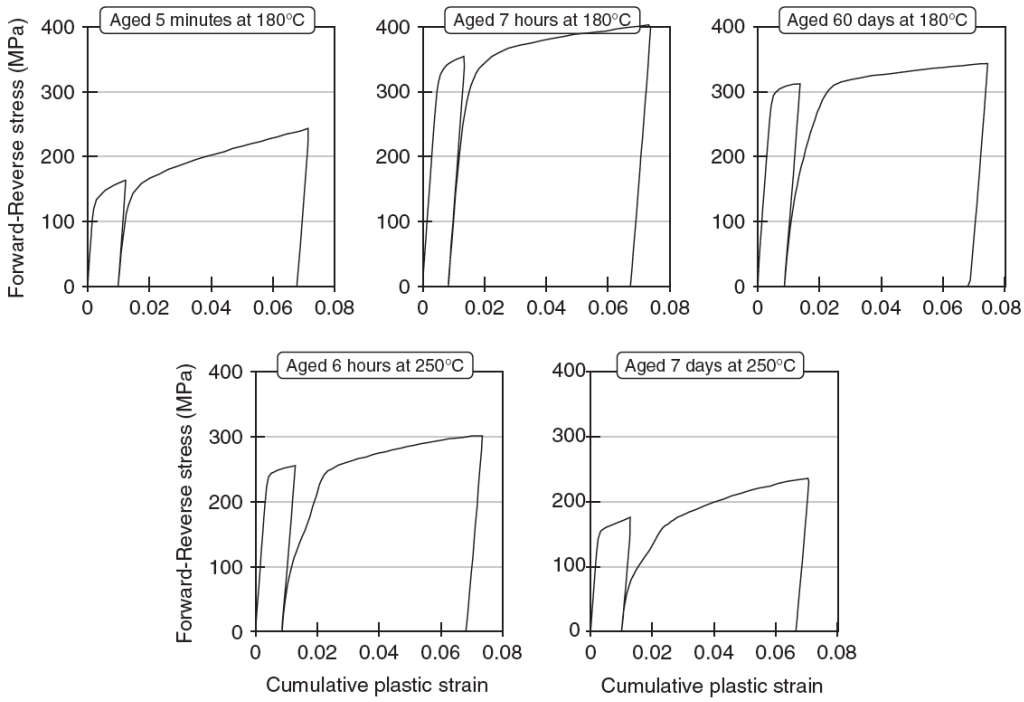

Fig. 3-8. Forward-reverse stress-strain curves for AA6111 at different heat treatment conditions [115].

3.3 Review of Precipitation Hardening Modeling

The physical effects of precipitation hardening are not simple to model owing to the many factors that must be considered for an accurate representation of the alloy. Most of the efforts in precipitation hardening literature has been towards the development of yield strength models since the yield strength is quite sensitive to the state of precipitation. However, there has been some recent interest towards modeling the entire flow stress curve, which has sprung the adoption of many other theories. In this section, a review of several precipitate modeling techniques is conducted. This list is not fully exhaustive of the literature but outlines some of the major areas of research in the simulation of precipitation hardening.

3.3.1 Dislocation-Based Models

Dislocation-based models are those that relate the strengthening of the alloy to some aspect of dislocation behavior. Perhaps the very first model for precipitation hardening was developed by Mott and Nabarro in 1940 [116] who hypothesized that the increase in strength was due to the interaction between dislocations and the internal strains generated by precipitates. A similar

model was later developed by Fisher et al. [117] who considered the Orowan looping effect of dislocations. They related the CRSS to the average number of dislocation loops surrounding each particle and was of the first to discuss the impact of precipitate-induced backstress. Many of the earlier models were largely superseded by a universal model for yield strengthening by Kocks [118], which was used to model the yield effect from any kind of randomly arranged obstacle, including precipitates. In the Kocks model, strengthening was caused by changes to the dislocation-mean free path and the work hardening behavior was captured from the accumulation of dislocations in the microstructure. With the adoption of computing power, Foreman and Makin [119] were able to validate Kocks' work using the direct numerical simulation of dislocations through an array of particles. Today, the modeling of yield strength and flow stress rely on fundamentally the same theories as those proposed by Kocks [19, 57]. The articles by Ardell [120] and Lloyd [121] provide an in-depth review of dislocation-based precipitate strengthening methods while a summary is presented as follows.

3.3.1.1 Yield Strength Modeling

The variation of the yield strength with ageing is primarily due to changes in the dislocation-mean free path as precipitates nucleate out of solid solution. Precipitates act as obstacles to dislocation motion and provide resistance to the onset of crystallographic slip. Numerically, the increase in critical shear stress (CSS) relies on the Peach-Koehler relationship

$$\tau = \frac{F}{Lb} \tag{37}$$

where τ is the CSS, F is the obstacle strength, L is the effective spacing between precipitates and b is the Burgers vector. This equation can also be graphically interpreted as the resistance provided by a pair of obstacles when a force is applied to a dislocation line, as shown in Fig. 3-9. The angle θ is the critical angle right before the particle is sheared through by the dislocation.

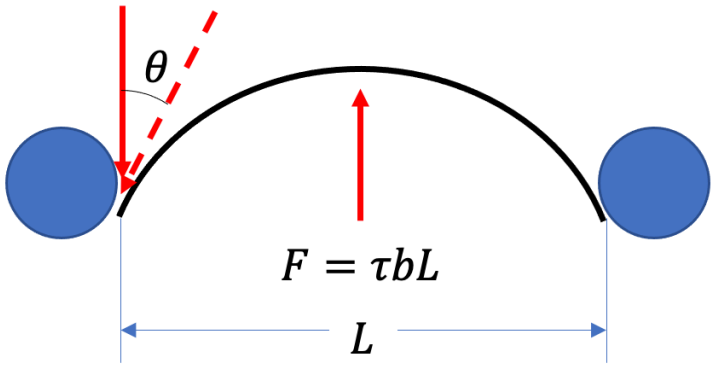

Fig. 3-9. Graphical interpretation of the Peach-Koehler effect showing the interaction between a dislocation and precipitates.

The strength of the particles can be calculated with a force balance on the dislocation line

$$F = 2\beta\mu b^2 \cos\theta \qquad \textbf{(38)}$$

where the term $\beta\mu b^2$ is the dislocation line tension and β is a material constant. The strength and shearability of the particles is dependent on an accurate definition of θ, which is related to the particle size [31].

Much of the recent research has been centered on the accurate estimation of the obstacle spacing, L. This is because many precipitates are non-spherical in morphology, which affects the average interparticle spacing calculation. For instance, Esmaeili et al. [99] developed a model for needle-shaped precipitates in AA6111. Nie and Muddle [122] proposed a similar relationship for plate-shaped precipitates in Al-Cu-Sn. The work by Esmaeili in particular has been developed further by many authors for application to other AA6000-series materials [112, 123–126]. The extension by Bardel et al. [100] was especially important in this field of research as they developed an implementation to account for the entire particle-size distribution. In their method, the precipitates in a predefined distribution are categorized as either weak or strong based on a defined radius criterion. The contribution from each type of precipitate is then calculated and superimposed using the equation

$$\tau_p = \left(\tau_{weak}^n + \tau_{strong}^n\right)^{\frac{1}{n}} \qquad \textbf{(39)}$$

3.3.1.2 Geometrically Necessary Dislocations

A related lineage of precipitation strengthening models is based on geometrically necessary dislocations (GNDs). The concept of GNDs was popularized by Ashby [127] to model the additional hardening observed in certain deformation modes. Specifically, GNDs are dislocations that are absolutely required for the material to accommodate a specific strain state. They are formed when a plastic strain gradient is generated. As shown in Fig. 3-10, a matrix containing a near-rigid particle will require GNDs to accommodate the plastic deformation zone around the particle.

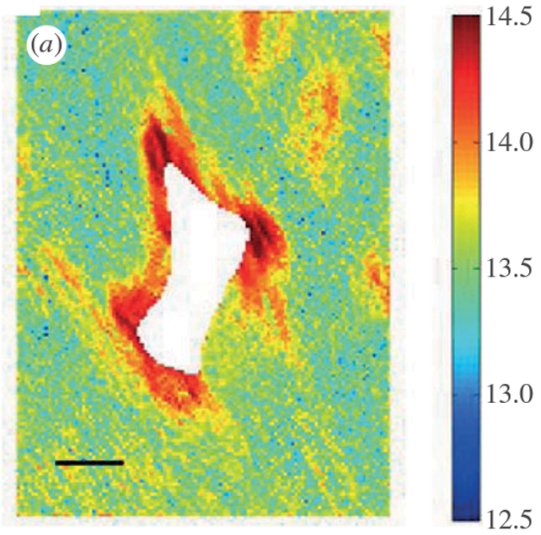

Fig. 3-10. Visual distribution of geometrically necessary dislocations in a Ni single crystal with a single carbide particle [128].

The objective of GND-based models is to determine the quantity of additional GNDs due to precipitation. First, the dislocation density is separated between those that are statistically stored from homogeneous plastic deformation (SSD) and those that are geometrically necessary from plastic strain gradients (GND)

$$\rho = \rho_{SSD} + \rho_{GND} \quad \textbf{(40)}$$

An estimate can then be made based on the approach by Ashby [127] where the GNDs are calculated from the length or spacing of the particles

$$\rho_{GND} \propto \frac{\gamma}{L_p b} \quad \textbf{(41)}$$

where γ is the plastic shear strain in the matrix and L_p is the interparticle spacing. The SSDs are calculated using any traditional dislocation density evolution law, such as the one by Kocks and Mecking [57, 58]. Finally, the strength is modeled using a relationship between the critical shear stress and ρ, such as with Eq. (5). As the material is plastically deformed, both ρ_{SSD} and ρ_{GND} contribute to the hardness of the crystal.

GND-based models are used often throughout literature because the stress-strain curves of artificially aged alloys can deviate from the curves generated by standard dislocation density models. GNDs are often required to simulate over-aged alloys to capture the large elastic-plastic transition in the stress-strain curve. The dislocation density model by Cheng et al. [129] was a significant contribution as they were of the first to introduce GNDs for the modeling of AA6000-series alloys. This was followed by Poole and Lloyd [130] and Sehitoglu et al. [131] who used similar approaches with slight modifications. More recent works that also employ a GND-based approach include Myhr et al. [132, 133], Khadyko et al. [134] and Bardel et al. [112].

Along a similar line of modeling, strain gradient plasticity (SGP) [135, 136] is a theory that is specifically used to calculate GNDs more accurately within a microstructure. In SGP, the gradient of plastic strain is introduced as a separate equilibrium equation to be solved. These models have been used to study size-dependent effects, such as the effect of grain size or particle size [137]. However, SGP formulations are often mathematically complex, making their implementation challenging. Furthermore, all precipitates must be individually meshed into the SGP problem, which makes the computation somewhat difficult for materials with a dense particle distribution.

3.3.1.3 Dislocation Loops

The concept of dislocation looping was initially proposed by Orowan [138] to describe the interactions between dislocations and other obstacles. However, Fisher et al. [117] were the first to directly relate the number of Orowan loops to precipitation hardening. Their theory was that as dislocations accumulated against precipitates, the effective particle size increases, which ultimately raises the critical stress required to activate slip. Further development towards this type of modeling was rare until the recent work by Proudhon et al. [115], who re-introduced the Orowan looping concept to calculate the internal stress caused by precipitates. In their model, a

relationship was made between the number of loops surrounding the average particle and the shear strain in the crystal

$$\frac{dn}{d\gamma} = \frac{l\cos\theta}{b\,\sin\theta}\left(1 - \frac{n}{n^*}\right) \quad \textbf{(42)}$$

where n is the number of dislocation loops, γ is the shear strain, l is the precipitate length, and n^* is the maximum number of loops a dislocation can hold prior to fracturing. The model was further used by Fribourg et al. [105] for the simulation of an AA7000-series alloy, and then later by Bardel et al. [112], who formed an additional relationship between the number of dislocation loops and the magnitude of dynamic recovery in the material.

3.3.2 Inclusion-Based Models

A separate class of models for precipitation hardening relies on incorporating the precipitates as inclusions. In contrast to dislocation-based models where the strengthening effect of precipitation is modeled through changes in dislocation behavior, inclusion-based models directly simulate the stress and strain state of the precipitate. Possibly the earliest type of inclusion-based model was developed by Hosford and Zeisloft [107]. Their model, known as the plastic inclusion model, allowed the precipitates to deform and rotate plastically to maintain compatibility during large deformations. The overall stress of the crystal was calculated based on the work required to deform both the matrix and precipitate such that

$$\sigma = (1 - f)M\tau_m + f\sigma_{ppt}N \quad \textbf{(43)}$$

where M is the Taylor factor, τ_m is the CSS of the matrix, f is the volume fraction of precipitate, σ_{ppt} is the flow stress of the precipitate, and N is an accommodation factor that relates the strain in the precipitate to the strain in the matrix. In their original work, N is defined based on assumptions of the behavior of the precipitates, where certain orientations were permitted to rotate while others were allowed to deform. At about the same time, Brown et al. [139, 140] introduced a similar model, now known as the elastic inclusion model, which employed Eshelby mechanics to model the precipitate. Fundamentally, the elastic inclusion model follows the same idea as the plastic inclusion model, with the exception that the strain inside the particle is solved with simplified mean-field homogenization techniques. In their work, the overall stress is calculated as

$$\sigma = (1 - f)M\tau_m + 2f\mu D\epsilon^p \quad \textbf{(44)}$$

where μ is the shear modulus, D is the accommodation scalar related to the geometry of the precipitate, and ϵ^p is the transformation strain or eigenstrain of the precipitate that can be assumed equal to the plastic strain of the matrix if the precipitate and matrix share similar elastic constants. This idea was adopted by Bate et al. [106, 113] who in a series of articles demonstrated the effectiveness of the elastic inclusion model for predicting backstress and precipitate-induced anisotropy in Al-Cu alloys. The elastic inclusion model was further implemented within a constitutive framework by Barlat and Choi et al. [108, 141] in order to simulate the effect of artificial ageing on complete yield surfaces.

Hargarter et al. [142] demonstrated that both the plastic and elastic inclusion models performed similarly when tasked with predicting plastic anisotropy. These inclusion-based models are effective at making predictions of anisotropy because the deformation of the precipitate is connected to the crystallographic texture. For instance, Hosford and Zeisloft [107] initially found that weaker crystal orientations were strengthened more by precipitates than stronger ones. Dislocation-based models do not account for such behavior and are inherently isotropic in nature. The elastic inclusion model has the advantage of being self-consistent as the solution to the stress in the precipitate is solved via Eshelby mechanics. The backstress that is introduced is also capable of capturing the Bauschinger effect associated with the precipitates. Recently, the elastic inclusion model has been extended further by Bhattacharyya et al. [65] who proposed an elastic-plastic self-consistent micromechanics scheme to homogenize the precipitates in AA7085. This implementation was particularly important as they were one of the first to use a complete homogenization framework to calculate the strain inside the precipitate. Their method allowed for all stress and strain components to be obtained in the precipitate phase and also provided the possibility to incorporate multiple precipitate variants.

3.3.3 Direct Simulation Methods

Another method of modeling precipitation hardening is by directly simulating the precipitate and its interactions with the surrounding matrix. For instance, Qiu et al. [82] used molecular dynamics to investigate the structure and deformation behavior of Mg_5Si_6 precipitates. They were able to simulate the stress-strain curves of these nanoparticles with various additions of other solutes. Queyreau et al. [143, 144] used dislocation dynamics to simulate the interactions

between dislocations and particles. They were able to validate common phenomenological theories of precipitation hardening using only simulation results. Zain-ul-abdein and Nelias [145] incorporated precipitates directly within an FEM framework and investigated the stress and strain fields from coherent and incoherent precipitates. A similar crystal plasticity FEM approach was used by Jung et al. [146] to simulate the effect of precipitation on surface roughness. While direct simulation approaches are valuable for investigating precipitate interactions, many of these methods are limited in application due to stringent computational costs.

3.4 Review of Precipitation Kinetics Modeling

3.4.1 Classical Theory

The modeling of precipitation kinetics is largely based on classical nucleation and growth theory (CNGT) due to its broad applicability and wide material coverage. These models originated from works by Volmer and Weber [147], Zeldovich [148] and Zener [149] among many others. The early nucleation models were developed for understanding the condensation of droplets from vapor. Precipitation kinetics models were not popularized until the late 20th century with works by Shercliff and Ashby [150, 151] who consolidated the nucleation, growth and coarsening equations into a single age hardening model. However, their model was very simplistic and based on independent calculations for volume fraction, solute concentration, and radius. Deschamps and Brechet [31] introduced the generally accepted form of CNGT based on works by Langer and Schwartz [152] and Kampmann and Wagner [153], where nucleation, growth and coarsening were simulated as concurrent processes that interacted with one another. Soon after, Myhr et al. [76] followed the KWN method and developed a control volume approach for the simulation of the kinetic equations. Their numerical method is widely used in the literature today to simulate the full particle-size distribution during artificial ageing. A similar line of research was proposed by Du et al. [154] that focused on incorporating multi-solute and multi-phase capabilities as well as CALPHAD compatibility. At about the same time, Esmaeili et al. [99, 155] developed a precipitation model that utilized an Avrami equation for the simulation of precipitate volume fraction and size.

Many of the earlier kinetics models assumed that the precipitates were spherical. This was a valid assumption for a large class of alloys; however, it is well known that Al-Cu and Al-Mg-Si alloys have large aspect ratios with geometries close to cylinders. Ferrante and Doherty [32] was

of the first to incorporate the aspect ratio of non-spherical precipitates into a growth and coarsening model. Liu et al. [156] and Song [157] then advanced this work by combining it with a simple nucleation equation and applying the model to AA6061. Bahrami et al. [123] later introduced a model that rederived the kinetics equations under a cylindrical precipitate assumption. This was shown to improve the accuracy of existing models while also introducing a way to investigate the effects of aspect ratio on ageing. This idea was then further improved by Bardel et al. [100], who introduced multiple solutes and used the KWN method to simulate the entire particle-size distribution. Later, Holmedal et al. [158] developed shape factors for prolate and cuboid particles that could be easily substituted into existing spherical models.

Classical nucleation and growth models have gained considerable attention in the recent decades due to their success in modeling precipitation kinetics. Notable examples include publications by Myhr et al. [76, 93, 132], who developed two iterations of their industrial software, NaMo as well as Wu et al. [159] for their development of commercial software, TC-PRISMA. Both models utilize the classical theories coupled with CALPHAD to predict the particle-size distribution of any heat-treatable alloy. Recently, CNGT has been applied to simulate precipitation in Al-Si-Mg-Mn by Cinkilic et al. [160], Al-Cu-Cd by Hu et al. [125], Al-Cu and Al-Zn-Mg by Li et al. [161], Al-Si-Mg by Chen et al. [162], Al-Mg by Yi et al. [163], and others [40, 94, 101, 164–166].

3.4.2 Alternative Kinetics Models

Alternative models for precipitation have also been developed that are based on non-classical approaches. Clouet et al. [85, 167] utilized the lattice kinetic Monte Carlo (LKMC) approach to simulate the early stages of ageing in aluminum alloys. De Geuser et al. [168] used a similar model in combination with a CALPHAD database to simulate the direct formation of GP zones in Al-Cu alloys. Their method successfully predicted the widely accepted disk morphology of GP zones. This work was also reproduced by Gorbatov et al. [169] through a coupling with ab initio calculations. KMC is largely inhibited by short ageing durations due to the small time increments required to simulate vacancy diffusion. To combat this, Henkelman and Jonsson [170] introduced an atomistic Monte Carlo approach with a relaxed lattice constraint that allowed for longer time scales. Sigli et al. [80] also suggested the coupling of KMC with cluster dynamics (CD) to simulate the complete precipitation cycle. The theory of cluster dynamics is largely influenced by the works of Clouet [171–173] who was perhaps one of the first to introduce CD

for precipitation in aluminum alloys. Lepinoux [174] later introduced a modification to the CD approach with a new representation of precipitation kinetics that enhanced the model's predictions for ageing in Al-Zr. More recently, Stegmuller and Hader [175] introduced a multi-scale CD model coupled with atomistic calculations that was used to simulate precipitation in Al-Cu. Their model was advantageous as it contained few parameters and could also simulate long durations of ageing.

A simulation approach that has gained prominence in the last decade is the phase field method [176]. This approach is a full-field continuum method that can model the interactions between precipitates as well as their morphological transitions [177]. Zhu et al. [178] used a 3D phase field approach to model the coarsening kinetics in Ni-Al alloys. They were able to predict the evolution of precipitate morphology, size, and distribution, which matched well with experimental observations. The phase field method was also used by Gao and Liu et al. [179, 180] to model the β' phase in Mg alloys and by Ji et al. [181] and Hu et al. [182] to model the θ' phase in Al-Cu alloys.

3.5 Deficiencies in Literature

While a considerable amount of research exists on the modeling of precipitation hardened alloys, there are still some deficiencies in the literature that this research aims to address. First, the literature of precipitation hardening is predominantly focused on yield strength and hardening behavior [112, 120, 130, 160, 183]. The literature on the effect of artificial ageing on plastic anisotropy or backstress is relatively weak, especially for AA6000-series alloys. Second, given the large amount of data on the precipitation effect, there is still a substantial degree of mechanical modeling that does not account for the precipitates [109, 184–187]. Granted, these works were not focused on modeling the precipitate hardening response in particular, but they still neglect the potential kinematic and anisotropic effects associated with ageing. Third, the concept of precipitate morphology is largely overlooked in both constitutive models and precipitation kinetics models [65, 111, 132, 133]. This is largely due to the simplicity of the spherical assumption that avoids many implementation issues. However, there is a long lineage of publications on the effect of particle morphology that should be considered in modern numerical frameworks [32, 99, 107, 121, 156, 157]. Finally, there are relatively few works that relate the initial ageing process all the way to the localization and large plastic deformation

behavior of the material. Existing through-process models have primarily focused on accurately simulating the yield strength from artificial ageing [40, 80, 94, 123, 159, 160, 165, 166].

4 Research Scope and Objectives

The focus of this research is to develop a simulation framework that can efficiently and accurately capture the physical effects caused by precipitation hardening in aluminum alloys. In particular, the goal is to capture the four mechanical properties of precipitation hardening discussed in Section 3.2: yield strength, work hardening, plastic anisotropy, and the Bauschinger effect. It is proposed that a physics-based constitutive model that incorporates the structure and properties of the underlying precipitates will achieve the successful prediction of these physical effects. This will be combined with a precipitation kinetics model to simulate the precipitate distribution for a prescribed heat treatment profile. Ultimately, the joint through-process model will create a relationship between the initial heat treatment and the large deformation response of precipitation hardened aluminum alloys. The proposed methodology will be evaluated using AA6000-series aluminum alloys due to the availability of material as well as to accommodate the recent surge of interest in these alloys by the academic community. Experimental characterization will be conducted at various states of artificial ageing to obtain a reasonable understanding of the material at different heat treatment conditions. However, the numerical framework will be indifferent to the material used as long as the alloy consists of similar characteristics for precipitation.

In summary, this research will accomplish three objectives:

1. Develop a physics-based precipitation hardening constitutive model to capture the mechanical effects caused by a precipitate distribution.
2. Develop a precipitation kinetics framework to simulate the precipitate distribution for a prescribed heat treatment.
3. Conduct experimental testing for the calibration and validation of the above numerical models.

4.1 Summary of Contributions

The work completed to achieve the research objectives are presented in the subsequent chapters. Research objective (1) is completed in Chapter 5 while research objective (2) is completed in Chapter 6. The experimental characterization in research objective (3) is completed in both Chapters 5 and 6. These chapters are based on the following published manuscripts:

Chapter 5 Li, Y.L., Kohar, C.P., Mishra, R.K., Inal, K., 2020. A new crystal plasticity constitutive model for simulating precipitation-hardenable aluminum alloys. International Journal of Plasticity 132, 102759. https://doi.org/10.1016/j.ijplas.2020.102759

Chapter 6 Li, Y.L., Kohar, C.P., Muhammad, W., Inal, K., 2022. Precipitation Kinetics and Crystal Plasticity Modeling of Artificially Aged AA6061. International Journal of Plasticity 103241. https://doi.org/10.1016/j.ijplas.2022.103241

In addition to these publications, the following manuscripts have also been written during the current research. However, these works do not have a direct impact on the research objectives of this thesis and are referenced only as supporting work:

Iftikhar, C.M.A., Li, Y.L., Kohar, C.P., Inal, K., Khan, A.S., 2021. Evolution of subsequent yield surfaces with plastic deformation along proportional and non-proportional loading paths on annealed AA6061 alloy: Experiments and crystal plasticity finite element modeling. International Journal of Plasticity 143, 102956. https://doi.org/10.1016/j.ijplas.2021.102956

5 A New Crystal Plasticity Constitutive Model for Simulating Precipitation-Hardenable Aluminum Alloys

Y. Larry Li [a], Christopher P. Kohar [a], Raja K. Mishra [a], Kaan Inal [a]

[a] Department of Mechanical and Mechatronics Engineering, University of Waterloo, Waterloo, Canada N2L 3G1

Abstract

Age hardened aluminum alloys have superior strengths compared to non-age hardenable alloys due to the growth of a secondary phase of precipitates. This work presents a new crystal plasticity numerical framework to simulate the mechanical properties of precipitation-hardened aluminum alloys. A precipitation hardening constitutive law is implemented into the crystal plasticity finite element method (CPFEM) to simulate the localized deformation behavior of a commercially available AA6060-T6 extrusion. Experimental characterization in the form of uniaxial tension and cyclic simple shear is performed on the alloy of interest to validate the formulation. The framework uses information obtained from transmission electron microscopy (TEM) on a similar alloy for the simulation of the precipitate hardening response. This information is incorporated into an elastic-viscoplastic homogenization scheme to predict the behavior of the precipitate directly. The model is shown to capture the stress-strain response, precipitate-induced anisotropy, and the observed Bauschinger effect with good agreement. A series of parametric analyses are then performed to show the effects of precipitation on the bulk and localized necking response. It is observed that the precipitate configuration heavily influences the polycrystalline behavior, and the localized behavior is also affected in a rather complex way. The model captures the general reduction of anisotropy in age-hardened alloys and serves as a good physics-based foundation for future investigative studies.

Keywords: Crystal plasticity finite element method; Precipitation hardening; Homogenization; Anisotropy; Bauschinger effect.

5.1 Introduction

Age hardened aluminum alloys derive their strength from the introduction of a second phase of precipitates. This is accomplished through carefully designed heat treatments that allow for any alloying elements to diffuse out as particles. The alloys possess excellent strength-to-weight ratios and have many other properties that make them desirable for engineering applications. However, it is well known that precipitates introduce complex dynamics that have been historically difficult to characterize and also challenging to model. Fortunately, advancements in experimental techniques have enabled researchers to observe precipitates with refined detail, which have provided theoretical evidence for the development of new physics-based models.

The most notable effects of precipitation hardening are changes to the yield strength and work hardening. However, it has also been observed that artificial ageing can affect plastic anisotropy and introduce a Bauschinger effect [110, 188, 189]. These changes are caused by the ability for precipitates to directly hinder crystallographic slip, resulting in complex dislocation-precipitate interactions that affect the material at the macroscopic scale [190]. The magnitude of precipitation-induced effects is sensitive to the parameters of the heat treatment (i.e. temperature, duration, quench rate, etc.) and vary non-linearly across tempers. Common variables of importance in determining an alloy's properties include precipitate morphology, orientation, volume fraction and size. These factors should be considered in physical models to distinguish between alloys of different heat treatment conditions.

Many models for precipitation hardening are described in Chapter 3.3 of this dissertation. These models are often classified as theories based on dislocations or theories based on the Eshelby inclusion method. Dislocation-based models rely on simulating the interactions between precipitates and dislocations. This includes the lineage of yield strength models [99, 100, 121] as well as models based on geometrically necessary dislocations (GND) [127, 132, 137]. The focus of these models has been to incorporate the effect of precipitates on dislocations into the yield and work hardening equations to model the flow stress more accurately. On the other hand, inclusion-based models rely on treating the precipitates as an independent phase embedded within a large aluminum matrix [65, 106, 108]. The objective of inclusion-based modeling is to simulate the stress inside the precipitate that is responsible for kinematic hardening and changes to plastic anisotropy. In theory, a combination of both dislocation-based modeling and inclusion-based modeling is required to fully account for the physical effects of artificial ageing.

In this chapter, a unified constitutive model is proposed to capture the effects of precipitation hardening in aluminum alloys. The model is aimed at simulating AA6000-series materials in particular; however, the framework can be applied to other series of heat-treatable alloys as well with minor adjustments. The constitutive framework is based on a combination of several precipitation theories to capture different aspects of ageing. This includes a precipitate strengthening model inspired by Esmaeili et al. [99] for capturing the variation in yield strength and a micromechanics framework similar to Bhattacharyya et al. [65] for capturing precipitate-induced anisotropy and Bauschinger effects. What is new in this research is the utilization of a viscous rate-dependent crystal plasticity formulation for homogenizing the precipitate that is fundamentally different than previous attempts for modeling precipitation hardening. Notably, the model directly considers the orientation and morphology of the various precipitate variants as a variable in the simulations. The model is incorporated at the single crystal scale that allows for the prediction of precipitate-induced effects in individual grains. This constitutive framework is then implemented into 3D CPFEM to simulate the localized deformation response of a representative microstructure. The numerical framework is evaluated using a commercially available AA6060-T6 alloy, which was taken from the extruded profile of an automotive crash structure. A combination of EBSD imaging and mechanical testing was used to evaluate the accuracy of the proposed simulation method. The model also uses information obtained from TEM of a similar AA6000-series alloy for the modeling of the precipitate hardening response. This data was taken from Teichmann et al. [191], which allowed for the calibration of the model to precipitate properties at multiple heat treatment conditions. The numerical model is assessed based on its ability to predict the stress-strain behavior, Bauschinger effect and anisotropy of the AA6060 alloy. Finally, the framework is used to investigate the physical behavior at the single crystal scale to obtain a theoretical understanding of the effects of precipitate morphology on common FCC orientations.

5.2 Experiments

5.2.1 Material

An extruded AA6060-T6 aluminum alloy is used in the present work. The material was taken from a single cell extrusion profile that was developed as an automotive energy absorption component [37]. Table 5-1 lists the chemical composition of this aluminum alloy. Fig. 5-1 shows

the heterogeneous microstructure of the as-received material that was obtained from EBSD imaging in three orthogonal planes. There exists a noticeable grain size gradient in the through-thickness direction: the center of the material consists of an equiaxed structure of smaller grains with a predominantly Cube texture, whereas the material near the surface is composed of significantly coarser grains that consist of a stronger Goss texture. This gradient is caused by the extrusion process that generates varying degrees of peripheral coarse grain (PCG) structuring on the outer surfaces due to different recrystallization and cooling rates.

Table 5-1. Chemical composition of aluminum alloy AA6060-T6 (wt%).

Al	Mg	Mn	Fe	Si	Cu	Ti	Cr	Zn
Bal	0.450	0.044	0.109	0.480	0.047	0.019	0.017	0.011

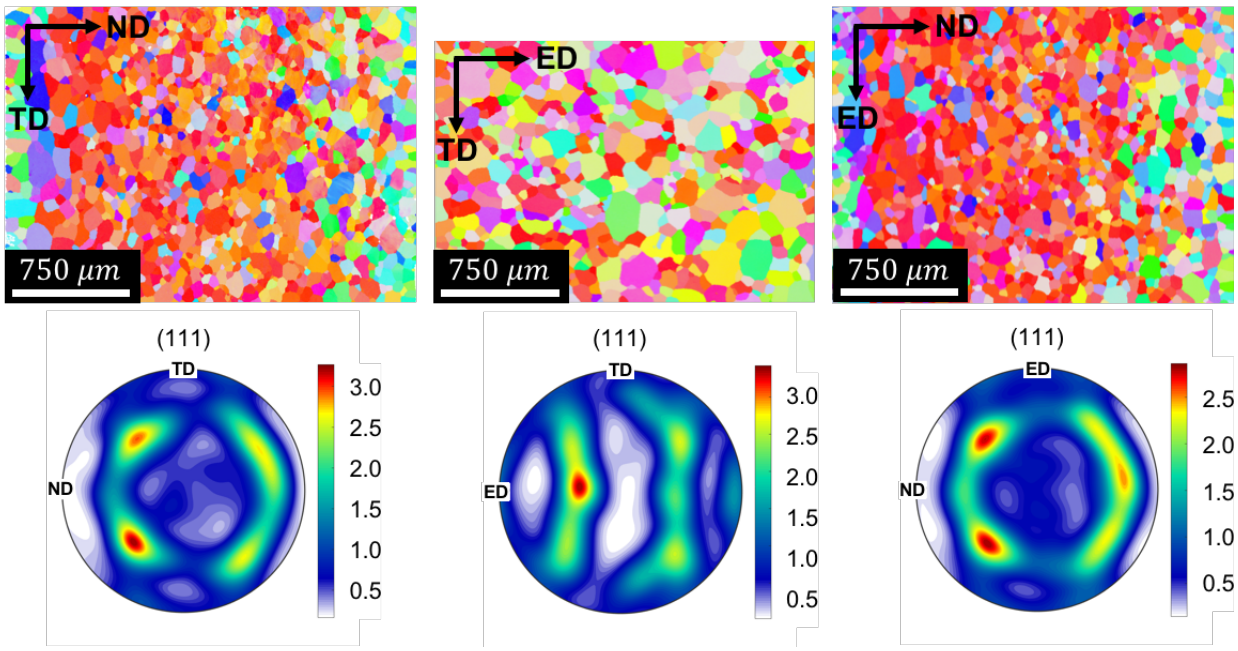

Fig. 5-1. Microstructure of the as-received aluminum material [37].

5.2.2 Mechanical Testing

Kohar et al. [37] previously performed a mechanical testing program that characterized the mechanical properties of the AA6060-T6 extrusion. This mechanical testing program consisted of uniaxial tension, plane strain tension, and simple shear testing in the extrusion direction (ED),

transverse direction (TD), and 45° diagonal direction (DD). The Lankford coefficients (R-value) were also reported for the uniaxial tensile samples. The geometries used in this characterization consisted of a modified ASTM-E8M specimen, a plane strain notch specimen adopted from Achani et al. [192], and an in-plane simple shear specimen adopted from Gruben et al. [193]. In particular, the ASTM-E8M specimens have nominal gauge dimensions of 40.9 mm (L) x 10 mm (W) x 2.4 mm (T). The specimens were directly machined from the as-extruded profile without the removal of the large surface grains. Details regarding the test procedure and the specimen dimensions are described in Kohar et al. [37]. Fig. 5-2 presents the uniaxial tensile stress-strain response and Lankford coefficients (R-values) obtained by the authors. The uniaxial tensile responses are graphed until the ultimate tensile strength (UTS) was reached.

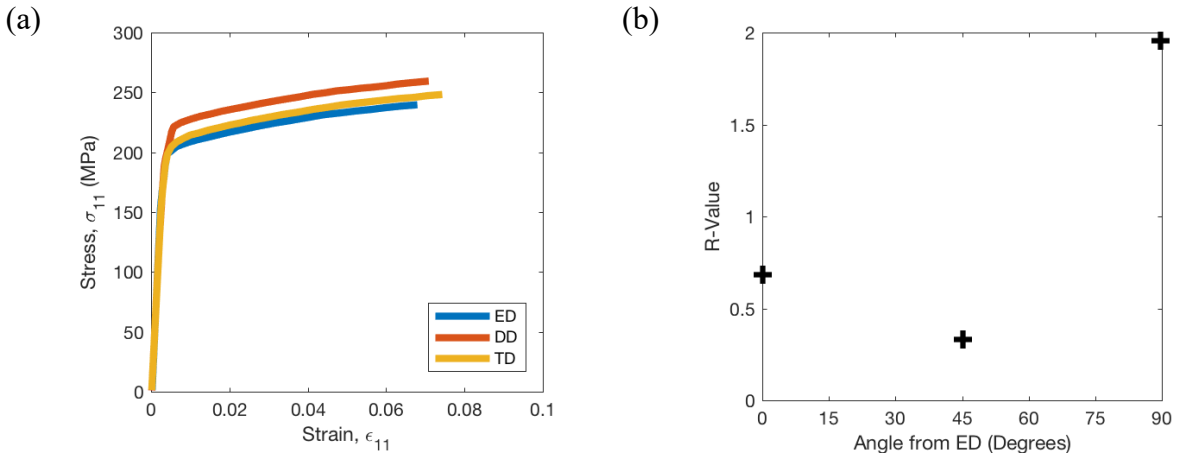

Fig. 5-2. (a) Uniaxial tension stress-strain response in ED, TD, and DD [37]. (b) R-value variation vs. extrusion direction [37].

New experimentation in the form of cyclic simple shear was conducted during this work to characterize the Bauschinger behavior during large deformations. Fig. 5-3 presents the geometry of the specimen used to obtain the simple shear results. Fig. 5-3 also presents a schematic of the experimental setup and a representative image of the field of view. The test geometry is a modified "mini-shear" specimen that was taken from Rahmaan et al. [42]. The specimens were directly machined from the as-extruded profile, without the removal of the surface grains. These shear tests were performed at room temperature using an MTS Criterion 45 servo-hydraulic tensile machine with a 100 kN load cell. The experiments were executed under quasi-static loading conditions ($\dot{\epsilon} = 0.001s^{-1}$) with three repeats for each test condition. The shear characterization program includes cyclic forward-reverse-forward (FRF), cyclic reverse-forward-

reverse (RFR) in addition to fully forward and fully reverse experiments. The cyclic tests were performed at shear reversals of approximately 5%, 10%, and 15% shear strain. Each experiment was also recorded using stereoscopic Point Grey GRAS-50S5M-C cameras with Tamron AF Micro 180 mm lenses and 1.4x Kenko Teleplus Pro 300 teleconverters for digital image correlation.

(a) (b)

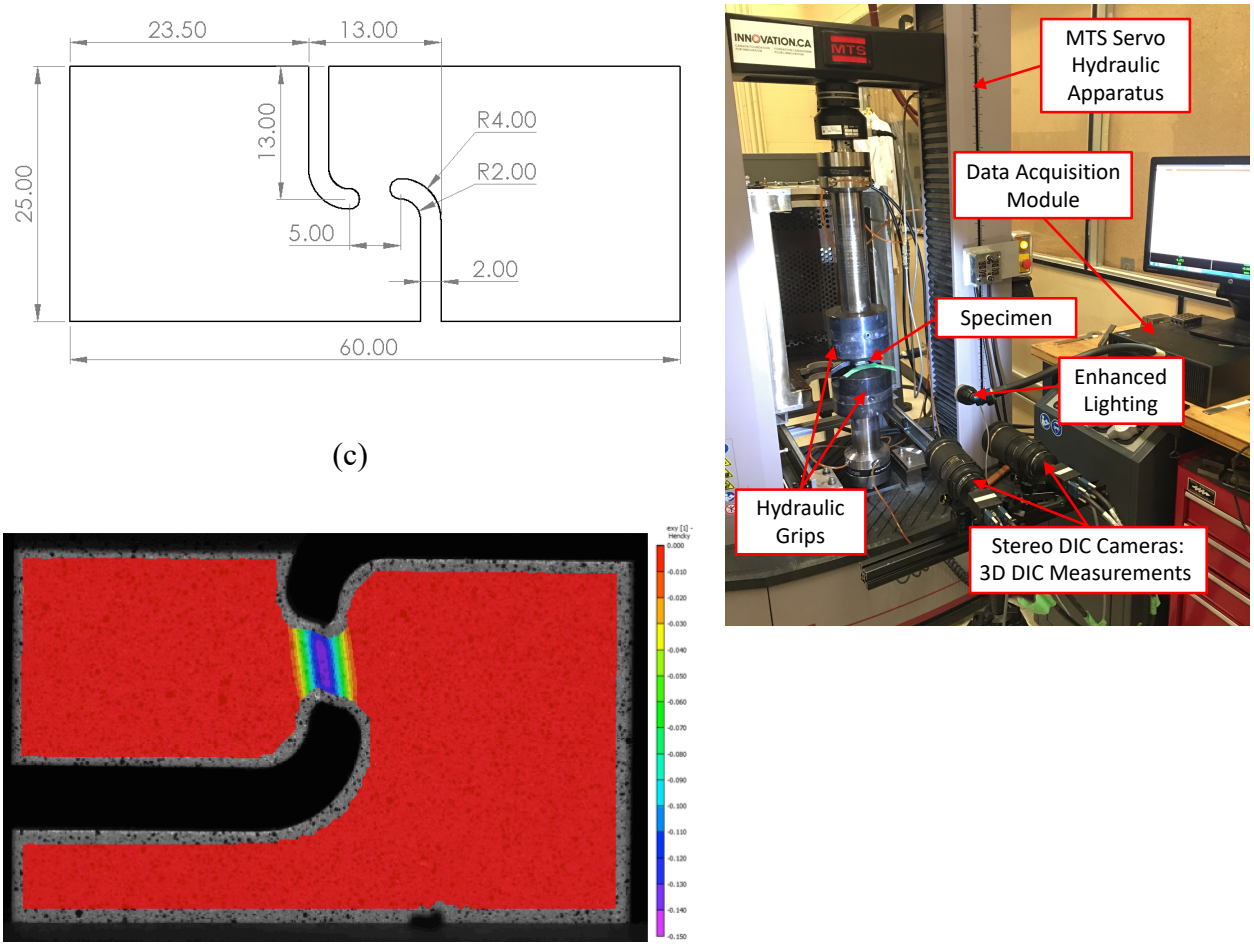

(c)

Fig. 5-3. (a) Mini-shear specimen used for shear characterization (this work). Dimensions in millimeters, (b) Setup of the mini-shear experimental apparatus, and (c) representative field of view during testing.

Fig. 5-4 presents the fully forward and fully reverse simple shear responses for the extruded alloy. Fig. 5-5 presents the cyclic FRF and RFR shear responses for 5%, 10%, and 15% strain reversals. The shear stress was obtained by dividing the measured force by the minimum cross-

sectional area in the gauge section of the shear specimen. The shear strain response was obtained by using a virtual strain gauge of 1 mm diameter at the center of the specimen and calculating the largest in-plane shear strain using

$$\gamma_{12} = 2\epsilon_{12} = 2\sqrt{\left(\frac{\epsilon_{xx} - \epsilon_{yy}}{2}\right)^2 + \left(\epsilon_{xy}\right)^2} \quad (45)$$

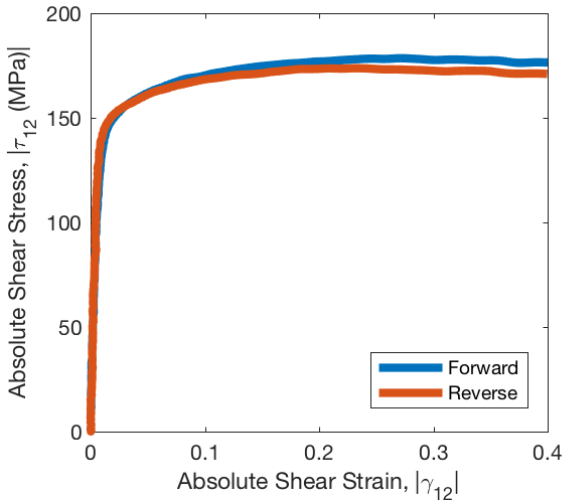

Fig. 5-4. In-plane simple shear stress-strain response for fully forward and reverse shear tests.

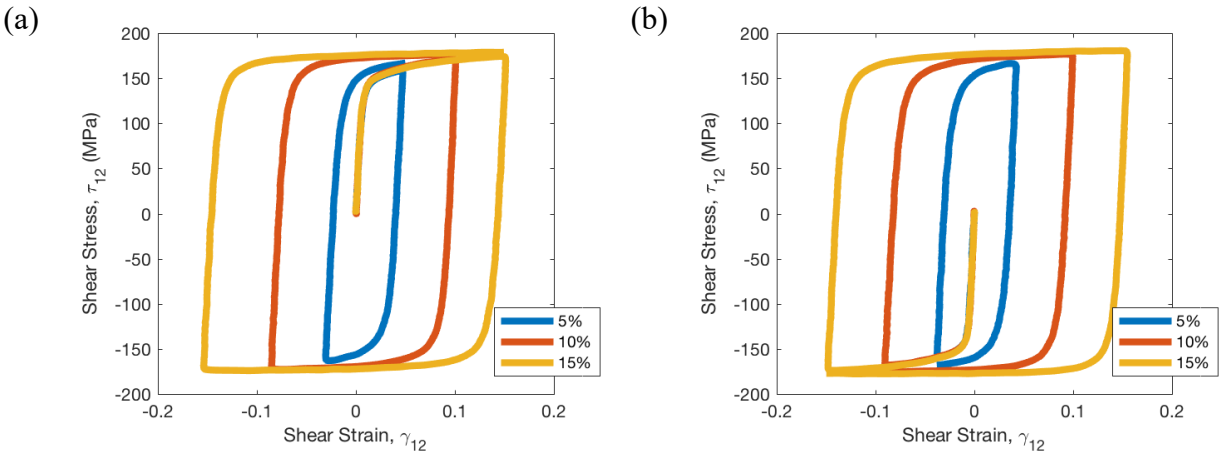

Fig. 5-5. In-plane simple shear responses for (a) FRF experiments and (b) RFR experiments.

5.3 Model Approach

5.3.1 Summary of Methodology

A new precipitation hardening crystal plasticity model is developed in this work to simulate the effect of an existing precipitate distribution on the stress-strain results. The model is implemented at the single crystal scale in order to capture the precipitate-induced response within individual grains. In particular, the precipitates are directly incorporated into each single crystal through a micromechanics framework. In AA6000-series alloys where the precipitates are oriented along the <100> lattice directions, three variants of high aspect ratio inclusions are introduced into the homogenization, where each variant is aligned with one of the <100> directions. A schematic of this orientation dependence is presented in Fig. 5-6: each crystal has a unique set of precipitates that are positioned with respect to the orientation of the grain. The methodology follows a similar approach to the EPSC model by Bhattacharyya et al. [65]; however, the formulation here relies on the use of an elastic-viscoplastic medium in the Green function solution [70]. The precipitate variants are incorporated as three separate phases that are all embedded within the same aluminum matrix. The stress within the matrix and precipitate phases are then calculated via a classical Eshelby mechanics formulation. Inside the matrix phase, hardening is described with a dislocation density law that also includes the effect of precipitation on the dislocation-mean free path. This is accomplished using a precipitate yield strength model following the methodology by Esmaeili et al. [99] for AA6000-series materials. Finally, the single crystal constitutive model is implemented using the crystal plasticity finite element method (CPFEM) with commercial software LS-DYNA in the form of a user-defined material (UMAT) subroutine. The geometry used in the CPFEM simulations is a representative volume element (RVE) that is generated from the EBSD images of the material microstructure.

There are several reasons for developing this model using a crystal plasticity foundation. First, crystal plasticity is a physics-based constitutive model that has been shown to be an effective simulation tool for metals [194]. It is widely used in the academic community for its ability to incorporate crystallographic texture while still being a continuum model. As a result, it has the capabilities to simulate bulk material properties with relatively short runtimes compared to atomistic approaches. Second, crystal plasticity is fundamentally based on modeling the aggregate behavior of dislocation slip. This is advantageous because crystal plasticity can be

used to observe the effect of incorporating a precipitate inclusion on the behavior at a slip system level. Phenomenological approaches cannot easily incorporate these types of physics without considerable modifications to the existing theories. Finally, perhaps the biggest reason for using crystal plasticity in this work is the ability to incorporate precipitates into the single crystal response. Physically, the precipitates' orientations are dependent on the orientation of each grain, which has been observed via TEM in several AA6000-series alloys. These effects can be incorporated with relatively minimal effort using a crystal plasticity foundation and enables the investigation of precipitate-induced effects on the behavior of single crystals.

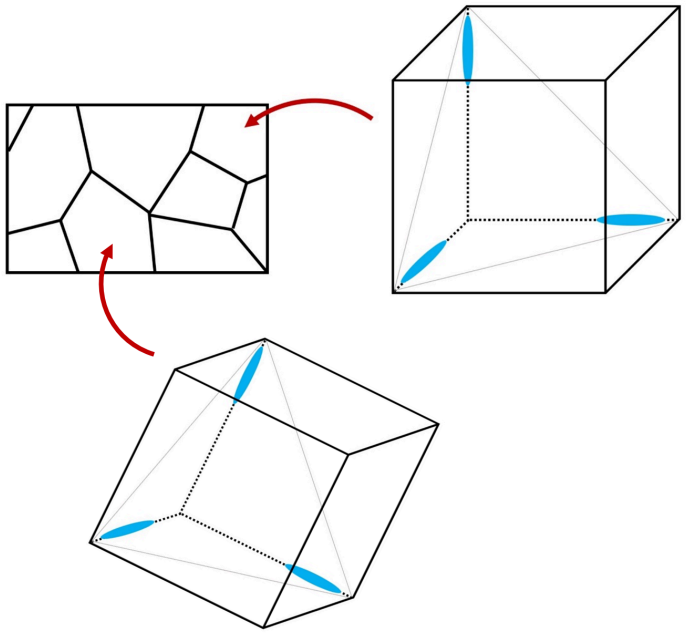

Fig. 5-6. Schematic representation of precipitate orientations within a grain. The (blue) precipitates have high aspect ratios and are oriented orthogonally along the <100> directions of each crystal.

5.3.2 Constitutive Model

5.3.2.1 Crystal Plasticity

The single crystal constitutive model is based on a homogenization of a matrix phase and three precipitate phases. While the overall behavior of the crystal is calculated via an averaging of the properties across all phases, the phases themselves are governed by crystal elasticity and plasticity. The formulation used in this work is based on Peirce et al. [49], which was introduced

earlier in Section 2.5.2. In this chapter, a comprehensive description of their theory is provided. Additional implementation details can be obtained from other resources [5, 195–197].

The total deformation in any phase is due to plastic slip on active slip systems and elastic lattice distortion. As a result, the overall deformation gradient, $\boldsymbol{F}$, is decomposed into

$$\boldsymbol{F} = \boldsymbol{F}^{*}\boldsymbol{F}^{p} \tag{46}$$

where $\boldsymbol{F}^{p}$ is the plastic component, representing crystallographic slip, and $\boldsymbol{F}^{*}$ is the elastic component, representing elastic distortion and rigid body rotation. Each slip system, α is defined with slip direction, $\boldsymbol{s}^{*(\alpha)}$ and slip normal, $\boldsymbol{n}^{*(\alpha)}$ lattice vectors. The lattice vectors are unaffected by any plastic deformation, but undergo a stretch and rotation based on the elastic deformation gradient

$$\begin{aligned} \boldsymbol{s}^{*(\alpha)} &= \boldsymbol{F}^{*}\boldsymbol{s}^{(\alpha)} \\ \boldsymbol{n}^{*(\alpha)} &= \boldsymbol{n}^{(\alpha)}\boldsymbol{F}^{*-1} \end{aligned} \tag{47}$$

where $\boldsymbol{s}^{(\alpha)}$ and $\boldsymbol{n}^{(\alpha)}$ are the lattice vectors prior to any elastic deformation of the crystal lattice. The updated lattice vectors are used to define symmetric and antisymmetric second-order slip system tensors, $\boldsymbol{P}^{(\alpha)}$ and $\boldsymbol{W}^{(\alpha)}$

$$\begin{aligned} \boldsymbol{P}^{(\alpha)} &= \frac{1}{2}(\boldsymbol{s}^{*(\alpha)} \otimes \boldsymbol{n}^{*(\alpha)} + \boldsymbol{n}^{*(\alpha)} \otimes \boldsymbol{s}^{*(\alpha)}) \\ \boldsymbol{W}^{(\alpha)} &= \frac{1}{2}(\boldsymbol{s}^{*(\alpha)} \otimes \boldsymbol{n}^{*(\alpha)} - \boldsymbol{n}^{*(\alpha)} \otimes \boldsymbol{s}^{*(\alpha)}) \end{aligned} \tag{48}$$

that are subsequently used to define the plastic strain rate and spin rate tensors, $\boldsymbol{D}^{p}$ and $\boldsymbol{W}^{p}$

$$\boldsymbol{D}^{p} = \sum_{\alpha} \boldsymbol{P}^{(\alpha)}\dot{\gamma}^{(\alpha)} \tag{49}$$

$$\boldsymbol{W}^{p} = \sum_{\alpha} \boldsymbol{W}^{(\alpha)}\dot{\gamma}^{(\alpha)} \tag{50}$$

The variable $\dot{\gamma}^{(\alpha)}$ is the shear strain rate on slip system α, calculated using a rate-dependent power-law kinetics formula [52]

$$\dot{\gamma}^{(\alpha)} = \dot{\gamma}_{0}\left|\frac{\tau^{(\alpha)}}{g^{(\alpha)}}\right|^{\frac{1}{m}} \tag{51}$$

where $\dot{\gamma}_0$ is a reference shear strain, m is the rate sensitivity exponent, $\tau^{(\alpha)}$ is the resolved shear stress and $g^{(\alpha)}$ is the CSS of slip system α. The resolved shear stress is calculated with Schmid's law

$$\tau^{(\alpha)} = \boldsymbol{\sigma} : \boldsymbol{P}^{(\alpha)} \quad (52)$$

while the CSS is computed from a hardening law representative of the material's physical behavior, described further in Section 5.3.2.3.

Finally, the constitutive update of the single crystal is defined by the relationship

$$\widehat{\boldsymbol{\sigma}} = \mathbb{L}^e : \boldsymbol{D} - \sum_{\alpha} \boldsymbol{R}^{(\alpha)} \dot{\gamma}^{(\alpha)} - \boldsymbol{\sigma}\mathrm{tr}(\boldsymbol{D}) \quad (53)$$

where $\widehat{\boldsymbol{\sigma}}$ is the Jaumann rate of Cauchy stress, $\boldsymbol{D}$ is the rate of strain tensor, $\mathbb{L}^e$ is the convected fourth order elastic modulus defined by

$$\mathbb{L}^{\mathrm{e}} = F^* F^* \mathbb{C}^e F^{*T} F^{*T} \quad (54)$$

where $\mathbb{C}^e$ is the standard elastic modulus and $\boldsymbol{R}^{(\alpha)}$ is defined with

$$\boldsymbol{R}^{(\alpha)} = \mathbb{L}^e : \boldsymbol{P}^{(\alpha)} + \boldsymbol{W}^{(\alpha)}\boldsymbol{\sigma} - \boldsymbol{\sigma}\boldsymbol{W}^{(\alpha)} \quad (55)$$

5.3.2.2 Homogenization

The elastic-viscoplastic homogenization scheme by Molinari et al. [70] is used in this work to model the interactions between the constituent phases of each crystal. In this homogenization scheme, all phases must follow a constitutive law of the form

$$\boldsymbol{D} = \boldsymbol{D}^e + \boldsymbol{D}^v \quad (56)$$

where $\boldsymbol{D}^e$ is the elastic strain rate and $\boldsymbol{D}^v$ is the viscoplastic strain rate. To accomplish this, the crystal plasticity constitutive law of Eq. (53) is rewritten, such that

$$\boldsymbol{D} = \mathbb{M}^e : \widehat{\boldsymbol{\sigma}} + \mathbb{M}^v : \boldsymbol{\sigma} \quad (57)$$

where $\mathbb{M}^e = (\mathbb{L}^e)^{-1}$ is the elastic compliance tensor and $\mathbb{M}^v$ is the viscoplastic compliance tensor. Following the standard Eshelby mechanics approach, a reference matrix is introduced that obeys the same constitutive behavior as Eq. (57) such that

$$\boldsymbol{D}_0 = \mathbb{M}_0^e : \widehat{\boldsymbol{\sigma}}_0 + \mathbb{M}_0^v : \boldsymbol{\sigma}_0 \quad (58)$$

where the subscript 0 is used to denote parameters of the reference matrix. The individual phases are embedded individually within this reference matrix as an inclusion, where the goal is to

determine the strain and stress inside the phase if the reference matrix is subject to a boundary strain. It is important to note that the viscous term, $\mathbb{M}^v$, is nonlinear with strain and can be approximated using various forms of linearization [68, 198]. The choice of linearization is important in determining the strength of the interactions between the inclusion and the reference medium. In this work, $\mathbb{M}^v$ is calculated using the so-called n-effective linearization scheme

$$\mathbb{M}^v = n_e \mathbb{M}^{sec} \tag{59}$$

where $\mathbb{M}^{sec}$ is obtained via rearrangement of Eq. (53) and the substitution of Eq. (55)

$$\mathbb{M}^{sec}_{ijml} = \sum_{\alpha} \left[\frac{\dot{\gamma}_0}{g^{(\alpha)}} \left| \frac{\tau^{(\alpha)}}{g^{(\alpha)}} \right|^{\frac{1}{m}-1} P^{(\alpha)}_{ij} P^{(\alpha)}_{ml} + \mathbb{M}^e_{ijkl} W^{(\alpha)}_{km} \dot{\gamma}^{(\alpha)} - \mathbb{M}^e_{ijmk} W^{(\alpha)}_{lk} \dot{\gamma}^{(\alpha)} \right] \tag{60}$$

The n_e parameter is used as an adjustable value to soften the moduli of the reference matrix [68, 198, 199]. This is similar to the isotropisation method of Pierard et al. [200, 201].

The homogenization of materials that are either fully elastic or fully viscoplastic has been discussed in much detail throughout literature [72, 202]. However, the constitutive model in this work is both elastic *and* viscoplastic, which makes a direct application of Green's function not directly applicable as there are two stiffness moduli. Though it is possible to form a single elastic-viscoplastic tangent modulus that would enable the regular Green function solution, previous attempts at creating the tangent modulus in crystal plasticity led to results that were excessively stiff [70, 203]. It turns out that a simple but approximate solution to this issue can be obtained by separating the elastic and viscoplastic components and solving for their effects independently. The resulting elastic-viscoplastic solution can then be obtained by summing the results from the independent elastic and viscoplastic interactions [204, 205].

To illustrate this, the elastic portion of the interaction law is derived first. The viscous portion follows a nearly identical derivation procedure. The elastic constitutive law for any phase is expressed as

$$\boldsymbol{D}^e_i = \mathbb{M}^e_i : \widehat{\boldsymbol{\sigma}}_i \tag{61}$$

where the subscript i is used to denote the particular phase. The index $i = 0$ is specifically the reference matrix while $i = 1, 2, \ldots N$ refers to each precipitate phase. From here, Eshelby's equivalent inclusion method is used to rewrite the constitutive law using the compliance of the reference matrix

$$\boldsymbol{D}_i^e = \mathbb{M}_0^e : \widehat{\boldsymbol{\sigma}}_i + \boldsymbol{D}_i^{e^*} \tag{62}$$

where $\boldsymbol{D}_i^{e^*}$ is the elastic eigenstrain rate introduced to accommodate the difference between $\mathbb{M}_i^e$ and $\mathbb{M}_0^e$. This equation can be rewritten in terms of the disturbance tensors $\widetilde{\widehat{\boldsymbol{\sigma}}}_i = \widehat{\boldsymbol{\sigma}}_i - \widehat{\boldsymbol{\sigma}}_0$ and $\widetilde{\boldsymbol{D}}_i^e = \boldsymbol{D}_i^e - \boldsymbol{D}_0^e$ such that

$$\widehat{\boldsymbol{\sigma}}_i = \mathbb{L}_0^e : \left(\boldsymbol{D}_i^e - \boldsymbol{D}_i^{e^*}\right) \tag{63}$$

$$\widehat{\boldsymbol{\sigma}}_0 + \widetilde{\widehat{\boldsymbol{\sigma}}}_i = \mathbb{L}_0^e : \left(\boldsymbol{D}_0^e + \widetilde{\boldsymbol{D}}_i^e - \boldsymbol{D}_i^{e^*}\right) \tag{64}$$

Now, taking the equilibrium equation $\nabla \cdot \widehat{\boldsymbol{\sigma}} = 0$, Eq. (64) can be expressed as

$$\mathbb{L}_{0_{ijkl}}^e \tilde{v}_{i_{k,lj}}^e - \left(\mathbb{L}_{0_{ijkl}}^e D_{i_{kl}}^{e^*}\right)_{,j} = 0 \tag{65}$$

which is now conveniently in the appropriate form that can be solved with Green's functions. The Green's function solution is described in detail in Section 2.5.3.1 and will not be reiterated here. The solution results in the following relationships

$$\widetilde{\boldsymbol{D}}_i^e = \mathbb{P}_i^e : \mathbb{L}_0^e : \boldsymbol{D}_i^{e^*} \tag{66}$$

$$\widetilde{\boldsymbol{W}}_i^e = \mathbb{B}_i^e : \mathbb{L}_0^e : \boldsymbol{D}_i^{e^*} \tag{67}$$

where $\mathbb{P}_i^e$ and $\mathbb{B}_i^e$ are the fourth order symmetric and axisymmetric components of the elastic auxiliary tensor, $\mathbb{T}^e$

$$\mathbb{P}_i^e = -\frac{1}{4}\left(\mathbb{T}_{ijkl}^e + \mathbb{T}_{jikl}^e + \mathbb{T}_{ijlk}^e + \mathbb{T}_{jilk}^e\right) \tag{68}$$

$$\mathbb{B}_i^e = -\frac{1}{4}\left(\mathbb{T}_{ijkl}^e - \mathbb{T}_{jikl}^e + \mathbb{T}_{ijlk}^e - \mathbb{T}_{jilk}^e\right) \tag{69}$$

where $\mathbb{T}$ is defined in Eq. (21) that can be solved using elliptical integral. The substitution of Eq. (66) into Eq. (64) and Eq. (67) into Eq. (66) results in the expressions

$$\widetilde{\boldsymbol{D}}_i^e = \left(\mathbb{L}_0^e - \mathbb{P}_i^{e^{-1}}\right)^{-1} : \widetilde{\widehat{\boldsymbol{\sigma}}}_i \tag{70}$$

$$\widetilde{\boldsymbol{W}}_i^e = \mathbb{B}_i^e : \mathbb{P}_i^{e^{-1}} : \widetilde{\boldsymbol{D}}_i^e \tag{71}$$

which are called the interaction equations for the elastic micromechanics model.

Now, this process is repeated for the viscoplastic constitutive law that has the expression

$$\boldsymbol{D}_i^v = \mathbb{M}_i^v : \boldsymbol{\sigma}_i \tag{72}$$

A viscoplastic eigenstrain rate $\boldsymbol{D}_i^{v^*}$ is introduced such that

$$\boldsymbol{\sigma}_0 + \widetilde{\boldsymbol{\sigma}}_i = \mathbb{L}_0^v : \left(\boldsymbol{D}_0^v + \widetilde{\boldsymbol{D}}_i^v - \boldsymbol{D}_i^{v^*}\right) \tag{73}$$

Application of Green's function results in the expressions

$$\widetilde{\boldsymbol{D}}_i^v = \mathbb{P}_i^v : \mathbb{L}_0^v : \boldsymbol{D}_i^{v^*} \quad (74)$$

$$\widetilde{\boldsymbol{W}}_i^v = \mathbb{B}_i^v : \mathbb{L}_0^v : \boldsymbol{D}_i^{v^*} \quad (75)$$

where $\mathbb{P}_i^v$ and $\mathbb{B}_i^v$ are the fourth order symmetric and axisymmetric components of the viscoplastic auxiliary tensor $\mathbb{T}^v$. The viscous interaction equations are then calculated as

$$\widetilde{\boldsymbol{D}}_i^v = \left(\mathbb{L}_0^v - \mathbb{P}_i^{v^{-1}}\right)^{-1} : \widetilde{\boldsymbol{\sigma}}_i \quad (76)$$

$$\widetilde{\boldsymbol{W}}_i^v = \mathbb{B}_i^v : \mathbb{P}_i^{v^{-1}} : \widetilde{\boldsymbol{D}}_i^v \quad (77)$$

which are analogous to Eq. (70) and Eq. (71).

To obtain the combined elastic-viscoplastic interaction equations, the strain rate and spin rates are expressed as additive decompositions

$$\boldsymbol{D_i} - \boldsymbol{D_0} = (\boldsymbol{D_i^e} - \boldsymbol{D_0^e}) + (\boldsymbol{D_i^v} - \boldsymbol{D_0^v}) \quad (78)$$

$$\boldsymbol{W_i} - \boldsymbol{W_0} = (\boldsymbol{W_i^e} - \boldsymbol{W_0^e}) + (\boldsymbol{W_i^v} - \boldsymbol{W_0^v}) \quad (79)$$

The substitution of Eq. (70), (71), (76) and (77) then results in the expressions

$$\boldsymbol{D}_i - \boldsymbol{D}_0 = (\mathbb{L}_0^e - (\mathbb{P}_i^e)^{-1})^{-1} : (\widehat{\boldsymbol{\sigma}}_i - \widehat{\boldsymbol{\sigma}}_0) + (\mathbb{L}_0^v - (\mathbb{P}_i^v)^{-1})^{-1} : (\boldsymbol{\sigma}_i - \boldsymbol{\sigma}_0) \quad (80)$$

$$\boldsymbol{W}_i - \boldsymbol{W}_0 = \mathbb{B}^e : (\mathbb{P}_i^e)^{-1} : (\boldsymbol{D}_i^e - \boldsymbol{D}_0^e) + \mathbb{B}^v : (\mathbb{P}_i^v)^{-1} : (\boldsymbol{D}_i^v - \boldsymbol{D}_0^v) \quad (81)$$

These interaction laws couple the properties between the precipitate phase to the reference medium. In the above equations, a trivial solution is obtained when $i = 0$ such that $\boldsymbol{D}_0$ and $\boldsymbol{W}_0$ cannot be determined directly. As a result, an additional equation is required to fully solve for $\boldsymbol{D}_i$ and $\boldsymbol{W}_i$ across all phases. The additional equation is obtained by volume averaging Eq. (80) and Eq. (81) such that

$$\boldsymbol{D}_0 = \overline{\boldsymbol{D}} - \sum_{i=1} f_i(\boldsymbol{D}_i^e - \boldsymbol{D}_0^e) - \sum_{i=1} f_i(\boldsymbol{D}_i^v - \boldsymbol{D}_0^v) \quad (82)$$

$$\boldsymbol{W}_0 = \overline{\boldsymbol{W}} - \sum_{i=1} f_i(\boldsymbol{W}_i^e - \boldsymbol{W}_0^e) - \sum_{i=1} f_i(\boldsymbol{W}_i^v - \boldsymbol{W}_0^v) \quad (83)$$

where $\overline{\boldsymbol{D}}$ and $\overline{\boldsymbol{W}}$ are the macroscopic strain rate and spin rates applied to the entire crystal and f_i is the volume fraction of phase i.

Lastly, it is important to define the reference matrix used in the Eshelby scheme. The current work uses the Mori-Tanaka (MT) approach [73, 204, 206], which assumes that the reference matrix has the same properties as that of the aluminum crystal. This must be explicitly said because it contrasts with the more commonly used self-consistent (SC) method that assumes the reference medium has the volume averaged properties of all phases. The reason for the use of the MT method is because the volume fraction of the precipitate phase is normally very low (under 2%) for Al-Mg-Si alloys. In this case, the MT approach is more representative of the physics of the actual aggregate than the SC assumption [204]. However, both MT and SC approaches would lead to similar results owing to the low precipitate volume fractions present in the alloy.

Finally, to calculate the macroscopic properties for each crystal, a volume averaging is performed across the properties of the constituent phases

$$\overline{\boldsymbol{\sigma}} = \sum_{i=0} f_i \boldsymbol{\sigma}_i \qquad \textbf{(84)}$$

Despite the fact that the constitutive model and homogenization scheme is elastic-viscoplastic, the precipitates here are modeled as fully elastic for the time being using only crystal elasticity (i.e. the viscoplastic portion is assumed to be negligible in the precipitate phase). This is due to several reasons: first, modeling the plastic deformation of precipitates is a significant numerical challenge that requires extensive implementation effort. Even though there are publications that describe the shearing of precipitates during deformation [102, 207], this shearing is not governed by traditional plastic mechanisms and is instead due to the passing of dislocations from the matrix through the precipitate. As a result, plasticity models must include the strength and coherency of the matrix-precipitate interface, which is not a simple implementation. Second, the modeling of particle shearing requires considerable experimentation for a proper validation of the model. Without this experimentation, any plastic theory would introduce unnecessary complexity and additional parameters for calibration. As a result, the precipitates are assumed to be elastic in this work and the effects of shearing are captured indirectly through the calibration of the interaction strength, n_e. It is however, worth mentioning that the matrix phase and the resulting homogenization are both elastic-viscoplastic and that the model is fully capable of accommodating a flow rule in the precipitate if needed in future studies.

5.3.2.3 Hardening

The hardening of the aluminum matrix is defined using the critical shear stress $g^{(\alpha)}$

$$g^{(\alpha)} = \tau_0 + \tau_d + \tau_p \quad \textbf{(85)}$$

where τ_0 is the initial yield stress of the matrix material, τ_d is a forest hardening term due to internal dislocation interactions, and τ_p is the strengthening contribution from precipitation hardening. τ_0 is a calibrated term that is based on the intrinsic strength of aluminum. It should be mentioned that the effect of solid solution strengthening is captured in τ_0 in the current approach. Any differences caused by solute concentrations cannot be modeled explicitly in this work due to insufficient experimentation.

To calculate the forest hardening term τ_d, a dislocation density-based relationship is employed based on the theory by Taylor [10]

$$\tau_d = \kappa \mu b \sqrt{\sum_{\alpha} \rho^{(\alpha)}} \quad \textbf{(86)}$$

where κ is the obstacle strength of dislocation interactions, μ is the shear modulus of the crystal, b is the magnitude of the Burgers vector, and $\rho^{(\alpha)}$ is the dislocation density on slip system α. The dislocation content on active slip systems evolves during plastic deformation and is described by a Kocks-Mecking (KM) type evolution law that was presented by Kitayama et al. [45]

$$d\rho^{(\alpha)} = \frac{1}{bk_1} \sqrt{\sum_{\alpha} \rho^{(\alpha)}}\ d\gamma^{(\alpha)} - k_2 \rho^{(\alpha)} d\Gamma \quad \textbf{(87)}$$

where k_1 and k_2 are constants related to the multiplication and recovery of dislocations, respectively, and $d\Gamma = \sum_{\alpha} \left| d\gamma^{(\alpha)} \right|$.

The precipitate hardening term, τ_p, arises from the obstruction of dislocation movement due to precipitates. An approach that is similar to Esmaeili et al. [99] is used to model the strengthening contribution from rod-shaped precipitates aligned with the <100> directions. This effect is governed by the Peach-Koehler equation

$$\tau_p = \frac{F}{L_f b} \quad \textbf{(88)}$$

where F is the obstacle strength of the precipitate and L_f is the effective mean spacing of precipitates. The obstacle strength F varies depending on the size of the precipitate and is determined according to the radius of the smallest cross-section r, assuming that the particles can be modeled as cylinders. Once the particle is above some critical radius r_c, the obstacle strength

saturates and any further increases in precipitate size do not affect the obstacle strength. Mathematically, this is expressed as

$$F = 2\beta\mu b^2\left(\frac{r}{r_c}\right) \qquad \text{for } r < r_c \qquad \textbf{(a)}$$
$$F = 2\beta\mu b^2 \qquad \text{for } r \geq r_c \qquad \textbf{(b)} \qquad \textbf{(89)}$$

where β is a constant associated with the tension of a dislocation line, and μ is the shear modulus of the matrix. Following the methodology by Esmaeili et al. [99], the precipitate is categorized as either "weak" or "strong" depending on the breaking angle of the dislocation line with respect to the precipitate obstacle. Their theory is that weak precipitates will naturally have larger particle spacings as it is possible for dislocations to shear through the particles [119]. It is assumed that the critical transition between weak and strong obstacles is defined according to the ratio $\frac{r}{r_c} = \frac{\sqrt{3}}{2}$. The effective mean spacing, L_f, is then defined according to these two regimes

$$L_f = \sqrt{\frac{\sqrt{3}r_c}{2r}}L - 2r \qquad \text{for } r < \frac{\sqrt{3}}{2}r_c \qquad \textbf{(a)}$$
$$L_f = L - 2r \qquad \text{for } r \geq \frac{\sqrt{3}}{2}r_c \qquad \textbf{(b)} \qquad \textbf{(90)}$$

where L is the center-to-center spacing for a triangular grid of non-shearable particles [99]

$$L = \sqrt{\frac{2\pi}{f}}r \qquad \textbf{(91)}$$

and f is the total volume fraction of all precipitate phases. In Eq. (90)a, the effective spacing is altered according to the Friedel estimate to account for the shearability of weak precipitates. It should be noted that Eq. (90) and (91) are only valid for rod-shaped precipitates that are aligned with the <100> directions of the crystal. Any other orientation or shape would require a rederivation of the effective mean spacing as the calculation is dependent on the needle-shaped assumption. The volume fraction f is calculated by

$$f = N\pi r^2 l \qquad \textbf{(92)}$$

where l is the average length and N is the number density of precipitates. Lastly, the variable A is introduced as the precipitate aspect ratio

$$A = \frac{l}{2r} \qquad \textbf{(93)}$$

An important note is that the precipitate hardening term, τ_p, is meant to capture the effect of precipitation on dislocation behavior in the aluminum matrix. This should not be confused with the homogenization scheme introduced in Chapter 5.3.2.2 that is used to simulate the deformation of the precipitates directly. While it may seem like the precipitate is accounted for twice in this framework, these two approaches are actually separate mechanisms that contribute to slightly different properties in the crystal. Specifically, the homogenization introduces kinematic hardening, which can be used to capture the Bauschinger effect and any precipitate-induced changes to anisotropy. Whereas the dislocation-precipitate hardening term introduces a particle size effect that is essentially isotropic. Both the loading within the precipitate as well as its effect on the dislocation substructure must be considered to obtain a representative model of the material physics.

5.3.3 Finite Element Modeling in LS-Dyna

The single crystal constitutive model in Chapter 5.3.2 is implemented as an explicit dynamic UMAT following the methodology outlined by Rossiter et al. [195]. The CPFEM framework uses a 3D equivalent representative volume element (RVE) as the geometry in the simulations. This RVE was generated from three orthogonal EBSD images of the material's microstructure and replicates the crystallographic orientation, misorientation distribution, and grain morphology of the EBSDs. The reader is referred to Kohar et al. [37] and Brahme et al. [208] for additional details of the generation procedure. The RVE was meshed with a regular array of equal-sized elements. Each element was assigned a single crystal orientation, and the collection of several elements was used to represent a grain. The mesh size was selected to allow for the smallest grains in the RVE to be represented by more than one element. This provided a good balance between granular resolution and computational efficiency.

5.4 Simulation Results

5.4.1 Calibration

Fig. 5-7 presents the cubic RVE used in this work, which was constructed using 125,000 elements with 50 elements in each direction. The length of each side is 2.4 mm, which is consistent with the nominal thickness of the specimen used during uniaxial tensile characterization. The global X, Y, and Z axes of the geometry correspond to the ED, TD, and ND axes of the microstructure, respectively. In all simulations, periodic boundary constraints

were used to ensure periodicity on the ED and TD surfaces while the ND surface was left unconstrained to imitate the free surfaces in the actual experiments.

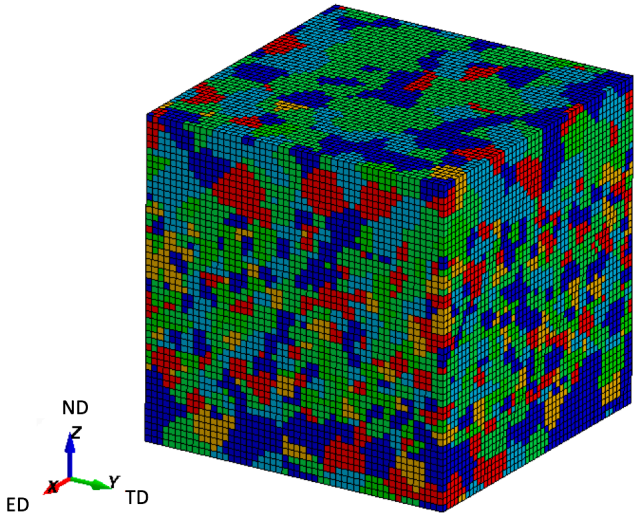

Fig. 5-7. Finite element mesh of the reconstructed microstructure (125,000 elements).

Calibration of the model was accomplished in two-steps where the yield strength was calibrated first and then the work hardening rate was calibrated afterwards. It is important to mention that TEM data was not available for the AA6060-T6 material characterized in Chapter 5.2; therefore, the calibration of the yield strength was performed with the experimental dataset by Teichmann et al. [191] on an AA6060 alloy with similar composition. In their research, the mean precipitate length, cross-sectional area, number density, and corresponding yield strength were characterized at various aging conditions. The calibration utilized these precipitation parameters for the 100 min at 190ºC sample and 300 min at 190ºC sample to determine the value of the critical radius, r_c. A critical transition radius of $r_c = 3\ nm$ was estimated to be suitable for their AA6060 alloy, which resulted in an excellent fit as seen in Fig. 5-8. Assuming the same r_c value for the AA6060-T6 alloy used in the current work, a precipitate length and radius was selected to match the experimental yield strength measured in Fig. 5-2. The parameters were chosen based on the assumptions of a larger length, radius, and aspect ratio compared to the material by Teichmann et al. [191]. Table 5-2 presents the parameters obtained from this calibration. The precipitates have an aspect ratio of 14 and the radius of the T6 alloy is smaller than the critical transition radius. These parameters agree with experimental observations of β'' precipitates in the peak-aged state [183, 191, 207].

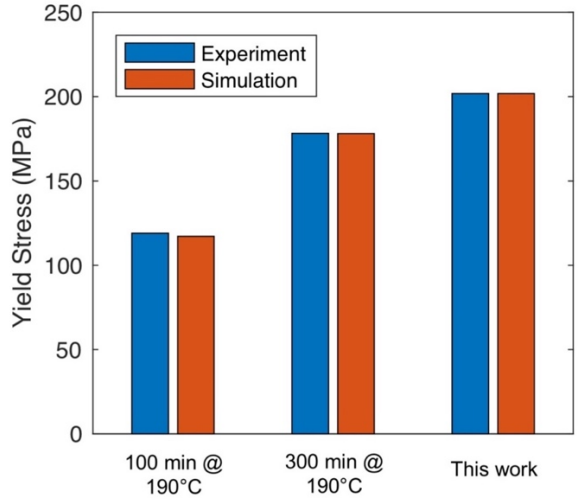

	l (nm)	r (nm)	N (μm^{-3})
AA6060 – 100 min @ 190ºC	35.0	2.26	2000
AA6060 – 300 min @ 190 ºC	44.0	1.70	11500
AA6060-T6	50.0	1.78	11500

Fig. 5-8. Calibration of the model to the experimental dataset from Teichman et al. [191].

Table 5-2. Precipitation hardening parameters for AA6060-T6.

r_c (nm)	l (nm)	r (nm)	N (μm^{-3})	β	b (nm)
3.0	50.0	1.78	11500	0.5	0.286

The work hardening behavior of the AA6060-T6 alloy was calibrated using the stress-strain results obtained from experimental testing. Strain hardening parameters, κ, k_1 and k_2 of Eq. (87) were used to capture the "isotropic" component of the stress-strain curve, while n_e in Eq. (59) of the homogenization scheme was used to capture the "kinematic" component. It should be mentioned that the model cannot be calibrated to a single uniaxial stress-strain curve as the contribution from the isotropic and kinematic components cannot be uniquely determined. The model was instead calibrated using the 10% FRF simple shear curve obtained earlier in this work, so that the Bauschinger behavior can be used to determine the kinematic component of work hardening [66]. The calibration was performed by minimizing an objective function between the experimental stress response, σ_t^{Exp}, and the predicted stress response, σ_t^{Sim}. The mean squared error objective function was used and is defined as

$$MSE = \sum_t^n \left(\frac{\sigma_t^{Exp} - \sigma_t^{Sim}}{\sigma_t^{Exp}} \right)^2 \quad \textbf{(94)}$$

where n is the number of experimental sample points. The parameters were determined through a manual process until an acceptable tolerance was achieved. The elastic constants used in the constitutive model are presented in Table 5-3 and Table 5-4. The matrix is composed of three independent coefficients with cubic symmetry while the precipitates are assumed to be β'' (Mg_5Si_6) [209] with orthotropic symmetry. It is assumed that $\kappa = 0.3$ [130], $\dot{\gamma} = 0.001/s$ and $m = 0.02$ for the remaining parameters in the crystal plasticity model [5, 195]. A complete list of simulation constants is presented in Table 5-5.

Table 5-3. Elastic constants of the matrix phase.

Parameter	Value
C_{11}^m (GPa)	103.3
C_{12}^m (GPa)	51.7
C_{44}^m (GPa)	25.8

Table 5-4. Elastic constants of the precipitate phase.

Parameter	Value	Parameter	Value	Parameter	Value
C_{11}^p (GPa)	101.0	C_{44}^p (GPa)	16.0	C_{12}^p (GPa)	50.0
C_{22}^p (GPa)	80.0	C_{55}^p (GPa)	30.0	C_{13}^p (GPa)	50.0
C_{33}^p (GPa)	80.0	C_{66}^p (GPa)	30.0	C_{23}^p (GPa)	50.0

Table 5-5. Crystal plasticity constitutive model parameters.

κ	k_1	k_2	$\dot{\gamma}_0$ (s^{-1})	m	n_e	τ_0 (MPa)
0.3	60.0	12.0	0.001	0.02	10.0	17.0

5.4.2 Evaluation

After calibration with the 10% FRF simple shear curve, the numerical framework was used to predict other cyclic strain paths at different strain reversal levels to verify the model's predictive capability. Fig. 5-9 presents the cyclic results for 5%, 10%, and 15% FRF simple shear. The calibration is presented with dotted lines in the figure. The predicted stress results are normalized by the material's initial yield stress since the geometry of the actual test specimen was not considered in the simulation. The simulated 5% and 15% FRF curves are in good agreement with the experimental data and both the yield stress upon strain reversal and the subsequent rate of strain hardening was captured by the constitutive model. Additional verification was accomplished by predicting the deformation responses of 5%, 10%, and 15% RFR cyclic shear. Fig. 5-10 presents the experimental and simulated results for the RFR data. As shown, the model was also able to predict the RFR responses with reasonable accuracy.

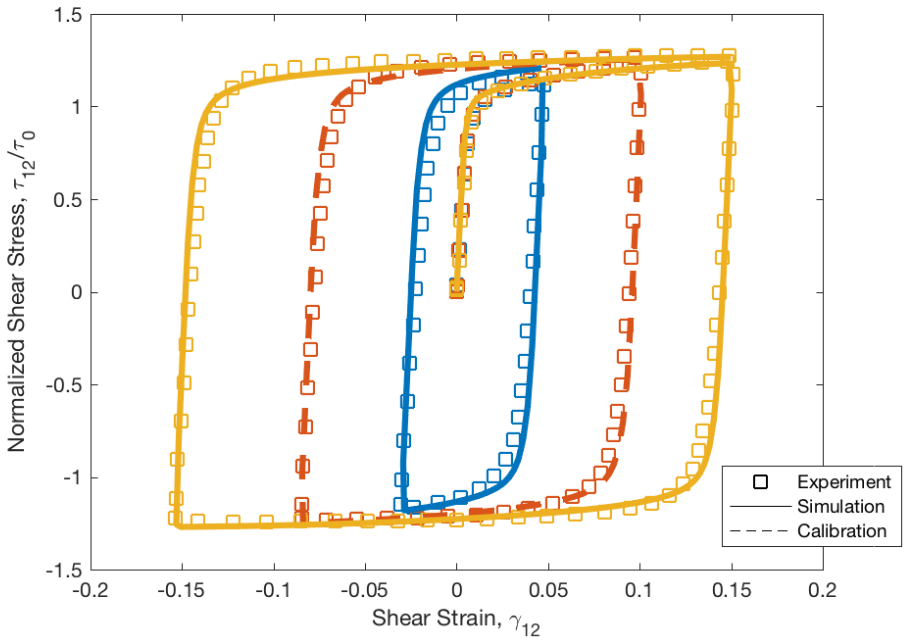

Fig. 5-9. Experimental and simulated FRF cyclic simple shear responses. The 10% FRF curve is used to calibrate the numerical model.

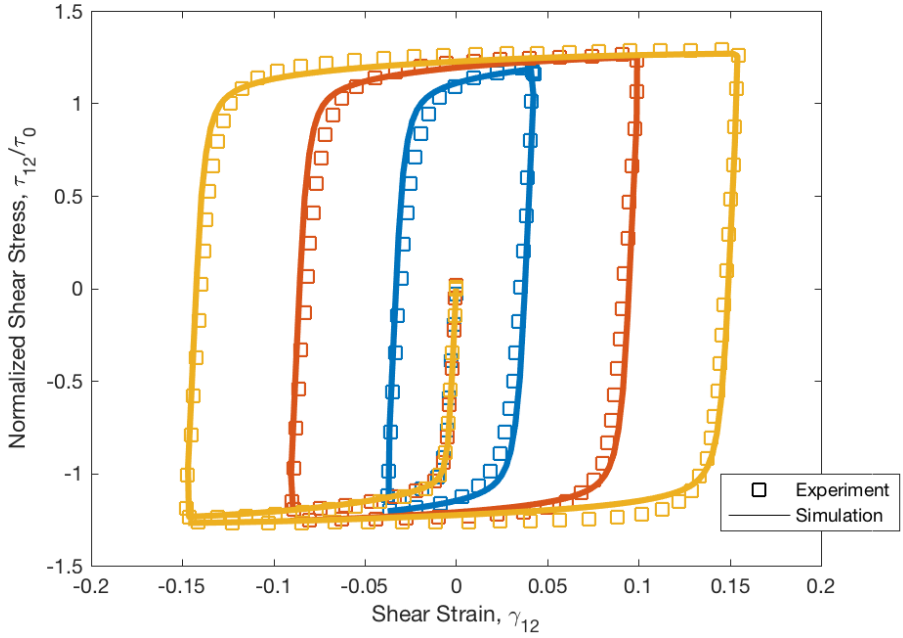

Fig. 5-10. Experimental and simulated RFR simple shear responses.

Fig. 5-11 presents the simulated uniaxial tensile response compared to the experimental tensile behavior observed in ED. The stress-strain curve is captured well with both the yield strength and work hardening rate predicted with good accuracy. Next, the material's anisotropic properties are shown in Fig. 5-12. The predicted yield strength and R-values in the ED and DD directions are in good agreement with the experimental values. It should be mentioned however that there is a difference in the prediction of the R-value in TD compared to the experimental measurement. This can be attributed to the difference in dimensions used in the RVE model (2.4 mm × 2.4 mm) compared to a 25 mm × 10 mm virtual line extensometer in the experimental test. Nevertheless, the model is able to successfully predict the general trends, providing confidence in the integrity of the framework.

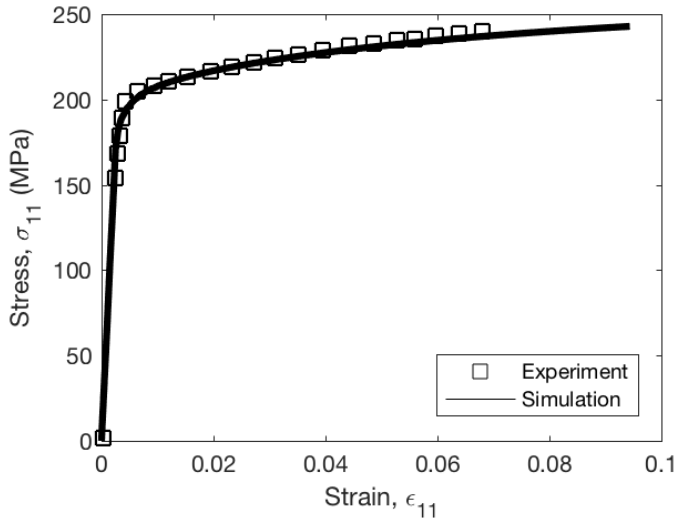

Fig. 5-11. Experimental and simulated uniaxial tensile stress-strain response in the extrusion direction (ED).

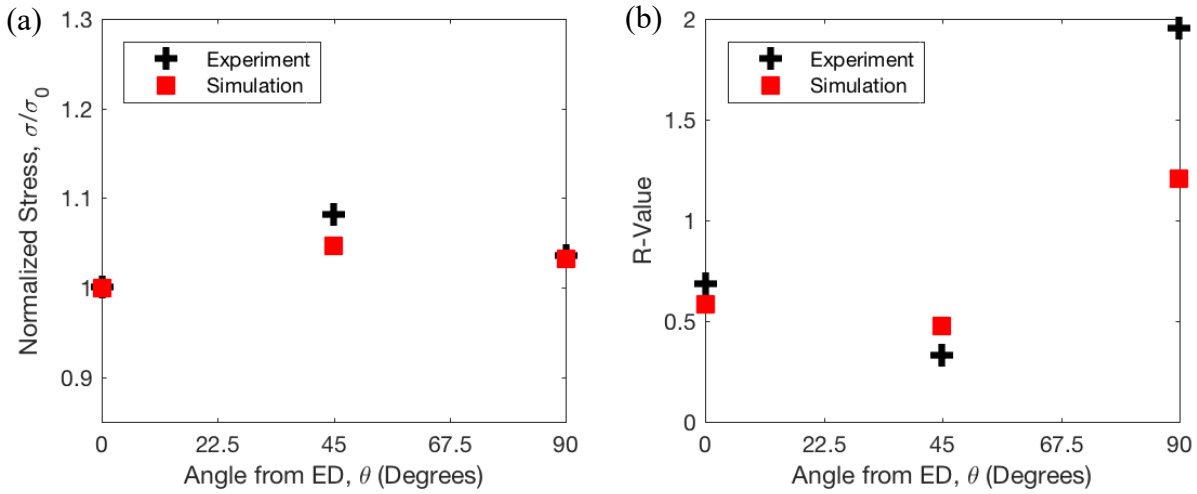

Fig. 5-12. (a) Normalized yield stress and (b) R-value variation relative to ED.

Based on the results presented so far, the proposed numerical framework is capable of capturing the general mechanical behavior of the AA6060-T6 alloy. As the model is based on CPFEM, a subsequent study was conducted to investigate the material's localized deformation response using the same modeling parameters. The precipitation constants remain unadjusted in these simulations and are defined in Table 5-2. The modeling of localization is possible because of the full-field finite element framework used in this work. Fig. 5-13 shows the development of the material's geometry and plastic strain contours at different time intervals under uniaxial

tension. The RVE was pulled along the X (ED) direction, and only the Z (ND) direction was left unconstrained. It should be mentioned that the undeformed RVE does not contain any geometric imperfections. The localization patterns shown in the figure are caused by heterogeneities introduced from crystallographic texture and grain morphology. These effects influence the local constitutive response within each element, resulting in variations in deformation behavior across the RVE.

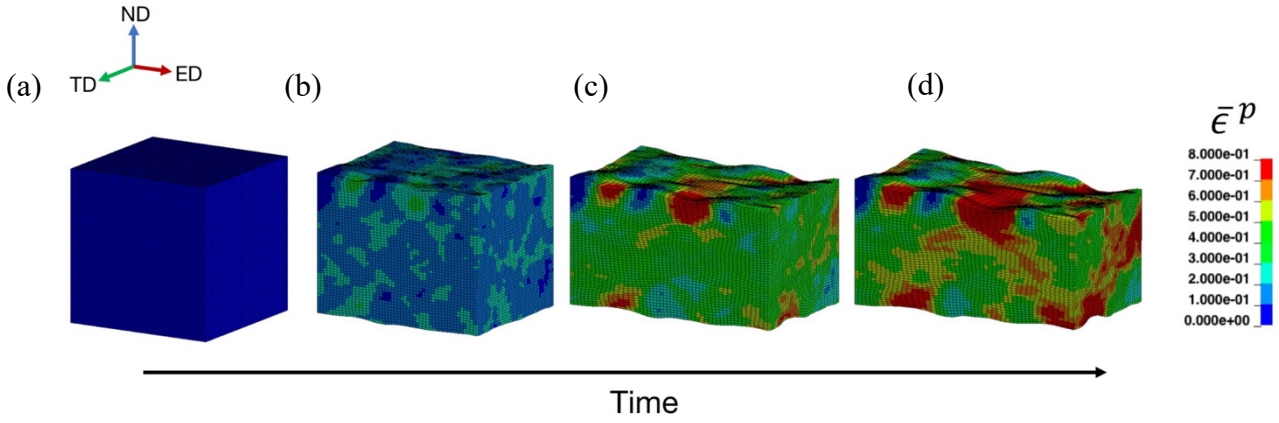

Fig. 5-13. Equivalent plastic strain contours in quasi-static uniaxial tension simulation. Simulation results for (a) $t = 0\ s$; (b) $t = 180\ s$; (c) $t = 465\ s$; (d) $t = 675\ s$.

During the early stages of the simulation (Fig. 5-13b), the RVE deforms rather uniformly as expected due to the initially smooth geometry. As the simulation progresses, it is observed that areas near the ND surface begin to localize high concentrations of strain. These regions are the red spots of Fig. 5-13c, which correspond to locations where a surface valley has formed. The peaks and valleys are caused by differences in grain orientation present along the surface. The valleys seem to originate from grain orientations that are nearly Cube, which is known to accommodate deformation rather easily. This observation is in line with research by Muhammad et al. [210] in their study of aluminum bendability. As deformation continues, strain tends to accumulate within these highly deformed regions, leading to the formation of shear bands, as illustrated in Fig. 5-13d. Interestingly, multiple shear bands are formed in all planes of the RVE. The shear bands originate from existing surface valleys and are observed to propagate across other soft regions throughout the thickness of the sample.

5.5 Analysis and Discussion

In this section, several analytical studies are performed and discussed that investigate the effects of precipitation hardening on material anisotropy and work hardening. This is of interest as it is still somewhat unclear from the literature the extent to which precipitates can affect an alloy's mechanical properties. For instance, Crooks et al. [211] were unable to associate plastic anisotropy to different aging conditions; however, Bate et al. [106] observed a strong correlation between anisotropy and temper. A detailed review of experimental work is provided in Khadyko et al. [109] for various age hardening alloys. Since the material model used in the current work directly incorporates the precipitates into each crystal, the precipitation-induced effects are explored in a series of investigations at both the single crystal and polycrystal scales.

5.5.1 Effects of Precipitation Hardening on Single Crystals

Many studies have shown that precipitates can affect different orientations with differing magnitudes [141, 212]. In this first investigation, common aluminum rolling textures (i.e., Cube, Goss, Copper, and Brass) were simulated to large deformations to determine the relative effect of precipitation on single crystal orientations. The Euler angles for the four texture components used in this study are presented in Table 2-2. The stress-strain behaviors of these single crystals were simulated with and without the precipitate phases for each orientation. The simulations with precipitates were conducted using the parameter set described in Table 5-2. A secondary set of simulations was also performed by reducing the length of the precipitates to that of the radius (named as spherical tests) to illustrate differences from morphology. The non-precipitation hardened simulations were conducted by removing all subroutines associated with computing the stress and strains in the precipitate. This includes the removal of the homogenization scheme and the yield strength model. As such, the UMAT was reduced to a classical dislocation density hardening crystal plasticity formulation. The remaining simulation parameters, presented in Table 5-5, were used in all simulations without any adjustments between the tests.

Fig. 5-14 presents the normalized uniaxial tensile yield stress variations at multiple levels of specific plastic work. The stresses are normalized with respect to ED for each plastic work state. Based on the simulation results, precipitation hardening has a minor effect on the variation of yield strength as there are only slight differences between the precipitation hardened and non-precipitation hardened states. This observation was also noted by Choi et al. [141] using a

phenomenological study of the same crystal orientations. Though there are slight deviations in the shape and magnitudes of the stress anisotropy curves, the results suggest that the anisotropy is mostly driven by crystallographic orientation. Fig. 5-15 shows the ratio of the cross-sectional strains for the same plastic work states, where the R-values are defined in this work as $r = \frac{\epsilon_{22}(\theta)}{\epsilon_{33}(\theta)}$ and θ is the loading direction about the ED-TD plane. Interestingly, there are large differences in the R-value variations between the three precipitation conditions. Both the spherical and elongated precipitation hardened crystals were consistently more isotropic immediately after yielding than the non-precipitation hardened state. These results confirm the observations made by other authors that artificial ageing generally reduces R-value anisotropy [65, 106, 107, 109, 213]. An important observation to note is that the crystals with spherical precipitates were affected much less than the crystals with high aspect ratio precipitates. In both the yield strength and R-value simulations, the spherical simulation results were very similar to the non-precipitation hardened results.

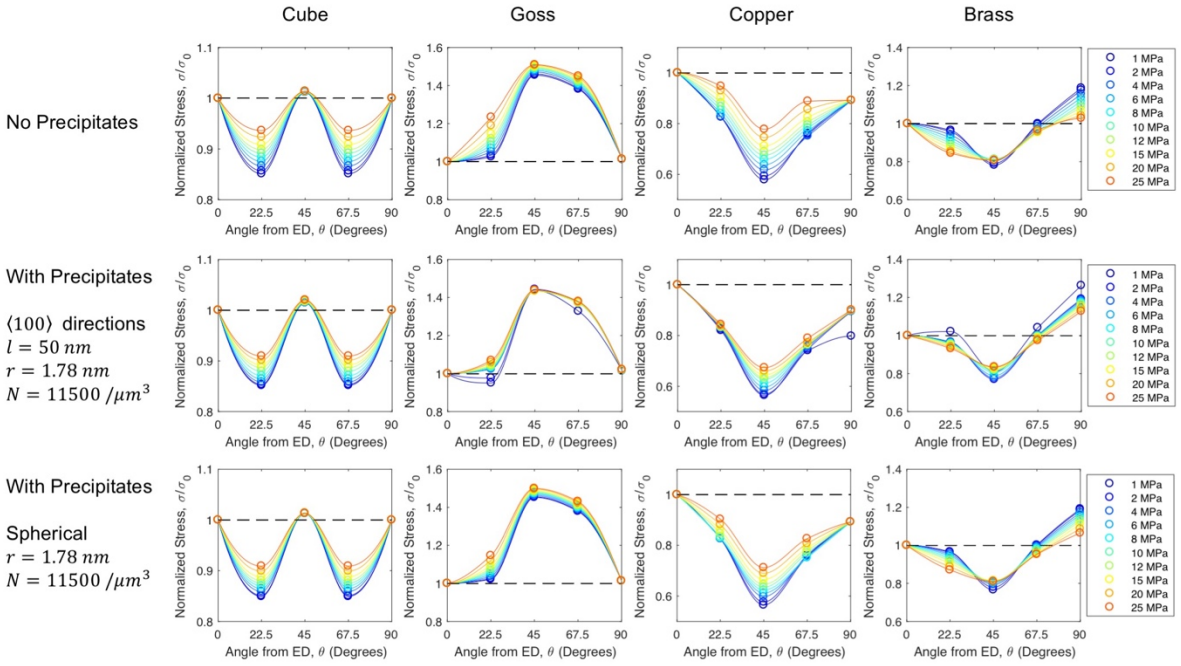

Fig. 5-14. Simulated normalized yield stress variations for common rolling aluminum single crystals.

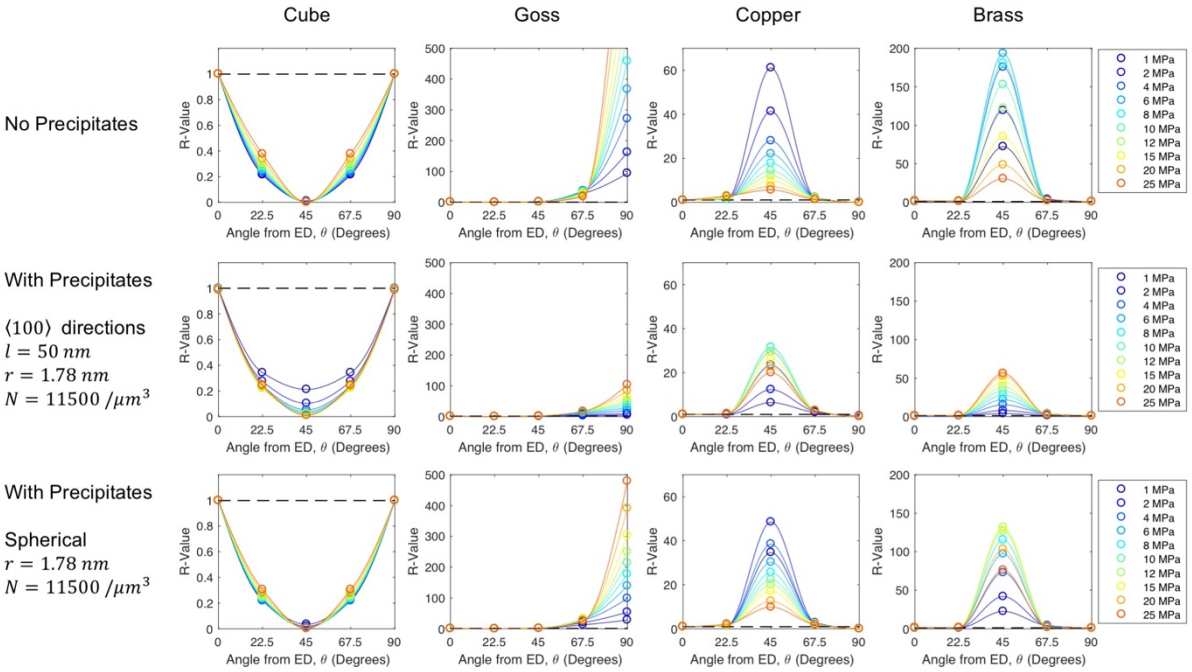

Fig. 5-15. Simulated R-value variations for common rolling aluminum single crystals.

What is particularly interesting is the evolution of R-values across different crystal orientations. In the Cube texture component, high aspect ratio precipitates increased the initial R-values relative to other precipitation states. The R-values then approached the non-precipitation hardened behavior as deformation continued. In the Goss texture simulations, precipitation significantly lowered the R-values compared to the non-aged response. In the Copper texture simulations, high aspect ratio precipitates caused the crystal to become more anisotropic with strain, while the inverse response was observed for Copper crystals with spherical precipitates or without precipitates. Finally, the Brass texture component showed increases in anisotropy with deformation for both spherical and elongated precipitates while the non-aged crystal showed a reduction of anisotropy at larger strains.

To better understand how the model captures the precipitation effect, a series of additional simulations were conducted with the Cube texture component using a single precipitate variant. These simulations were performed with two configurations: (a) a Cube crystal with a precipitate on the [100] lattice direction and (b) a Cube crystal with a precipitate on the [001] lattice direction. The crystals were deformed at angles, θ, relative to the [100] (ED) axis. All simulations employed the same parameters found from the initial calibration process. The results from this study are presented in Fig. 5-16. As shown from the simulations for Configuration (a),

both the yield stress variation and R-value variation appear to be asymmetric about the DD. This was somewhat expected for this configuration as having an angle between the precipitate and loading direction generates a degree of anisotropy. The highest strengthening was provided by the 0-degree orientation, which suggests that the precipitate accommodates the highest load when it is aligned with the loading direction. A closer inspection of the R-value results shows that deformation along the axis coinciding with the precipitate was slightly inhibited. This was responsible for the drop in the R-value for $\theta = 90°$. In Configuration (b), the results for both yield strength variation and R-value variation were symmetric about DD. This was because the precipitate remained orthogonal to the loading direction at all loading angles. By investigating the R-values in this configuration, one can observe again that the precipitate inhibits deformation along its longitudinal axis, as illustrated by the relatively large R-values for $\theta = 0°$ and $\theta = 90°$. These results help to illustrate the mechanisms responsible for the observations in Fig. 5-14 and Fig. 5-15. The precipitates are able to accentuate or resist material deformation depending on their orientation to the loading direction. For instance, the relatively minor effects of precipitation on the Cube texture component can be explained by the fact that the three precipitate variants are orthogonal to one another. When the Cube crystal is loaded parallel to a precipitate (i.e. along the <100> directions), the other precipitates accommodate equal amounts of strain, resulting in an essentially uniform response along the width and thickness directions as opposed to the anisotropic response observed in Fig. 5-16. On the other hand, the significant reduction of anisotropy near the $\theta = 90°$ orientation of the Goss crystal can be explained by the fact that one of the precipitate variants is directly perpendicular to the width axis. This precipitate provides additional resistance to straining in ϵ_w, which ultimately reduces the R-value. The above theoretical studies show that precipitates indeed affect particular orientations more heavily than others by providing additional modes of deformation. They are also constrained along specific directions within each crystal that further accentuates their effects. Although a more thorough single crystal investigation could be conducted, these simulations can be used as a guide for the polycrystal simulations in the next chapter.

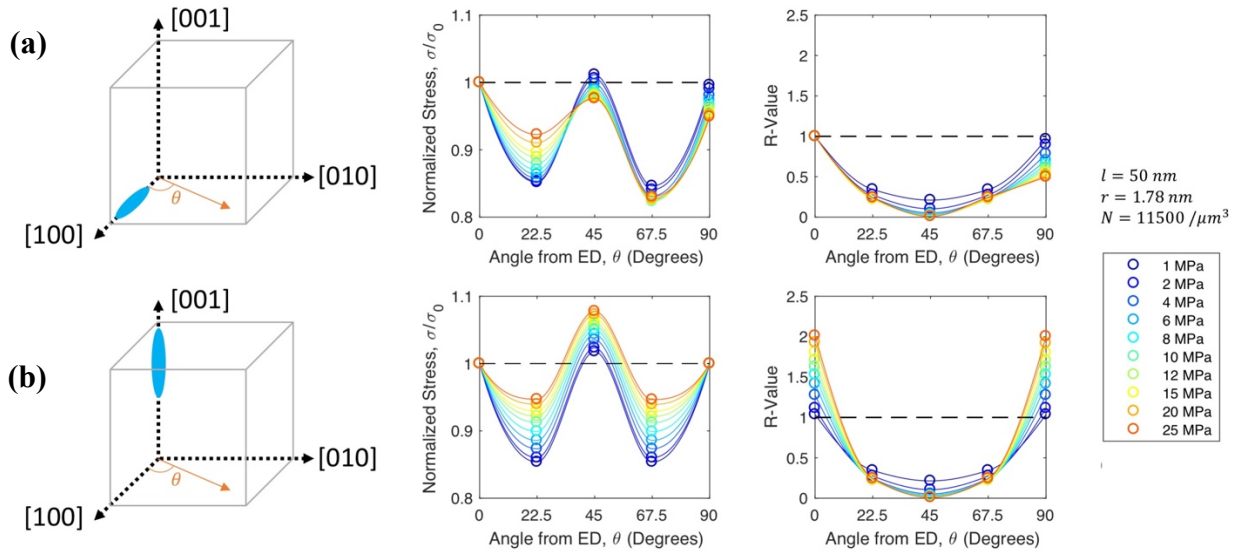

Fig. 5-16. Analysis of two precipitate configurations in the Cube single crystal. Configuration (a) shows the anisotropic properties observed with the [100] precipitate variant. Configuration (b) shows the anisotropic properties observed with the [001] precipitate variant.

Lastly, it should be mentioned that the incorporation of the precipitation subroutines increased the total simulation time by approximately N times, where N is the total number of precipitate phases in the crystal. This increase in computation is because the local properties of each phase is determined through the additional calculation of Eshelby tensors for each phase that is added. The calculation of these fourth-order tensors requires a numerical integration scheme if the materials are anisotropic [202, 214], which is responsible for the majority of the runtime.

5.5.2 Effects of Precipitation Hardening on Polycrystals

In this next investigation, the effect of precipitation hardening on the polycrystalline response is analyzed using a series of RVE simulations. These studies explore the effects of precipitate volume fraction and aspect ratio on the resulting stress-strain response. The precipitation parameters were adjusted during this study to generate "virtual" alloys of different heat treatment conditions. However, the objective was to keep the yield strength identical throughout all simulations to isolate the effect of the proposed homogenization scheme. The volume fraction of precipitates was confined between the range $0\% \leq f \leq 2\%$ and the aspect ratio was confined to $1 \leq A \leq 64$, determined from existing literature on AA6000-series alloys

[91, 98]. All simulations were performed with identical strain hardening parameters in the matrix phase to ignore the effect of other mechanisms on the stress-strain response. Lastly, the 3D RVE shown in Fig. 5-7 was used in all simulations.

Fig. 5-17 illustrates the bulk uniaxial stress-strain curves resulting from the parametric study. Each graph shows the stress-strain responses of different precipitate aspect ratios at fixed volume fractions of 0.25%, 0.5%, 1%, and 2%. It is observed that the stress-strain curve is sensitive to both parameters in the study, but appears to be more responsive to variations in aspect ratio. Since the hardening laws were kept identical in all simulations, the differences in work hardening were due to the additional loading of the precipitate phase calculated with the micromechanics scheme. A detailed investigation of the plots shows that larger aspect ratios resulted in larger degrees of work hardening. This implies that higher aspect ratio precipitates accumulate larger loads. On the other hand, the precipitate volume fraction seems to play a multiplicative role in the simulation results. A comparison of Fig. 5-17a with Fig. 5-17d shows that the stress-strain curve is essentially unaffected when the aspect ratio is 1. However, there is a large difference in the maximum stress value when the aspect ratio is raised to 64. Additionally, when the volume fraction approaches 0, the stress-strain responses all appear to converge to a single curve. This further confirms the multiplicative effect of volume fraction in the constitutive model.

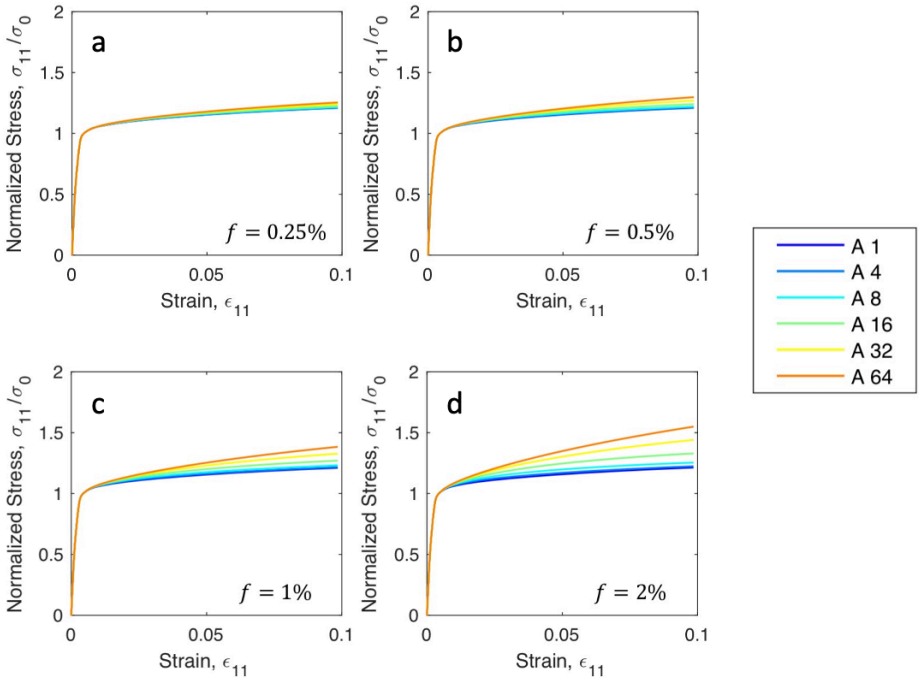

Fig. 5-17. Normalized stress-strain behaviors for increasing precipitate aspect ratios at volume fractions of (a) 0.25%, (b) 0.5%, (c) 1% and (d) 2%.

In Fig. 5-18, the evolution of the yield stress variation is presented for various precipitate aspect ratios at volume fractions of 1% and 2%. At each state of plastic work, the stresses are normalized about the ED stress value with the aspect ratio of 1. It is observed that the yield stress anisotropy does not vary significantly across all permutations of precipitation parameters. There is a slight tendency towards isotropy for higher aspect ratios and volume fractions, but the difference is rather small. These results are in agreement with the previous single crystal studies. Fig. 5-19 presents the evolution of the R-value variation using the same parametric values. The R-values show a general reduction in anisotropy with higher aspect ratio precipitates. This effect was also enhanced at larger plastic strains. Similar to what was observed previously, the precipitate volume fraction seems to only intensify the effect of aspect ratio. It should be mentioned that the microstructure used in this investigation is predominantly Cube. Yet, the polycrystalline simulations show an overriding Goss-type behavior in both the yield and R-value variations. This is due to the overly large anisotropic response of Goss crystals that dominate over the relatively insensitive Cube crystal.

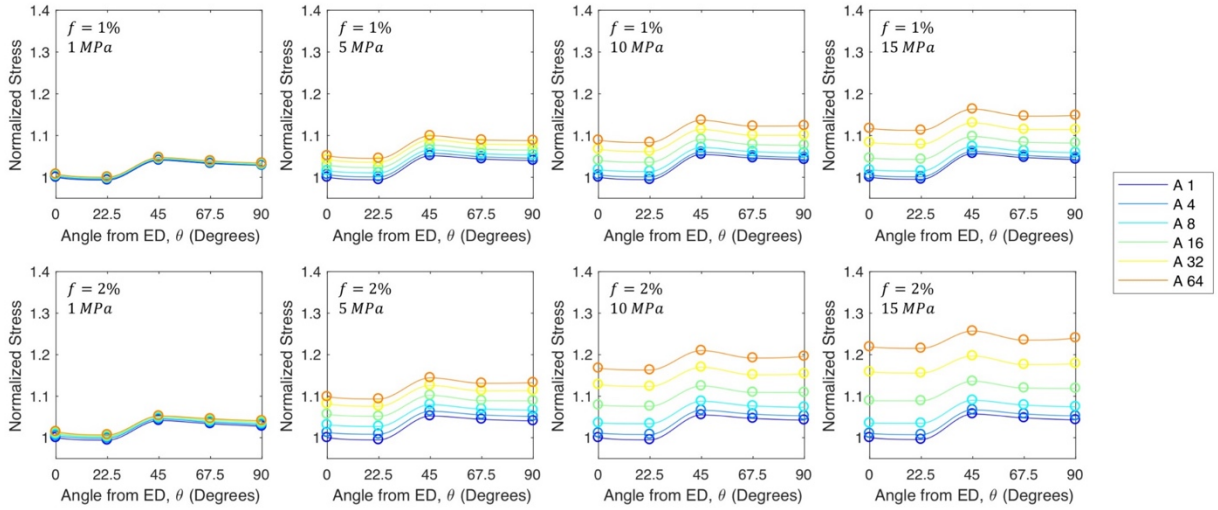

Fig. 5-18. Parametric analysis of yield stress variation at different plastic work levels.

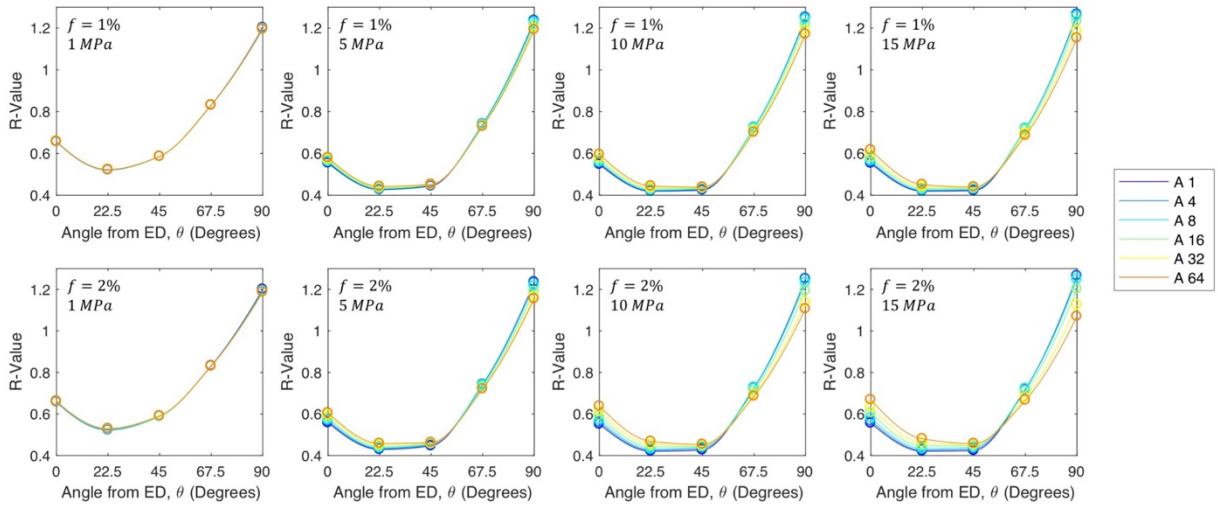

Fig. 5-19. Parametric analysis of R-value variation at different plastic work levels.

Finally, in Fig. 5-20 the RVE is simulated in tension followed by compression to illustrate the effect of precipitation on the Bauschinger effect. One of the advantages in using an Eshelby-based approach is the ability to capture the loading of the precipitates within each crystal. When the loading direction is reversed, the stresses in the precipitate are also unloaded, but at a different rate due to the difference in properties between the precipitate and matrix phases. The Bauschinger effect is as a result of this loading and unloading, which causes the generation of internal stresses within each crystal. As shown in the figure, the Bauschinger effect becomes more prominent as the precipitate volume fraction and aspect ratios are increased. This is due to

the larger load bearing capability of higher aspect ratio inclusions, which would need to be released as the material is unloaded. There is also an asymmetric behavior in the stress-strain curve, where the stress prior to unloading is higher for larger aspect ratio inclusions but the yield point after reversing the strain is lower. In the absence of a Bauschinger effect, it would be expected that higher stresses prior to the reversal would lead to higher stresses after. This asymmetric response is believed to be responsible for the large backstresses in over-aged materials [113, 114, 188].

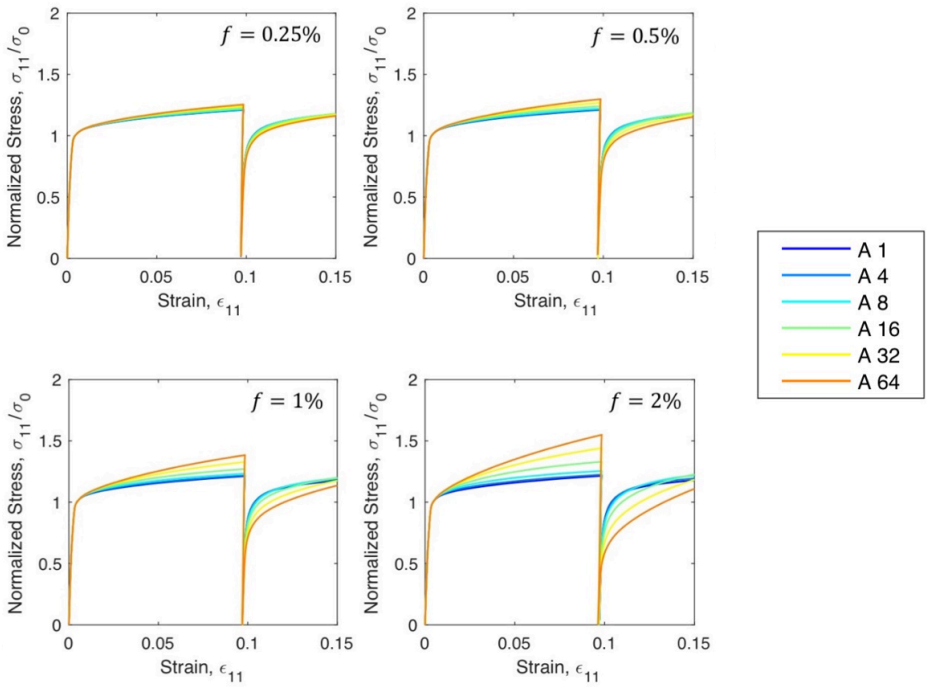

Fig. 5-20. Normalized absolute cyclic stress-strain curves for various levels of precipitate volume fractions and aspect ratios.

To illustrate this behavior in detail, a Cube crystal with a single precipitate is simulated under cyclic tension. Both the tensile stress inside the matrix and the precipitate are shown and compared to the stress of the homogenized material in Fig. 5-21. As observed from the first column, as the crystal is first deformed in tension, both the matrix and precipitate undergo tensile stresses. Since the particle is elastic, the stress inside the precipitate is much higher than that of the matrix. Upon reaching a desired strain level (in this case, 2% strain), the strain path is reversed into compression. The figures in the middle column illustrate that as the crystal is deformed to a state of zero stress, there remains a residual stress in the precipitate and matrix that

arises due to the difference in mechanical properties between the two phases. The precipitate is still loaded in tension while the matrix has a slight compressive stress. Now upon further deformation in compression, the crystal eventually yields and plastically deforms. It is observed from the third column that even as the entire crystal undergoes high compressive stresses, the stress inside the inclusion is still under tension as it has not completely unloaded from the initial tensile strain path. This behavior is what is responsible for the large Bauschinger effects at the macroscopic scale.

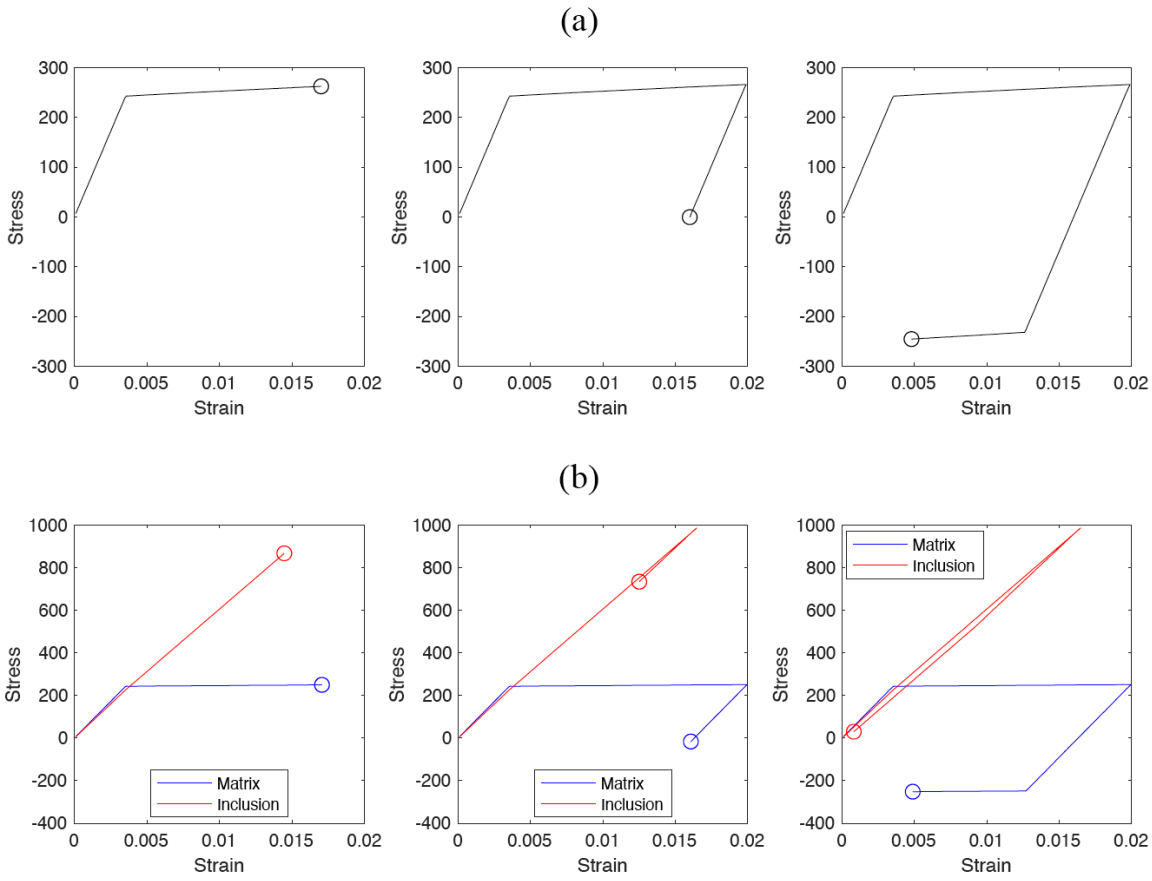

Fig. 5-21. Simulations of cyclic tension-compression in a Cube crystal with a single precipitate: (a) macroscopic stress-strain curve for entire crystal; (b) individual stress-strain curves of the matrix and precipitate phases.

In all of the prior studies, there have been large differences between the spherical and highly elongated precipitates. The high aspect ratio simulations generated a larger degree of work hardening, reduction to anisotropy and backstress. In contrast, the spherical precipitates did not contribute to plastic anisotropy or backstress to any significant extent, even at a volume fraction

of 2%. This phenomenon was also observed by Bate et al. [106] after over-aging an Al-Cu alloy until the precipitates were nearly equiaxed. Though the effect of morphology is comparatively small for this AA6060 alloy as shown in Fig. 5-18 and Fig. 5-19, the model provides some validation of previous experimental results showing reduced anisotropy in materials with a precipitate distribution. A possible reason for the minimal effects seen in this work is due to the moderately low precipitate volume fractions in 6000-series alloys. These effects are expected to be more significant in Al-Cu [27, 108] and certain Al-Zn [215] alloys that have a combination of high aspect ratio precipitates and larger volume fractions (~5%). It should also be mentioned that the examined AA6060 material came from an extruded profile where Cube texture dominated the microstructure. The Cube orientation itself is relatively insensitive to precipitation, as observed in the single crystal studies. It would be expected that sheet materials would undergo a larger precipitate response due to the typically higher concentrations of Goss, Copper, and Brass [97, 216].

Lastly, a final set of simulations was performed to investigate the localized deformation response with different precipitation parameters. The results from this study are presented in Fig. 5-22 for various volume fractions and aspect ratios. All simulations were performed with identical boundary conditions with prescribed velocity constraints on the nodes of the ED surface. Each subfigure was taken at the same simulation time (i.e. identical displacement). It is observed that all simulations with an aspect ratio of 1 displayed similar localization patterns. A large shear band can be seen that propagates across the ND. In the higher aspect ratio simulations, increasing the volume fraction seems to delay the formation of the shear band, which agrees with the Considère criterion. What is particularly interesting in this study is the localization pattern of the $f = 2\%$ and $A = 64$ simulation. Not only is localization delayed, but the deformed geometry appears to be different to the remaining RVEs. This is more specifically shown in Fig. 5-23 with equivalent strain rate contours. The strain appears to accumulate in different regions on the ND surface and shear bands form in different directions. A careful inspection also shows the development of a different surface texture. A possible reason for this behavior is due to the anisotropic effects of precipitation on different crystal orientations. Since specific orientations are more sensitive to precipitation than others, an initially soft grain may become comparable in strength to its neighbours after introducing precipitates. This would have a direct impact on the localization pattern since the shear banding process appears to be initiated from the softest

regions in the sample. Furthermore, it was shown by Brahme et al. [38] that the generation of internal stresses is able to change the location of the dominant slip band, which could be another factor at play in the current constitutive model. This study shows that precipitation plays an interesting role in the resulting localization response and highlights the importance of incorporating precipitate physics into constitutive FE models.

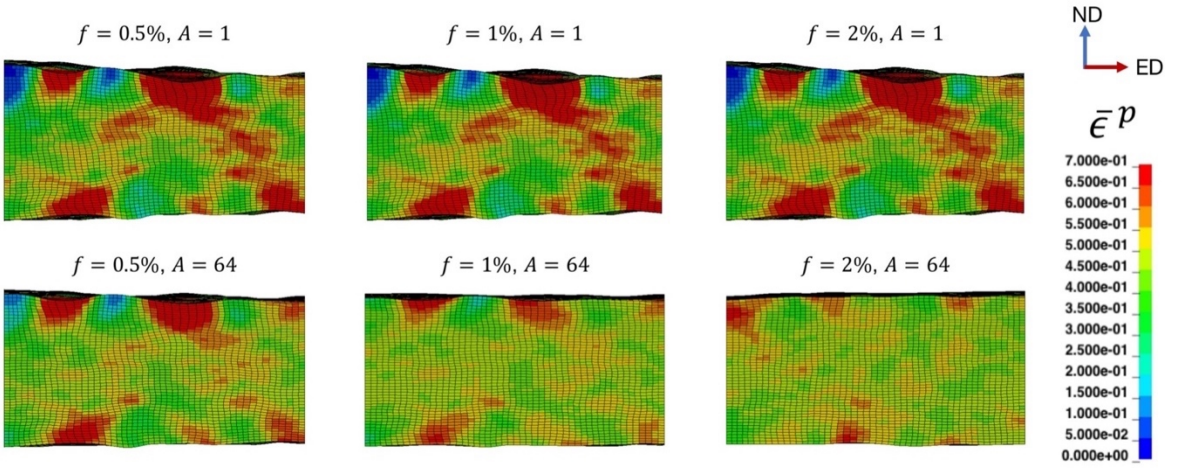

Fig. 5-22. Localized geometry and plastic strain distributions for the parametric study. All figures are taken after the same amount of displacement.

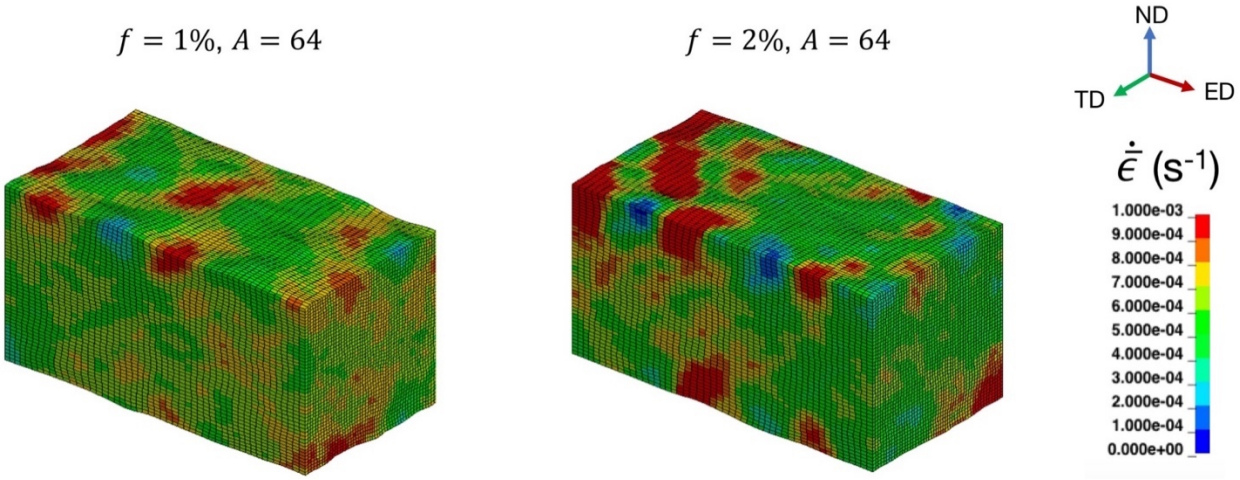

Fig. 5-23. Deformed RVEs of (a) $f = 1\%$ and $A = 64$ and (b) $f = 2\%$ and $A = 64$ simulations.

5.6 Chapter Conclusions

This chapter presented a new crystal plasticity model for precipitation hardening in aluminum alloys for use within an FE framework. The formulation uses a precipitate-dislocation

yield model and a single crystal homogenization scheme to capture the effects of precipitates. A key advantage in the proposed model is the ability to incorporate the orientation relationship between the precipitate and the matrix as well as the precipitate's morphology to simulate the constitutive response. In particular, this work utilized the TEM observation that precipitates are orientated along specific <100> lattice directions in AA6000-series aluminum alloys, which has large implications on the resulting deformation properties. However, it should be mentioned that the framework can be easily generalized to other precipitation-hardenable aluminum alloys that contain different shapes and orientations of precipitates. The numerical model was implemented into a user-defined material subroutine in the commercial FE software, LS-DYNA. This model was then calibrated and evaluated using a combination of new and existing experimental data for an extruded aluminum alloy AA6060 in the T6 state. The framework was used to conduct both single crystal and polycrystal simulations to investigate the effect of precipitates on the properties of the material. The model showed good capabilities in capturing the strain hardening rate, Bauschinger effect, and plastic anisotropy. Key conclusions of this work are summarized as follows:

1. In the single crystal studies, the precipitation hardening mechanism did not affect the anisotropic response of yield stress to a large degree compared to the model without the mechanism. However, it had a significant impact on the Lankford coefficient (R-value) of certain single crystal textures. This was due to the precipitate providing an additional deformation mechanism to accommodate or resist crystallographic slip and thinning.
2. The orientation of high aspect ratio precipitates along the <100> lattice directions was able to account for the reduction in plastic anisotropy in the polycrystal simulations. Furthermore, the magnitude of the precipitate volume fraction intensified these high aspect ratio effects.
3. Spherical precipitates had a minor (nearly negligible) effect on the work hardening and anisotropic response relative to pure aluminum.
4. The Bauschinger effect was captured by the crystal plasticity constitutive model through the generation and release of internal stresses simulated through an Eshelby inclusion methodology.

5. The localized deformation response is indeed affected by precipitation hardening but is slightly more complicated than expected. At low volume fractions and aspect ratios, localization is primarily microstructurally driven, and precipitates simply accelerate or delay the onset of necking. However, at higher volume fractions and aspect ratios, it appears that the precipitates completely change the banding and localization response.

6 Precipitation Kinetics and Crystal Plasticity Modeling of Artificially Aged AA6061

Y. Larry Li [a], Christopher P. Kohar [a], Waqas Muhammad [a], Kaan Inal [a]

[a] Department of Mechanical and Mechatronics Engineering, University of Waterloo, Waterloo, Canada N2L 3G1

Abstract

An artificially aged AA6061 alloy was investigated at multiple heat treatment conditions with monotonic tensile and cyclic shear testing to characterize the effect of precipitation on the alloy's mechanical properties. The microstructure was first measured with scanning electron microscopy, which was observed to remain fairly constant throughout all aging conditions. Mechanical testing showed that artificial aging reduced the initial work hardening rate without affecting dynamic recovery. The alloy also exhibited a reduction in plastic anisotropy and an increase in kinematic hardening with increased aging time. Afterwards, a numerical through-process framework was introduced to predict both the precipitation kinetics and mechanical behavior of AA6000-series materials. The kinetics model was calibrated and validated with transmission electron microscopy measurements on several Al-Mg-Si alloys. The mechanical model uses the simulated precipitate distribution in a modified crystal plasticity framework to calculate the alloy's constitutive response. The framework was able to simulate the yield strength, work hardening, plastic anisotropy and Bauschinger behavior of AA6061 with reasonable accuracy. Plastic anisotropy and kinematic hardening was specifically captured with an inclusion-based method of modeling the precipitates. The model was later used to simulate precipitation hardening in individual single crystals. It was observed that the effect of artificial aging is minor compared to the overall effect of texture on the material.

Keywords: Precipitation Kinetics; Precipitation Hardening; Crystal Plasticity; Anisotropy; Bauschinger effect

6.1 Introduction

Precipitation hardening is responsible for several changes to the mechanical properties of aluminum alloys. Many of these effects were captured previously with the crystal plasticity constitutive framework outlined in Chapter 5. However, the research made several assumptions on the properties of the precipitate distribution that was a critical input into the model. These inputs include precipitate length, radius, volume fraction and others, all of which can influence the physical properties of the material. Due to this precipitate-property relationship in precipitation hardened alloys, there has been considerable research interest on modeling the precipitation kinetics process. An accurate kinetics simulation can provide confidence in the product development cycle and offer potential cost and time savings during materials research and development.

First, a brief outline of the precipitation kinetics process is described as follows. Artificial ageing involves the use of temperature changes to create a chemical driving force for the nucleation of precipitates. This driving force initiates the formation of small solute clusters that ultimately grows to become precipitates. While the nucleation process is rather random, the growth of existing precipitates is driven by the diffusion of solute atoms from the supersaturated matrix. These processes occur concurrently until a state of equilibrium is attained where the excess solutes in the matrix are fully depleted and both nucleation and growth are no longer favorable. During the late stages of ageing, the material undergoes a coarsening process where smaller precipitates are dissolved and larger precipitates are made larger.

Despite the kinetic process being rather complex, there are several numerical methods in the existing literature that can be applied to simulate the ageing process. The modeling of aluminum precipitation in particular is predominantly based on classical nucleation and growth theory (CNGT), which is summarized in Chapter 2.5.5. The benefits of classical nucleation and growth modeling is its computational speed and range of applicability for various thermodynamic processes. As shown by previous authors [78, 93, 100], the combination of CNGT and the Kampmann and Wagner numerical (KWN) approach allows for the simulation of the entire precipitate size-distribution over time. This is especially important for the subsequent modeling of physical properties as it is well known that the shearability of precipitates depends on its size [99, 102].

Though there have been significant development towards the modeling of precipitation kinetics, the literature on the through-process modeling of artificial ageing has been weak. This is unfortunate as the outputs from precipitation kinetics models are essentially the inputs for mechanical models. A framework for simulating artificial ageing should account for both types of modeling. Myhr et al. [132] was one of the first to simulate the yield strength and work hardening rate of AA6000-series materials with their NaMo precipitation kinetics model. Anjabin et al. [124] then developed a model combining precipitation kinetics and crystal plasticity mechanics to simulate the monotonic response of an Al-Mg-Si alloy. Bardel et al. [100, 112] developed a plasticity model as an extension to their needle precipitate kinetics framework to simulate the deformation response of AA6061. This model was then extended by Chen et al. [162] to simulate the deformation behavior of an Al-Si-Mg alloy with satisfactory results. The research on the through-process modeling of artificial aged alloys has been mostly limited to predictions of yield strength and work hardening [40, 101, 160, 161, 166]. This is understandable as the yield strength is one of the most commonly used values, as well as a parameter that many engineers would consider as a material failure point. However, properties such as plastic anisotropy or the Bauschinger effect is also important as they often influence the fabrication process for metallic products [111, 134, 213].

In the current work, a numerical framework is introduced that links nucleation and growth modeling with precipitation hardening in crystal plasticity. The kinetics framework is inspired from the KWN method [76, 93] and is extended to incorporate the evolution of precipitate morphology [158, 164]. The generated precipitate size distribution is then passed into the crystal plasticity model developed in Chapter 5 to simulate the mechanical properties affected by ageing. Crystal plasticity is valuable as the precipitates are orientation dependent (aligned with the <100> directions of each crystal), which can be captured with single crystal modeling. This work is particularly focused on the simulation of precipitate-induced anisotropy and Bauschinger effects for single crystals and polycrystals. Whereas “virtual” alloys were generated in the previous chapter to demonstrate the application of the constitutive model, this chapter uses realistic simulations of the precipitate distribution to investigate the performance of the alloys. To support the development of this framework, experimental testing was conducted for an AA6061 sheet metal alloy that was artificially aged to multiple conditions ranging between 15 minutes and 48 hours. The microstructure across different heat treatments was measured with scanning electron

microscopy (SEM) to examine for changes in the grains during ageing. Monotonic tensile and shear tests were performed across different sheet orientations to capture the material's anisotropy. Additionally, cyclic shear tests were performed at several plastic strain levels to investigate the Bauschinger behavior across heat treatment conditions. The experiments were used to calibrate and validate the numerical framework and the overall effects of precipitation are discussed from both an experimental and theoretical perspective.

6.2 Experimental Setup

6.2.1 Material

The material used in the current study is a rolled AA6061 aluminum alloy from McMaster-Carr with a nominal thickness of 1.27 mm. The chemical composition of the alloy is shown in Table 6-1. The material was received in the T6 condition and then laser cut into individual blanks for subsequent fabrication into test specimens. Each test sample was solution heat treated in a sand bath furnace at 530°C for 30 minutes and then water quenched to room temperature. To conduct the artificial ageing heat treatments, samples were placed back into the sand bath furnace at a stabilized temperature of 190°C for various durations ranging between 15 minutes and 48 hours. The complete heat treatment schedule is presented in Table 6-2. The samples were stored in a deep freezer at -40°C between and after heat treatments to prevent natural ageing.

The microstructure of the material was characterized using a scanning electron microscope (SEM) equipped with an electron backscatter diffraction (EBSD) detector. Fig. 6-1 shows three EBSD images of the as-quenched (AQ) microstructure along the primary orthogonal planes. Each EBSD image encompasses a region of approximately 1.2 mm x 0.85 mm and the average measured grain size is 20.6 μm across all three planes. The corresponding (111) pole figures are also shown on the right-hand side of each EBSD image. It is observed from the EBSD maps that the microstructure has undergone considerable flattening across the normal direction (ND). The grains are stretched along the rolling direction (RD) and transverse direction (TD), as expected from a typical rolling process. From additional inspection of the pole figures, it appears that the microstructure is dominated by strong Cube and Goss texture components. This suggests that recrystallization also took place to some degree during the solution heat treatment process.

Table 6-1. Chemical composition of as-received AA6061 (wt-%).

Al	Mg	Si	Fe	Cu	Cr	Mn	Other
Bal	1.0	0.64	0.4	0.26	0.16	0.08	0.19

Table 6-2. Summary of complete precipitation hardening heat treatment schedule.

Index	Temper	Heat Treatment Process
1	AQ	530°C for 30 minutes → Water quench
2	15m	530°C for 30 minutes → Water quench → 190°C for 15 minutes
3	30m	530°C for 30 minutes → Water quench → 190°C for 30 minutes
4	1h	530°C for 30 minutes → Water quench → 190°C for 1 hour
5	2.5h	530°C for 30 minutes → Water quench → 190°C for 2.5 hours
6	6h	530°C for 30 minutes → Water quench → 190°C for 6 hours
7	24h	530°C for 30 minutes → Water quench → 190°C for 24 hours
8	48h	530°C for 30 minutes → Water quench → 190°C for 48 hours

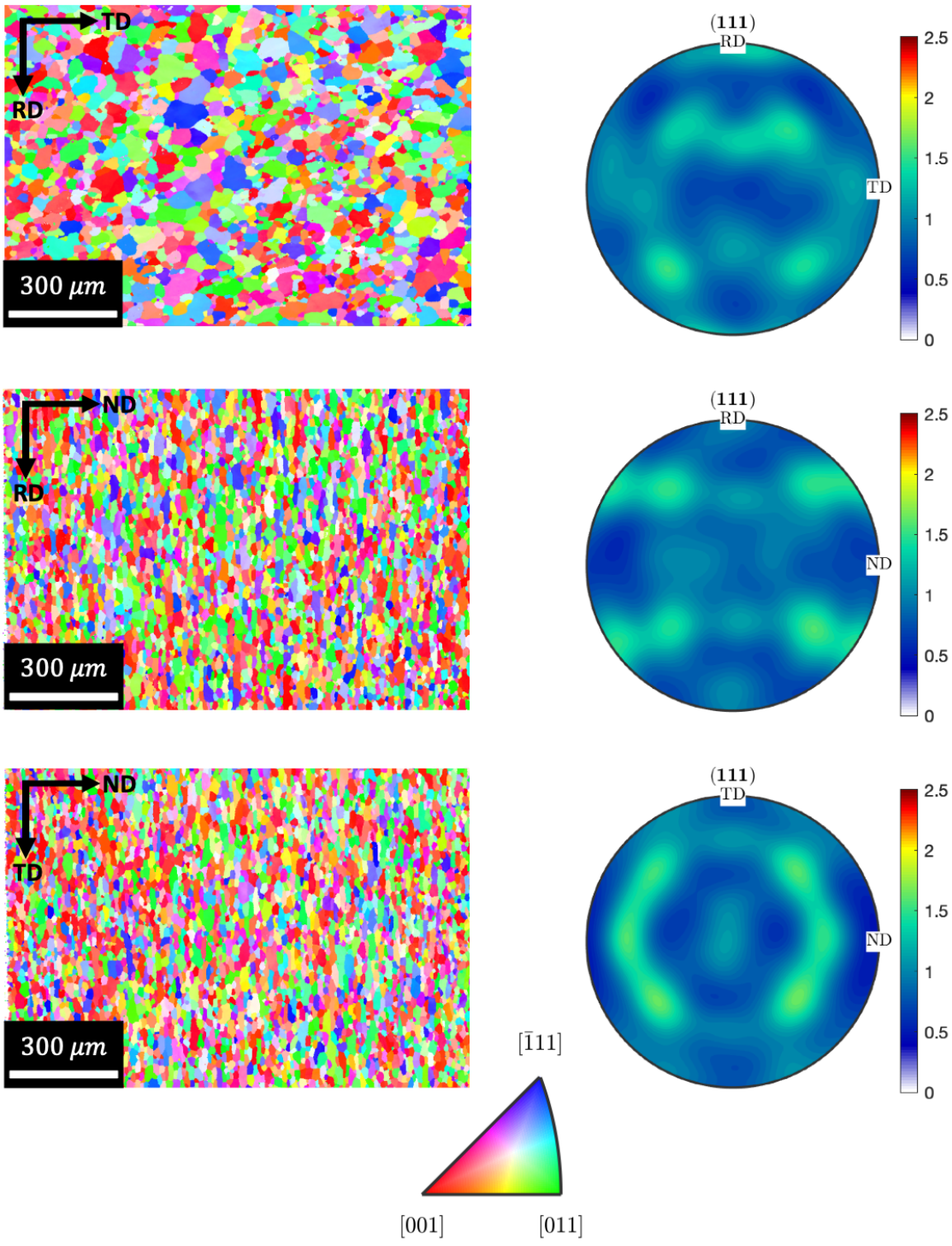

Fig. 6-1. EBSD images and (111) pole figure of as-quenched AA6061 microstructure.

6.2.2 Mechanical Testing

The mechanical testing program consisted of uniaxial tension in the RD, TD, and 45° diagonal direction (DD), as well as monotonic and cyclic simple shear along RD. The geometry used for uniaxial tension is a standard ASTM-E8 specimen, as shown in Fig. 6-2, with a nominal gage length of 50 mm. The tensile specimens were laser cut from the as-received sheet prior to all artificial heat treatments. For simple shear testing, the geometry used is a modified mini-shear specimen that was initially adopted from Rahmaan et al. [42]. The specimen is shown in detail in Fig. 6-3. This specimen was used in the previous chapter to characterize the large deformation shear response of an AA6060 alloy, making it again a suitable choice for the current study. The outer perimeter of the shear specimens was laser cut from the as-received sheet material; however, the gage section itself was cut using computer numerical control (CNC) machining. The machining was done after heat treating the samples to prevent potential warpage near the thin gage section.

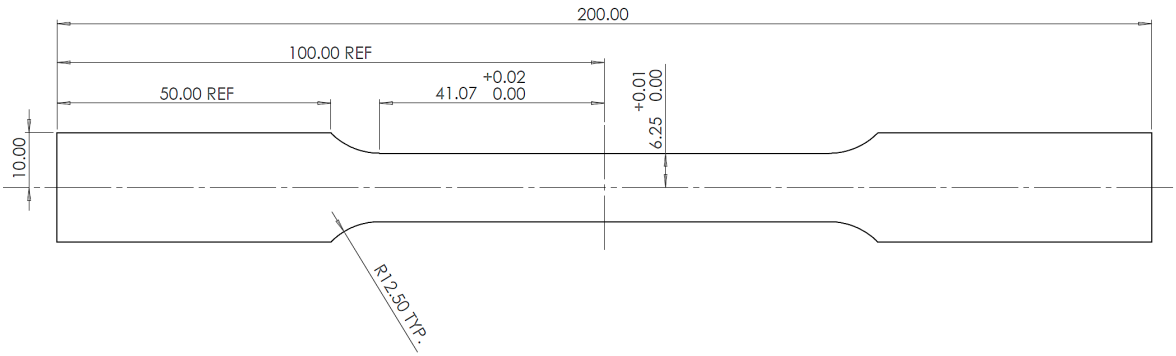

Fig. 6-2. ASTM-E8 uniaxial tensile specimen. Dimensions in millimeters.

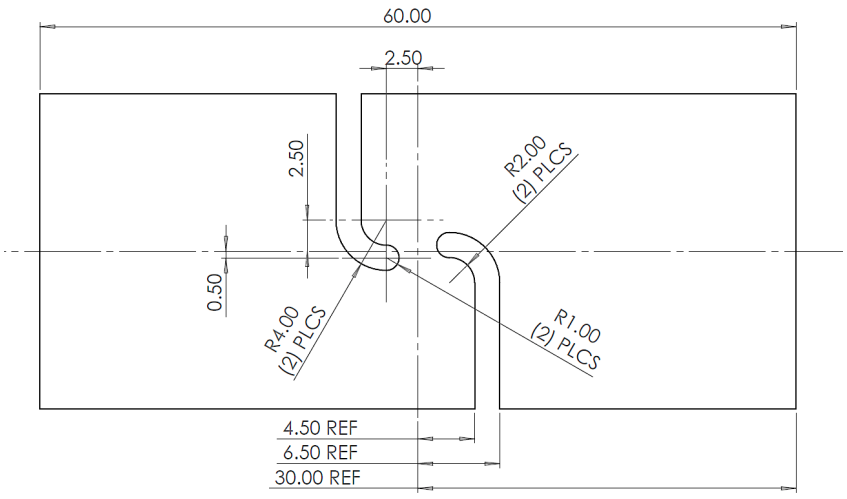

Fig. 6-3. Modified mini-shear specimen. Dimensions in millimeters.

The mechanical experiments were conducted using an MTS Criterion 45 servo-hydraulic tensile machine with a 100 kN load cell. Details of the machinery and setup can be found in Kohar et al. [37]. An image of the setup was presented earlier in Fig. 5-3. All tests were performed under quasi-static loading conditions ($\dot{\epsilon} = 0.001/s$) at room temperature. Three repeats were conducted for each condition and the average is presented in the results. The uniaxial and monotonic shear tests were conducted until fracture while the cyclic shear tests consisted of forward-reverse-forward (FRF) reversals at approximately 3%, 6% and 9% shear strain. The experiments were also recorded using stereoscopic Point Grey GRAS-50S5M-C cameras for digital image correlation (DIC) with 80 mm lenses for uniaxial tension tests and 180 mm lenses for simple shear tests. Commercial software, VIC3D by Correlated Solutions Inc., was used to analyze and process the DIC results to obtain a full-field logarithmic strain map. The in-plane shear strain of the mini-shear specimens was calculated using Eq. (95).

$$\gamma_{12} = 2\sqrt{\left(\frac{\epsilon_{xx} - \epsilon_{yy}}{2}\right)^2 + \epsilon_{xy}^2} \qquad (95)$$

6.3 Experimental Results and Discussion

6.3.1 Microstructure

Fig. 6-4 illustrates the pole figures of the artificially aged microstructures measured along the RD-TD plane. As shown, the microstructural differences between different tempers are rather minor. The (111) poles are all comparable in magnitude and location across different heat

treatment conditions, exhibiting Cube and Goss texture components at all tempers. Table 6-3 presents the measured average grain size for each heat treatment, measured with the MTEX-MATLAB microstructural analysis module. It is observed that a slight trend towards larger grains is found with longer durations of artificial ageing. The larger grains can be explained by the material undergoing a minor degree of recrystallization at the artificial ageing temperature. However, this temperature is still rather low to cause significant changes to the microstructure. Overall, the differences across heat treatments are small and it can be practically stated that the microstructure does not change during artificial ageing at 190°C.

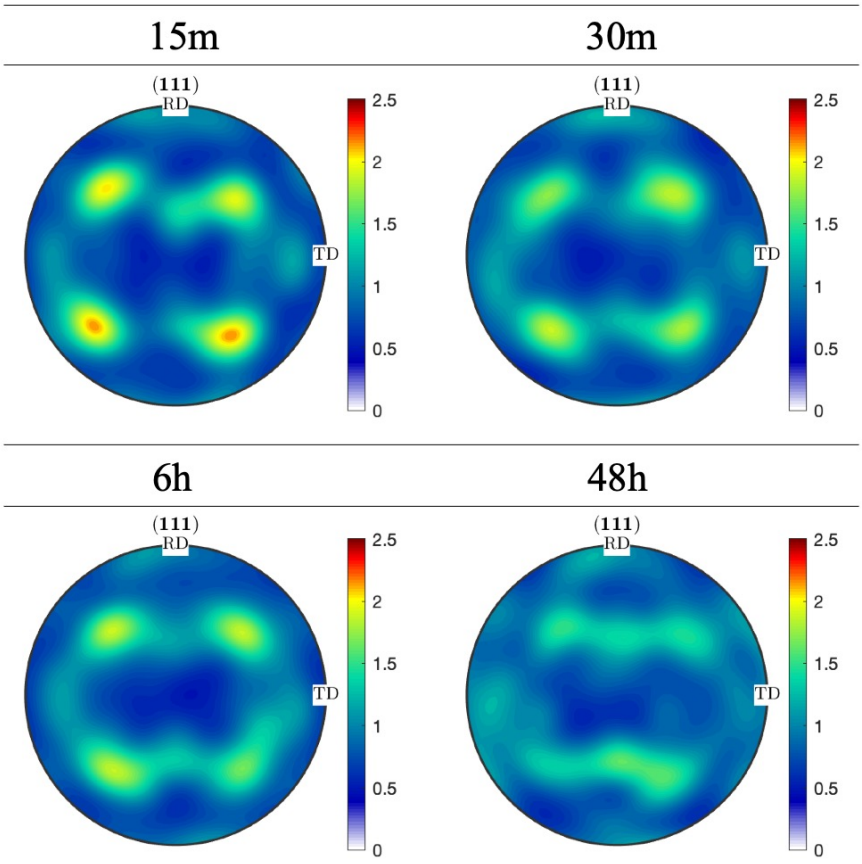

Fig. 6-4. Pole figures of AA6061 microstructure for various artificial ageing times at 190°C.

Table 6-3. Average grain size of AA6061 microstructure at various artificial ageing times at 190°C. Measurements calculated from EBSDs of the RD-TD plane.

	AQ	15m	30m	6h	48h
Grain Size (μm)	22.4	22.8	23.1	24.4	24.1

6.3.2 Tensile Tests

Fig. 6-5 presents the uniaxial tensile experimental data for RD, DD, and TD, respectively for the tested artificial ageing conditions. The corresponding work hardening plots are also shown in Fig. 6-6 as a function of the flow stress after 0.2% offset yield. All stress-strain plots were terminated upon reaching the ultimate tensile strength (UTS). As observed, there is an obvious difference in both the yield strength and work hardening behaviors across the various heat treatments. The 6h sample appears to be the closest to peak-aged, defined as the condition with the highest initial yield strength. However, the highest UTS was actually observed for the 2.5h sample with a slightly lower yield strength but considerably higher work hardening rate and elongation. The yield strength follows the expected behavior starting with the lowest value in the AQ condition, reaching a peak at 6h and then declining in the over-aged samples. Similarly, the highest rate of hardening was found in the AQ condition, which then steadily declined with artificial ageing time. As seen in Fig. 6-6, the work hardening plots appears to approach a constant slope over time across all tempers. This suggests that the dynamic recovery constant is comparable in magnitude across all heat treatment conditions and that only the initial work hardening rate was noticeably affected by precipitation [57]. This is an interesting result because the conventional explanation for changes in the work hardening curve is due to changes in the dynamic recovery constant [112, 124, 132, 162]. The results shown here are in contradiction with much of the existing literature for AA6000-series alloys, suggesting the possibility of other complex mechanisms at play. It should be mentioned that this is not the first observation where dynamic recovery was found constant across heat treatments. da Costa Teixeira et al. [217] also made a similar observation in Al-Cu alloys suggesting that the depletion of solute has a stronger effect on the dislocation-dislocation junction strength than on dislocation recovery mechanisms. This effect could also be explained by dynamic strain ageing (DSA) that can occur during the deformation process. During DSA, the nucleation of additional precipitate can raise the overall

work hardening rate without causing substantial changes to dynamic recovery [218]; however, this would require extensive experimentation to verify. Regardless of the mechanism underlying this effect, it is found that dynamic recovery is rather unaffected by artificial ageing, which implies that the change in the hardening rate is due to a dependence of dislocation generation mechanisms on the state of precipitation.

It is worth mentioning that a slight inflection of the elastoplastic transition exists in the peak and over-aged stress-strain curves. This has been observed in other artificially aged alloys as well [105, 129] and is believed to be due to the shearable-non-shearable transition of the precipitates during ageing [102, 115]. As the precipitates transition from being coherent to incoherent, it becomes increasingly capable of blocking dislocation glide, which can mask the dislocation hardening behavior at the early stages of deformation. Though the effect is rather minor for this particular alloy, it demonstrates that the precipitates are capable of inducing a behavior that is comparable to advanced steel, titanium or magnesium alloys, which have highly anisotropic slip systems and other mechanisms such as twinning [219–221].

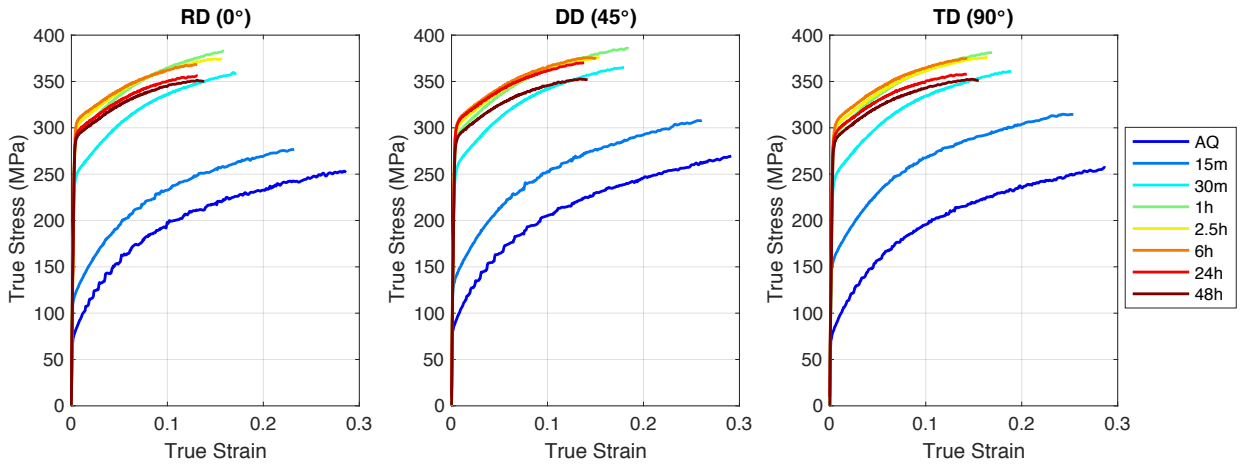

Fig. 6-5. Experimental uniaxial stress-strain curves across all heat treatment conditions for RD, DD and TD orientations.

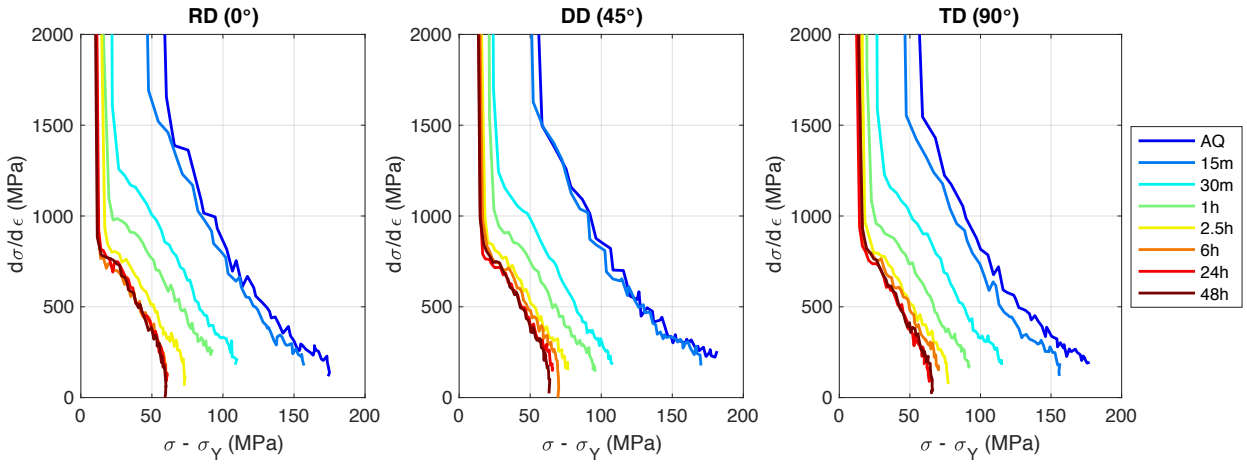

Fig. 6-6. Experimental work hardening plots across all heat treatment conditions for RD, DD and TD orientations.

It is further observed that there is relatively low flow stress anisotropy between the RD, DD and TD orientations. This is shown in detail in Fig. 6-7 with plots of the yield stress variation (normalized with respect to TD) showing a reasonably flat profile, with the exception of the 15m sample. A possible reason for the deviation of the 15m tests may be due to excessive exposure of the samples to room temperature during specimen preparation; the AQ and 15m conditions are particularly susceptible to natural ageing as the precipitates are more unstable in the early stages of heat treatment. Nevertheless, there is no obvious trend across the different tempers. It appears that the DD stress is always higher than the stress in the RD and TD orientations; however, there is no distinctive pattern as both under-aged and over-aged samples demonstrate this behavior. Overall, these results demonstrate that the flow stress is mostly isotropic in this material.

In contrast, Fig. 6-8 shows a notable degree of anisotropy in the measured R-values across RD, DD and TD. The R-values here are calculated using the strain ratio

$$r = \frac{\epsilon_y}{\epsilon_z} \qquad (96)$$

where y refers to the width axis and z refers to the thickness axis of each test sample. From Fig. 6-8, it is possible to make two important observations. First, the degree of anisotropy reduces at higher plastic strain values as shown by a vertical shift of the overall R-values towards unity. Second, the degree of anisotropy also reduces with longer artificial ageing times as shown by a flattening of the R-value variation with stronger heat treatments. The second effect is particularly important and can be explained by the increasing volume fraction of precipitates at longer ageing

times, where a larger and denser precipitate distribution allows for more uniform dislocation behavior. The precipitates are also more capable of accommodating deformation, which can strengthen softer crystal orientations through the transferring of load [106, 107, 213, 222].

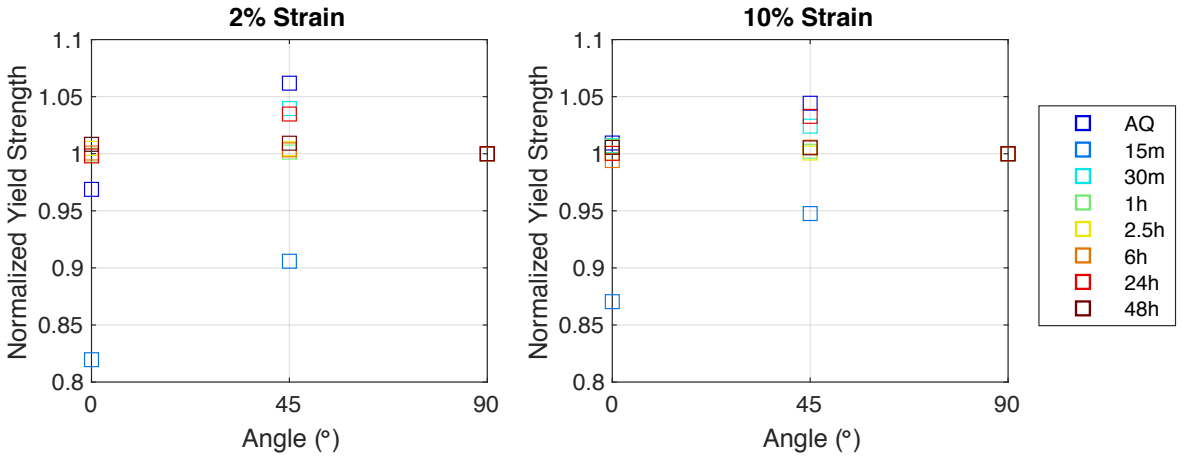

Fig. 6-7. Experimental yield stress variation across all heat treatments at 2% and 10% plastic strain.

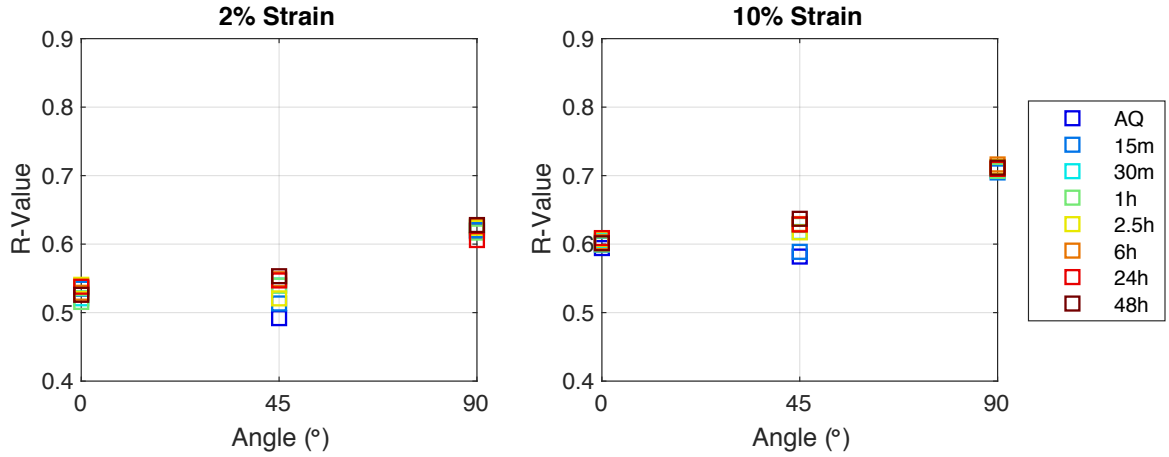

Fig. 6-8. Experimental R-value variation across all heat treatments at 2% and 10% plastic strain.

6.3.3 Shear Tests

The monotonic forward shear stress-strain curves are presented in Fig. 6-9 for all heat treatments and the cyclic FRF shear stress-strain curves are presented in Fig. 6-10. The cyclic FRF tests were conducted at reversals of 3%, 6% and 9% shear strain, measured using DIC. The behavior of the monotonic shear results are similar to the tensile experiments, showing an increase in yield strength with artificial ageing until the peak aged condition, followed by a

decrease during over-ageing. The corresponding work hardening rate steadily decreases with artificial ageing up to about the peak-aged state and then remains relatively constant in the over-aged regime. From the cyclic shear testing, it is first observed that the stress-strain behavior is relatively smooth and in the absence of non-linear Bauschinger effects, as is sometimes observed in materials undergoing cyclic testing [115, 223]. This is likely due to the general isotropy of rolled sheet, which makes for a uniform distribution of precipitates across the alloy. The Bauschinger effect is measured for each of the three strain reversal levels in Fig. 6-11 with the use of a stress reversal parameter that quantifies the degree of reduction in yield stress [224]

$$\beta = \frac{\sigma_f - \sigma_r}{\sigma_f} \quad \textbf{(97)}$$

where σ_f is the value of stress right before a strain reversal and σ_r is the subsequent yield stress after. In this work, σ_r is calculated using a 1% plastic strain offset to accommodate the rather large elastic-plastic transition observed during strain reversals. As shown, the magnitude of the Bauschinger effect steadily creeps higher with longer ageing times. There appears to be a large jump in β between the 15m and 30m samples for the 3% and 6% plastic strain tests. This is somewhat expected in precipitation hardening alloys as the precipitates increase in size and quantity with the duration of artificial ageing. Between 15 minutes and 30 minutes of ageing is likely when the material undergoes the largest growth of precipitate during artificial ageing. Larger precipitates are more capable of storing deformation [106, 107] and also more effective at trapping dislocations in the form of Orowan loops [105, 115, 144]. Both attributes would lead to a large Bauschinger effect during strain reversals. It should be mentioned that other heterogeneities, such as grain boundaries or dislocation cell-structures, could also be responsible for causing the Bauschinger effect; however, these effects should remain relatively persistent across all heat treatment conditions. This would not explain the large differences in β across different heat treatments, which implies that precipitates are most likely responsible for the Bauschinger effect.

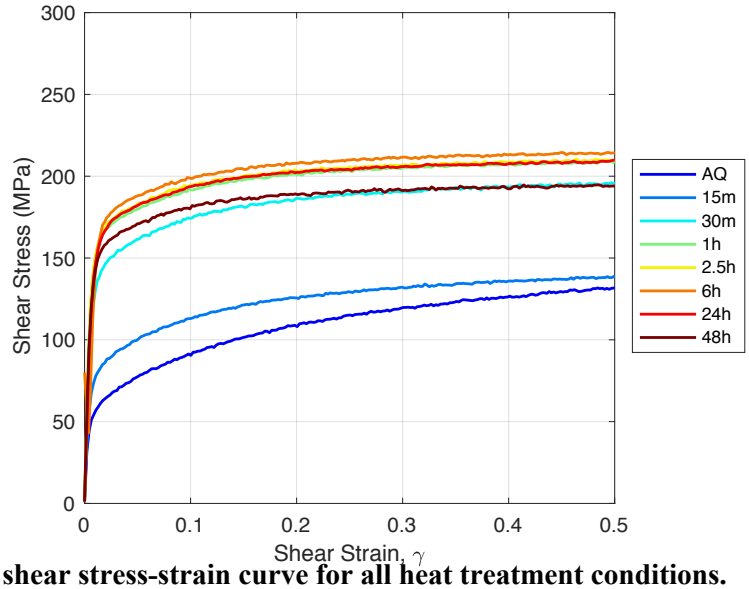

Fig. 6-9. Monotonic shear stress-strain curve for all heat treatment conditions.

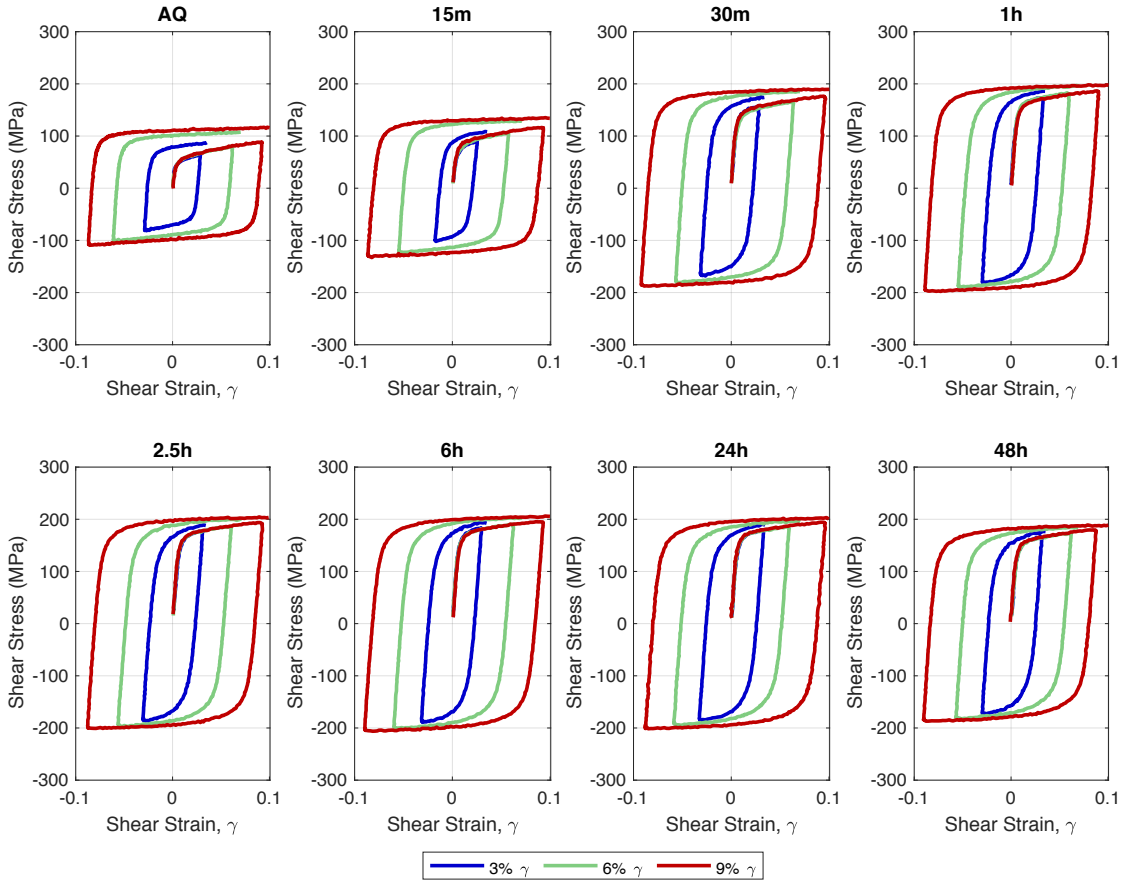

Fig. 6-10. Cyclic shear stress-strain curves for 3%, 6%, and 9% shear strain reversals.

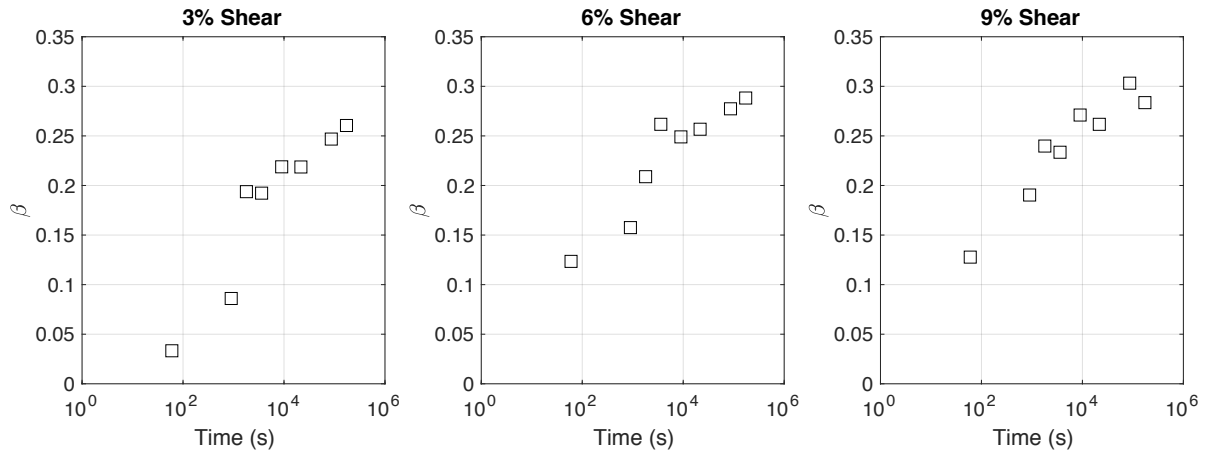

Fig. 6-11. Magnitude of Bauschinger effect over artificial ageing time for cyclic shear tests at 3%, 6% and 9% shear strain reversals.

6.4 Model Description

The simulation method used in this work employs two types of models: a classical nucleation and growth model to capture the kinetics of precipitation during artificial ageing and a crystal plasticity model to capture the deformation response of the aged alloys. The objective of the kinetics model is to predict the overall precipitate distribution due to a given temperature, time, and compositional input. These results are then conveyed to the crystal plasticity constitutive model for the simulation of the stress-strain results. It should be mentioned that the two models are not coupled together; in other words, results from crystal plasticity do not affect precipitation kinetics. A key component in the current framework is the consideration of precipitate morphology throughout both models. This idea stems from previous works demonstrating that deviations from the spherical assumption causes considerable changes to both the kinetic behavior [123, 158, 166] and plastic behavior [99, 141, 225] in artificially aged alloys.

CNGT was selected for simulating precipitation kinetics as it is perhaps the most well-developed theory for thermodynamic processes. Though there are advantages in using lower length scale methods such as cluster dynamics or phase field modeling, there are certain limitations in the other approaches that affect the ease of implementation for AA6000-series materials. For instance, cluster dynamics is typically limited to binary alloys as the clusters are defined based on size rather than composition. A cluster dynamic implementation for the ternary Al-Mg-Si system would not be trivial. The limitation for phase field modeling is in the computational demand for simulating large domains. This can be troublesome for calculating the

precipitate distribution across several grains. It is also plagued with similar issues as CNGT, where several parameters must be introduced to calibrate the model to experiments. CNGT provides a good balance between accuracy and computation speed and has been used widely throughout literature for precipitation processes. A review of recent CNGT modeling efforts in literature is provided in Section 3.4.1.

6.4.1 Precipitation Kinetics

The kinetics calculations are based on the KWN model by Myhr et al. [76], where precipitation is considered as concurrent nucleation, growth and mass rebalancing processes. Input parameters into the model include ageing temperature, ageing time, initial concentration of Mg and Si, as well as material parameters that are either calibrated or selected from existing literature. The outputs of the model are properties of the precipitate distribution, including length, radius, volume fraction and quantity (per unit volume). Given that precipitates in AA6000-series alloys contain both Mg and Si elements, a multi-component precipitation model is used in all aspects of the work [154]. The stoichiometry of precipitates is presumed to be Mg_2Si, which is a reasonable assumption given that it is the stable equilibrium phase as well as the phase with the most reliable thermodynamic data [226, 227]. The solubility product C_e for Mg_2Si is expressed as

$$\log C_e = \frac{\Delta S}{R_g} - \frac{\Delta H}{R_g T} \quad \textbf{(98)}$$

where ΔS and ΔH are the entropy and enthalpy of reaction found from Grong [228], R_g is the universal gas constant, and T is the ageing temperature.

The kinetics approach discussed in this section follows the introduction provided in Section 2.5.5; however, the full formulation is provided here as this work is based on an extension that utilizes both a non-spherical methodology and the use of multiple solutes.

The nucleation rate of precipitates $\dot{N}$ from supersaturated solution is described by an Arrhenius equation of the form

$$\dot{N} = j_0 \exp\left(\frac{-\Delta G_c}{K_b T}\right) \exp\left(\frac{-Q_d}{R_g T}\right) \exp\left(\frac{-\tau}{t}\right) \quad \textbf{(99)}$$

where j_0 is a calibrated pre-exponential parameter, Q_d is the activation energy for diffusion [93], τ is the incubation time, t is the current ageing time, K_b is the Boltzmann constant, and ΔG_c is

the energy barrier for nucleation. The energy barrier is obtained from the Gibbs free energy change for nucleation, expressed as

$$\Delta G = -\frac{4}{3}\pi R^3 \Delta g_{ch} + 4\pi R^2 g\sigma \quad \textbf{(100)}$$

where R is the volume-equivalent spherical radius of the nucleus, Δg_{ch} is the chemical driving force, σ is the interface energy and g is a shape factor to account for the non-spherical geometry of the nucleus. The nucleation radius can be obtained via differentiation of Eq. (100) with respect to R and finding the maxima

$$R_c = \frac{2g\sigma}{\Delta g_{ch}} \quad \textbf{(101)}$$

The energy barrier for nucleation is then obtained from substitution of Eq. (101) into Eq. (100)

$$\Delta G_c = \frac{16}{3}\pi \frac{g^3\sigma^3}{\Delta g_{ch}^2} \quad \textbf{(102)}$$

Following a similar method to Myhr et al. [76], the energy barrier is modified using a material parameter A_0 to account for the non-homogeneous nature of nucleation

$$\Delta G_c = \frac{A_0\sigma^3}{\Delta g_{ch}^2} \quad \textbf{(103)}$$

The incubation time τ is defined by [79]

$$\tau = \frac{1}{2\beta^* Z} \quad \textbf{(104)}$$

where Z is the Zeldovich factor with a value of $Z = 1/300$ [40] and β^* is the condensation rate of solute [100]

$$\beta^* = \frac{4\pi R_c^2}{a^4}\left[\frac{X_{Mg}^p}{D_{Mg}X_{Mg}^m} + \frac{X_{Si}^p}{D_{Si}X_{Si}^m}\right] \quad \textbf{(105)}$$

where a is the lattice parameter, X^p is the solute concentration within the precipitate, X^m is the solute concentration in the matrix, and D_k is the diffusion coefficient for solute k. The diffusion coefficient D_k for each solute is expressed as

$$D_k = D_k^0 \exp\left(\frac{-Q_d}{R_g T}\right) \quad \textbf{(106)}$$

where D_k^0 is a material coefficient for solute k [93]. For precipitates with a stoichiometry of Mg_xSi_y, the chemical driving force is defined as

$$\Delta g_{ch} = \frac{K_b T}{v^p (x+y)} \ln\left(\frac{\left(X_{Mg}^i\right)^x \left(X_{Si}^i\right)^y}{C_e}\right) \quad \textbf{(107)}$$

where v^p is the mean atomic volume of the precipitate phase.

After a stable nucleus has been established via Eq. (99), its growth is driven by the diffusion of solutes from the supersaturated matrix. The steady-state growth rate is expressed as

$$\frac{dR}{dt} = f \frac{X_k^m - X_k^i}{\alpha X_k^p - X_k^i} \frac{D_k}{R} \qquad \text{for } k = \text{Mg, Si} \quad \textbf{(108)}$$

where f is a shape factor that accounts for the growth of non-spherical particles, X^i is the solute concentration at the precipitate-matrix interface, and $\alpha = v^m/v^p$ is the atomic volume ratio. Since the precipitate is composed of multiple solutes, the amount of growth determined by Eq. (108) is contained by the solute that depletes first during artificial ageing, which depends on the initial solute concentration. The interface concentration X^i is calculated by considering the Gibbs-Thomson effect [77]

$$\left(X_{Mg}^i\right)^x \left(X_{Si}^i\right)^y = C_e \exp\left(\frac{2g\sigma v^p}{RK_b T}(x+y)\right) \quad \textbf{(109)}$$

In this work, the precipitates are assumed to have a prolate geometry. The shape factors for prolate particles were derived by Holmedal and Du et al. [158, 164] as

$$f(\zeta) = \frac{2\sqrt{\zeta^2 - 1}}{\sqrt[3]{\zeta} \ln\left(2\zeta^2 + 2\zeta\sqrt{\zeta^2 - 1} - 1\right)} \quad \textbf{(110)}$$

$$g(\zeta) = \frac{1}{2\zeta^{\frac{2}{3}}}\left(1 + \frac{\zeta^2}{\sqrt{\zeta^2 - 1}} \sin^{-1}\left(\frac{\sqrt{\zeta^2 - 1}}{\zeta}\right)\right) \quad \textbf{(111)}$$

where the variable ζ is the aspect ratio between the major and minor axes of the precipitate, $\zeta = l/2r$. Both shape factors approach the spherical assumption of unity as $\zeta \to 1$. Since it is well known that the precipitate aspect ratio evolves throughout an artificial ageing process [156, 159, 164], the aspect ratio is also updated in this work based on a relationship between the cross-sectional area and the length of the precipitates. First, the following expression is introduced [158]

$$A_c = ml \quad \textbf{(112)}$$

where A_c is the cross-sectional area, l is the length of precipitates and m is a parameter that can be either obtained from experiments or used as a calibration constant. While A_c is calculated via

$A_c = \pi r^2$, the radius r is related to the effective spherical radius R using the expression $r = \sqrt[3]{\frac{2}{3\zeta}R^3}$. Substitution of these expressions into Eq. (112) results in the final relationship for the aspect ratio

$$\zeta = \left(\frac{\pi R}{2m}\right)^{\frac{3}{4}} \left(\frac{2}{3}\right)^{\frac{1}{4}} \quad \textbf{(113)}$$

The aspect ratio ζ evolves over ageing time due to the increase in R from precipitate growth.

Lastly, the solute concentrations inside the matrix X_k^m are computed from solving a mass balance equation between the interior and exterior sides of the precipitate

$$\alpha N \frac{4}{3}\pi R^3 X_k^p + \left(1 - N\frac{4}{3}\pi R^3\right) X_k^m = X_k^0 \qquad \text{for } k = \text{Mg, Si} \quad \textbf{(114)}$$

where X_k^0 is the initial concentration of solute k in the material.

The kinetic equations are implemented using the upwind finite volume numerical method, the procedure of which is described in detail by Myhr et al. [76]. This KWN implementation is advantageous as it naturally leads to the coarsening of precipitates during the later stages of artificial ageing and is also capable of accommodating the shape factors in Eq. (110) and (111). Furthermore, similar frameworks have been recently used by other researchers that have produced excellent results for other precipitation hardening alloys [40, 94, 101, 160]. In the KWN method, the precipitate radius is discretized into several size classes of equivalent width and the corresponding number density N is calculated for each size class. Instead of calculating a nucleation and growth rate for the precipitates on average, the kinetic equations are computed for each size class to obtain a full particle size distribution. The total volume fraction of particles in the entire particle distribution is then computed by

$$f = \sum_i \frac{4}{3}\pi N_i R_i^3 \quad \textbf{(115)}$$

where R_i is the radius and N_i is the number density for size class i. The rate of growth of each class is determined by the interfacial solute concentration X_k^i, which is dependent on the Gibbs-Thomson equation for the corresponding radius class. The calculations are performed across incremental steps in time until the desired artificial ageing duration is reached. A schematic of the discretization scheme in the KWN method is introduced in Section 2.5.5.1.

6.4.2 Crystal Plasticity

The crystal plasticity model employed in this work uses the elastic-viscoplastic homogenization method described in Section 5.3.2. For brevity, the constitutive model will not be reiterated here. However, there are some differences in the hardening model used in this work, which will be discussed in the following section. Additionally, in contrast with the finite element modeling performed in Chapter 5, the work here utilizes the Taylor averaging scheme where the polycrystal response is simply calculated from the volume averaged responses across all crystals. The Taylor averaging scheme was selected as the purpose of this work is to demonstrate the connection between the precipitation kinetics and crystal plasticity models. The extension of this research to CPFEM would follow the same approach as discussed in Chapter 5.

6.4.3 Hardening

The hardening of the matrix phase is defined using the critical shear stress g^{α}

$$g^{\alpha} = \tau_0 + \tau_s + \tau_d + \tau_p \qquad \textbf{(116)}$$

where τ_0 is the initial shear strength of pure aluminum with a value of $\tau_0 = 3$ MPa, τ_s is the additional hardening due to solid solutes in the matrix, τ_d is the hardening caused by dislocation-dislocation interactions, and τ_p is the strengthening caused by dislocation-precipitate interactions.

The effect of solid solution strengthening is incorporated into the current work and is expressed as a function of solute concentration in the aluminum matrix [93]

$$\tau_s = \sum_j k_j \left(X_j^m\right)^{2/3} \qquad \textbf{(117)}$$

where k_j is a scaling factor for solute j. Only primary solutes Mg and Si are considered here for AA6000-series alloys. The scaling parameters k_j are taken from Myhr et al. [93] and normalized by their Taylor factor for use in the single crystal plasticity model of the current work.

The hardening contribution from dislocation-dislocation interactions is defined using the Taylor hardening equation

$$\tau_d = \kappa \mu b \sqrt{\sum_{\alpha} \rho^{\alpha}} \qquad \textbf{(118)}$$

where κ is the dislocation obstacle strength that is commonly set to 0.3 for FCC materials, μ is the shear modulus, b is the magnitude of the Burgers vector, and ρ^{α} is the dislocation density on

slip system α. The dislocation densities evolve during plastic deformation by the evolutionary law [45]

$$d\rho^{\alpha} = \frac{1}{bc_1}\sqrt{\sum_{\alpha}\rho^{\alpha}}\, d\gamma^{\alpha} - c_2\rho^{\alpha} d\Gamma \qquad \textbf{(119)}$$

where c_1 and c_2 are constants related to the multiplication and dynamic recovery of dislocations, respectively and $d\Gamma = \sum_{\alpha}|d\gamma^{\alpha}|$ is the accumulated plastic shear strain across all slip systems. Eq. (119) is the single crystal equivalent of the conventional Kocks-Mecking hardening law for FCC metals [47] and is also the same as the hardening equation employed in the previous chapter. As shown earlier in the work hardening plots of Fig. 6-6, artificial ageing did not affect the dynamic recovery constant to any substantial degree. As a result, the c_2 parameter is kept constant across all heat treatment conditions in the subsequent modeling. The initial work hardening rate was however affected by precipitation, the effect of which is captured by c_1. To simulate the dependence of the initial work hardening rate, a new relationship is proposed for c_1 that is defined with respect to the solute concentration in the matrix

$$\frac{1}{c_1} = \frac{1}{c_0} + c_3\left(\frac{X_k^m - X_k^e}{X_k^0 - X_k^e}\right) \qquad \textbf{(120)}$$

where $1/c_0$ determines the hardening rate after solutes have been depleted, c_3 is a scaling parameter, and X_k^e is determined from the solubility product of Mg_2Si at the test temperature (i.e. room temperature). This equation assumes that the initial hardening rate follows a linear dependence to the concentration of solute remaining in the matrix. As the solutes are depleted during the artificial ageing process, the work hardening rate drops proportionally to c_3. Eq. (120) is empirical in nature; however, its implementation can be physically justified as either a reduction of the dislocation-dislocation junction strength while solutes are depleted or as a proxy for the effects of DSA when the material is plastically deformed [217]. The subscript k can be either Mg or Si as both of the solutes are inherently connected via the common-ion effect.

Finally, the strengthening from dislocation-precipitate interactions arises due to a reduction of the dislocation mean-free path when precipitates are present in the material. In this work, the method by Bardel et al. [100] is used to model this strengthening contribution. The method is adopted from the work of Esmaeili et al. [99], but adapted to account for the full particle size distribution produced by the KWN kinetics framework. The main concept behind this yield stress

model is that a fraction of the precipitates are weak and shearable, while the remaining are strong and non-shearable. The effects due to weak and strong precipitates are not identical and thus should be considered separately. In Bardel et al. [100], a quadratic summation is used to combine the strengthening from weak and strong particles

$$\left(\tau_p\right)^2 = \left(\tau_p^w\right)^2 + \left(\tau_p^s\right)^2 \quad \textbf{(121)}$$

The distinction between weak and strong precipitates is determined by the radius of the particles relative to a critical radius r_c. Though this summation is phenomenological, some justification for the use of a quadratic law can be found in the dislocation dynamic studies by Queyreau et al. [144]. For strong precipitates with $r_i \geq r_c$, the strengthening is expressed as

$$\tau_p^s = \sqrt{2}\beta G b \sqrt{\sum_{i \geq i_c} N_i l_i} \quad \textbf{(122)}$$

where β is a dislocation line tension constant that ranges between 0.2 and 0.5, G is the shear modulus of aluminum, b is the Burgers vector, and l_i is the length of precipitates associated with size class i, for all classes where $r_i \geq r_c$. On the other hand, for weak precipitates with $r_i < r_c$, the precipitate hardening is expressed as

$$\tau_p^w = \frac{\bar{F}^{\frac{3}{2}}}{b} \sqrt{\frac{\sum_{i<i_c} N_i l_i}{2\sqrt{3}\beta G b^2}} \quad \textbf{(123)}$$

where the summation is across size classes $r_i < r_c$ and $\bar{F}$ is average obstacle strength defined by

$$\bar{F} = \frac{2\beta G b^2 \sum_{i<i_c} N_i r_i}{r_c \sum_{i<i_c} N_i} \quad \textbf{(124)}$$

6.5 Simulation Results and Discussion

6.5.1 Calibration

The purpose of the precipitation kinetics simulation is to generate realistic distributions of precipitation. Naturally, this requires TEM or other atomistic tools to make a proper calibration. In this work, the experimental dataset by Kim et al. [40] was used to calibrate the kinetics model. TEM measurements of the volume fraction, length and radius of precipitates in their Al-0.65Mg-0.92Si alloy was used to determine the parameters j_0, A_0, σ and m. The calibration was conducted with a multi-objective genetic algorithm that intelligently parsed through the parameter space until a reasonable fit was achieved across the volume fraction, length and radius measurements. The complete set of parameters for the precipitation kinetics simulation is presented in Table 6-4.

Table 6-4. Summary of parameters used for precipitation kinetics simulations.

Parameter	Value
j_0 ($\mathrm{m^{-3}\ s^{-1}}$)	2.055×10^{35}
A_0	2
σ ($\mathrm{J\ m^{-2}}$)	0.17
Q_d (J)	2.16×10^{-19}
D_{Mg}^0 ($\mathrm{m^2\ s^{-1}}$)	2.2×10^{-4}
D_{Si}^0 ($\mathrm{m^2\ s^{-1}}$)	2.2×10^{-4}
v^p ($\mathrm{m^3}$)	2.13×10^{-29}
v^m ($\mathrm{m^3}$)	1.66×10^{-29}
m (nm)	0.6

The calibrated model was verified with two additional Al-Mg-Si alloys that were also examined by Kim et al. [40] with TEM. These two additional materials contain different concentrations of Mg and Si, providing useful test scenarios for the kinetics program. Fig. 6-12 illustrates the calibration and predictions compared to the experimental values for the three Al-Mg-Si alloys. The alloy used for calibration is depicted with dashed lines, while the remaining two simulations are shown in solid lines. It is observed that the kinetics model does a relatively accurate prediction of the overall kinetics process; in particular, it captures the vertical shift in the volume fraction caused by different solute concentrations. The length and radius predictions were also well within 1 standard deviation of the experimental measurements, though the variations in precipitate geometry were minimal between the three alloys.

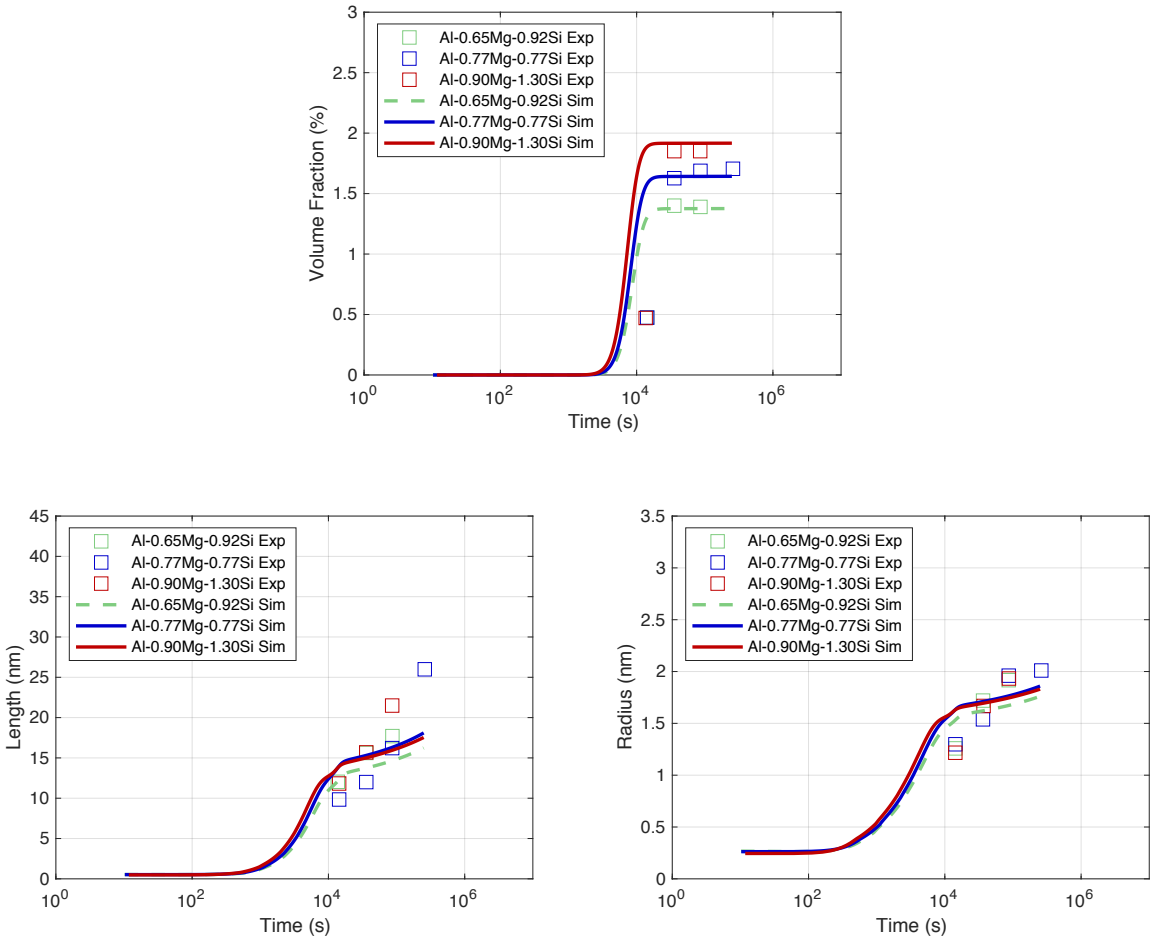

Fig. 6-12. Simulated precipitate volume fraction, length and radius for three Al-Mg-Si alloys by Kim et al. [40]. The dashed lines refer to the dataset used for calibration while solid lines are predictions.

The calibrated parameter set was further validated using two additional materials from research conducted by Du et al. [164] and Yang et al. [126]. They obtained TEM data on AA6000-series alloys that contained different chemical compositions that were aged at different temperatures. Fig. 6-13 shows the predicted volume fraction and equivalent spherical radius using the calibrated kinetics framework. The simulated volume fraction captures the general trend in the experimental values though there are some deviations in the prediction of particle radius for both materials. It should be mentioned that the variation in TEM measurements is quite large with reported standard deviations of approximately 10%. The error in the simulations are likely caused by the deficiencies in the current model that overlooks certain aspects of the artificial ageing process. For example, the current model does not distinguish between different solution-heat treatments, nor does it consider the effect of secondary solutes such as Cu and Fe, both of which can alter the final precipitate distribution and perhaps even the precipitation sequence.

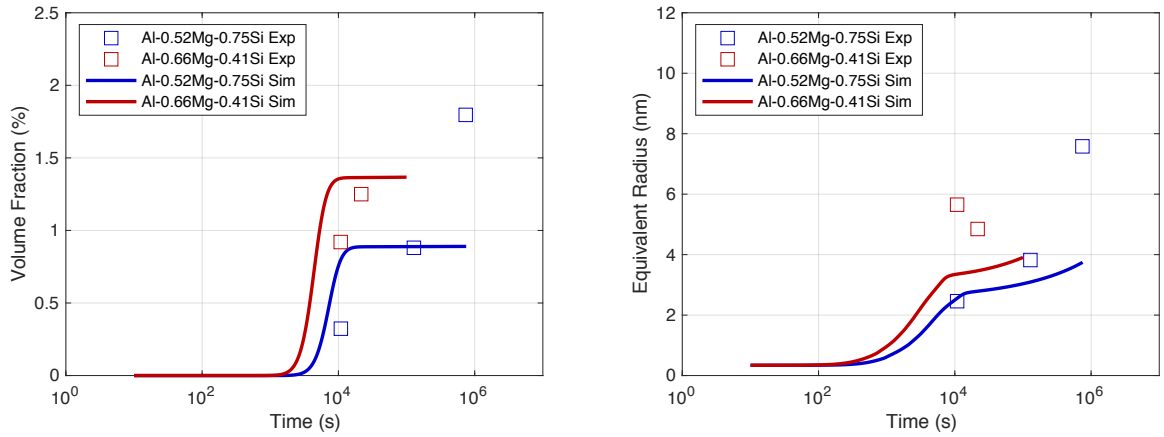

Fig. 6-13. Predicted volume fraction and equivalent precipitate radius for Al-Mg-Si alloys by Du et al. [164] (blue) and Yang et al. [126] (red).

The primary input into crystal plasticity models is a representative microstructure of the test sample. In this work, an aggregate of 2083 crystal orientations were used, which were individually weighted by their respective volume fractions. The pole figures are shown in Fig. 6-14, showing a predominant Cube texture component in the microstructure. The crystals were sampled from the entire distribution of orientations across all of the microstructures presented in Fig. 6-4. This was a reasonable sampling as the microstructure was relatively similar across different heat treatments.

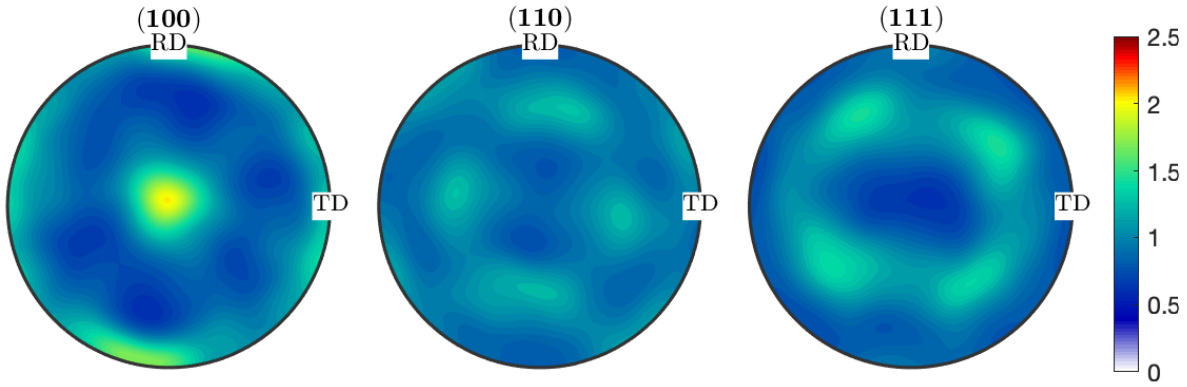

Fig. 6-14. Representative microstructure used in crystal plasticity modeling containing 2083 volume weighted orientations. Orientations were sampled from the RD-TD planes of all heat treatment conditions.

The calibrated kinetics framework was first used to generate a particle size distribution over time for the AA6061 alloy used in this work. The simulated volume fraction, mean particle length, number density and particle size distributions for AA6061 are shown in Fig. 6-15. The crystal plasticity model calibration was then conducted with the use of the AQ, 6h and 48h tempers specifically to sample from the under-aged, peak-aged and over-aged regimes of the ageing profile. The parameters in the model were determined by capturing the best fit of the stress-strain curves across all three heat treatments. Fig. 6-16 presents the calibrated stress-strain responses after achieving an excellent fit for both the yield strength and work hardening. The ability to capture the mechanical differences between the three stress-strain curves is promising as it provides confidence in the new hardening equation defined in Eq. (120). It should be mentioned that the interaction strength between matrix and precipitates was also calibrated simultaneously with the aid of a cyclic shear test at the 6h condition. The complete set of parameters used in the crystal plasticity modeling is presented in Table 6-5. The elastic properties used for the precipitate are shown in Table 5-4 from the previous chapter.

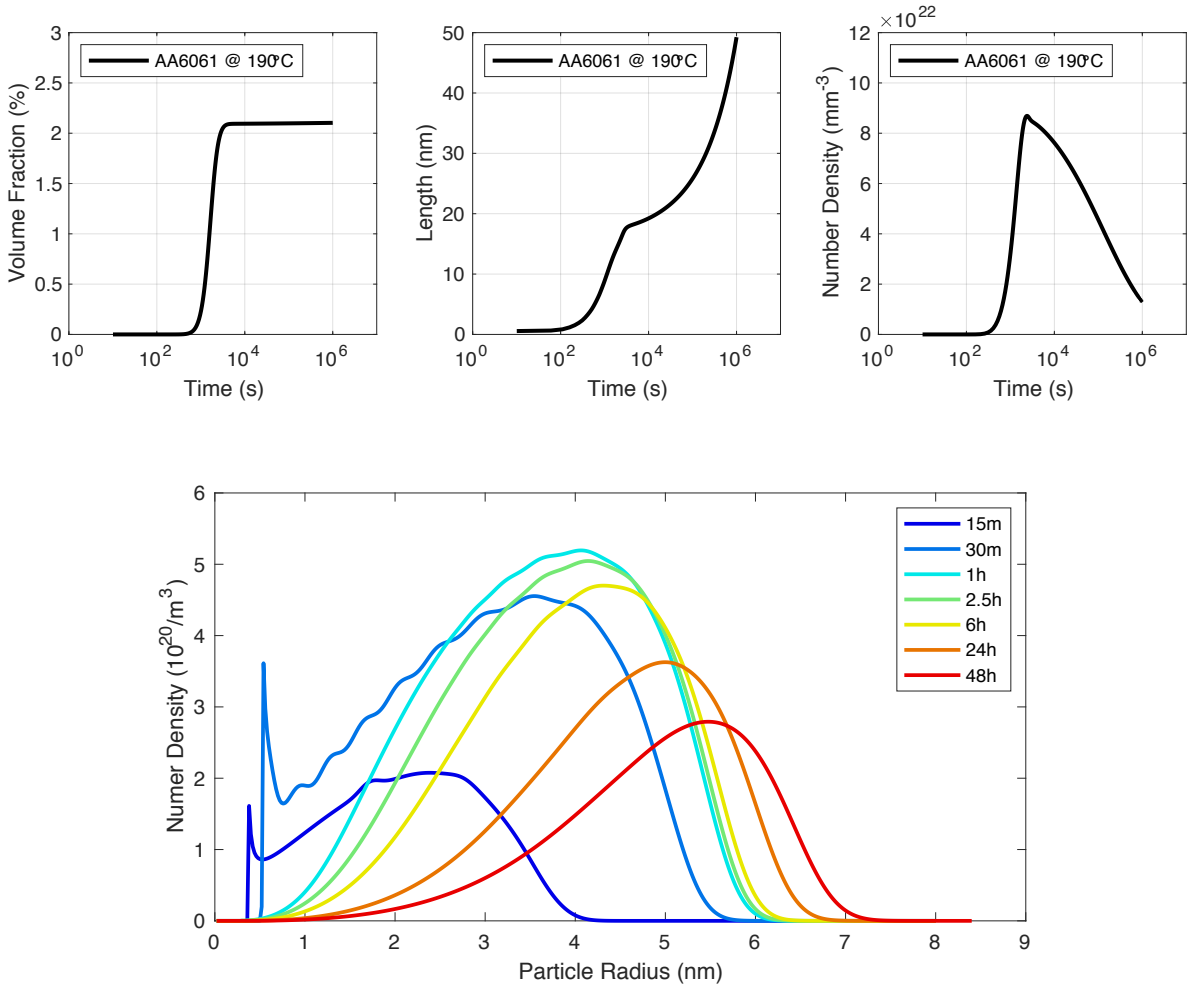

Fig. 6-15. Simulated volume fraction, average particle length, average number density, and particle size (equivalent radius) distribution over time for artificially aged AA6061 at 190°C.

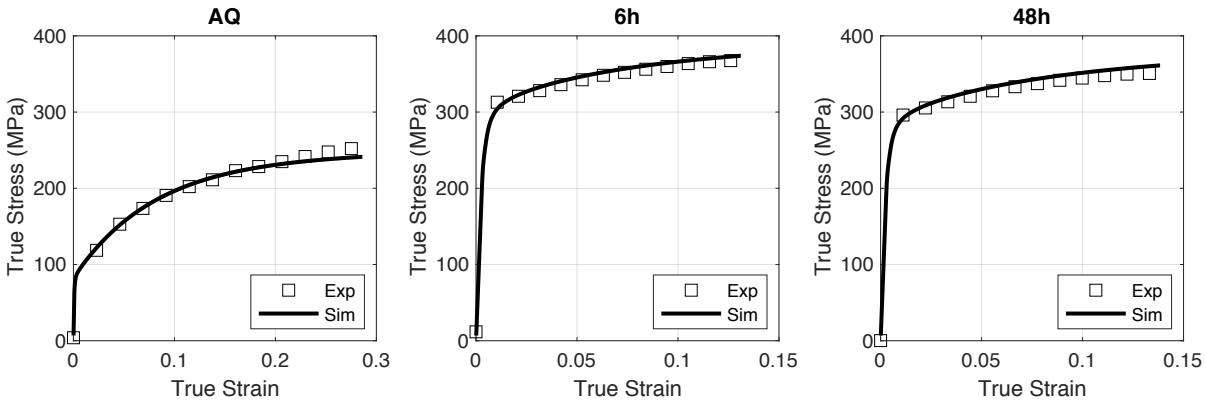

Fig. 6-16. Calibrated stress-strain curves for as-quenched, 6 hour and 48 hour aged samples.

Table 6-5. Summary of parameters used for crystal plasticity simulations.

Parameter	Value
c_{11} (GPa)	103.350
c_{12} (GPa)	51.675
c_{44} (GPa)	25.840
$\dot{\gamma}_0$ (s^{-1})	0.001
m	0.01
τ_0 (MPa)	3
r_c (nm)	3.4
β	0.265
κ	0.3
k_{Mg} (MPa at%$^{-2/3}$)	8.7246
k_{Si} (MPa at%$^{-2/3}$)	21.975
c_0	55
c_2	8.5
c_3	0.035
n_e	2

6.5.2 Evaluation

The full set of simulated stress-strain curves are presented in Fig. 6-17 for uniaxial tension in RD, DD and TD as well as for monotonic shear in RD. With the exception of the 15m tests, the predicted values in uniaxial tension are in good agreement with the experiments, even across the DD and TD directions. As briefly discussed earlier, the large deviations in the DD and TD tests of the 15m samples is possibly due to experimental error rather deficiencies in the simulation. This is more likely now as the 15m simulation in forward shear is in good agreement with the experiment. Overall, the shear simulations are in excellent agreement with the experiments up to a large shear strain of 50%. These results provide additional support for the

use of crystal plasticity since phenomenological constitutive models cannot typically capture the texture rotations involved in simple shear loading [229].

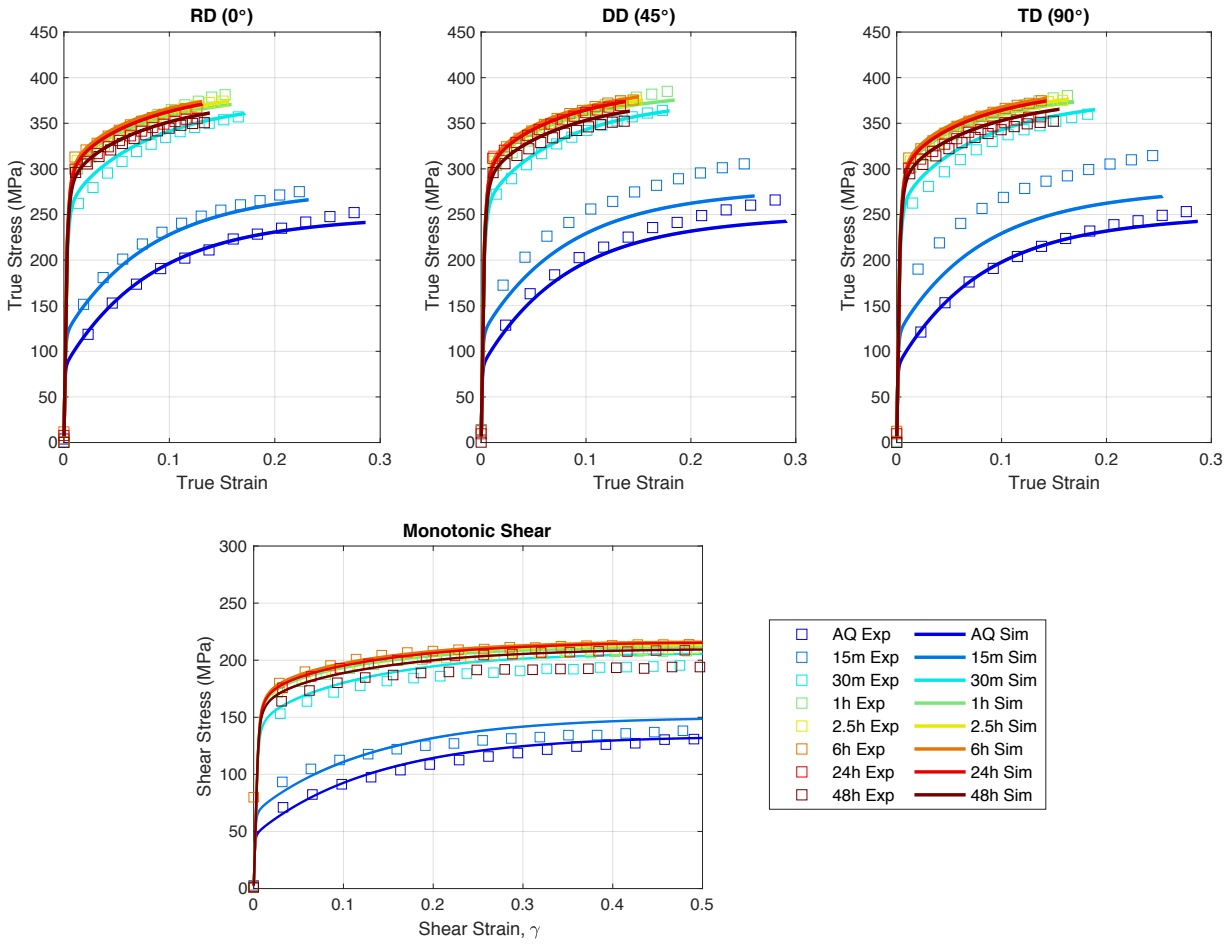

Fig. 6-17. Simulation of stress-strain curves across all heat treatments for uniaxial tension in RD, DD and TD, as well as for monotonic forward shear.

Fig. 6-18 presents the R-value calculations performed by the crystal plasticity model. The results are overall in good agreement with the experimental R-value variations presented in Fig. 6-8; however, the magnitudes of the R-values from the model are slightly higher. It should be mentioned that all simulations in the DD and TD orientations are directly as a result of the crystallographic texture input into the model since only experiments from the RD direction were used for calibration. A possible reason for the higher R-values may be due to the sampling of orientations used for the crystal plasticity calculations, which was kept constant across all heat treatments. It is also worth mentioning that the strains were measured over an area of interest of 12.5 mm length, whereas the EBSDs were sampled over a much smaller region. It is observed

that the material has a slight but consistent evolution towards isotropy with longer durations of artificial ageing. This trend is shown in both the 2% and 10% plastic strain simulations and continues to persist at even larger deformations. The results are in line with previous simulations from Chapter 5, as well as with other research on Al-Cu and Al-Zn precipitation hardening alloys [65, 106, 141, 189]. In addition, the simulated yield stress evolution is presented in Fig. 6-19 where the yield stress is normalized with respect to TD for each heat treatment. Compared to the experimental results in Fig. 6-7, the predicted yield stress variation is essentially isotropic at both 2% and 10% plastic strain.

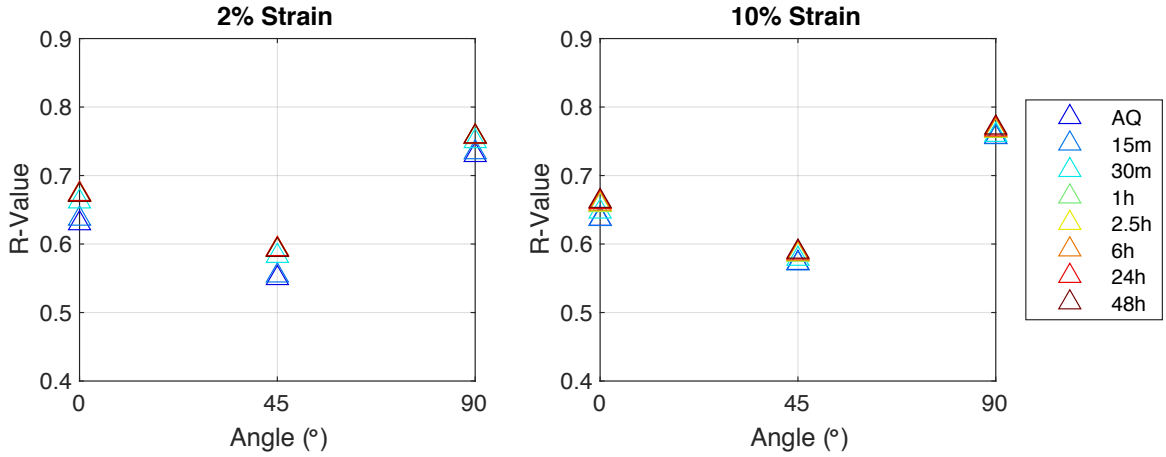

Fig. 6-18. Simulated R-value variation across all heat treatments at 2% and 10% plastic strain.

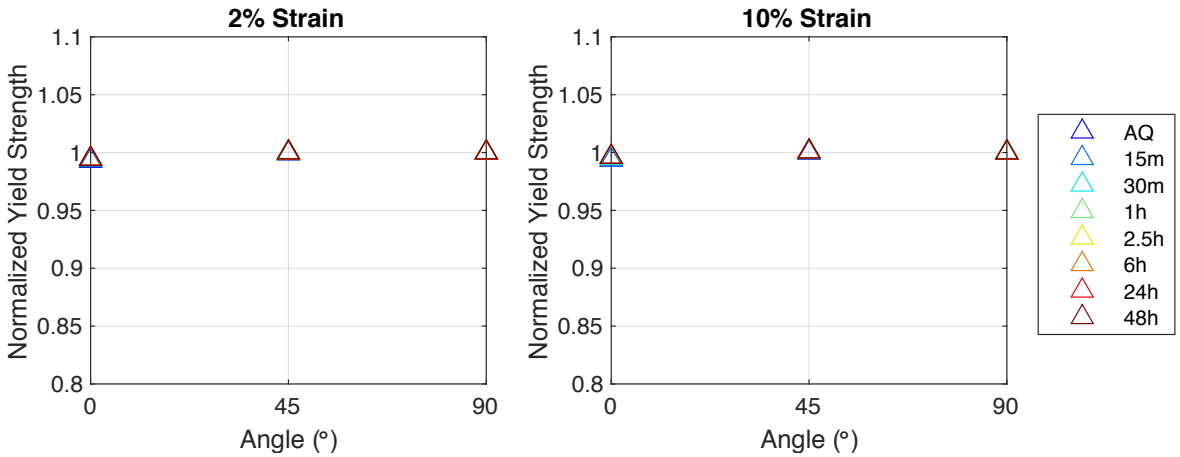

Fig. 6-19. Simulated yield stress variation across all heat treatments at 2% and 10% plastic strain.

Fig. 6-20 presents the cyclic FRF shear predictions from the simulation framework in comparison with experimental characterization of AA6061. Each subplot shows the 3%, 6% and

9% FRF tests at a specific heat treatment condition. Overall, the stress-strain curves are captured with excellent agreement, with the greatest errors seen in the AQ and under-aged simulations. The simulation of the Bauschinger effect is often overlooked in the existing literature due to the complexity associated with modeling kinematic hardening. In the current work, this effect is captured because the particles are able to deform within each single crystal. When the crystal is subject to an external load, the inclusions share a portion of the load. Then when the material undergoes a strain reversal, the stress inside the inclusions is released, resulting in the manifestation of the Bauschinger effect in the stress-strain curve. The schematic presented in Fig. 5-21 of the previous chapter illustrates the Bauschinger phenomenon in more detail. As observed in Fig. 6-21, a regular crystal plasticity code cannot capture this Bauschinger effect when calibrated to the same forward shear curve and with the same crystallographic texture. The regular model predicts an overly stiff response upon reloading, which although comparatively minor, can still influence the placement and initiation of localization during large plastic deformation [38, 225].

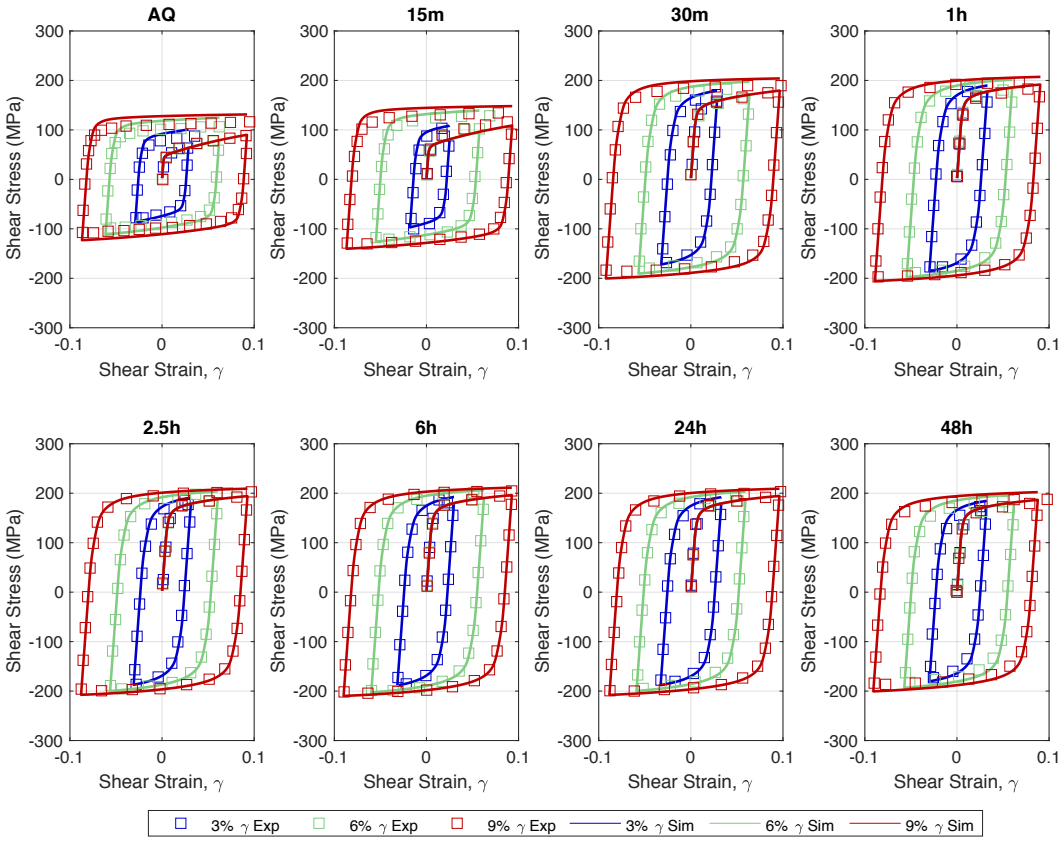

Fig. 6-20. Simulated cyclic shear compared to experiments across all heat treatment conditions.

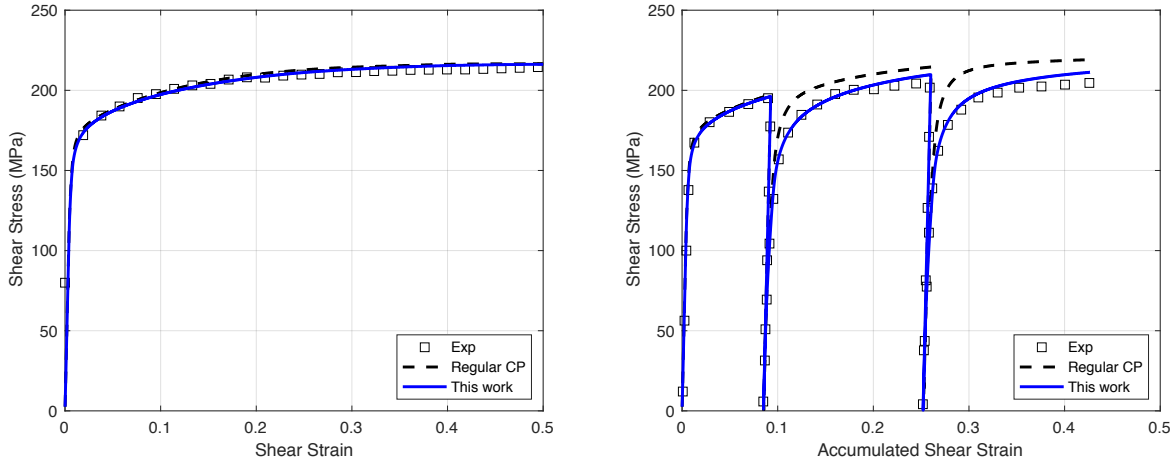

Fig. 6-21. Forward and cyclic shear stress-strain curves generated with regular crystal plasticity and modified precipitation hardening crystal plasticity. Experiments and simulations shown for the 6h heat treatment condition.

A more detailed representation of the Bauschinger effect is seen in Fig. 6-22 that shows the absolute stress-strain plots for both the monotonic and cyclic shear simulations. The stresses are normalized to the yield strength in each respective ageing condition to make the curves comparable across different tempers. It is observed that materials aged for a longer duration have a higher degree of Bauschinger effect, as seen by the difference between the forward shear curve and reverse shear curves after reloading. In the as-quenched and under-aged materials, the alloys almost immediately return to their original yield strength and hardening rate following the strain reversal. However, it takes much longer for the peak-aged and over-aged conditions to return to their pre-reversal levels. The testing of other AA6000-series alloys also show similar evolutions of backstress [188, 230].

The differences in backstress can be explained in the model as variations in the volume fraction and size of precipitates. When the alloy is under-aged, the volume fraction of precipitates is low, and the precipitates are generally close to spherical. Due to these properties, less strain is partitioned into the precipitate phases and thus the precipitates do not contribute substantially to the backstress in the model. As the material is aged for a longer duration, the volume fraction increases to a saturation value while the precipitates also become increasingly elongated. Both effects contribute to a larger backstress as more strain is partitioned into the precipitates in the homogenization scheme. The model suggests that an inclusion-based approach such as the one used here is only necessary for alloys that are aged to near peak-strength

condition. Due to the low volume fractions of precipitate in under-aged materials, the micromechanics framework does not provide any significant contribution to the stress-strain behavior and thus has a negligible effect on kinematic hardening.

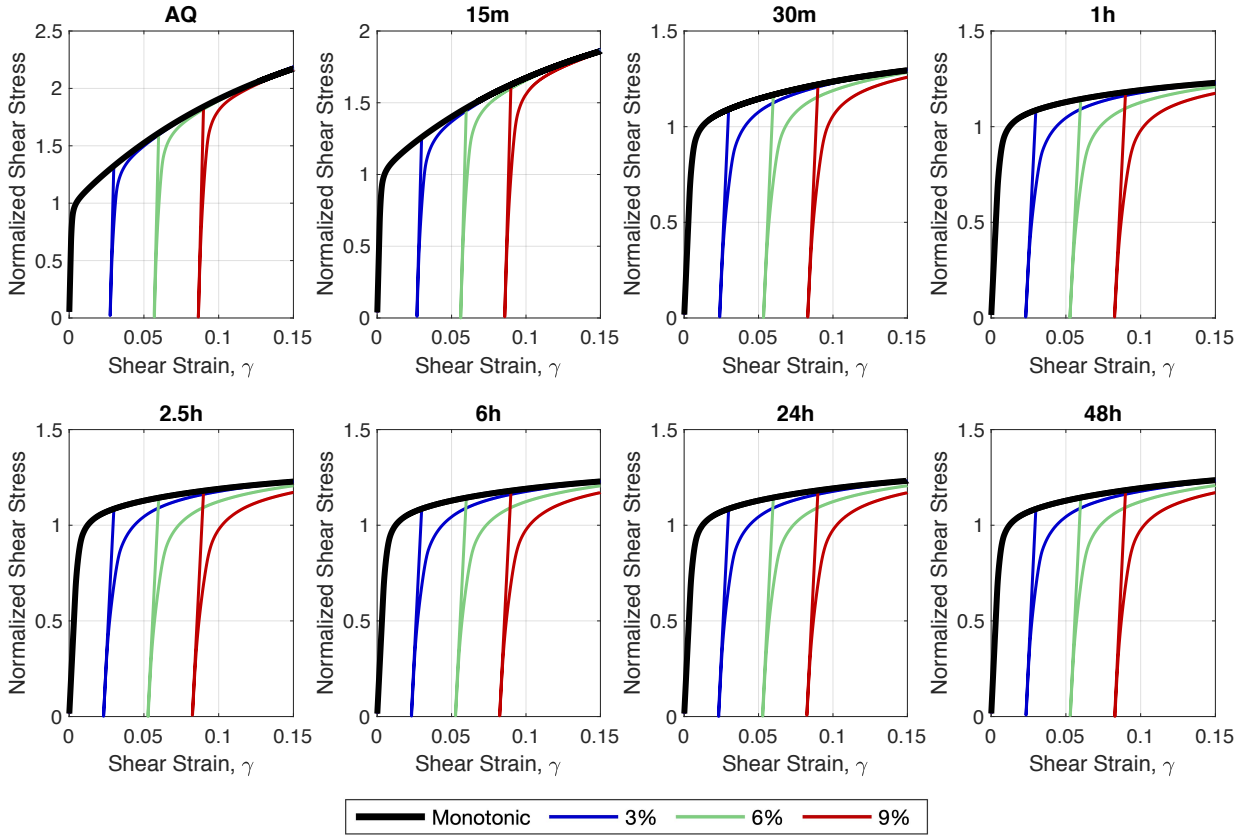

Fig. 6-22. Simulated monotonic and cyclic shear stress-strain curves for all heat treatments. The stress is normalized to the yield strength of each heat treatment.

6.5.3 Single Crystal Simulations

A subsequent set of simulations was also performed using the single crystal orientations that were formerly defined in Table 2-2. The investigation here is similar to the previous study in Chapter 5.5.1; however, the current work improves on this investigation by introducing more realistic heat treatment parameters into the single crystal simulations. In particular, there are additional effects due to solute concentration, which would affect the work hardening behavior across artificial ageing conditions. The yield strength is also free to change in this study while it was fixed in the prior one. These physics were not considered in Chapter 5 as the precipitation kinetics model had not been implemented at the time.

The single crystal R-values are shown in Fig. 6-23 and the yield stress variations in Fig. 6-24. Each column corresponds to a different crystal orientation, while each row corresponds to a specific level of plastic strain. It should be mentioned that these results are purely theoretical and that no single crystal experiments were performed for the study. One can observe that the effect of heat treatments is more noticeable at the single crystal level compared to the polycrystal results of Fig. 6-18 and Fig. 6-19. By analyzing the R-value simulations, it is possible to see a transition towards isotropy with longer durations of artificial ageing at all magnitudes of plastic strain. This behavior is reflected in the polycrystalline results of Fig. 6-18, which also shows a general reduction of anisotropy with longer ageing times. The relatively weaker effects of precipitation observed in the polycrystal is likely due to the fact that the texture is predominantly composed of Cube, which appears to be somewhat unaffected by artificial ageing. What is interesting to observe in the single crystal study is the evolution of the R-values as a function of plastic strain: the R-values for Cube texture appears to be fairly consistent for all heat treatments and across all plastic strain values; the Goss component shows a steady increase in R-values with plastic strain; the R-values of Copper seem to rapidly increase during the early stages of deformation before falling into a steady decline; the R-values for Brass increase in the under-aged regime and decrease in the peak and over-aged regimes. These effects are not particularly noticeable in the polycrystal response due to the cancelling effects of different crystal orientations. As explained in the previous work, the responses caused by the precipitates for different single crystals are due to the additional mode of deformation introduced by the inclusion-based approach. Since precipitates are aligned to specific axes of each crystal orientation, the precipitate response will also differ between grains of different orientations. For the orientations examined here, it appears that the precipitate enables more thinning (z-axis strain) for crystals that are normally stiff, which reduces the overall anisotropy experienced by the alloy. Similar conclusions have been found by other authors using different methods of analysis [189, 231].

The simulations of yield stress variation show a similar response where the behavior at the single crystal level is more apparent than the polycrystal response. There is a reduction in the plastic anisotropy of flow stress with increased artificial ageing as demonstrated by the gradual progression of stress values towards unity. This is a striking observation because the polycrystalline results of Fig. 6-19 are essentially isotropic at all levels of artificial ageing. This

shows that the effect of artificial ageing is basically cancelled out due to the presence of other crystal orientations and suggests that crystallographic texture dominates over the precipitate hardening response.

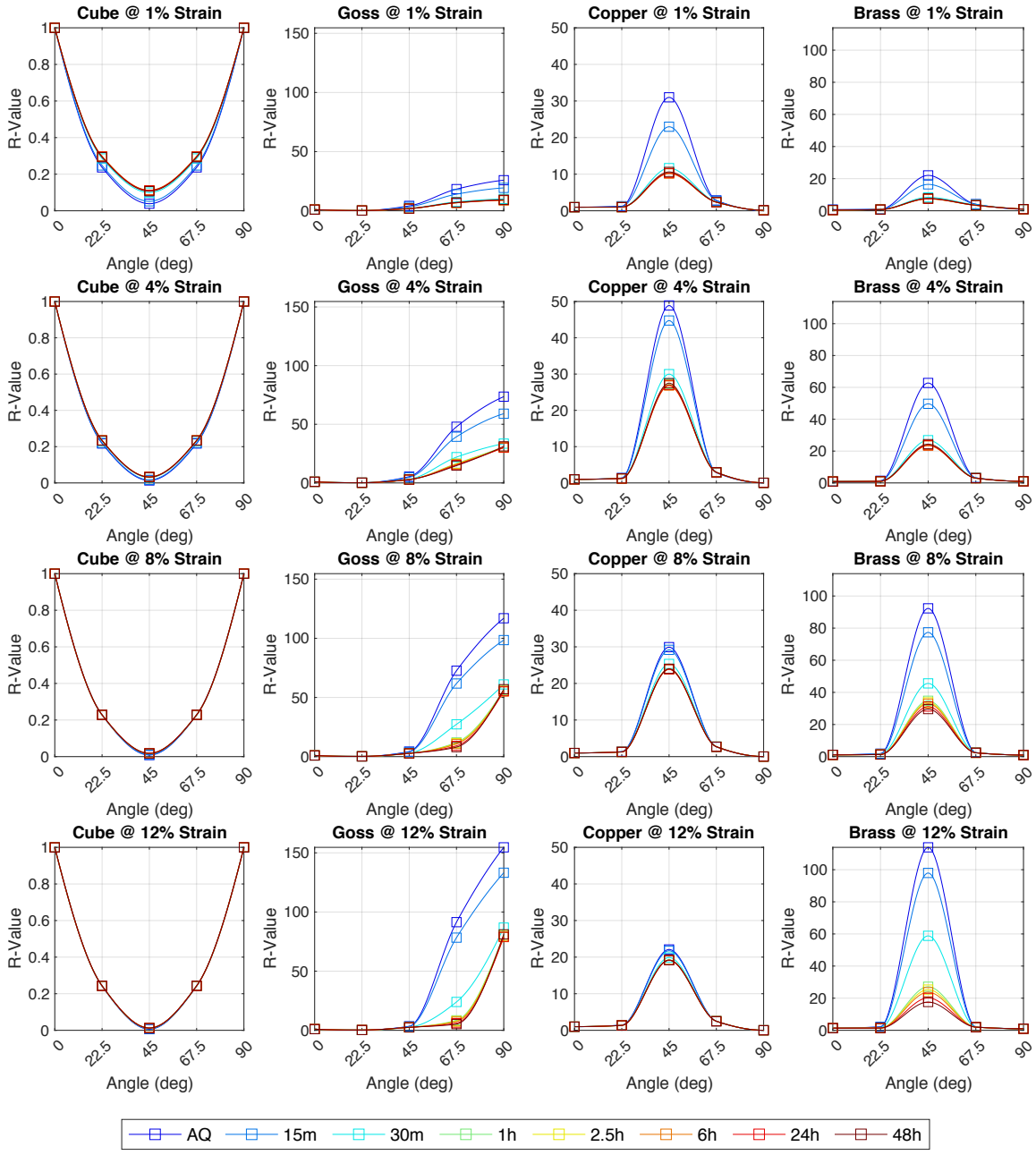

Fig. 6-23. R-value variation of common single crystal orientations at varying degrees of heat treatment and plastic strain.

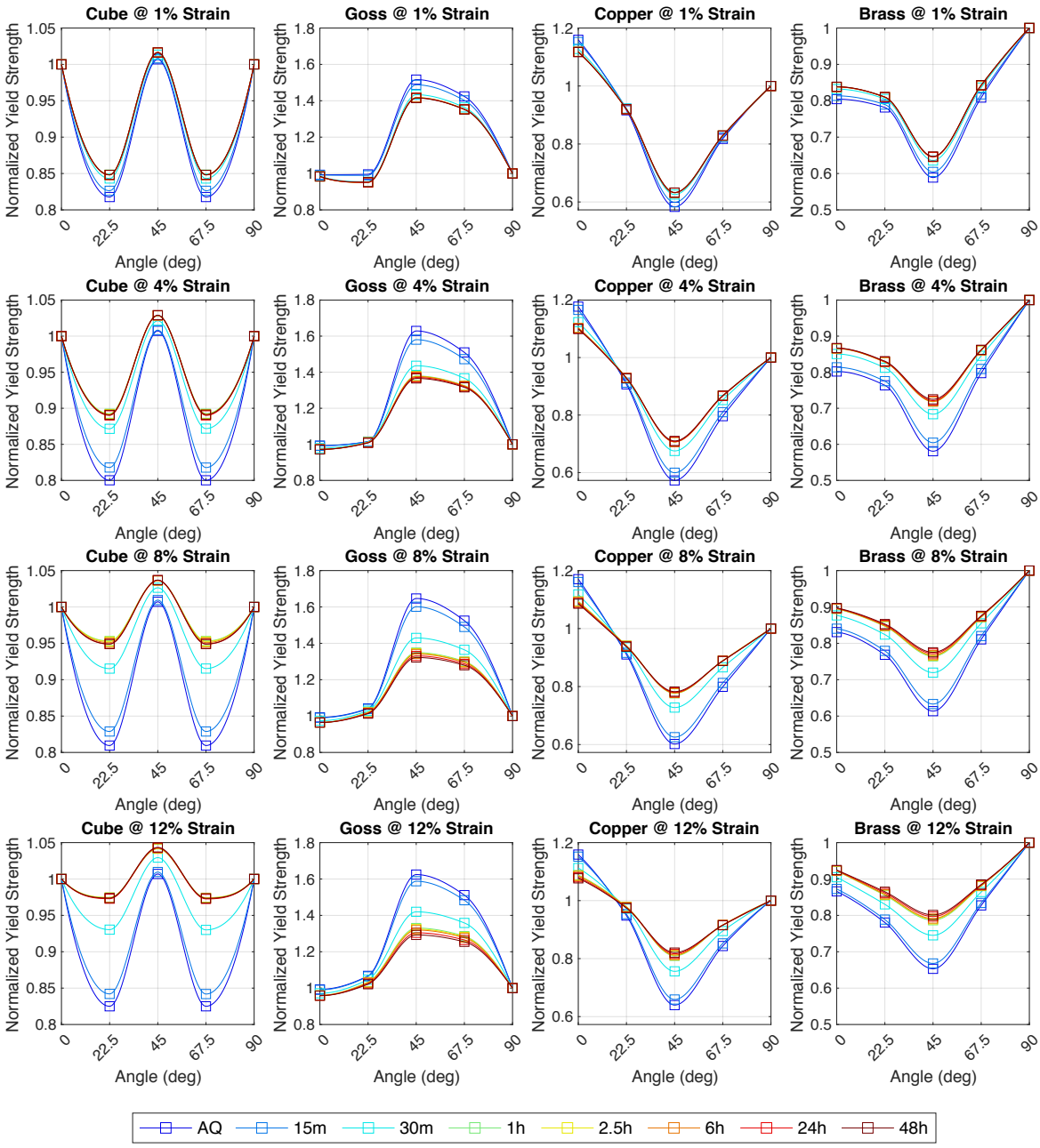

Fig. 6-24. Yield stress variation of common single crystal orientations at varying degrees of heat treatment and plastic strain.

6.5.4 Effect of Mg and Si Concentration

Lastly, to demonstrate the strength of the model, the initial Mg and Si solute concentrations were adjusted to investigate their effects on the material's properties. For brevity, only two additional scenarios were studied: the first scenario with double the Mg and Si concentrations and the second with half the Mg and Si concentrations. All simulations were performed at an artificial ageing temperature of 190°C with the crystallographic texture shown in Fig. 6-14. The results were compared to the results for the base case, defined by the nominal concentrations in Table 6-1. All of the remaining parameters have the same values as those found through the initial calibration.

The properties of the precipitate distribution are first presented in Fig. 6-25, which were generated using the precipitation kinetics simulation. It is observed that a doubling or halving of the initial solute concentration resulted in the direct doubling or halving of the saturation volume fraction. The average length and number density of the precipitates were also increased and decreased respectively for the double and half simulations, though in non-linear proportions. It is interesting to note that even though the volume fraction was altered by a factor of two, the length of the precipitates remained relatively similar across all instances. This suggests that solute concentration has a large effect on the quantity of precipitates, but the evolution of their morphology maybe dominated by other factors. What is also important to note is that a higher solute concentration resulted in an overall faster artificial ageing response, where the state of maximum number density and volume fraction was achieved at an earlier ageing duration.

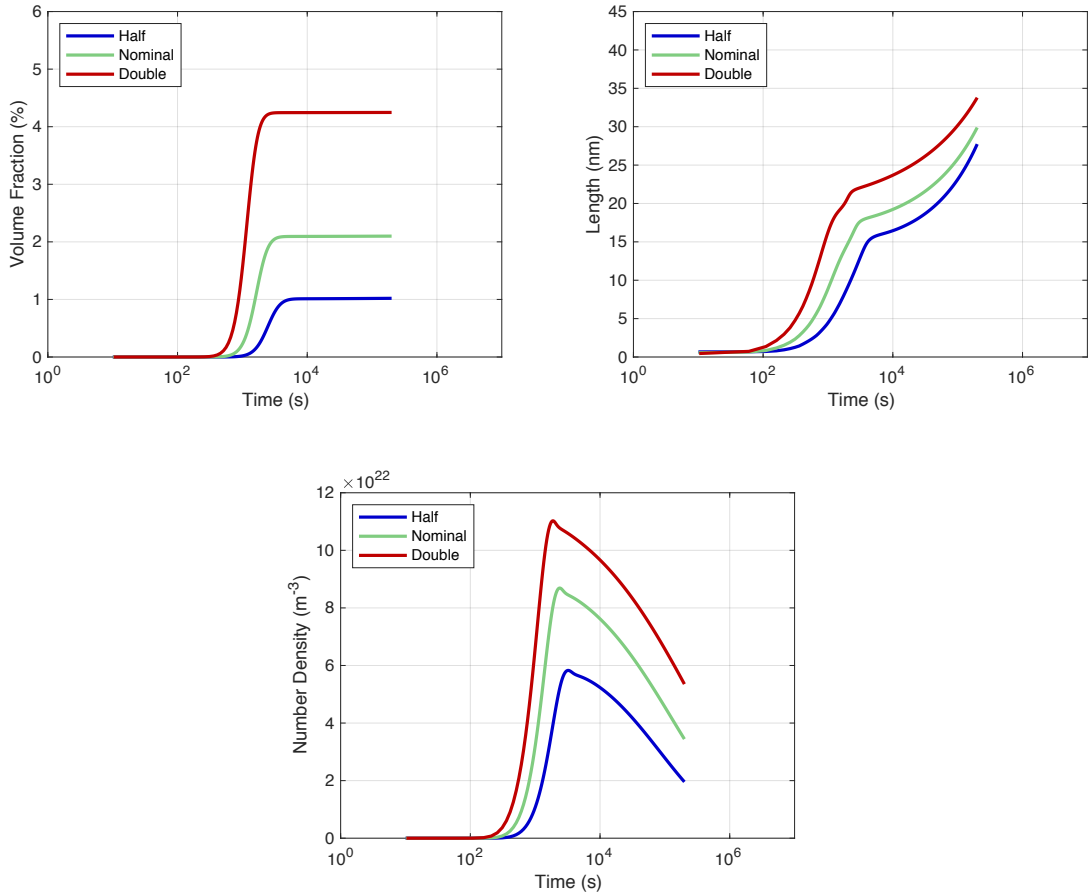

Fig. 6-25. Predicted volume fraction, length and number density curves for the nominal-solute, double-solute and half-solute simulations.

The results from the artificial ageing simulations are important as they highlight the changes that the subsequent crystal plasticity calculations rely upon. Fig. 6-26 presents the yield strength curves for the three alloy concentrations calculated using the crystal plasticity model. Only the results for the as-quenched, 15 min, 30 min, 1 hour, 2.5 hour, 6 hour, 24 hour, and 48 hour simulations were plotted, following the same heat treatment schedule presented earlier in this work. The as-quenched results were plotted at a simulation time of 10^1 seconds for reference. As expected, there is a noticeable increase in yield strength with increasing solute concentrations at all durations of artificial ageing. This increase appears to be proportional to the change in precipitate number density presented in Fig. 6-25.

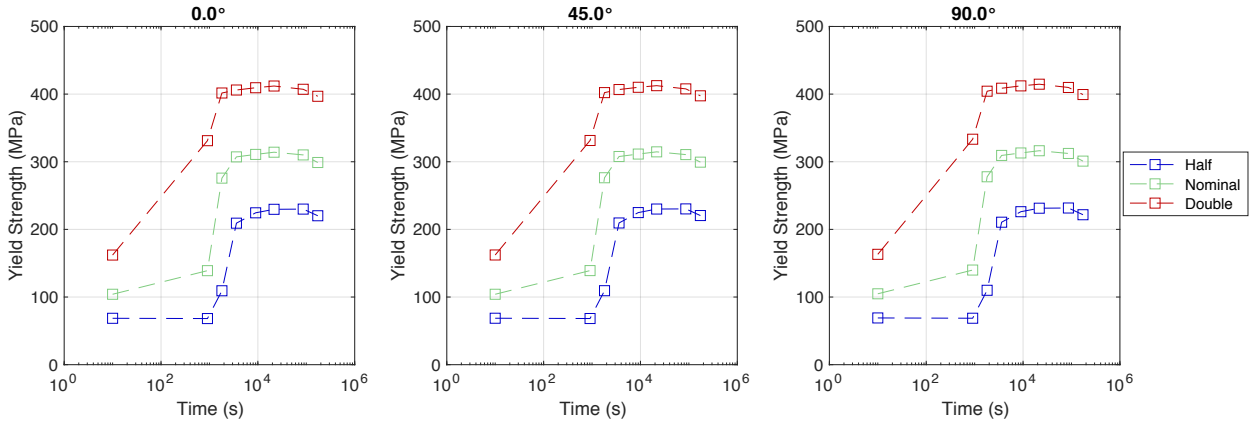

Fig. 6-26. Predicted yield strength evolution across time for the nominal-solute, double-solute and half-solute simulations.

From an initial observation, the effect of solute concentration is rather uniform across RD, DD and TD. However, further inspection at different strain levels shows that higher solute concentrations resulted in a generally lower level of anisotropy. These results are presented in Fig. 6-27 and Fig. 6-28 for the yield strengths and R-values, respectively. Each row reflects the results after a particular duration of artificial ageing while each column refers to a different plastic strain state. From the yield strength plots, the 2.5h and 48h simulations at 8% and 12% strain with double the solute concentration demonstrated an inverse behavior compared to the nominal and half simulations. This is interesting as it suggests a possible inflection point in the yield strength variation for certain grains caused by the addition of solute. However, these results are not convincing of any general behavior as the yield strengths are all within 1% of the RD stress. Inspection of the R-values shows a slightly larger effect, where higher solute concentrations resulted in a lowering of the strain ratio, especially in TD. This drop is likely a result of the Goss texture component, which had significant reductions in R-value with the extent of artificial ageing – see Fig. 6-23. Since the doubling of initial solute concentration resulted in a doubling of the precipitate volume fraction, it would be expected that the Goss texture component would face even stronger reductions in material anisotropy that is subsequently reflected in the polycrystalline response. Nonetheless, the effect of solute concentration appears to be rather minor in both the yield strength and R-value responses. This again suggests that the overall texture plays a much larger role in the anisotropic response.

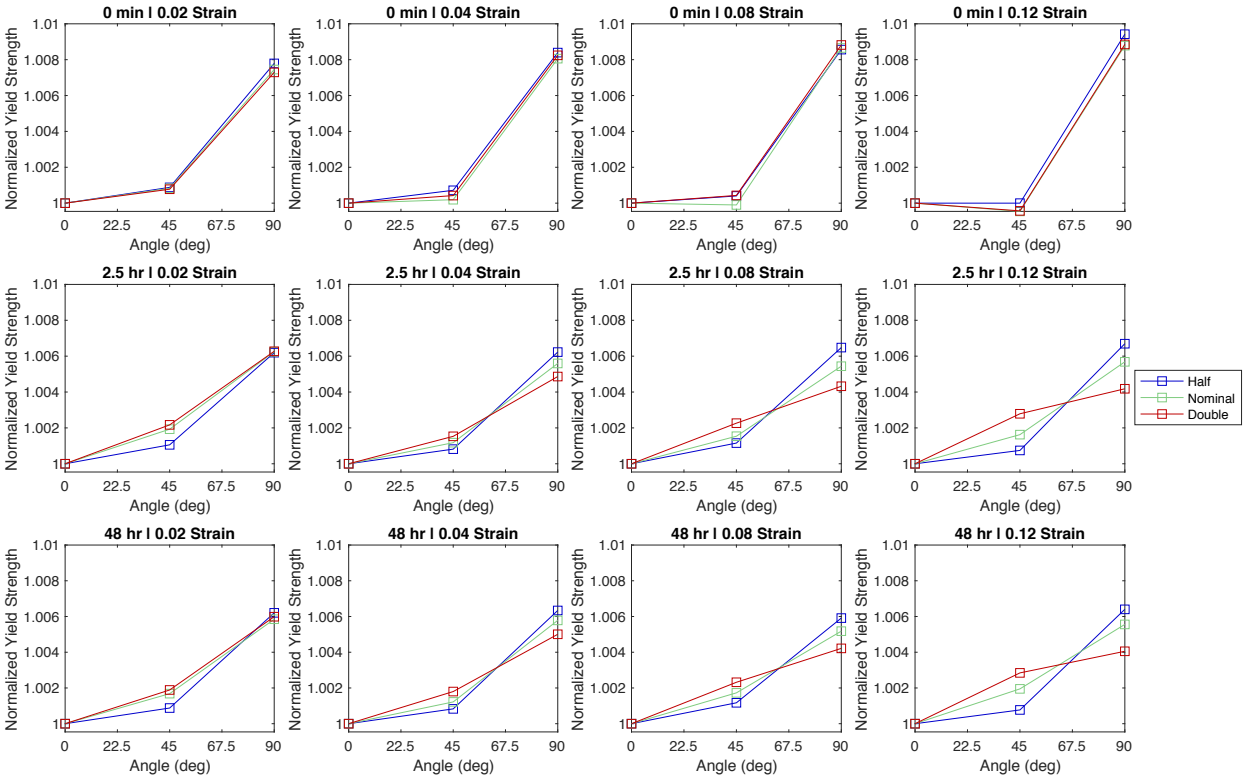

Fig. 6-27. Simulated normalized yield strength behavior across different plastic strain levels for the AQ, 2.5h and 48h samples with different initial solute concentrations.

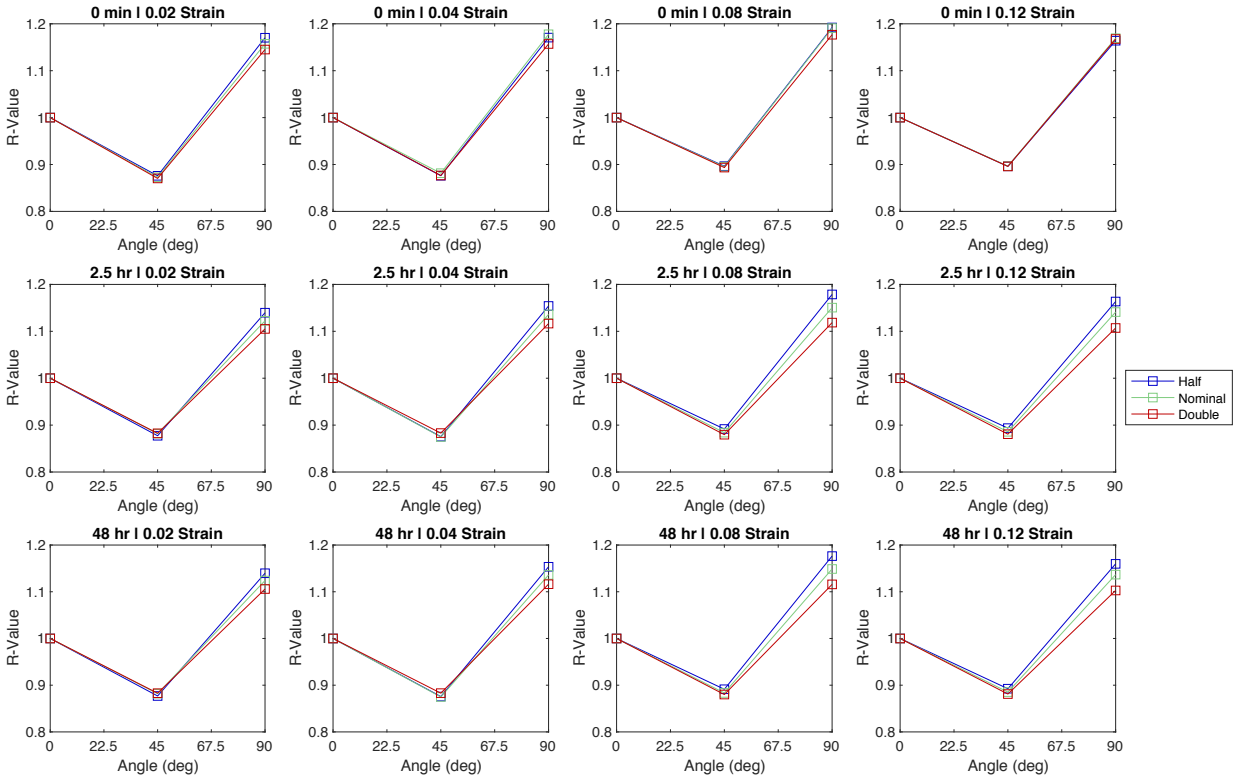

Fig. 6-28. Simulated R-value behavior across different plastic strain levels for the AQ, 2.5h and 48h samples with different initial solute concentrations.

6.6 Chapter Conclusions

This work presented a computational framework for modeling precipitation kinetics and plasticity in AA6000-series alloys. The kinetics model was based on the KWN method, which generated the precipitate size distribution over time for a given alloy composition, temperature and ageing time input. The results from the kinetics model were subsequently used for the simulation of the alloy's mechanical response with a modified crystal plasticity constitutive model. The complete numerical framework was calibrated using mechanical test data of an AA6061 alloy that was artificially aged to various tempers, as well as TEM data for a similar AA6000-series alloy from Kim et al. [40]. The model showed excellent capabilities in capturing the precipitation kinetics of several Al-Mg-Si alloys and was able to reasonably match the yield strength, work hardening, Bauschinger effect and plastic anisotropy of the tested AA6061 material. Conclusions about the experiments and simulations are summarized as follows:

1. The microstructure of AA6061 remained relatively constant over long periods of artificial ageing at 190°C. Only a slight increase in grain size was observed, which suggests minor degrees of recrystallization during the heat treatment process.
2. The change in work hardening across different heat treatments of AA6061 was observed to be a result of changes to the initial work hardening rate rather than changes to dynamic recovery. This effect was captured using a modified dislocation density hardening model where the dislocation multiplication parameter was varied based on the amount of Mg and Si solute remaining in the supersaturated matrix.
3. A slight reduction in material anisotropy was observed for AA6061 with increasing durations of artificial ageing. This was demonstrated as a gradual progression towards an R-value variation of unity during uniaxial tension testing. However, the flow stress was observed to be rather isotropic across RD, DD and TD.
4. There was a consistent increase in the magnitude of the Bauschinger effect with artificial ageing, even in the over-aged regime. This effect was well captured by an inclusion-based precipitation model. The lower degree of kinematic hardening found in under-aged samples was captured due to the lower volume fractions of precipitate in the under-aged regime. The stronger Bauschinger effect found in peak and over-aged samples were captured by the overall higher precipitate volume fractions that enabled the particles to accumulate and release a substantial portion of the total stress.
5. Theoretical simulations of individual single crystals showed that common FCC orientations exhibited substantial reductions in plastic anisotropy. However, many of these effects were not observed in the polycrystal simulations. This analytical investigation suggests that crystallographic texture dominates over the precipitate hardening response.

7 Conclusions and Future Work

The objective of this thesis was to develop a simulation framework to capture the physical properties of precipitation hardened aluminum alloys. Accordingly, in Chapter 5, a new crystal plasticity based constitutive model was developed to simulate the precipitation hardening behavior of AA6060. The precipitation effect was captured via the combination of a precipitate-dislocation strengthening law and an Eshelby inclusion homogenization scheme. The strengthening law was used to predict the isotropic component of hardening while the inclusion method was used to predict the kinematic component. The model was subsequently utilized to investigate the behavior of common FCC single crystal orientations under various precipitation states. In Chapter 6, the crystal plasticity framework was then extended to incorporate the effect of solute on the yield and work hardening behaviors. At the same time, a precipitation kinetics model was introduced to generate realistic precipitate distributions for various heat treatment conditions. The precipitation model was based on classical nucleation and growth theory, with slight modifications to predict the morphological evolution of the precipitates. The combined kinetics and plasticity framework was utilized to simulate the properties for an AA6061 sheet alloy. The framework demonstrated the ability to relate the yield strength, work hardening, plastic anisotropy and Bauschinger effect to the parameters of the initial heat treatment. Key conclusions from this research are provided in the following sections.

7.1 A New Crystal Plasticity Constitutive Model for Simulating Precipitation-Hardenable Aluminum Alloys

- Incorporating the precipitates along the <100> lattice directions allowed a crystal plasticity model to capture the reduction in plastic anisotropy expected in AA6000-series aluminum alloys.
- The precipitation hardening mechanism affected the R-value variation much more than the yield stress variation, as observed from single crystal simulations of Cube, Goss, Copper and Brass.
- Spherical precipitates did not affect the stress-strain response to any large degree relative to the non-precipitation hardened state.
- The Bauschinger effect was captured via the generation of internal stresses between the matrix and precipitate phases.

7.2 Precipitation Kinetics and Crystal Plasticity Modeling of Artificially Aged AA6061

- The work hardening behavior of AA6061 was observed to change with artificial ageing due to differences in the dislocation generation mechanism.
- This effect was incorporated into the previously developed constitutive model by relating the dislocation generation rate to the concentration of solutes in the matrix.
- A reduction in material anisotropy was observed for AA6061 with increasing duration of artificial ageing. This was more prevalent in the alloy's R-value variation than the flow stress variation.
- A consistent increase in the magnitude of the Bauschinger effect was observed with longer durations of artificial ageing. This effect was captured by the model via the loading and unloading of the precipitate phase.
- Simulations of individual single crystals exhibited substantial reductions in plastic anisotropy. However, these effects were not observed in the polycrystal simulations, which suggests that crystallographic texture dominates over the precipitate hardening response.

7.3 Advantages of the Simulation Framework

The key contribution from this work is the incorporation of precipitates as an explicit phase in single crystal plasticity modeling. This is advantageous since both the morphology and orientation-dependence of the precipitates are captured with the current approach. The homogenization used to simulate the precipitate effect has provided a multi-scaling between the micro and nano length scales. As demonstrated using a series of theoretical studies, the model can directly simulate the effect of precipitation on the single crystal response, which can be further extrapolated using a polycrystal scheme to obtain bulk material properties. This is a considerable advantage as these results can be directly compared to single and polycrystal experiments for validation. Furthermore, the model does not rely on direct simulation of the precipitate, such as with dislocation dynamics or molecular dynamics. Instead, it is implemented at a continuum level, which is advantageous from both an implementation and computational point of view. This allows the model to be easily incorporated within FEM frameworks that are already used ubiquitously throughout the industry.

The addition of a precipitation kinetics model allows the framework to simulate an alloy from the initial heat treatment all the way to its large deformation properties. This bridge between the process and the resultant properties has many applications in industrial settings. For instance, alloys of specific chemical compositions can be simulated prior to fabrication, which can improve the speed of research and development tremendously. Furthermore, the framework can also be used to maximize specific properties, such as yield strength, with respect to composition or temperature. Implementation of the kinetics model with CPFEM can provide additional details about the formability of the alloy under a given heat treatment and strain path. To the author's knowledge, there are no other integrated computational materials engineering (ICME) researches that relate the heat treatment to anisotropy, Bauschinger effect, or localization.

7.4 Limitations of the Simulation Framework

Despite the excellent agreement between the simulations and experiments presented in this thesis, there are certain limitations to the numerical framework that is worth mentioning. First, the precipitation kinetics model requires TEM for a proper calibration of the model. Naturally, this can be problematic as TEM is often subject to considerable sampling error as well as other artifacts that cannot be captured by the model [27, 36, 39]. For the imaging of precipitates, it is good practice to prepare several samples at different regions of a material to obtain a representative characterization of the precipitates' features. However, this can become very costly as TEM imaging requires a considerable amount of time for sample preparation.

There are also several limitations in using a classical nucleation and growth model due to the underlying assumptions used to develop the theory. First, CNGT is relatively sensitive to the parameters used in the model and in particular the interface energy σ that governs the Gibbs free energy change for nucleation. Due to the lack of experimental support for this parameter, σ is typically treated as a calibration parameter. Second, the evolution of the stoichiometry of precipitates is entirely ignored in CNGT models. This is a limitation as the precipitate composition is a strong driver for the growth rate of particles. While there are implementations that can account for the simultaneous nucleation and growth of several phases, the transition between phases is still a difficult phenomenon to capture [94, 154, 163].

There are similar limitations in the proposed crystal plasticity model that can hinder its effectiveness. First, the model assumes that plasticity is driven by the single mechanism of

crystallographic slip. This was not exactly problematic for the research conducted here; however, the model would require substantial improvements to capture other deformation mechanisms including those caused by temperature [55], dynamic precipitation [218], dislocation cell formation [232] or any other phenomena active in precipitation hardening alloys. Furthermore, the fidelity of crystal plasticity calculations is largely dependent on the microstructural input used in the model. In this work, the microstructure appeared to be relatively constant across ageing conditions; however, this may not necessarily be true at higher ageing temperatures where recrystallization is more active. In this case, the constitutive model would require additional crystallographic information or the integration of a grain growth model to obtain a representative simulation of the alloy. If the microstructure is affected during the artificial ageing process, the hardening equations will also need to be modified as the grain-size can contribute to differences in the intrinsic strength of the crystal via the Hall-Petch effect [21, 22]. Finally, despite the ability to incorporate this model into full-field CPFEM, these calculations still require considerable computational power to simulate full RVEs. The use of numerical acceleration techniques is a possibility to enable the efficient application of the current model in larger scale applications [7, 233].

7.5 Future Work

The logical extension of this research is to incorporate the modeling within a CPFEM framework to simulate the localized deformation response for different ageing conditions. The precipitation kinetics model would be beneficial in this investigation as it would be used to generate realistic distributions of precipitate for each heat treatment. From there, it is possible to study formability through the generation of forming limit diagrams (FLD) across various ageing conditions. This can be accomplished via a Marciniak and Kuczynski (MK) based approach or from the direct simulation of forming specimens via FEM.

The framework also provides the right environment to conduct theoretical analyses of artificial ageing. The effect of varying solute concentrations and artificial ageing temperatures can be directly related to the performance of the alloy. This allows researchers to virtually design a heat treatment process to optimize certain properties in the material. Possible investigations include optimizing for the ageing temperature that provides the most strengthening within a

predefined time constraint, or the minimum concentration of solute required to obtain a certain UTS.

From a modeling perspective, a natural extension to this work would be to couple the kinetics and plasticity equations into a single thermodynamically consistent model. For instance, the quantity of dislocations can be related to the rate of heterogeneous nucleation, which would then affect the precipitate distribution and ultimately the strength of the crystal. Furthermore, the model can be extended to incorporate dynamic precipitation during the deformation process. For applications involving large temperature changes such as warm forming, the model can be further extended to include the effect of temperature on the stress-strain properties.

References

[1] O. US EPA, “Midterm Evaluation of Light-Duty Vehicle Greenhouse Gas Emissions Standards for Model Years 2022-2025,” Oct. 06, 2016. https://www.epa.gov/regulations-emissions-vehicles-and-engines/midterm-evaluation-light-duty-vehicle-greenhouse-gas (accessed Feb. 09, 2022).

[2] UACJ, “Types and applications of aluminum alloys for vehicles - Aluminum Automobile Technology,” *UACJ Automobile Technology*, 2019. https://uacj-automobile.com/types_and_applications.html (accessed Sep. 04, 2019).

[3] C. Kohar, “Multi-scale Modeling and Optimization of Energy Absorption and Anisotropy in Aluminum Alloys,” University of Waterloo, 2017. Accessed: Sep. 08, 2019. [Online]. Available: https://uwspace.uwaterloo.ca/handle/10012/11759

[4] D. N. Booth, C. P. Kohar, and K. Inal, “Multi-objective optimization of a multi-cellular aluminum extruded crush rail subjected to dynamic axial and oblique impact loading conditions,” *Thin-Walled Struct.*, vol. 166, p. 108021, Sep. 2021, doi: 10.1016/j.tws.2021.108021.

[5] A. K. Inal, “Numerical Simulation of Sheet Metal Forming Processes and Localized Deformation Phenomena for FCC Polycrystals [microform],” Thesis (Ph.D.)--Université de Sherbrooke, 2001. [Online]. Available: https://books.google.ca/books?id=8iG2YgEACAAJ

[6] T. Kuwabara, T. Mori, M. Asano, T. Hakoyama, and F. Barlat, “Material modeling of 6016-O and 6016-T4 aluminum alloy sheets and application to hole expansion forming simulation,” *Int. J. Plast.*, vol. 93, pp. 164–186, Jun. 2017, doi: 10.1016/j.ijplas.2016.10.002.

[7] O. Ibragimova, A. Brahme, W. Muhammad, J. Lévesque, and K. Inal, “A new ANN based crystal plasticity model for FCC materials and its application to non-monotonic strain paths,” *Int. J. Plast.*, vol. 144, p. 103059, 2021, doi: https://doi.org/10.1016/j.ijplas.2021.103059.

[8] Lumen Learning, *Bonding in Metals: The Electron Sea Model*. Accessed: Dec. 08, 2021. [Image]. Available: https://courses.lumenlearning.com/introchem/chapter/bonding-in-metals-the-electron-sea-model/

[9] *Common metallic crystal structures*. Accessed: Jan. 10, 2022. [Image]. Available: https://www.britannica.com/science/face-centred-cubic-structure

[10] G. I. Taylor, “The mechanism of plastic deformation of crystals. Part I.—Theoretical,” *Proc. R. Soc. Lond. Ser. Contain. Pap. Math. Phys. Character*, vol. 145, no. 855, pp. 362–387, 1934.

[11] P. B. Hirsch, “50 Years of transmission electron microscopy of dislocations: Past, present, and future,” *Her. Russ. Acad. Sci.*, vol. 76, no. 5, pp. 430–436, Oct. 2006, doi: 10.1134/S1019331606050042.

[12] D. R. Askeland, P. P. Fulay, and W. J. Wright, *The science and engineering of materials*. Nelson Education, 2011.

[13] D. Hull and D. J. Bacon, *Introduction to dislocations*, 5. ed. Amsterdam: Elsevier/Butterworth-Heinemann, 2011.

[14] W. D. Callister, *Materials science and engineering: an introduction*, 7th ed. New York: John Wiley & Sons, 2007.

[15] "DOE fundamentals handbook: Material science. Volume 1," United States, Jan. 1993. doi: 10.2172/10154822.
[16] F. C. Frank and W. T. Read, "Multiplication Processes for Slow Moving Dislocations," *Phys. Rev.*, vol. 79, no. 4, pp. 722–723, Aug. 1950, doi: 10.1103/PhysRev.79.722.
[17] R. Madec, B. Devincre, and L. P. Kubin, "From Dislocation Junctions to Forest Hardening," *Phys. Rev. Lett.*, vol. 89, no. 25, p. 255508, Dec. 2002, doi: 10.1103/PhysRevLett.89.255508.
[18] U. F. O. Themes, "Chapter 26 – Biomechanics," *Musculoskeletal Key*, Sep. 07, 2020. https://musculoskeletalkey.com/chapter-26-biomechanics/ (accessed Jan. 30, 2022).
[19] U. F. Kocks, A. S. Argon, and M. F. Ashby, *Thermodynamics and Kinetics of Slip*. Pergamon Press, 1975. [Online]. Available: https://books.google.ca/books?id=B0AkMgEACAAJ
[20] A. Crosky, M. Hoffman, P. Munroe, and B. Allen, "Materials Science: Tutorials: Light Alloys." https://textbooks.elsevier.com/manualsprotectedtextbooks/9780750663809/static/alloys/alloys2a.htm (accessed Jan. 31, 2022).
[21] E. Hall, "The deformation and ageing of mild steel: III discussion of results," *Proc. Phys. Soc. Sect. B*, vol. 64, no. 9, p. 747, 1951.
[22] N. Petch, "The cleavage strength of polycrystals," *J. Iron Steel Inst.*, vol. 174, pp. 25–28, 1953.
[23] T. G. Langdon, "Grain boundary sliding revisited: Developments in sliding over four decades," *J. Mater. Sci.*, vol. 41, no. 3, pp. 597–609, Feb. 2006, doi: 10.1007/s10853-006-6476-0.
[24] A. Wilm, "Physikalisch-metallurgische Untersuchungen über magnesiumhaltige Aluminiumlegierungen," *Metall. Z. Für Gesamte Hüttenkd.*, vol. 8, no. 8, pp. 225–227, 1911.
[25] P. D. Merica and R. G. Waltenberg, "Heat treatment of duralumin," *Sci. Pap. Bur. Stand.*, vol. 347, 1919.
[26] A. Guinier, "Structure of age-hardened aluminium-copper alloys," *Nature*, vol. 142, no. 3595, pp. 569–570, 1938.
[27] S. J. Andersen, C. D. Marioara, J. Friis, S. Wenner, and R. Holmestad, "Precipitates in aluminium alloys," *Adv. Phys. X*, vol. 3, no. 1, p. 1479984, Jan. 2018, doi: 10.1080/23746149.2018.1479984.
[28] J.-F. Nie, "Precipitation and hardening in magnesium alloys," *Metall. Mater. Trans. A*, vol. 43, no. 11, pp. 3891–3939, 2012.
[29] T. Gladman, "Precipitation hardening in metals," *Mater. Sci. Technol.*, vol. 15, no. 1, pp. 30–36, Jan. 1999, doi: 10.1179/026708399773002782.
[30] P. K. Jayashree, M. C. Shankar, A. Kinia, S. S. Sharma, and R. Shetty, "Review on Effect of Silicon Carbide (SiC) on Stir Cast Aluminium Metal Matrix Composites," *Int J Curr Eng Technol*, vol. 3, pp. 1061–1071, Jan. 2013.
[31] A. Deschamps and Y. Brechet, "Influence of predeformation and ageing of an Al–Zn–Mg alloy—II. Modeling of precipitation kinetics and yield stress," *Acta Mater.*, vol. 47, no. 1, pp. 293–305, 1998.
[32] M. Ferrante and R. D. Doherty, "Influence of interfacial properties on the kinetics of precipitation and precipitate coarsening in aluminium-silver alloys," *Acta Metall.*, vol. 27, no. 10, pp. 1603–1614, Oct. 1979, doi: 10.1016/0001-6160(79)90043-9.

[33] J. D. Robson, “Modelling the overlap of nucleation, growth and coarsening during precipitation,” *Acta Mater.*, vol. 52, no. 15, pp. 4669–4676, Sep. 2004, doi: 10.1016/j.actamat.2004.06.024.
[34] L. Ratke and P. W. Voorhees, *Growth and coarsening: Ostwald ripening in material processing*. Springer Science & Business Media, 2002.
[35] JEOL, *Schematic of EBSD pattern acquisition*. Accessed: Jan. 31, 2022. [Image]. Available: https://www.jeol.co.jp/en/words/semterms/search_result.html?keyword=electron%20backscatter%20diffraction%2C%20EBSD
[36] Y. Matsukawa, “Crystallography of Precipitates in Metals and Alloys:(1) Analysis of Crystallography,” in *Crystallography*, IntechOpen, 2019.
[37] C. P. Kohar, A. Brahme, F. Hekmat, R. K. Mishra, and K. Inal, “A computational mechanics engineering framework for predicting the axial crush response of Aluminum extrusions,” *Thin-Walled Struct.*, vol. 140, pp. 516–532, Jul. 2019, doi: 10.1016/j.tws.2019.02.007.
[38] A. P. Brahme, K. Inal, R. K. Mishra, and S. Saimoto, “The backstress effect of evolving deformation boundaries in FCC polycrystals,” *Int. J. Plast.*, vol. 27, no. 8, pp. 1252–1266, Aug. 2011, doi: 10.1016/j.ijplas.2011.02.006.
[39] T. Zhou, R. P. Babu, Z. Hou, and P. Hedström, “On the role of transmission electron microscopy for precipitation analysis in metallic materials,” *Crit. Rev. Solid State Mater. Sci.*, pp. 1–27, Jul. 2021, doi: 10.1080/10408436.2021.1941751.
[40] Y. Kim, R. K. Mishra, A. K. Sachdev, and K. S. Kumar, “A combined experimental-analytical modeling study of the artificial aging response of Al–Mg–Si alloys,” *Mater. Sci. Eng. A*, vol. 820, p. 141566, Jul. 2021, doi: 10.1016/j.msea.2021.141566.
[41] Y. Li, Z. Shi, and J. Lin, “Experimental investigation and modelling of yield strength and work hardening behaviour of artificially aged Al-Cu-Li alloy,” *Mater. Des.*, vol. 183, p. 108121, Dec. 2019, doi: 10.1016/j.matdes.2019.108121.
[42] T. Rahmaan, A. Abedini, C. Butcher, N. Pathak, and M. J. Worswick, “Investigation into the shear stress, localization and fracture behaviour of DP600 and AA5182-O sheet metal alloys under elevated strain rates,” *Int. J. Impact Eng.*, vol. 108, pp. 303–321, Oct. 2017, doi: 10.1016/j.ijimpeng.2017.04.006.
[43] T. Rahmaan, J. Noder, A. Abedini, P. Zhou, C. Butcher, and M. J. Worswick, “Anisotropic plasticity characterization of 6000- and 7000-series aluminum sheet alloys at various strain rates,” *Int. J. Impact Eng.*, vol. 135, p. 103390, Jan. 2020, doi: 10.1016/j.ijimpeng.2019.103390.
[44] L. GmbH, *Digital Image Correlation (DIC)*. Accessed: Jan. 31, 2022. [Image]. Available: https://www.lavision.de/en/techniques/dic-dvc/
[45] K. Kitayama, C. N. Tomé, E. F. Rauch, J. J. Gracio, and F. Barlat, “A crystallographic dislocation model for describing hardening of polycrystals during strain path changes. Application to low carbon steels,” *Int. J. Plast.*, vol. 46, pp. 54–69, Jul. 2013, doi: 10.1016/j.ijplas.2012.09.004.
[46] E. F. Rauch, J. J. Gracio, F. Barlat, and G. Vincze, “Modelling the plastic behaviour of metals under complex loading conditions,” *Model. Simul. Mater. Sci. Eng.*, vol. 19, no. 3, p. 035009, Apr. 2011, doi: 10.1088/0965-0393/19/3/035009.
[47] U. Kocks, “Laws for work-hardening and low-temperature creep,” *J. Eng. Mater. Technol.*, vol. 98, no. 1, pp. 76–85, 1976.

[48] R. J. Asaro and J. Rice, “Strain localization in ductile single crystals,” *J. Mech. Phys. Solids*, vol. 25, no. 5, pp. 309–338, 1977.
[49] D. Peirce, R. J. Asaro, and A. Needleman, “Material rate dependence and localized deformation in crystalline solids,” *Acta Metall.*, vol. 31, no. 12, pp. 1951–1976, Dec. 1983, doi: 10.1016/0001-6160(83)90014-7.
[50] R. J. Asaro, “Material modelling and failure modes in metal plasticity,” *Mech. Mater.*, vol. 4, no. 3–4, pp. 343–373, Dec. 1985, doi: 10.1016/0167-6636(85)90032-8.
[51] A. Needleman, R. J. Asaro, J. Lemonds, and D. Peirce, “Finite element analysis of crystalline solids,” *Comput. Methods Appl. Mech. Eng.*, vol. 52, no. 1–3, pp. 689–708, Sep. 1985, doi: 10.1016/0045-7825(85)90014-3.
[52] J. W. Hutchinson, “Bounds and Self-Consistent Estimates for Creep of Polycrystalline Materials,” *Proc. R. Soc. Math. Phys. Eng. Sci.*, vol. 348, no. 1652, pp. 101–127, Feb. 1976, doi: 10.1098/rspa.1976.0027.
[53] D. S. Connolly, C. P. Kohar, R. K. Mishra, and K. Inal, “A new coupled thermomechanical framework for modeling formability in transformation induced plasticity steels,” *Int. J. Plast.*, vol. 103, pp. 39–66, Apr. 2018, doi: 10.1016/j.ijplas.2017.12.008.
[54] D. S. Connolly, “A New Crystal Plasticity Model for Steels Exhibiting Transformation Induced Plasticity with Application to Quenched and Partitioned Steel,” University of Waterloo, 2021.
[55] E. D. Cyr, A. Brahme, M. Mohammadi, R. K. Mishra, and K. Inal, “A new crystal plasticity framework to simulate the large strain behaviour of aluminum alloys at warm temperatures,” *Mater. Sci. Eng. A*, vol. 727, pp. 11–28, Jun. 2018, doi: 10.1016/j.msea.2018.04.020.
[56] E. Cyr, M. Mohammadi, A. Brahme, R. K. Mishra, and K. Inal, “Modeling the formability of aluminum alloys at elevated temperatures using a new thermo-elasto-viscoplastic crystal plasticity framework,” *Int. J. Mech. Sci.*, vol. 128–129, pp. 312–325, Aug. 2017, doi: 10.1016/j.ijmecsci.2017.05.005.
[57] U. F. Kocks and H. Mecking, “Physics and phenomenology of strain hardening: the FCC case,” *Prog. Mater. Sci.*, vol. 48, no. 3, pp. 171–273, Jan. 2003, doi: 10.1016/S0079-6425(02)00003-8.
[58] H. Mecking and U. F. Kocks, “Kinetics of flow and strain-hardening,” *Acta Metall.*, vol. 29, no. 11, pp. 1865–1875, Nov. 1981, doi: 10.1016/0001-6160(81)90112-7.
[59] G. Sachs, “Zur ableitung einer fliessbedingung,” *Mitteilungen Dtsch. Mater.*, pp. 94–97, 1929.
[60] G. I. Taylor and C. F. Elam, “Bakerian lecture: the distortion of an aluminium crystal during a tensile test,” *Proc. R. Soc. Lond. Ser. Contain. Pap. Math. Phys. Character*, vol. 102, no. 719, pp. 643–667, 1923.
[61] T. H. Lin, “Analysis of elastic and plastic strains of a face-centred cubic crystal,” *J. Mech. Phys. Solids*, vol. 5, no. 2, pp. 143–149, Mar. 1957, doi: 10.1016/0022-5096(57)90058-3.
[62] E. Kröner, “Zur plastischen verformung des vielkristalls,” *Acta Metall.*, vol. 9, no. 2, pp. 155–161, Feb. 1961, doi: 10.1016/0001-6160(61)90060-8.
[63] B. Budiansky and T. T. Wu, “Theoretical prediction of plastic strains of polycrystals,” 1961. [Online]. Available: https://apps.dtic.mil/docs/citations/AD0269234
[64] R. Hill, “Continuum micro-mechanics of elastoplastic polycrystals,” *J. Mech. Phys. Solids*, vol. 13, no. 2, pp. 89–101, Apr. 1965, doi: 10.1016/0022-5096(65)90023-2.

[65] J. J. Bhattacharyya, B. Bittmann, and S. R. Agnew, “The effect of precipitate-induced backstresses on plastic anisotropy: Demonstrated by modeling the behavior of aluminum alloy, 7085,” *Int. J. Plast.*, vol. 117, pp. 3–20, Jun. 2019, doi: 10.1016/j.ijplas.2018.04.011.
[66] R. P. Mulay, B. Clausen, and S. R. Agnew, “In-Situ Neutron Diffraction Study of the Bauschinger Effect in B2 Structured CoZr,” *Metall. Mater. Trans. A*, vol. 42, no. 1, pp. 60–70, Jan. 2011, doi: 10.1007/s11661-010-0389-x.
[67] R. A. Lebensohn, C. N. Tomé, and P. P. CastaÑeda, “Self-consistent modelling of the mechanical behaviour of viscoplastic polycrystals incorporating intragranular field fluctuations,” *Philos. Mag.*, vol. 87, no. 28, pp. 4287–4322, Oct. 2007, doi: 10.1080/14786430701432619.
[68] C. N. Tomé, “Self-consistent polycrystal models: a directional compliance criterion to describe grain interactions,” *Model. Simul. Mater. Sci. Eng.*, vol. 7, no. 5, pp. 723–738, Sep. 1999, doi: 10.1088/0965-0393/7/5/305.
[69] R. Kouddane, N. Zouhal, A. Molinari, and G. R. Canova, “Complex loading of viscoplastic materials: micro-macro modelling,” *Mater. Sci. Eng. A*, vol. 175, no. 1–2, pp. 31–36, Feb. 1994, doi: 10.1016/0921-5093(94)91041-3.
[70] A. Molinari, S. Ahzi, and R. Kouddane, “On the self-consistent modeling of elastic-plastic behavior of polycrystals,” *Mech. Mater.*, vol. 26, no. 1, pp. 43–62, Jul. 1997, doi: 10.1016/S0167-6636(97)00017-3.
[71] H. Wang, P. D. Wu, C. N. Tomé, and Y. Huang, “A finite strain elastic–viscoplastic self-consistent model for polycrystalline materials,” *J. Mech. Phys. Solids*, vol. 58, no. 4, pp. 594–612, Apr. 2010, doi: 10.1016/j.jmps.2010.01.004.
[72] J. D. Eshelby, “The determination of the elastic field of an ellipsoidal inclusion, and related problems,” *Proc. R. Soc. Lond. Ser. Math. Phys. Sci.*, vol. 241, no. 1226, pp. 376–396, 1957.
[73] T. Mori and K. Tanaka, “Average stress in matrix and average elastic energy of materials with misfitting inclusions,” *Acta Metall.*, vol. 21, no. 5, pp. 571–574, May 1973, doi: 10.1016/0001-6160(73)90064-3.
[74] M. Hori and S. Nemat-Nasser, “Double-inclusion model and overall moduli of multi-phase composites,” *Mech. Mater.*, vol. 14, no. 3, pp. 189–206, 1993.
[75] M. Khadyko, C. D. Marioara, I. G. Ringdalen, S. Dumoulin, and O. S. Hopperstad, “Deformation and strain localization in polycrystals with plastically heterogeneous grains,” *Int. J. Plast.*, vol. 86, pp. 128–150, Nov. 2016, doi: 10.1016/j.ijplas.2016.08.005.
[76] O. R. Myhr and Ø. Grong, “Modelling of non-isothermal transformations in alloys containing a particle distribution,” *Acta Mater.*, vol. 48, no. 7, pp. 1605–1615, Apr. 2000, doi: 10.1016/S1359-6454(99)00435-8.
[77] M. Perez, “Gibbs–Thomson effects in phase transformations,” *Scr. Mater.*, vol. 52, no. 8, pp. 709–712, Apr. 2005, doi: 10.1016/j.scriptamat.2004.12.026.
[78] M. Perez, M. Dumont, and D. Acevedo-Reyes, “Implementation of classical nucleation and growth theories for precipitation,” *Acta Mater.*, vol. 56, no. 9, pp. 2119–2132, May 2008, doi: 10.1016/j.actamat.2007.12.050.
[79] C. R. Hutchinson, “Modeling the kinetics of precipitation in aluminium alloys,” *Fundam. Alum. Metall.*, pp. 422–467, 2011, doi: 10.1533/9780857090256.2.422.
[80] C. Sigli, F. De Geuser, A. Deschamps, J. Lépinoux, and M. Perez, “Recent advances in the metallurgy of aluminum alloys. Part II: Age hardening,” *Comptes Rendus Phys.*, vol. 19, no. 8, pp. 688–709, Dec. 2018, doi: 10.1016/j.crhy.2018.10.012.

[81] L. A. Zepeda-Ruiz, A. Stukowski, T. Oppelstrup, and V. V. Bulatov, “Probing the limits of metal plasticity with molecular dynamics simulations,” *Nature*, vol. 550, no. 7677, pp. 492–495, 2017.

[82] Y. Qiu, Y. Kong, S. Xiao, and Y. Du, “Mechanical properties of β″ precipitates containing Al and/or Cu in age hardening Al alloys,” *J. Mater. Res.*, vol. 31, no. 5, pp. 580–588, Mar. 2016, doi: 10.1557/jmr.2016.63.

[83] D. Giofré, T. Junge, W. A. Curtin, and M. Ceriotti, “Ab initio Modelling of the Early Stages of Precipitation in Al-6000 Alloys,” *Acta Mater.*, vol. 140, pp. 240–249, Nov. 2017, doi: 10.1016/j.actamat.2017.08.017.

[84] S. He, J. Wang, D. Zhang, Q. Wu, Y. Kong, and Y. Du, “A First-Principles Study of the Cu-Containing β″ Precipitates in Al-Mg-Si-Cu Alloy,” *Materials*, vol. 14, no. 24, p. 7879, Dec. 2021, doi: 10.3390/ma14247879.

[85] E. Clouet, C. Hin, D. Gendt, M. Nastar, and F. Soisson, “Kinetic Monte Carlo Simulations of Precipitation,” *Adv. Eng. Mater.*, vol. 8, no. 12, pp. 1210–1214, Dec. 2006, doi: 10.1002/adem.200600183.

[86] M. Murayama and K. Hono, “Pre-precipitate clusters and precipitation processes in Al–Mg–Si alloys,” *Acta Mater.*, vol. 47, no. 5, pp. 1537–1548, 1999, doi: https://doi.org/10.1016/S1359-6454(99)00033-6.

[87] K. Matsuda *et al.*, “High-resolution electron microscopy on the structure of Guinier-Preston zones in an Al-1.6 mass Pct Mg2Si alloy,” *Metall. Mater. Trans. A*, vol. 29, no. 4, pp. 1161–1167, Apr. 1998, doi: 10.1007/s11661-998-0242-7.

[88] C. D. Marioara, S. J. Andersen, J. Jansen, and H. W. Zandbergen, “The influence of temperature and storage time at RT on nucleation of the β″ phase in a 6082 Al–Mg–Si alloy,” *Acta Mater.*, vol. 51, no. 3, pp. 789–796, Feb. 2003, doi: 10.1016/S1359-6454(02)00470-6.

[89] H. W. Zandbergen, S. J. Andersen, and J. Jansen, “Structure Determination of Mg_5Si_6 Particles in Al by Dynamic Electron Diffraction Studies,” *Science*, vol. 277, no. 5330, pp. 1221–1225, 1997, doi: 10.1126/science.277.5330.1221.

[90] S. J. Andersen, H. W. Zandbergen, J. Jansen, C. TrÆholt, U. Tundal, and O. Reiso, “The crystal structure of the β″ phase in Al–Mg–Si alloys,” *Acta Mater.*, vol. 46, no. 9, pp. 3283–3298, 1998, doi: https://doi.org/10.1016/S1359-6454(97)00493-X.

[91] C. D. Marioara, S. J. Andersen, H. W. Zandbergen, and R. Holmestad, “The influence of alloy composition on precipitates of the Al-Mg-Si system,” *Metall. Mater. Trans. A*, vol. 36, no. 3, pp. 691–702, Mar. 2005, doi: 10.1007/s11661-005-0185-1.

[92] R. Vissers, M. A. van Huis, J. Jansen, H. W. Zandbergen, C. D. Marioara, and S. J. Andersen, “The crystal structure of the β′ phase in Al–Mg–Si alloys,” *Acta Mater.*, vol. 55, no. 11, pp. 3815–3823, 2007, doi: https://doi.org/10.1016/j.actamat.2007.02.032.

[93] O. Myhr, Ø. Grong, and S. Andersen, “Modelling of the age hardening behaviour of Al–Mg–Si alloys,” *Acta Mater.*, vol. 49, no. 1, pp. 65–75, 2001.

[94] Q. Du, K. Tang, C. D. Marioara, S. J. Andersen, B. Holmedal, and R. Holmestad, “Modeling over-ageing in Al-Mg-Si alloys by a multi-phase CALPHAD-coupled Kampmann-Wagner Numerical model,” *Acta Mater.*, vol. 122, pp. 178–186, Jan. 2017, doi: 10.1016/j.actamat.2016.09.052.

[95] C. D. Marioara, H. Nordmark, S. J. Andersen, and R. Holmestad, “Post-β″ phases and their influence on microstructure and hardness in 6xxx Al-Mg-Si alloys,” *J. Mater. Sci.*, vol. 41, no. 2, pp. 471–478, Jan. 2006, doi: 10.1007/s10853-005-2470-1.

[96] M. H. Jacobs, “The structure of the metastable precipitates formed during ageing of an Al-Mg-Si alloy,” *Philos. Mag. J. Theor. Exp. Appl. Phys.*, vol. 26, no. 1, pp. 1–13, 1972, doi: 10.1080/14786437208221015.
[97] O. Engler and J. Hirsch, “Texture control by thermomechanical processing of AA6xxx Al–Mg–Si sheet alloys for automotive applications—a review,” *Mater. Sci. Eng. A*, vol. 336, no. 1, pp. 249–262, Oct. 2002, doi: 10.1016/S0921-5093(01)01968-2.
[98] Ø. Ryen, B. Holmedal, K. Marthinsen, and T. Furu, “Precipitation, strength and work hardening of age hardened aluminium alloys,” *IOP Conf. Ser. Mater. Sci. Eng.*, vol. 89, p. 012013, Aug. 2015, doi: 10.1088/1757-899X/89/1/012013.
[99] S. Esmaeili, D. J. Lloyd, and W. J. Poole, “A yield strength model for the Al-Mg-Si-Cu alloy AA6111,” *Acta Mater.*, vol. 51, no. 8, pp. 2243–2257, May 2003, doi: 10.1016/S1359-6454(03)00028-4.
[100] D. Bardel *et al.*, “Coupled precipitation and yield strength modelling for non-isothermal treatments of a 6061 aluminium alloy,” *Acta Mater.*, vol. 62, pp. 129–140, Jan. 2014, doi: 10.1016/j.actamat.2013.09.041.
[101] A. Assadiki, V. A. Esin, R. Martinez, W. J. Poole, and G. Cailletaud, “Modelling precipitation hardening in an A356+0.5 wt%Cu cast aluminum alloy,” *Mater. Sci. Eng. A*, vol. 819, p. 141450, Jul. 2021, doi: 10.1016/j.msea.2021.141450.
[102] W. J. Poole, X. Wang, D. J. Lloyd, and J. D. Embury, “The shearable–non-shearable transition in Al–Mg–Si–Cu precipitation hardening alloys: implications on the distribution of slip, work hardening and fracture,” *Philos. Mag.*, vol. 85, no. 26–27, pp. 3113–3135, Sep. 2005, doi: 10.1080/14786430500154935.
[103] S. Nandy, K. Kumar Ray, and D. Das, “Process model to predict yield strength of AA6063 alloy,” *Mater. Sci. Eng. A*, vol. 644, pp. 413–424, Sep. 2015, doi: 10.1016/j.msea.2015.07.070.
[104] S. Esmaeili, L. M. Cheng, A. Deschamps, D. J. Lloyd, and W. J. Poole, “The deformation behaviour of AA6111 as a function of temperature and precipitation state,” *Mater. Sci. Eng. A*, vol. 319–321, pp. 461–465, Dec. 2001, doi: 10.1016/S0921-5093(01)01113-3.
[105] G. Fribourg, Y. Bréchet, A. Deschamps, and A. Simar, “Microstructure-based modelling of isotropic and kinematic strain hardening in a precipitation-hardened aluminium alloy,” *Acta Mater.*, vol. 59, no. 9, pp. 3621–3635, May 2011, doi: 10.1016/j.actamat.2011.02.035.
[106] P. Bate, W. T. Roberts, and D. V. Wilson, “The plastic anisotropy of two-phase aluminium alloys—I. Anisotropy in unidirectional deformation,” *Acta Metall.*, vol. 29, no. 11, pp. 1797–1814, Nov. 1981, doi: 10.1016/0001-6160(81)90106-1.
[107] W. F. Hosford and R. H. Zeisloft, “The anisotropy of age-hardened Al-4 pct Cu single crystals during plane-strain compression,” *Metall. Mater. Trans. B*, vol. 3, no. 1, pp. 113–121, Jan. 1972, doi: 10.1007/BF02680590.
[108] F. Barlat and J. Liu, “Precipitate-induced anisotropy in binary Al-Cu alloys,” *Mater. Sci. Eng. A*, vol. 257, no. 1, pp. 47–61, 1998.
[109] M. Khadyko, C. D. Marioara, S. Dumoulin, T. Børvik, and O. S. Hopperstad, “Effects of heat-treatment on the plastic anisotropy of extruded aluminium alloy AA6063,” *Mater. Sci. Eng. A*, vol. 708, pp. 208–221, Dec. 2017, doi: 10.1016/j.msea.2017.09.133.
[110] K. Liu, F. Mirza, and X. Chen, “Effect of Overaging on the Cyclic Deformation Behavior of an AA6061 Aluminum Alloy,” *Metals*, vol. 8, no. 7, p. 528, Jul. 2018, doi: 10.3390/met8070528.

[111] O. R. Myhr, T. Børvik, C. D. Marioara, S. Wenner, and O. S. Hopperstad, "Nanoscale modelling of combined isotropic and kinematic hardening of 6000 series aluminium alloys," *Mech. Mater.*, vol. 151, p. 103603, Dec. 2020, doi: 10.1016/j.mechmat.2020.103603.
[112] D. Bardel, M. Perez, D. Nelias, S. Dancette, P. Chaudet, and V. Massardier, "Cyclic behaviour of a 6061 aluminium alloy: Coupling precipitation and elastoplastic modelling," *Acta Mater.*, vol. 83, pp. 256–268, Jan. 2015, doi: 10.1016/j.actamat.2014.09.034.
[113] P. Bate, W. T. Roberts, and D. V. Wilson, "The plastic anisotropy of two-phase aluminium alloys—II. anisotropic behaviour in load-reversal tests," *Acta Metall.*, vol. 30, no. 3, pp. 725–737, Mar. 1982, doi: 10.1016/0001-6160(82)90122-5.
[114] D. V. Wilson, "Reversible work hardening in alloys of cubic metals," *Acta Metall.*, vol. 13, no. 7, pp. 807–814, Jul. 1965, doi: 10.1016/0001-6160(65)90145-8.
[115] H. Proudhon, W. J. Poole, X. Wang, and Y. Bréchet, "The role of internal stresses on the plastic deformation of the Al–Mg–Si–Cu alloy AA6111," *Philos. Mag.*, vol. 88, no. 5, pp. 621–640, Feb. 2008, doi: 10.1080/14786430801894569.
[116] N. Mott and F. N. Nabarro, "An attempt to estimate the degree of precipitation hardening, with a simple model," *Proc. Phys. Soc.*, vol. 52, no. 1, p. 86, 1940.
[117] J. C. Fisher, E. W. Hart, and R. H. Pry, "The hardening of metal crystals by precipitate particles," *Acta Metall.*, vol. 1, no. 3, pp. 336–339, May 1953, doi: 10.1016/0001-6160(53)90109-6.
[118] U. F. Kocks, "A statistical theory of flow stress and work-hardening," *Philos. Mag.*, vol. 13, no. 123, pp. 541–566, Mar. 1966, doi: 10.1080/14786436608212647.
[119] A. J. E. Foreman and M. J. Makin, "Dislocation movement through random arrays of obstacles," *Philos. Mag. J. Theor. Exp. Appl. Phys.*, vol. 14, no. 131, pp. 911–924, Oct. 1966, doi: 10.1080/14786436608244762.
[120] A. J. Ardell, "Precipitation hardening," *Metall. Trans. A*, vol. 16, no. 12, pp. 2131–2165, Dec. 1985, doi: 10.1007/BF02670416.
[121] D. Lloyd, "Precipitation hardening," in *Strength of Metals and Alloys (ICSMA 7)*, Elsevier, 1986, pp. 1745–1778.
[122] J. F. Nie and B. C. Muddle, "Strengthening of an Al–Cu–Sn alloy by deformation-resistant precipitate plates," *Acta Mater.*, vol. 56, no. 14, pp. 3490–3501, Aug. 2008, doi: 10.1016/j.actamat.2008.03.028.
[123] A. Bahrami, A. Miroux, and J. Sietsma, "An Age-Hardening Model for Al-Mg-Si Alloys Considering Needle-Shaped Precipitates," *Metall. Mater. Trans. A*, vol. 43, no. 11, pp. 4445–4453, Nov. 2012, doi: 10.1007/s11661-012-1211-8.
[124] N. Anjabin, A. Karimi Taheri, and H. S. Kim, "Crystal plasticity modeling of the effect of precipitate states on the work hardening and plastic anisotropy in an Al–Mg–Si alloy," *Comput. Mater. Sci.*, vol. 83, pp. 78–85, Feb. 2014, doi: 10.1016/j.commatsci.2013.09.031.
[125] Y. Hu, G. Wang, M. Ye, S. Wang, L. Wang, and Y. Rong, "A precipitation hardening model for Al-Cu-Cd alloys," *Mater. Des.*, vol. 151, pp. 123–132, Aug. 2018, doi: 10.1016/j.matdes.2018.04.057.
[126] M. Yang *et al.*, "Quantified contribution of β″ and β′ precipitates to the strengthening of an aged Al–Mg–Si alloy," *Mater. Sci. Eng. A*, vol. 774, p. 138776, Feb. 2020, doi: 10.1016/j.msea.2019.138776.

[127] M. F. Ashby, “The deformation of plastically non-homogeneous materials,” *Philos. Mag. J. Theor. Exp. Appl. Phys.*, vol. 21, no. 170, pp. 399–424, Feb. 1970, doi: 10.1080/14786437008238426.
[128] F. P. E. Dunne, R. Kiwanuka, and A. J. Wilkinson, “Crystal plasticity analysis of micro-deformation, lattice rotation and geometrically necessary dislocation density,” *Proc. R. Soc. Math. Phys. Eng. Sci.*, vol. 468, no. 2145, pp. 2509–2531, Sep. 2012, doi: 10.1098/rspa.2012.0050.
[129] L. M. Cheng, W. J. Poole, J. D. Embury, and D. J. Lloyd, “The influence of precipitation on the work-hardening behavior of the aluminum alloys AA6111 and AA7030,” *Metall. Mater. Trans. A*, vol. 34, no. 11, pp. 2473–2481, Nov. 2003, doi: 10.1007/s11661-003-0007-2.
[130] W. J. Poole and D. J. Lloyd, “Modelling the Stress-Strain Behaviour for Aluminum Alloy AA611,” in *International Conference on Aluminum Alloys*, 2004, p. 6.
[131] H. Sehitoglu, T. Foglesong, and H. Maier, “Precipitate effects on the mechanical behavior of aluminum copper alloys: Part II. Modeling,” *Metall. Mater. Trans. A*, vol. 36, no. 13, pp. 763–770, 2005.
[132] O. R. Myhr, Ø. Grong, and K. O. Pedersen, “A Combined Precipitation, Yield Strength, and Work Hardening Model for Al-Mg-Si Alloys,” *Metall. Mater. Trans. A*, vol. 41, no. 9, pp. 2276–2289, Sep. 2010, doi: 10.1007/s11661-010-0258-7.
[133] O. R. Myhr, C. Schafer, Ø. Grong, O. Engler, H. J. Brinkman, and J. Hirsch, “Modelling the Combined Effect of Room Temperature Storage and Cold Deformation on the Age-Hardening Behaviour of Al-Mg-Si Alloys-Part 1,” *Mater. Sci. Forum*, vol. 794–796, pp. 670–675, Jun. 2014, doi: 10.4028/www.scientific.net/MSF.794-796.670.
[134] M. Khadyko, O. R. Myhr, and O. S. Hopperstad, “Work hardening and plastic anisotropy of naturally and artificially aged aluminium alloy AA6063,” *Mech. Mater.*, vol. 136, p. 103069, Sep. 2019, doi: 10.1016/j.mechmat.2019.103069.
[135] N. A. Fleck, G. M. Muller, M. F. Ashby, and J. W. Hutchinson, “Strain gradient plasticity: theory and experiment,” *Acta Metall. Mater.*, vol. 42, no. 2, pp. 475–487, 1994.
[136] L. Bardella, “A deformation theory of strain gradient crystal plasticity that accounts for geometrically necessary dislocations,” *J. Mech. Phys. Solids*, vol. 54, no. 1, pp. 128–160, Jan. 2006, doi: 10.1016/j.jmps.2005.08.003.
[137] H. Dai, “Geometrically-necessary dislocation density in continuum plasticity theory, FEM implementation and applications,” Massachusetts Institute of Technology, 1997.
[138] E. Orowan, “Symposium on internal stresses in metals and alloys,” *Inst. Met. Lond.*, vol. 451, 1948.
[139] L. M. Brown, “Back-stresses, image stresses, and work-hardening,” *Acta Metall.*, vol. 21, no. 7, pp. 879–885, Jul. 1973, doi: 10.1016/0001-6160(73)90145-4.
[140] L. M. Brown and D. R. Clarke, “Work hardening due to internal stresses in composite materials,” *Acta Metall.*, vol. 23, no. 7, pp. 821–830, 1975.
[141] S. H. Choi, F. Barlat, and J. Liu, “Effect of precipitates on plastic anisotropy for polycrystalline aluminum alloys,” *Metall. Mater. Trans. A*, vol. 32, no. 9, pp. 2239–2247, Sep. 2001, doi: 10.1007/s11661-001-0199-2.
[142] H. Hargarter, M. T. Lyttle, and E. A. Starke, “Effects of preferentially aligned precipitates on plastic anisotropy in Al-Cu-Mg-Ag and Al-Cu alloys,” *Mater. Sci. Eng. A*, vol. 257, no. 1, pp. 87–99, Nov. 1998, doi: 10.1016/S0921-5093(98)00826-0.

[143] S. Queyreau and B. Devincre, “Bauschinger effect in precipitation-strengthened materials: A dislocation dynamics investigation,” *Philos. Mag. Lett.*, vol. 89, no. 7, pp. 419–430, Jul. 2009, doi: 10.1080/09500830903005433.
[144] S. Queyreau, G. Monnet, and B. Devincre, “Orowan strengthening and forest hardening superposition examined by dislocation dynamics simulations,” *Acta Mater.*, vol. 58, no. 17, pp. 5586–5595, Oct. 2010, doi: 10.1016/j.actamat.2010.06.028.
[145] M. Zain-ul-abdein and D. Nélias, “Effect of coherent and incoherent precipitates upon the stress and strain fields of 6xxx aluminium alloys: a numerical analysis,” *Int. J. Mech. Mater. Des.*, vol. 12, no. 2, pp. 255–271, Jun. 2016, doi: 10.1007/s10999-015-9298-x.
[146] J. Jung, J. I. Yoon, J. H. Moon, H. K. Park, and H. S. Kim, “Effect of coarse precipitates on surface roughening of an FCC polycrystalline material using crystal plasticity,” *Comput. Mater. Sci.*, vol. 126, pp. 121–131, Jan. 2017, doi: 10.1016/j.commatsci.2016.09.017.
[147] M. Volmer and A. Weber, “Keimbildung in übersättigten Gebilden,” *Z. Für Phys. Chem.*, vol. 119, no. 1, pp. 277–301, 1926.
[148] Y. B. Zeldovich, “On the theory of new phase formation: cavitation,” *Acta Physicochem USSR*, vol. 18, p. 1, 1943.
[149] C. Zener, “Theory of Growth of Spherical Precipitates from Solid Solution,” *J. Appl. Phys.*, vol. 20, no. 10, pp. 950–953, Oct. 1949, doi: 10.1063/1.1698258.
[150] H. R. Shercliff and M. F. Ashby, “A process model for age hardening of aluminium alloys—I. The model,” *Acta Metall. Mater.*, vol. 38, no. 10, pp. 1789–1802, Oct. 1990, doi: 10.1016/0956-7151(90)90291-N.
[151] H. Shercliff and M. Ashby, “A process model for age hardening of aluminium alloys—II. Applications of the model,” *Acta Metall. Mater.*, vol. 38, no. 10, pp. 1803–1812, 1990.
[152] J. Langer and kAJ Schwartz, “Kinetics of nucleation in near-critical fluids,” *Phys. Rev. A*, vol. 21, no. 3, p. 948, 1980.
[153] R. Kampmann and R. Wagner, “Decomposition of Alloys, P. Haasen, ed,” 1984.
[154] Q. Du, W. J. Poole, and M. A. Wells, “A mathematical model coupled to CALPHAD to predict precipitation kinetics for multicomponent aluminum alloys,” *Acta Mater.*, vol. 60, no. 9, pp. 3830–3839, May 2012, doi: 10.1016/j.actamat.2012.02.050.
[155] S. Esmaeili, D. J. Lloyd, and W. J. Poole, “Modeling of precipitation hardening for the naturally aged Al-Mg-Si-Cu alloy AA6111,” *Acta Mater.*, vol. 51, no. 12, pp. 3467–3481, Jul. 2003, doi: 10.1016/S1359-6454(03)00167-8.
[156] G. Liu, G. J. Zhang, X. D. Ding, J. Sun, and K. H. Chen, “Modeling the strengthening response to aging process of heat-treatable aluminum alloys containing plate/disc- or rod/needle-shaped precipitates,” *Mater. Sci. Eng. A*, vol. 344, no. 1, pp. 113–124, Mar. 2003, doi: 10.1016/S0921-5093(02)00398-2.
[157] M. Song, “Modeling the hardness and yield strength evolutions of aluminum alloy with rod/needle-shaped precipitates,” *Mater. Sci. Eng. A*, vol. 443, no. 1, pp. 172–177, Jan. 2007, doi: 10.1016/j.msea.2006.08.025.
[158] B. Holmedal, E. Osmundsen, and Q. Du, “Precipitation of Non-Spherical Particles in Aluminum Alloys Part I: Generalization of the Kampmann–Wagner Numerical Model,” *Metall. Mater. Trans. A*, vol. 47, no. 1, pp. 581–588, Jan. 2016, doi: 10.1007/s11661-015-3197-5.

[159] K. Wu, Q. Chen, and P. Mason, “Simulation of Precipitation Kinetics with Non-Spherical Particles,” *J. Phase Equilibria Diffus.*, vol. 39, no. 5, pp. 571–583, Oct. 2018, doi: 10.1007/s11669-018-0644-1.
[160] E. Cinkilic, X. Yan, and A. A. Luo, “Modeling Precipitation Hardening and Yield Strength in Cast Al-Si-Mg-Mn Alloys,” *Metals*, vol. 10, no. 10, p. 1356, Oct. 2020, doi: 10.3390/met10101356.
[161] Y. Li, B. Holmedal, H. Li, L. Zhuang, J. Zhang, and Q. Du, “Precipitation and strengthening modeling for disk-shaped particles in aluminum alloys: Size distribution considered,” *Materialia*, vol. 4, pp. 431–443, Dec. 2018, doi: 10.1016/j.mtla.2018.11.001.
[162] R. Chen, Q. Xu, H. Guo, Z. Xia, Q. Wu, and B. Liu, “Modeling the precipitation kinetics and tensile properties in Al-7Si-Mg cast aluminum alloys,” *Mater. Sci. Eng. A*, vol. 685, pp. 403–416, Feb. 2017, doi: 10.1016/j.msea.2016.12.042.
[163] G. Yi, W. Zeng, J. D. Poplawsky, D. A. Cullen, Z. Wang, and M. L. Free, “Characterizing and modeling the precipitation of Mg-rich phases in Al 5xxx alloys aged at low temperatures,” *J. Mater. Sci. Technol.*, vol. 33, no. 9, pp. 991–1003, Sep. 2017, doi: 10.1016/j.jmst.2017.02.001.
[164] Q. Du, B. Holmedal, J. Friis, and C. D. Marioara, “Precipitation of Non-spherical Particles in Aluminum Alloys Part II: Numerical Simulation and Experimental Characterization During Aging Treatment of an Al-Mg-Si Alloy,” *Metall. Mater. Trans. A*, vol. 47, no. 1, pp. 589–599, Jan. 2016, doi: 10.1007/s11661-015-3196-6.
[165] Z. Zhang *et al.*, “ICME guided design of heat-treatable Zn-modified Al–Mg alloys,” *Calphad*, vol. 74, p. 102298, Sep. 2021, doi: 10.1016/j.calphad.2021.102298.
[166] N. Anjabin, “Modeling the Age-Hardening Process of Aluminum Alloys Containing the Prolate/Oblate Shape Precipitates,” *Met. Mater. Int.*, Jan. 2020, doi: 10.1007/s12540-019-00579-7.
[167] E. Clouet, M. Nastar, and C. Sigli, “Nucleation of Al 3 Zr and Al 3 Sc in aluminum alloys: From kinetic Monte Carlo simulations to classical theory,” *Phys. Rev. B*, vol. 69, no. 6, p. 064109, 2004.
[168] F. De Geuser, B. M. Gable, and B. C. Muddle, “CALPHAD based kinetic Monte Carlo simulation of clustering in binary Al-Cu alloy,” *Philos. Mag.*, vol. 91, no. 2, pp. 315–336, Jan. 2011, doi: 10.1080/14786435.2010.519354.
[169] O. I. Gorbatov, Yu. N. Gornostyrev, and P. A. Korzhavyi, “Many-body mechanism of Guinier-Preston zones stabilization in Al–Cu alloys,” *Scr. Mater.*, vol. 138, pp. 130–133, Sep. 2017, doi: 10.1016/j.scriptamat.2017.05.044.
[170] G. Henkelman and H. Jónsson, “Long time scale kinetic Monte Carlo simulations without lattice approximation and predefined event table,” *J. Chem. Phys.*, vol. 115, no. 21, pp. 9657–9666, Dec. 2001, doi: 10.1063/1.1415500.
[171] E. Clouet, A. Barbu, L. Laé, and G. Martin, “Precipitation kinetics of Al3Zr and Al3Sc in aluminum alloys modeled with cluster dynamics,” *Acta Mater.*, vol. 53, no. 8, pp. 2313–2325, May 2005, doi: 10.1016/j.actamat.2005.01.038.
[172] A. Barbu and E. Clouet, “Cluster dynamics modeling of materials: advantages and limitations.,” *Solid State Phenom.*, p. 8, 2007.
[173] T. Jourdan, F. Soisson, E. Clouet, and A. Barbu, “Influence of cluster mobility on Cu precipitation in α-Fe: A cluster dynamics modeling,” *Acta Mater.*, vol. 58, no. 9, pp. 3400–3405, 2010.

[174] J. Lepinoux, "Modelling precipitation in binary alloys by cluster dynamics," *Acta Mater.*, vol. 57, no. 4, pp. 1086–1094, 2009.
[175] T. Stegmüller and F. Haider, "Multi-scale Cluster Dynamics modelling of Guinier–Preston zone formation in binary Al–Cu alloys," *Acta Mater.*, vol. 177, pp. 240–249, Sep. 2019, doi: 10.1016/j.actamat.2019.07.032.
[176] L.-Q. Chen, "Phase-field models for microstructure evolution," *Annu. Rev. Mater. Res.*, vol. 32, no. 1, pp. 113–140, 2002.
[177] A. Deschamps and C. R. Hutchinson, "Precipitation kinetics in metallic alloys: Experiments and modeling," *Acta Mater.*, vol. 220, p. 117338, Nov. 2021, doi: 10.1016/j.actamat.2021.117338.
[178] J. Z. Zhu, T. Wang, A. J. Ardell, S. H. Zhou, Z. K. Liu, and L. Q. Chen, "Three-dimensional phase-field simulations of coarsening kinetics of γ′ particles in binary Ni–Al alloys," *Acta Mater.*, vol. 52, no. 9, pp. 2837–2845, May 2004, doi: 10.1016/j.actamat.2004.02.032.
[179] Y. Gao *et al.*, "Simulation study of precipitation in an Mg–Y–Nd alloy," *Acta Mater.*, vol. 60, no. 12, pp. 4819–4832, Jul. 2012, doi: 10.1016/j.actamat.2012.05.013.
[180] H. Liu, Y. Gao, J. Z. Liu, Y. M. Zhu, Y. Wang, and J. F. Nie, "A simulation study of the shape of β′ precipitates in Mg–Y and Mg–Gd alloys," *Acta Mater.*, vol. 61, no. 2, pp. 453–466, Jan. 2013, doi: 10.1016/j.actamat.2012.09.044.
[181] Y. Ji, B. Ghaffari, M. Li, and L.-Q. Chen, "Phase-field modeling of θ′ precipitation kinetics in 319 aluminum alloys," *Comput. Mater. Sci.*, vol. 151, pp. 84–94, Aug. 2018, doi: 10.1016/j.commatsci.2018.04.051.
[182] S. Y. Hu, J. Murray, H. Weiland, Z. K. Liu, and L. Q. Chen, "Thermodynamic description and growth kinetics of stoichiometric precipitates in the phase-field approach," *Calphad*, vol. 31, no. 2, pp. 303–312, Jun. 2007, doi: 10.1016/j.calphad.2006.08.005.
[183] X. Wang, J. D. Embury, W. J. Poole, S. Esmaeili, and D. J. Lloyd, "Precipitation strengthening of the aluminum alloy AA6111," *Metall. Mater. Trans. A*, vol. 34, no. 12, pp. 2913–2924, Dec. 2003, doi: 10.1007/s11661-003-0191-0.
[184] S. Dumoulin, O. Engler, O. S. Hopperstad, and O. G. Lademo, "Description of plastic anisotropy in AA6063-T6 using the crystal plasticity finite element method," *Model. Simul. Mater. Sci. Eng.*, vol. 20, no. 5, p. 055008, Jun. 2012, doi: 10.1088/0965-0393/20/5/055008.
[185] T. J. Barrett and M. Knezevic, "Deep drawing simulations using the finite element method embedding a multi-level crystal plasticity constitutive law: Experimental verification and sensitivity analysis," *Comput. Methods Appl. Mech. Eng.*, vol. 354, pp. 245–270, Sep. 2019, doi: 10.1016/j.cma.2019.05.035.
[186] Y. Choi, J. Lee, S. S. Panicker, H.-K. Jin, S. K. Panda, and M.-G. Lee, "Mechanical properties, springback, and formability of W-temper and peak aged 7075 aluminum alloy sheets: Experiments and modeling," *Int. J. Mech. Sci.*, vol. 170, p. 105344, Mar. 2020, doi: 10.1016/j.ijmecsci.2019.105344.
[187] A. Saai, I. Westermann, S. Dumoulin, and O. S. Hopperstad, "Crystal plasticity finite element simulations of pure bending of aluminium alloy AA7108," *Int. J. Mater. Form.*, vol. 9, no. 4, pp. 457–469, Sep. 2016, doi: 10.1007/s12289-015-1233-z.
[188] H. Proudhon and W. J. Poole, "The Bauschinger Effect in AA 6111," in *Materials Science Forum*, Jul. 2006, vol. 519–521, pp. 913–918. doi: 10.4028/www.scientific.net/MSF.519-521.913.

[189] S. Mishra, M. Yadava, K. N. Kulkarni, and N. P. Gurao, “A theoretical investigation of the effect of precipitate habit plane on plastic anisotropy in age hardenable aluminium alloys,” *Model. Simul. Mater. Sci. Eng.*, vol. 26, no. 5, p. 055011, Jun. 2018, doi: 10.1088/1361-651X/aac51a.
[190] Z. Guo and W. Sha, “Quantification of Precipitation Hardening and Evolution of Precipitates,” *Mater. Trans.*, vol. 43, no. 6, pp. 1273–1282, 2002, doi: 10.2320/matertrans.43.1273.
[191] K. Teichmann, C. D. Marioara, K. O. Pedersen, and K. Marthinsen, “The effect of simultaneous deformation and annealing on the precipitation behaviour and mechanical properties of an Al–Mg–Si alloy,” *Mater. Sci. Eng. A*, vol. 565, pp. 228–235, Mar. 2013, doi: 10.1016/j.msea.2012.12.042.
[192] D. Achani, O.-G. Lademo, O. Engler, and O. S. Hopperstad, “Evaluation of constitutive models for textured aluminium alloys using plane-strain tension and shear tests,” *Int. J. Mater. Form.*, vol. 4, no. 2, pp. 227–241, Jun. 2011, doi: 10.1007/s12289-011-1033-z.
[193] G. Gruben, E. Fagerholt, O. S. Hopperstad, and T. Børvik, “Fracture characteristics of a cold-rolled dual-phase steel,” *Eur. J. Mech. - ASolids*, vol. 30, no. 3, pp. 204–218, May 2011, doi: 10.1016/j.euromechsol.2011.01.004.
[194] F. Roters, P. Eisenlohr, L. Hantcherli, D. D. Tjahjanto, T. R. Bieler, and D. Raabe, “Overview of constitutive laws, kinematics, homogenization and multiscale methods in crystal plasticity finite-element modeling: Theory, experiments, applications,” *Acta Mater.*, vol. 58, no. 4, pp. 1152–1211, Feb. 2010, doi: 10.1016/j.actamat.2009.10.058.
[195] J. Rossiter, A. Brahme, M. H. Simha, K. Inal, and R. Mishra, “A new crystal plasticity scheme for explicit time integration codes to simulate deformation in 3D microstructures: Effects of strain path, strain rate and thermal softening on localized deformation in the aluminum alloy 5754 during simple shear,” *Int. J. Plast.*, vol. 26, no. 12, pp. 1702–1725, Dec. 2010, doi: 10.1016/j.ijplas.2010.02.007.
[196] K. Zhang, O. Hopperstad, B. Holmedal, and S. Dumoulin, “A robust and efficient substepping scheme for the explicit numerical integration of a rate-dependent crystal plasticity model,” *Int. J. Numer. Methods Eng.*, vol. 99, no. 4, pp. 239–262, 2014.
[197] K. Inal, P. D. Wu, and K. W. Neale, “Finite element analysis of localization in FCC polycrystalline sheets under plane stress tension,” *Int. J. Solids Struct.*, vol. 39, no. 13–14, pp. 3469–3486, Jun. 2002, doi: 10.1016/S0020-7683(02)00162-2.
[198] A. Molinari and L. S. Tóth, “Tuning a self consistent viscoplastic model by finite element results—I. Modeling,” *Acta Metall. Mater.*, vol. 42, no. 7, pp. 2453–2458, Jul. 1994, doi: 10.1016/0956-7151(94)90324-7.
[199] J. J. Bhattacharyya, T. T. Sasaki, T. Nakata, K. Hono, S. Kamado, and S. R. Agnew, “Determining the strength of GP zones in Mg alloy AXM10304, both parallel and perpendicular to the zone,” *Acta Mater.*, vol. 171, pp. 231–239, Jun. 2019, doi: 10.1016/j.actamat.2019.04.035.
[200] O. Pierard, J. LLorca, J. Segurado, and I. Doghri, “Micromechanics of particle-reinforced elasto-viscoplastic composites: Finite element simulations versus affine homogenization,” *Int. J. Plast.*, vol. 23, no. 6, pp. 1041–1060, Jun. 2007, doi: 10.1016/j.ijplas.2006.09.003.
[201] I. Doghri, L. Brassart, L. Adam, and J.-S. Gérard, “A second-moment incremental formulation for the mean-field homogenization of elasto-plastic composites,” *Int. J. Plast.*, vol. 27, no. 3, pp. 352–371, Mar. 2011, doi: 10.1016/j.ijplas.2010.06.004.

[202] R. A. Lebensohn and C. N. Tomé, “A self-consistent anisotropic approach for the simulation of plastic deformation and texture development of polycrystals: Application to zirconium alloys,” *Acta Metall. Mater.*, vol. 41, no. 9, pp. 2611–2624, Sep. 1993, doi: 10.1016/0956-7151(93)90130-K.
[203] S. Nemat-Nasser and M. Obata, “Rate-Dependent, Finite Elasto-Plastic Deformation of Polycrystals,” *Proc. R. Soc. Math. Phys. Eng. Sci.*, vol. 407, no. 1833, pp. 343–375, Oct. 1986, doi: 10.1098/rspa.1986.0101.
[204] S. Mercier and A. Molinari, “Homogenization of elastic–viscoplastic heterogeneous materials: Self-consistent and Mori-Tanaka schemes,” *Int. J. Plast.*, vol. 25, no. 6, pp. 1024–1048, Jun. 2009, doi: 10.1016/j.ijplas.2008.08.006.
[205] S. Mercier, A. Molinari, S. Berbenni, and M. Berveiller, “Comparison of different homogenization approaches for elastic–viscoplastic materials,” *Model. Simul. Mater. Sci. Eng.*, vol. 20, no. 2, p. 024004, Mar. 2012, doi: 10.1088/0965-0393/20/2/024004.
[206] A. Molinari, F. El Houdaigui, and L. S. Tóth, “Validation of the tangent formulation for the solution of the non-linear Eshelby inclusion problem,” *Int. J. Plast.*, vol. 20, no. 2, pp. 291–307, Feb. 2004, doi: 10.1016/S0749-6419(03)00038-X.
[207] B. Q. Li and F. E. Wawner, “Dislocation interaction with semicoherent precipitates (Ω phase) in deformed Al–Cu–Mg–Ag alloy,” *Acta Mater.*, vol. 46, no. 15, pp. 5483–5490, Sep. 1998, doi: 10.1016/S1359-6454(98)00188-8.
[208] A. Brahme, M. H. Alvi, D. Saylor, J. Fridy, and A. D. Rollett, “3D reconstruction of microstructure in a commercial purity aluminum,” *Scr. Mater.*, vol. 55, no. 1, pp. 75–80, Jul. 2006, doi: 10.1016/j.scriptamat.2006.02.017.
[209] A. Jain *et al.*, “Commentary: The Materials Project: A materials genome approach to accelerating materials innovation,” *APL Mater.*, vol. 1, no. 1, p. 011002, Jul. 2013, doi: 10.1063/1.4812323.
[210] W. Muhammad *et al.*, “Bendability enhancement of an age-hardenable aluminum alloy: Part II — multiscale numerical modeling of shear banding and fracture,” *Mater. Sci. Eng. A*, vol. 754, pp. 161–177, Apr. 2019, doi: 10.1016/j.msea.2019.03.050.
[211] R. Crooks, Z. Wang, V. I. Levit, and R. N. Shenoy, “Microtexture, micro structure and plastic anisotropy of AA2195,” *Mater. Sci. Eng. A*, vol. 257, no. 1, pp. 145–152, Nov. 1998, doi: 10.1016/S0921-5093(98)00833-8.
[212] S. Mishra, K. Kulkarni, and N. P. Gurao, “Effect of crystallographic texture on precipitation induced anisotropy in an aluminium magnesium silicon alloy,” *Mater. Des.*, vol. 87, pp. 507–519, Dec. 2015, doi: 10.1016/j.matdes.2015.08.008.
[213] P. Jobson and W. T. Roberts, “Directionality in a precipitation-hardened alloy,” *Metall. Trans. A*, vol. 8, no. 12, pp. 2013–2014, Dec. 1977, doi: 10.1007/BF02646576.
[214] D. Jiang, “The motion of deformable ellipsoids in power-law viscous materials: Formulation and numerical implementation of a micromechanical approach applicable to flow partitioning and heterogeneous deformation in Earth’s lithosphere,” *J. Struct. Geol.*, vol. 50, pp. 22–34, May 2013, doi: 10.1016/j.jsg.2012.06.011.
[215] A. Bendo *et al.*, “Characterisation of structural similarities of precipitates in Mg–Zn and Al–Zn–Mg alloys systems,” *Philos. Mag.*, vol. 99, no. 21, pp. 2619–2635, Nov. 2019, doi: 10.1080/14786435.2019.1637032.
[216] L. Zhang *et al.*, “Texture, Microstructure and Mechanical Properties of 6111 Aluminum Alloy Subject to Rolling Deformation,” *Mater. Res.*, vol. 20, pp. 1360–1368, 2017.

[217] J. da Costa Teixeira, Y. Bréchet, Y. Estrin, and C. Hutchinson, "The strain hardening behaviour of supersaturated Al-Cu alloys," presented at the Proceedings of the 12th International Conference on Aluminium Alloys, Sept, 2010.
[218] S. Khani Moghanaki and M. Kazeminezhad, "Modeling of the mutual effect of dynamic precipitation and dislocation density in age hardenable aluminum alloys," *J. Alloys Compd.*, vol. 683, pp. 527–532, Oct. 2016, doi: 10.1016/j.jallcom.2016.05.133.
[219] J. Jiang, A. Godfrey, W. Liu, and Q. Liu, "Microtexture evolution via deformation twinning and slip during compression of magnesium alloy AZ31," *Mater. Sci. Eng. A*, vol. 483–484, pp. 576–579, Jun. 2008, doi: 10.1016/j.msea.2006.07.175.
[220] K. Renard, H. Idrissi, D. Schryvers, and P. J. Jacques, "On the stress state dependence of the twinning rate and work hardening in twinning-induced plasticity steels," *Scr. Mater.*, vol. 66, no. 12, pp. 966–971, Jun. 2012, doi: 10.1016/j.scriptamat.2012.01.063.
[221] K. E. K. Amouzou, T. Richeton, A. Roth, M. A. Lebyodkin, and T. A. Lebedkina, "Micromechanical modeling of hardening mechanisms in commercially pure α-titanium in tensile condition," *Int. J. Plast.*, vol. 80, pp. 222–240, May 2016, doi: 10.1016/j.ijplas.2015.09.008.
[222] H. Sehitoglu, T. Foglesong, and H. Maier, "Precipitate effects on the mechanical behavior of aluminum copper alloys: Part I. Experiments," *Metall. Mater. Trans. A*, vol. 36, no. 3, pp. 749–761, 2005.
[223] R. E. Stoltz and R. M. Pelloux, "The Bauschinger effect in precipitation strengthened aluminum alloys," *Metall. Trans. A*, vol. 7, no. 8, pp. 1295–1306, Aug. 1976, doi: 10.1007/BF02658814.
[224] W. Gan, H. J. Bong, H. Lim, R. K. Boger, F. Barlat, and R. H. Wagoner, "Mechanism of the Bauschinger effect in Al-Ge-Si alloys," *Mater. Sci. Eng. A*, vol. 684, pp. 353–372, Jan. 2017, doi: 10.1016/j.msea.2016.12.020.
[225] Y. L. Li, C. P. Kohar, R. K. Mishra, and K. Inal, "A new crystal plasticity constitutive model for simulating precipitation-hardenable aluminum alloys," *Int. J. Plast.*, vol. 132, p. 102759, Sep. 2020, doi: 10.1016/j.ijplas.2020.102759.
[226] H. Feufel, T. Gödecke, H. L. Lukas, and F. Sommer, "Investigation of the Al-Mg-Si system by experiments and thermodynamic calculations," *J. Alloys Compd.*, vol. 247, no. 1, pp. 31–42, 1997, doi: https://doi.org/10.1016/S0925-8388(96)02655-2.
[227] H. Zhang *et al.*, "Solvus boundaries of (meta)stable phases in the Al–Mg–Si system: First-principles phonon calculations and thermodynamic modeling," *Calphad*, vol. 34, no. 1, pp. 20–25, Mar. 2010, doi: 10.1016/j.calphad.2009.10.009.
[228] O. Grong, *Metallurgical modelling of welding*. 1997.
[229] C. P. Kohar, J. L. Bassani, A. Brahme, W. Muhammad, R. K. Mishra, and K. Inal, "A new multi-scale framework to incorporate microstructure evolution in phenomenological plasticity: Theory, explicit finite element formulation, implementation and validation," *Int. J. Plast.*, p. S0749641917303157, Sep. 2017, doi: 10.1016/j.ijplas.2017.08.006.
[230] J. J. Gracio, F. Barlat, E. F. Rauch, P. T. Jones, V. F. Neto, and A. B. Lopes, "Artificial aging and shear deformation behaviour of 6022 aluminium alloy," *Int. J. Plast.*, vol. 20, no. 3, pp. 427–445, Mar. 2004, doi: 10.1016/S0749-6419(03)00095-0.
[231] B. Milligan, D. Ma, L. Allard, A. Clarke, and A. Shyam, "Crystallographic orientation-dependent strain hardening in a precipitation-strengthened Al-Cu alloy," *Acta Mater.*, vol. 205, p. 116577, Feb. 2021, doi: 10.1016/j.actamat.2020.116577.

[232] W. Muhammad, A. P. Brahme, J. Kang, R. K. Mishra, and K. Inal, “Experimental and numerical investigation of texture evolution and the effects of intragranular backstresses in aluminum alloys subjected to large strain cyclic deformation,” *Int. J. Plast.*, vol. 93, pp. 137–163, Jun. 2017, doi: 10.1016/j.ijplas.2016.11.003.
[233] J. S. Nagra, A. Brahme, R. A. Lebensohn, and K. Inal, “Efficient fast Fourier transform-based numerical implementation to simulate large strain behavior of polycrystalline materials,” *Int. J. Plast.*, vol. 98, pp. 65–82, Nov. 2017, doi: 10.1016/j.ijplas.2017.07.001.